3D brain tissue model for characterization of extracellular vesicles as diagnostic biomarkers of TBI

Peter Hsi[1,2,3], David L. Kaplan[1], Vishal Tandon[2,3]

[1]Department of Biomedical Engineering, Tufts University, [2]Division of Bioengineering, Draper, [3]Draper Scholar Program, Draper

ABSTRACT: Traumatic brain injuries (TBIs) present significant challenges in diagnosis and treatment due to their complex and heterogeneous nature. Limited methodologies for studying TBI hinder our comprehensive understanding of injury progression and development of treatments[1]. Extracellular vesicles (EVs) secreted by cells hold promise as diagnostic biomarkers for TBI because their cargo contents can reflect the state of the tissue they are from[2]. Here we 1) use an established in vitro 3D brain model of TBI[3] to characterize differences in EVs and their microRNA content after injury, and 2) integrate this model into Draper's multi-organ system (MOS) platform, as a step towards creating a neurovascular unit model to study injured brain tissue and EVs under fluid flow conditions. Initial findings indicate distinct microRNA alterations in EVs following tissue injury, and that the MOS platform supports robust neuron cultures for further investigation.

INTRODUCTION

Background:

Traumatic brain injury (TBI) leads to high rates of dysfunction as well as mortality and there are no effective therapeutics to ameliorate the effects[1]. Current diagnostic and prognostic tools struggle to capture the diverse nature and progression of TBI, complicating the development of new treatment strategies. Extracellular vesicles (EVs) play a key role in neurodevelopment and brain function, and their packaged contents make them potential biomarkers for TBI[2]. However, methods to study TBI are limited by low throughput animal models, and clinical samples that are difficult to obtain. This research focuses on studying EVs in an in vitro TBI model[3], and integrating the model into Draper's multi-organ system (MOS) platform.This work aims to improve the precision of TBI diagnostics and identify targets for future therapeutics.

Objective:

1) Isolate and characterize EVs from an in vitro 3D brain tissue model of TBI to better understand underlying pathways associated with injury progression
2) Integrate 3D brain tissue model into Draper's MOS system to create an advanced screening platform to evaluate neurological injury

METHODS

3D scaffolds are fabricated using silk biomaterial, and neural cultures are created following previously established protocols by the Kaplan Lab[3,4,5].

Injury Model and EV Analysis:

1. Culture neural cells and mature model
2. Injure tissue to simulate TBI (controlled cortical impact (CCI))
3. Collect neural cell culture supernatant post-injury
4. Isolation of EVs
5. Characterization of size, protein expression, and microRNA content

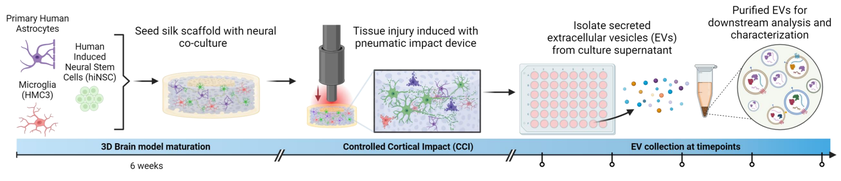

Figure 1. TBI model establishment and EV analysis workflow.

Platform Integration:

1. Silk scaffolds are trimmed and shaped with 3D printed molds
2. Scaffolds are seeded with neural stem cells and inserted into MOS plate
3. Cultures are monitored for proper growth and differentiation
4. Well adapters can be used to quickly transfer scaffolds into and out of platform for interrogation

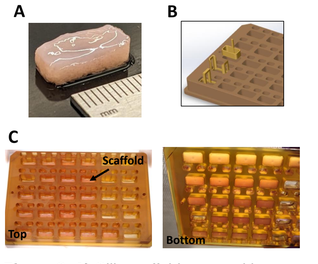

Figure 2. **A)** Silk scaffold encased in collagen. **B)** Example well adapter designs. **C)** Top and bottom view of MOS plate with inserted scaffold.

RESULTS

Neuronal networks are lost post tissue injury

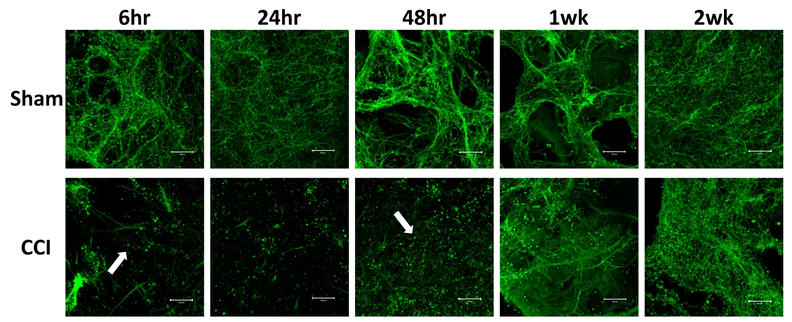

Figure 3. CCI leads to the destruction of neuronal networks indicated by white arrows. Representative confocal microscopy 10x magnification immunofluorescence images of Sham (not injured control) and CCI treatments over time. Neurons networks are stained with beta-III tubulin (TUJ1). Scale bar = 100 µm.

EVs from TBI model can be isolated and characterized

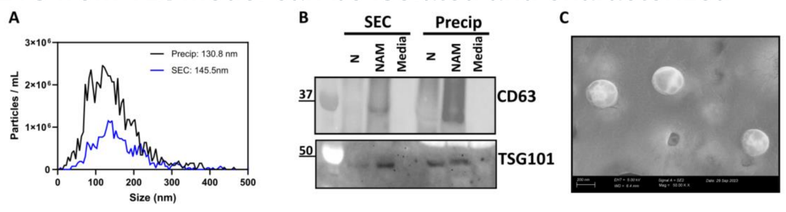

Figure 4. EVs isolated from 3D cultures with precipitation (precip) or size exclusion chromatography (SEC) methods. **A)** EV size (nm) plotted against concentration as measured by nanoparticle tracking analysis (ZetaView). **B)** Western blot for EV markers CD63 and TSG101 show positive staining in monocultures (N) and tricultures (NAM) and are negative in plain media controls. **C)** SEM imaging shows round particles near 200 nm in size.

miRNA isolated from EVs show differential expression

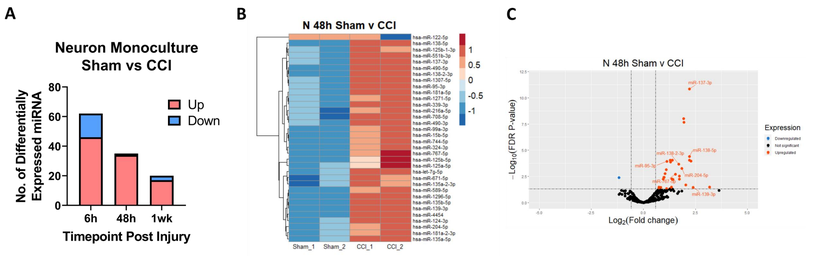

Figure 5. miRNA-sequencing show differential expression over time post-CCI. **A)** Total number of significantly upregulated (red) or downregulated (blue) miRNA across 3 timepoints in neuron monocultures. FDR adjusted p-value < 0.05, fold change +/- 1.5x. **B)** Heat map of 48h timepoint of differentially expressed miRNA. **C)** Volcano plot of 48h timepoint, with commonly differentially expressed miRNA from all timepoints labeled.

Platform Integration: Neural stem cells remain viable and mature into neurons in MOS system

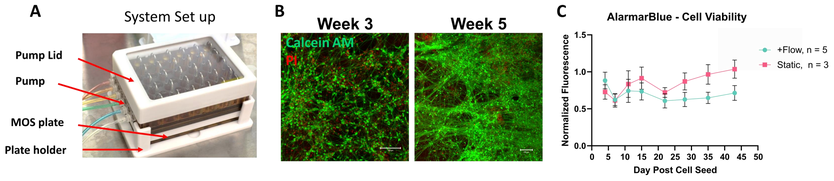

Figure 6. **A)** Full system set up including both the MOS plate and pump. **B)** Calcein AM / PI live dead staining show live cells and development of neuronal networks over time. **C)** AlamarBlue cell viability assay shows stable culture viability for 6 weeks in both tissues seeded into the system (+Flow) and to static controls.

DISCUSSION

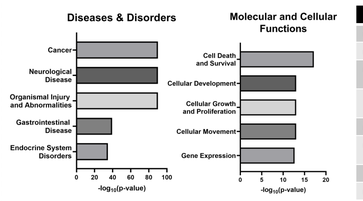

miRNA	Expression	Functions / Brain involvement
miR-490-3p	Up	May be involved in progression of glioma
miR-767-5p	Up	Found in plasma EVs collected from patients with neurodegenerative diseases
miR-204-5p	Up	May ameliorate neurological injury via the EphA4/ PI3K/AKT signaling pathway, may activate cleaved caspase 3
miR-138-2-3p	Up	High conserved and expressed in brain, overexpression may lead to Ab expression
miR-138-5p	Up	May modulate glioma cell growth by suppressing Akt / mTOR signaling pathway
miR-137-3p	Up	Important in neural development, downregulate oxidative stress, enriched in serum of TBI patients
miR-95-3p	Up	Increased in children experiencing persistent post concussion symptoms in saliva
miR-139-3p	Up	May be a negative regulator for NSC proliferation and neuronal

Figure 7. Top diseases and disorders, and molecular and cellular functions associated with the common differentially expressed miRNA found using Ingenuity Pathway Analysis. Table describes various functions and associations of the miRNA in the brain that have been reported in the literature.

EV characterization: miRNA from isolated EVs may show differences in expression after CCI. Pathway analysis of these miRNA are associated with cell injury and pathways of cell survival and apoptosis. Further validation of the mRNA targets is needed to better understand interactions.

Platform Integration: Neurons remain viable in the system over time, but additional cell types need to be incorporated to establish a blood-brain-barrier. Fluid flow will need to be tested to study the effect of different flow rates on tissue growth and viability. The tissue also needs to be injured or challenged in the system. Development of additional sensors, such as for continuous glutamate monitoring may help better characterize injury.

CONCLUSIONS

TBI presents a significant challenge in both clinical management and research due to its complexity and the limited study tools available. To address these challenges, we use a 3D brain tissue model to study TBI and analyze the secreted EVs to gain a deeper understanding of the underlying pathways associated with the progression of this disease. Additionally, integration of the model into Draper's MOS platform will allow for increased tissue complexity, and screening of additional injury mechanisms (ex. Blast). Findings may improve the precision of our diagnostic capabilities and identify targets for future therapeutics.

Next Steps:

- miRNA pathway analysis
- RNA-sequencing
- qPCR validation
- Correlate findings with in vivo and clinical data
- BBB model integration

REFERENCES / ACKNOWLEDGEMENTS

[1] Galgano, M., et al., *Traumatic Brain Injury: Current Treatment Strategies and Future Endeavors.* Cell Transplant, 2017. 26(7): p. 1118-1130.
[2] Guedes, V.A., et al., *Extracellular Vesicle Proteins and MicroRNAs as Biomarkers for Traumatic Brain Injury.* Front Neurol, 2020. 11: p. 663.
[3] Liaudanskaya, V., et al., *Modeling Controlled Cortical Impact Injury in 3D Brain-Like Tissue Cultures.* Adv Healthc Mater, 2020. 9(12): p.e2000122.
[4] Rockwood, D.N., et al., *Materials fabrication from Bombyx mori silk fibroin.* Nat Protoc, 2011. 6(10): p. 1612-31.
[5] Liaudanskaya, V., et al., *Mitochondria dysregulation contributes to secondary neurodegeneration progression post-contusion injury in human 3D in vitro triculture brain tissue model.* Cell Death and Disease, 2023.
[6] Di Pietro, V., et al., Salivary MicroRNAs: *Diagnostic Markers of Mild Traumatic Brain Injury in Contact-Sport.* Front Mol Neurosci, 2018. 11: p. 290.

We would like to thank the Draper Scholar Program, and the NIH (P41EB027062) as funding sources, Dr. Adam Mullis, Dr. Chunmei Li , Marilyn Kelly, Marly Coe and Liam Power for help with the brain tissue model and analyses, the Tufts Genomics Core for help with RNA-sequencing, Dr. Jenny Walker, Dr. Brett Isenberg, and Anthony Quinnert for help with the Draper platform development, and the Boston Children's Hospital Cell Function and Imaging Core for use of the ZetaView instrument.

Stereo Thermoclinometry (STC): A Method to Characterize Asteroid Shapes Using Infrared Images

Koundinya Kuppa[1,*], Jay W. McMahon[1,#], Ann B. Dietrich[¶]

[1]University of Colorado-Boulder, [2]Draper

[*]Draper Scholar, [#]Associate Professor, [¶]Senior Member of Technical Staff

ABSTRACT: Accurate shape characterization is vital to robust navigation efforts in the proximity of asteroids. Currently, a method known as stereo photoclinometry (SPC) is used to derive an accurate shape models from optical images but at a high computational cost. We propose a computationally efficient algorithm called stereo thermoclinometry (STC) to derive accurate shape models of asteroids using infrared (IR) images. The algorithm uses IR images to first derive the surface orientations of an asteroid which are subsequently used to derive the shape vertices using a numerical optimization algorithm. This work showcases a simplified demonstration of the proposed algorithm, using a spherical asteroid with a single crater. The resultant shape model showed approximately an 80% reduction in errors (on average) compared with the initial shape model. The resultant surface orientations of the crater rim are worse than the bottom of the crater. Due to these orientation errors, some artifacts are present in the resultant shape vertices.

INTRODUCTION

- **Accurate asteroid shapes** are necessary to ensure successful operations in the vicinity of asteroids
  - These models are vital to **robust navigation efforts** and are useful **scientific data products**
- Currently, a method known a **stereo photoclinometry** (SPC[1]) is extensively used to estimate asteroids shapes from spacecraft imagery[2,3]
  - While this method produces accurate shapes, it is **computationally expensive** and requires human-in-the-loop processing and thus **not autonomous**
- We propose **Stereo Thermoclinometry** (STC) in which **infrared (IR) images** are used to infer the shape of an asteroid
  - This method is designed to be **computationally efficient** with the intent to drive towards **autonomous** on-board usage

STC METHOD

- The method uses a **thermo-physical model[4]** (TPM) to predict temperatures on an initial shape model (with vertices $\boldsymbol{v}$ and facets F) of an asteroid
- Using the predicted sub-surface temperatures $\tilde{T}_{ss}$ (from the TPM) and measured surface temperatures T_{surf} (from IR images), the **surface orientations** $\hat{\boldsymbol{n}}_{est}$ for each facet F of the shape model are estimated ("*clinometry*")
  - $\hat{\boldsymbol{n}}_{est}$ can be derived from $\tilde{T}_{ss}$, T_{surf}, sun direction, and thermal properties
- A **trust-region optimization algorithm** is used to find vertices $\boldsymbol{v}^*$ corresponding to these **estimated facet orientations** $\hat{\boldsymbol{n}}_{est}$
- The updated vertices $\boldsymbol{v}^*$ and facets F can be used to re-predict temperatures using the TPM
  - When the residual between the measured T_{surf} and predicted $\tilde{T}_{surf}$ surface temperatures is less than a defined threshold ϵ, convergence is achieved

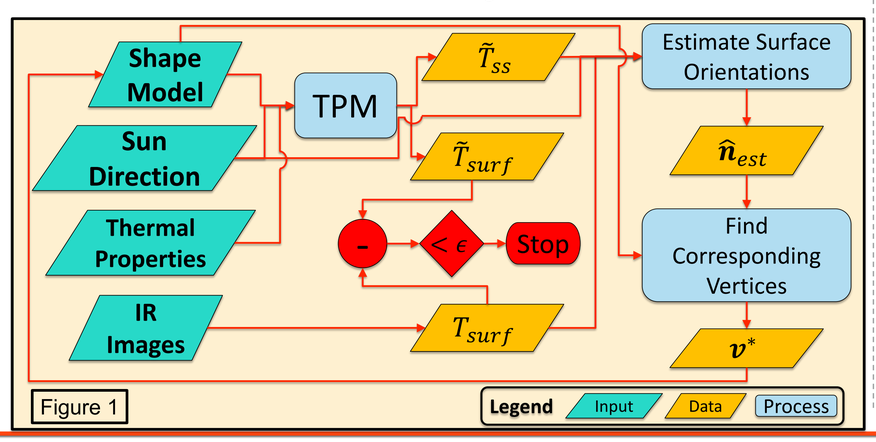

Figure 1

RESULTS

- A **sphere** of radius 250 m with a **crater** of 25 m depth is the **true shape model** (Figure 2)
  - A **perfect sphere** of the same radius is used as the **initial shape model** (left plot in Figure 4)
- A TPM[4] is used to simulate both the predicted ($\tilde{T}_{ss}$ and $\tilde{T}_{surf}$) and measured temperatures T_{surf} using the initial and true shape models respectively
  - **Gaussian measurement noise** with a σ of 1 K is added to the measured temperatures T_{surf} (shown in Figure 2)
- 73 images are taken over one spin period of the asteroid (~7.3hrs). One image approximately every 6 min
- **One iteration** of the STC method (Figure 1) is applied to derive an improved shape model
- Errors in estimated surface orientations $\hat{\boldsymbol{n}}_{est}$ for the crater facets are shown in Figure 3
  - Mean error for the crater bottom facets is **1.5 deg**
  - Mean error for the crater rim facets is **23.6 deg**
- Vertices $\boldsymbol{v}^*$ corresponding to these estimated orientations $\hat{\boldsymbol{n}}_{est}$ are derived using a **trust-region optimization method**. This **shape model** along with the **initial shape model** are shown in the right and left plots of Figure 4. This figure shows the error in each shape model vertex compared to its closest vertex in the reference/true shape model
  - The estimated vertices $\boldsymbol{v}^*$ (right plot of Figure 4) have a **mean error** of 0.821 m, **median error** of -1.93 m, and standard-deviation of 6.41 m
  - A comparison of the initial and optimized vertex errors is shown in the box-plot in Figure 5

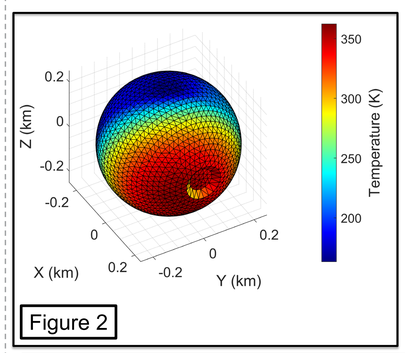

Figure 2

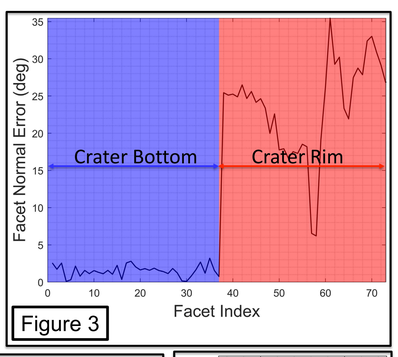

Figure 3

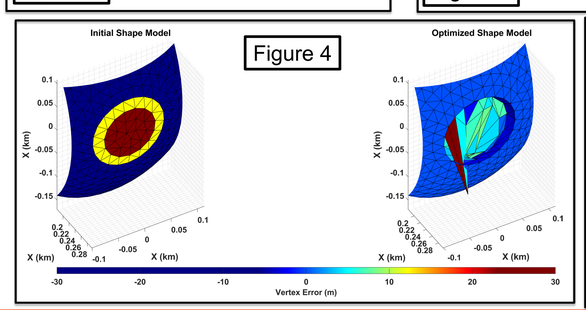

Figure 4

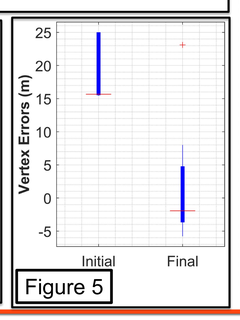

Figure 5

DISCUSSION

- The resultant shape model is an **improvement** (**80% reduction** in error on average) compared to the initial shape model albeit with **some artifacts** (as shown by the boxplot in Figure 5)
  - The initial errors range between **15 m and 25 m**
  - The final errors range between **-5 m and 5 m**
  - There is **one outlier with 25 m error** which corresponds to the protruding vertex in the right plot of Figure 4
- Surface orientation estimates $\hat{\boldsymbol{n}}_{est}$ are **significantly affected** by errors in **predicted sub-surface temperatures** $\tilde{T}_{ss}$ (as shown in Figure 3)
  - $\tilde{T}_{ss}$ for the crater bottom are well predicted and hence those $\hat{\boldsymbol{n}}_{est}$ are estimated well (with errors <3.2 deg)
  - $\tilde{T}_{ss}$ for the crater rim are not well predicted and hence those $\hat{\boldsymbol{n}}_{est}$ are correspondingly poor (with errors approximately 23 deg)
- Due to the **higher error** in the **crater rim facets** orientations, the resultant vertices **exhibit some artifacts** (Figure 4)
  - Some vertices are outside of the visual hull (protruding vertex in the right plot)
  - Some facets of the resultant shape model intersect other facets
  - The crater depth is not accurately captured (~5 m error)

CONCLUSIONS

- Demonstrated STC: a **computationally efficient** method of asteroid shape characterization
- Resultant shape model is an **improvement** over the initial model albeit with some artifacts
- Future work aims to alleviate these artifacts using one or more of the following techniques (**the first two show good initial results**):
  - Constraint the vertices to prevent them from going outside of the visual hull
  - Enforce a "no intersecting facets" constraint
  - Use artificial potential functions to the optimizer to shape the solution space and prevent artifacts in the presence of surface orientation errors
- Iterate on the STC method to and characterize shape model performance improvements for each iteration

REFERENCES

1. Gaskell, R. W., et al. (2008). Characterizing and navigating small bodies with imaging data. Meteoritics & Planetary Science, 43(6), 1049–1061.
2. Park, R. S., et al. (2019). High-resolution shape model of Ceres from stereophotoclinometry using Dawn Imaging Data. Icarus, 319, 812–827.
3. Gaskell, R. W., et al. (2023). Stereophotoclinometry on the OSIRIS-REx Mission: Mathematics and Methods. The Planetary Science Journal, 4(4), 63.
4. Kanamaru, M., et al. (2023). Thermophysical Model Development for Hera Mission to Simulate Non-Gravitational Acceleration on Binary Asteroid. 34th International Symposium on Space Technology and Science.

Robust, Chance-Constrained Spacecraft Guidance

Analyzing Uncertainty in the Mars Launch Test Case

Kristen Ahner[1,*], Daniel Scheeres[1], Jay McMahon[1], and Michele Carpenter[2]

[1]University of Colorado Boulder, [2]The Charles Stark Draper Laboratory, Inc., *Draper Scholar

ABSTRACT: Spacecraft state uncertainty is a critical challenge due to the unpredictable nature of space dynamics. As complex, nonlinear dynamics cause errors to grow over time and drive a trajectory to deviate from its planned path, corrective guidance algorithms must adaptively re-optimize the spacecraft thrust profile to **reach target states** and **achieve mission goals**. We study the Mars Sample Return launch problem to 1) better understand how uncertainties evolve throughout a guided trajectory and 2) build a plan to combine guidance with efficient uncertainty propagation and control theory techniques. The implemented linear tangent guidance enables trajectories to hit the desired altitude but yields a large variation in the resulting orbit. Future work aims to develop robust, chance-constrained guidance that bounds state uncertainty rather than constraining a single deterministic state.

INTRODUCTION

- Near-Earth and cislunar space are becoming increasingly congested, driving the need to proactively protect a growing number of spacecraft in regions with chaotic dynamics.
- Guidance under uncertainty offers an avenue to correct a spacecraft trajectory while accounting for an entire uncertainty volume.
- The Mars launch problem serves as a testing bed for application and improvement of analytical guidance techniques.

Mars Launch

- The Mars Ascent Vehicle (MAV) will be the first launch from the Mars Surface.
- It must reach a specified orbit to rendezvous with the Earth Return Orbiter.

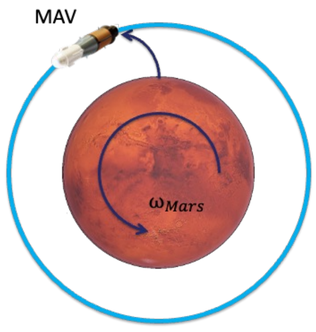

METHODS

- Linear tangent guidance → $\tan\theta = \tan\theta_0 - ct$
- Launch angle θ_0 and proportional thrust errors
  - $\theta_0 \sim \mathcal{N}(\theta_{0,nom},\ 0.01 * \theta_{0,nom})$
  - $F \sim \mathcal{N}(F_{nom},\ 0.1 * F_{nom})$
- Iteratively solve for control variable c
- Assume:
  - Locally flat Mars
  - Constant gravity
  - Constant mass

$$\dot{x}_1 = x_3$$
$$\dot{x}_2 = x_4$$
$$\dot{x}_3 = (F/m)\cos\theta$$
$$\dot{x}_4 = (F/m)\sin\theta - g$$

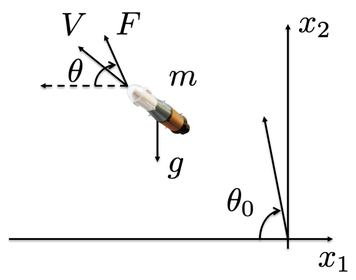

RESULTS

Launch Solver

- The perturbed trajectory (blue) deviates from the nominal trajectory (green) and fails to hit the desired altitude (black)
- Correcting for the errors (red) allows the MAV to hit the desired altitude after its coast phase

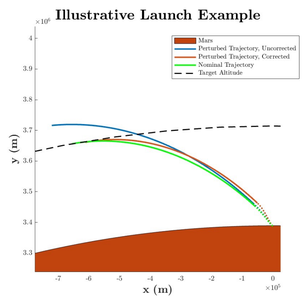

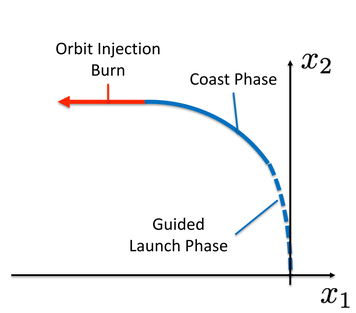

- Using the partial derivative calculated via finite differencing, an explicitly-implemented optimal guidance scheme iteratively solves for control c
- When verified against fmincon, $|\Delta c| < 1e\text{-}9$

Monte Carlo Simulations

- Distributions resulting from 1,000 sampled perturbations pre- and post-added Δv

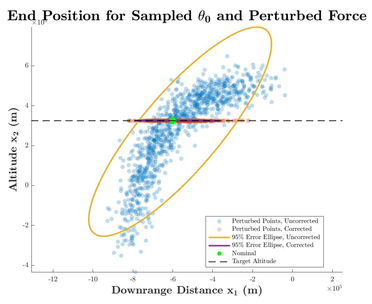

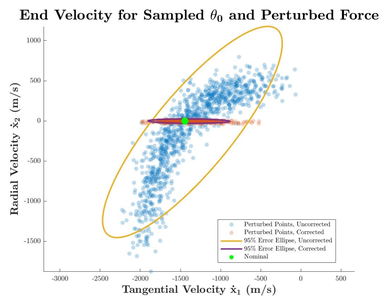

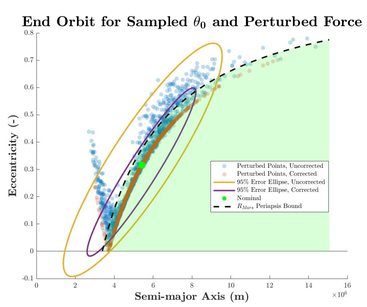

Applying a linear guidance law prevents Mars crashes but yields a distribution of orbits with high variance.

Controlled trajectory:
→ 92.9% of trajectories reach orbit
→ Eccentricity ∈ $[0.0026, 0.7010]$
→ Semi-major axis ∈ $[3010, 12422]$ km

DISCUSSION

- The Mars launch scenario highlights the shortcomings of linear tangent guidance in achieving the desired orbit.
- Our goal is to explore other guidance laws [1,2] and modify the guidance approach to reach the specified orbit with probabilistic guarantees.
- Uncertainty-based approaches (e.g. chance-constrained guidance) can aid in both space situational awareness and conjunction analysis.

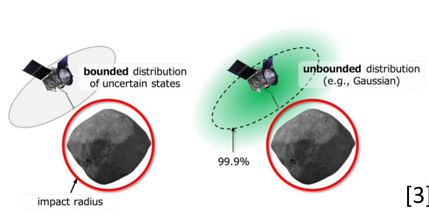

[3]

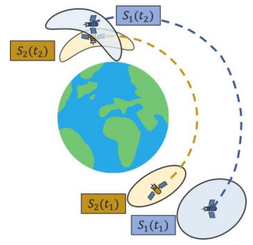

[4]

CONCLUSIONS

- Studying the effect of pure linear guidance on end uncertainty of various parameters shows:
  - The non-Gaussian distribution that develops when control is not corrected; and
  - The large spread in final orbit post-insertion when only targeting a final altitude.
- The Mars launch problem serves as a motivating example for developing applications of modern guidance and control techniques with the aim of shaping distribution for mission success.

ACKNOWLEDGEMENTS / REFERENCES

[1] Kuettel III, D. H., & McMahon, J. W. (2021). Low-thrust maneuverability using bilinear tangent guidance near small bodies. *Journal of Guidance, Control, and Dynamics*, *44*(8), 1425-1439.
[2] Jenson, E. L., Chen, X., & Scheeres, D. J. (2020). Optimal spacecraft guidance with asynchronous measurements and noisy impulsive controls. *IEEE Control Systems Letters*, *5*(5), 1813-1818.
[3] Oguri, K., & McMahon, J. W. (2021). Robust spacecraft guidance around small bodies under uncertainty: Stochastic optimal control approach. *Journal of Guidance, Control, and Dynamics*, *44*(7), 1295-1313.
[4] Khatri, Y., & Scheeres, D. J. (2023). Nonlinear semi-analytical uncertainty propagation for conjunction analysis. *Acta Astronautica*, *203*, 568-576.

Qualitative Evaluation of the Gravity Loading Countermeasure Skinsuit during Exercise and Functional Activity in Low-Earth Orbit and 1G

Rachel F. Bellisle[1,2], Katya Arquilla[3], Lonnie Petersen[1,4], Andrea Webb[5], Dava Newman[1, 4, 6]

[1]Harvard-MIT Health Sciences and Technology, Massachusetts Institute of Technology, [2]Draper Scholar, The Charles Stark Draper Laboratory, Inc., [3]Aerospace Engineering Sciences, University of Colorado Boulder, [4]Department of Aeronautics and Astronautics, Massachusetts Institute of Technology, [5]The Charles Stark Draper Laboratory, Inc., and, [6]MIT Media Lab

ABSTRACT: The Gravity Loading Countermeasure Skinsuit (GLCS or "Skinsuit") is a countermeasure garment for astronauts that provides axial loading on the body to simulate some effects of Earth's gravity (1G) and aims to mitigate physiological deterioration due to microgravity. A study was conducted with 7 participants to characterize the impact of the GLCS on daily activities and exercise, with one participant completing the study in microgravity during a 10-day mission to the International Space Station (ISS). A portion of the study aimed to address the following research questions:

- ***How does GLCS loading affect user discomfort, mobility, and exertion during daily activities and exercise?***
- ***How are discomfort, mobility, and exertion in the GLCS affected by gravity environment (1G and microgravity)?***

The results indicate that the suit is tolerable during ~1-2 hours of resistance exercise, provides potentially advantageous, but tolerable, resistance to movement, and is unlikely to negatively impact the user's ability to complete daily activities.

INTRODUCTION

The Gravity Loading Countermeasure Skinsuit (GLCS or "Skinsuit") is a musculoskeletal deconditioning countermeasure for spaceflight, consisting of a skin-tight garment that applies a vertical load from the shoulders to the feet (Fig. 1) [1]. The suit aims to mitigate musculoskeletal deconditioning (potentially including spine, muscle, sensorimotor) during exposure to microgravity by simulating some of the effects of Earth's gravity (1G) [2,3]. MIT and collaborators have tested the GLCS in multiple experimental campaigns in relevant environments: 1G [4-7], partial gravity analogs [4-7], parabolic flights [2], and the ISS [8]. As a musculoskeletal countermeasure, the GLCS could be used in several operational scenarios, in low-Earth orbit and future missions to the moon and Mars, including 1) acute ~2-hour use to augment exercise, 2) multi-hour use during daily activities, or 3) during sleep.

Fig. 1. The Gravity Loading Countermeasure Skinsuit *with A) shoulder yoke, B) longitudinal fabric tension providing axial load, C) circumferential fabric tension providing anchoring skin pressure, and D) stirrups secured at the shoes.*
Modified from Bellisle et al., 2022

A GLCS demonstration and one-participant evaluation was recently completed on a 10-day ISS mission to assess operational feasibility of the GLCS, characterizing its impact on daily activities and potential benefit for exercise. This was supplemented by a 6-participant study in 1G.

METHODS

- 7 participants (4 F, 3M, 60.5±8.8 kg, 167.3±2.8, 22-67 years) completed one unsuited (control) and one suited session in 1G.
- 1 participant additionally completed three suited (FD6, FD7, FD8) and one unsuited session (FD4) in µG during a 10-day ISS mission.
- Each data collection session included:

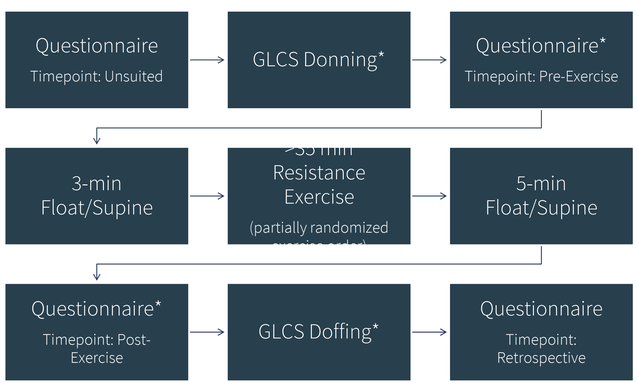

- Questionnaires included of discomfort (Fig. 2A), mobility (Fig. 2B).

RESULTS

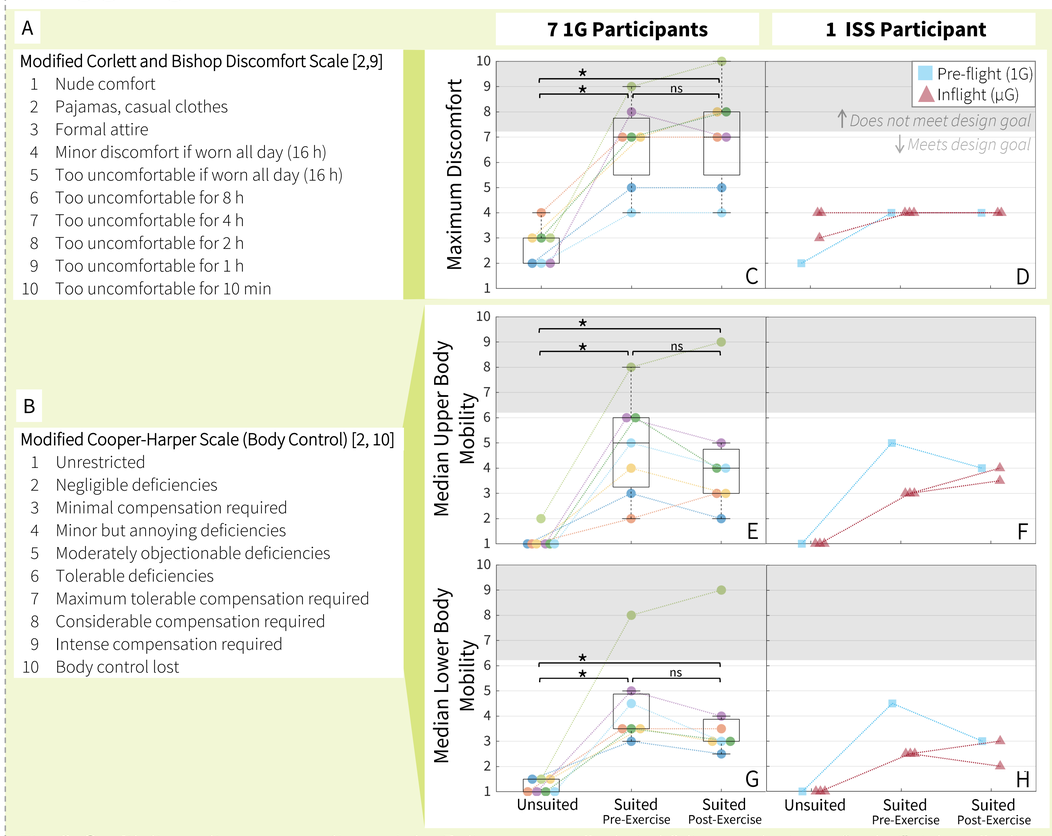

Fig. 2. Qualitative ratings across timepoints. Ratings were collected at 3 timepoints during "suited" data collection sessions. Unsuited ratings were collected before donning the suit. Suited ratings were collected before and after 60-90 minutes of suit wear and exercise. Boxplots show median, first (Q_1) and third (Q_3) quartiles, and non-outlier minimum/maximum ($Q_{[1,3]} - 1.5 * [Q_3 - Q_1]$). Discomfort ratings are presented as the maximum of ratings for 10 individual body parts. Upper body mobility is the median rating across the shoulder, torso, and waist. Lower body mobility is the median rating across the hip, knees, ankles, and feet/soles. Only participants 3 and 7 had custom-fabricated suits; all other participants were matched to existing suits. Friedman tests (1G only) for each metric indicate a significant effect of timepoints. * indicates $p<0.05$ using a post-hoc Wilcoxon Signed-Rank Test with Bonferroni correction. "**ns**" indicates $p>0.05$.

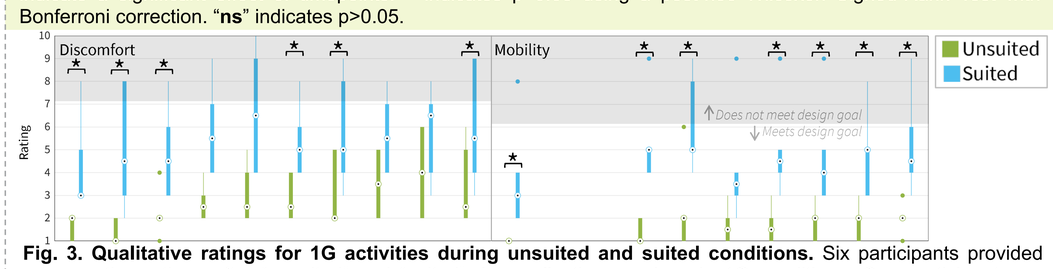

Fig. 3. Qualitative ratings for 1G activities during unsuited and suited conditions. Six participants provided retrospective ratings after "unsuited" and "suited" data collection sessions in 1G conditions. One participant was omitted from analysis due to a modified protocol. Boxplots show median, first (Q1) and third (Q3) quartiles, and non-outlier minimum/maximum ($Q_{[1,3]} - 1.5 * [Q_3 - Q_1]$). Outliers are indicated with circle markers. Mobility was not rated for supine rest or quiet standing. To address study hypotheses, pairwise Wilcoxon signed-rank tests were used to compare suited and unsuited conditions for each metric. * indicates $p<0.05$.

DISCUSSION

Discomfort

- The GLCS increased discomfort compared to unsuited ratings, and ratings varied across individuals, consistent with previous studies [3,5]
- **Median discomfort for all activities meets the design goal** of adequate comfort for 2 hours of wear, enabling use during exercise for most participants.
- Discomfort did not change over 60-90 minutes of GLCS wear.
- Compared to 1G ratings, the GLCS in µG was associated with a smaller increase in discomfort from unsuited ratings.

Mobility

- **Results suggest that the GLCS provides resistance to movement while remaining generally tolerable.**
- The GLCS worsened mobility compared to unsuited ratings, similarly to previous studies [3,5], and the median remained "tolerable" (i.e., <6) in all participants and activities.
- Non-significant trends indicate a possible improvement in perceived mobility across 60-90 min of suit wear.
- Compared to 1G, the GLCS in µG impacted mobility less.

CONCLUSIONS

- Based on discomfort ratings, the GLCS can likely be used during exercise (~2 hours) in most participants, with some able to tolerate it for longer periods during daily activities or sleeping.
- Mobility ratings were tolerable and decreased mobility may be advantageous to increase muscle activation with resistance to movement.
- A successful countermeasure prescription is required to access the proposed physiological benefits of the GLCS, and future work will use these results to inform and develop GLCS countermeasure prescriptions.

REFERENCES

[1] Waldie, J. M., and Newman, D. J. US 8,769,712 B2, 2014.
[2] Waldie, J. M., and Newman, D. J. *Acta Astronautica,* 2011.
[3] Bellisle, R, and Newman, D. *50th International Conference on Environmental Systems*, 2020.
[4] Attias, J., Carvil, P. A.T., Waldie, J., et al. *Acta Astronautica,* 2017.
[5] Carvil, P. A., Et al. *J. of Strength and Conditioning Research,* 2017.
[6]Diaz Artiles, A., et al. *IEEE Aerospace Conference*, 2016.
[7] Bellisle, R,. et al. *IEEE Aerospace Conference,* 2022.
[8] Stabler, R. A., Rosado, H., Doyle, R., et al. *Npj Microgravity*, 2017
[9] Corlett, E.N., and Bishop, R.P.A. *Ergonomics*, 1976.
[10] Cooper, G.E., and Harper, R.P. NASA-TN-D-5153, 1969.
[11] Borg, G. *Medicine and Science in Sports and Exercise*, 1982.

ACKNOWLEDGEMENTS

This work was supported by Draper Scholars Program at The Charles Stark Draper Laboratory, Inc. Thank you to our study participants, Golda Nguyen for data collection support, and all members of the MIT Skinsuit team. The authors would also like to thank MIT Space Exploration Initiative, and the payload integration support team for enabling the ISS experiment, Costume Works, Inc. (Somerville, Mass.) for GLCS fabrication, and Ministry of Supply (Boston, Mass.) for GLCS materials. Thank you to current and past GLCS collaborators at RMIT University, Human Aerospace (Australia), Kings College London, and the European Space Agency.

Engineering Quantum Materials for Infrared Detection and Optical Isolation

Morgan Blevins[1,2], Elizabeth Gerrish[3], Svetlana Boriskina[4]

[1]Department of Electrical Engineering, Massachusetts Institute of Technology, Cambridge, MA, USA mblevins@mit.edu
[2] Draper Scholar, Draper Labs, Cambridge, MA, USA, [3] Draper Labs, Cambridge, MA, USA egerrish@darper.com
[4] Department of Mechanical Engineering, Massachusetts Institute of Technology, Cambridge, MA, USA sborisk@mit.edu

ABSTRACT: Development of nonreciprocal photonic devices that enforce one-way propagation of light is vital for quantum communication, sensing, and radiation energy harvesting, but the state-of-the-art technology faces significant challenges in device integration and efficiency. To address these challenges, we present **the first comprehensive theory and feasibility analysis of nonreciprocal transport of optical surface modes (surface plasmon polaritons) via the current bias** in 3D quantum materials – where in a Doppler frequency shift imparted by current bias breaks the symmetry of the material.

INTRODUCTION

We are lacking **integrated photonics solutions for optical isolation**

- would enable high efficiency photonics for **visible and infrared detection** and **radiative energy harvesting**
- **Draper interest**: Enabling novel low SWAP sensors for optical and quantum sensing

Optical isolators protect optical systems

Without optical isolators

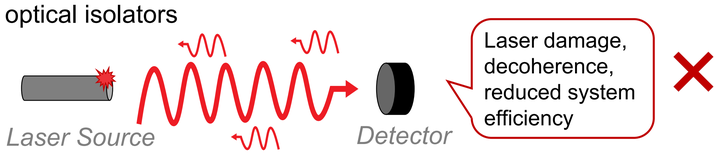

With optical isolators

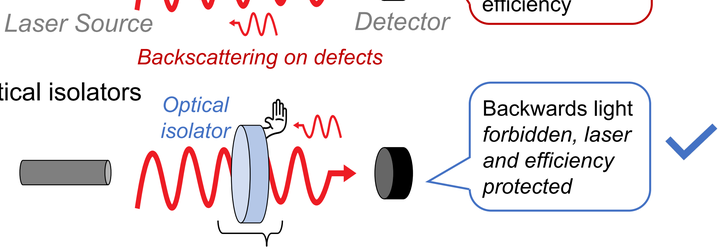

METHODS

Our solution: Current-biased Dirac and Weyl semimetals as new optical isolators

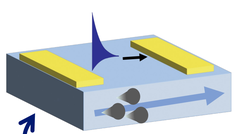

- Current bias **breaks material symmetry** and makes it **nonreciprocal,** now fit for optical isolation
- *However,* theoretical models are missing to describe this effect
- I derived the theory using semiclassical linear response theory:

materials that *can only be described using quantum mechanics* vs. classical physics

a. Under drift current bias, **equilibrium Fermi distribution is skewed:**

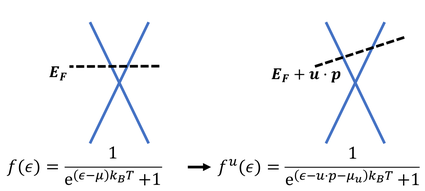

b. Effect of drift current on optical polarizability is a Quasi-Lorentz transformation

$$\omega_0 = \gamma(\omega - uq), \qquad q_0^z = \gamma\left(q^z - \frac{u}{v_F^2}\omega\right)$$

$$q_0^y = q^y, q_0^x = q^x, \gamma = 1/\sqrt{1-u^2/v_F^2}$$

c. Drift current modified optical polarizability is

$$\Pi^u(q,\omega) = -gN(\mu_0)\frac{q^2}{q_0^2}\left(\frac{\omega_0}{2q_0v_F}\ln\left(\frac{\omega_0 - q_0v_F}{\omega_0 + q_0v_F}\right)+1\right)$$

$$\sigma^u(\omega,q,\mu) = \frac{\omega}{\omega_0}\sigma_{zz}(\omega_0,q_0,\mu_0).$$

RESULTS

We modeled the optical surface modes to evaluate isolation performance

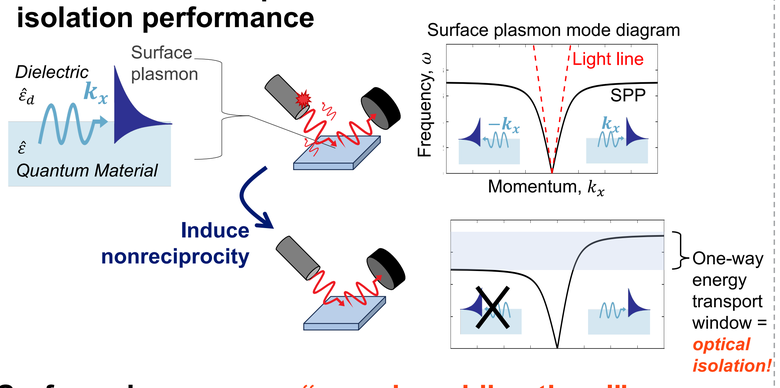

Surface plasmons are "pseudo-unidirectional"

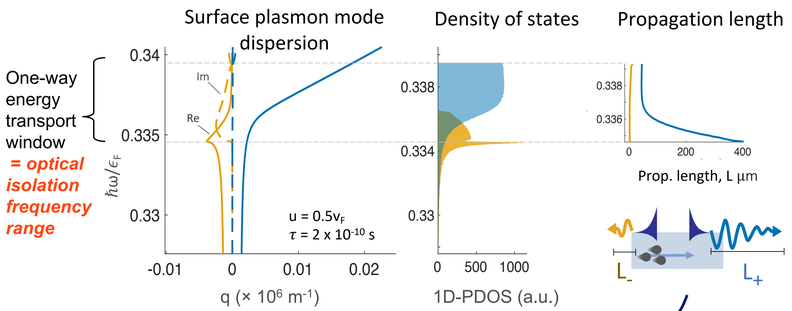

Pseudo-unidirectionality enabled by loss and nonlocality

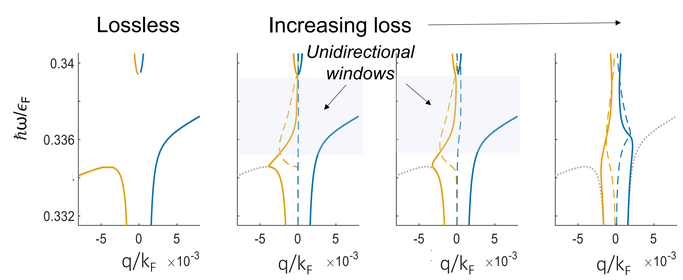

Comparison to state-of-the-art

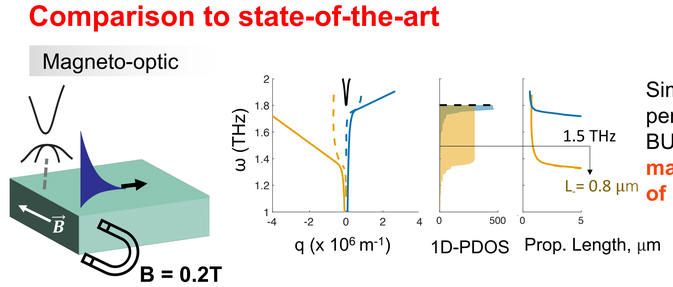

DISCUSSION

We have presented

- the theoretical framework for current-biased quantum materials
- a new **magnet-free** mechanisms for tuning the nonreciprocity of quantum materials, **competitive to magneto-optics**

We have shown that

- windows of pseudo-unidirectional transport are opened in the **THz window**
- unidirectionality is enabled by the unique blend of nonlocality and loss in Cd_3As_2

CONCLUSIONS

- Predicted a new unidirectional optoelectronic platform with
  - **(i) easy on-chip integration**
  - **(i) broader library of mature material platforms**
- Introduced a new opto-electronic application for quantum materials
- Experiments could enable **low SWAP** THz technology, energy harvesting, photonic sensing, thermal imaging, near-field heat transfer devices

ACKNOWLEDGEMENTS / REFERENCES

We thank Simo Pajovic, Thanh Nguyen (MIT), Dr. Yoichiro Tsurimaki, Dr. Shanhui Fan (Stanford), Dr. Mark Witinski and Dr. Pavlo Sukhachov (Yale) for helpful discussions.

Solution Processing for Rapid Exploration of Optical Phase Change Material Compositions

Brian Mills[1,2], Rashi Sharma[3], Casey Schwarz[4], Daniel Wiedeman[3], Marie Sykes[4], Jasper Stackawitz[4], Jake Klucinec[4], Eric Bissell[3], Dennis Callahan[5], Parag Banerjee[3], Kathleen Richardson[3], Juejun Hu[2]

[1]Draper Scholar, [2]Massachusetts Institute of Technology, Cambridge, MA, 02139, [3]University of Central Florida, Orlando, FL, 32816, [4]Ursinus College, Collegeville, PA, 129426, [5]The Charles Stark Draper Laboratory, Inc, Cambridge, MA, 02139

ABSTRACT: Chalcogenide optical phase change materials (O-PCMs) show great promise as active materials in non-volatile photonic systems. However, being limited to only a few different material compositions, O-PCM choice in these systems presents a limitation in optimization of the devices. We demonstrate solution processing as a reliable method to produce O-PCM films for high efficiency materials exploration through deposition of a known O-PCM, Sb_2Se_3, from solution. Initial characterization of the Sb_2Se_3 films show near complete removal of solvent constituents as well as a dense microstructure; a strong indication of the ability of solution processing to produce high quality films for evaluation of O-PCM candidate materials.

INTRODUCTION

Chalcogenide optical phase change materials (O-PCMs) have seen wide-spread adoption as the functional materials in a variety of actively controllable non-volatile optical and photonic systems[1,2]. Although a host of O-PCMs have been identified and demonstrated to be suitable for such devices, material choice and optimization remains as a challenge in extracting maximum device performance due to arduous material synthesis and film deposition. This work aims to streamline the O-PCM materials exploration process by developing a liquid solution-based approach to depositing high quality O-PCM films. We demonstrate synthesis and deposition of Sb_2Se_3, a common O-PCM, using this solution processing method.

METHODS

- Dissolve Sb_2Se_3 in organic solvent mixture of ethylenediamine (EDA) and ethanethiol (EtSH).
- Drop cast solution on Si substrate.
- Bake to remove solvent and form continuous film.

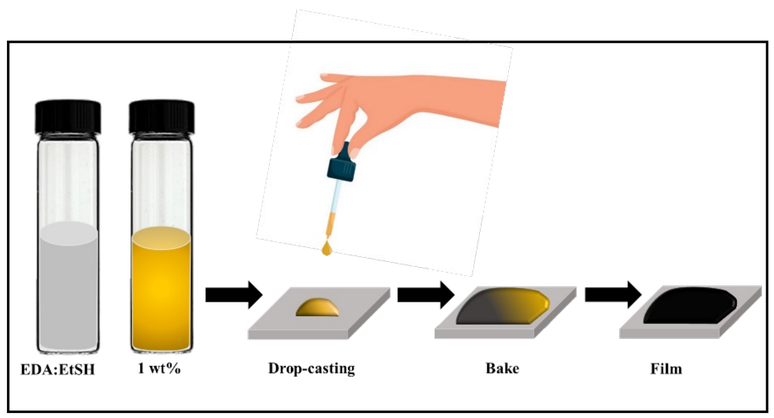

RESULTS

- SEM micrographs show microstructure of solution deposited Sb_2Se_3

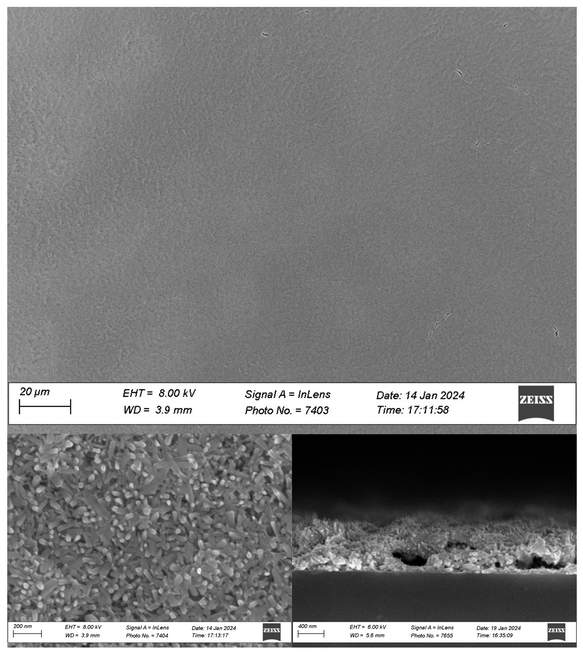

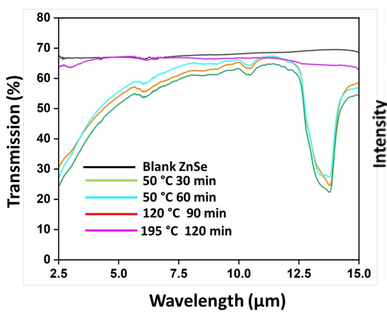

FTIR spectra of films baked at various temperatures

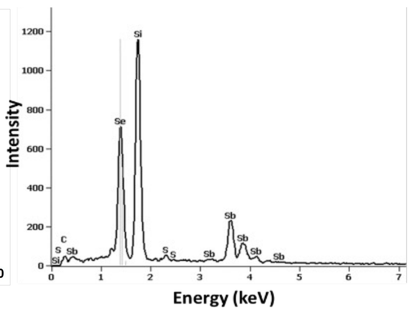

EDS spectrum of film baked at 195 C for 2 hours

DISCUSSION

- Film exhibits a granular microstructure.
- Cross-section reveals film to contain pores in some locations.
  - Potentially due to incongruent drying of solvent components.
- FTIR and EDS analysis confirms complete removal of solvent upon baking at 195 C for 2 hours.

CONCLUSIONS & FUTURE WORK`

- Solution processing is a promising method for efficient materials exploration of chalcogenide O-PCMs and their properties.
- Sb_2Se_3 is readily dissolved using a mixture of EDA and EtSH, producing a contaminant free film upon drying at sufficiently high temperatures
- Pores and surface roughness of film must be overcome to use these films for optical switching characterization or in optical devices.

ACKNOWLEDGEMENTS / REFERENCES

Funding support is provided by NSF award #2132929. B.M. acknowledges the support of the Draper Scholar Program and the Photonic Materials research group at MIT.

References:
1 - Delaney, Matthew, et al. Advanced Functional Materials 30.36 (2020): 2002447.
2 - Zhang, Yifei, et al. Nature communications 10.1 (2019): 4279.

Iterative Human-in-the-Loop Optimization for Aerial Robot Wildfire Detection

Christine T. Chang[1,2], Clare Lohrmann[1], Breanne Crockett[1], Maria P. Stull[1], Mitchell Hebert[3], and Bradley Hayes[1]

[1]University of Colorado Boulder, [2]Draper Scholar, [3]The Charles Stark Draper Laboratory, Inc.

ABSTRACT: Fluent and understandable human-autonomy teaming is essential for commercial, military, and public safety applications. Existing technology for facilitating human teaming with autonomous drones over large scale environments does not promote understanding or predictability. Our solution provides a human teammate with the ability to iteratively add latent knowledge and preferences to a trajectory optimization, via drawn annotations and natural language. By visually updating the trajectory at each iteration, our system aims to elicit more predictable robot behaviors and achieve better task outcomes. We aim to evaluate this system with a human subjects study that examines mission satisfaction and usability.

BACKGROUND AND MOTIVATION

- Current state-of-the-art allows a user to provide limited input to a path planner for an autonomous robot.
- Existing technology uses computer vision and machine learning to recognize signs of a fire from fixed cameras [1].
- Firefighters utilize uncrewed aerial systems to aid in wildland firefighting activities [2].
- Robot predictability [3, 4] has been studied extensively, though not over large spatial scales.
- A standard trajectory optimization [5] can maximize coverage but may be difficult to understand and time-consuming to complete, leading to confusion, mistrust, and risk, and compounding latency and observability concerns.
- We aim to provide iterative communication modes for human-robot teams to expose insights about human behavior and to elicit robot behavior incorporating human-provided insights.

REFERENCES

[1] PanoAI. 2023. https://www.pano.ai/
[2] H. M. Ray, R. Singer, and N. Ahmed, “A Review of the Operational Use of UAS in Public Safety Emergency Incidents,” in 2022 International Conference on Unmanned Aircraft Systems (ICUAS), Jun. 2022, pp. 922–931. doi: 10.1109/ICUAS54217.2022.9836061.
[3] Tathagata Chakraborti, Anagha Kulkarni, Sarath Sreedharan, David E. Smith, and Subbarao Kambhampati. 2019. Explicability? Legibility? Predictability? Transparency? Privacy? Security? The Emerging Landscape of Interpretable Agent Behavior. Proceedings of the International Conference on Automated Planning and Scheduling 29 (ICRA 2019), 86–96. https://doi.org/10.1609/icaps.v29i1.3463
[4] J. Reinhardt, A. Pereira, D. Beckert, and K. Bengler, “Dominance and movement cues of robot motion: A user study on trust and predictability,” in 2017 IEEE International Conference on Systems, Man, and Cybernetics (SMC), Banff, AB: IEEE, Oct. 2017, pp. 1493–1498. doi: 10.1109/SMC.2017.8122825.
[5] [1] M. Kalakrishnan, S. Chitta, E. Theodorou, P. Pastor, and S. Schaal, “STOMP: Stochastic trajectory optimization for motion planning,” in 2011 IEEE International Conference on Robotics and Automation, May 2011, pp. 4569–4574. doi: 10.1109/ICRA.2011.5980280.
[6] [1] J. Brooke, “SUS: A quick and dirty usability scale,” Usability Eval. Ind., vol. 189, Nov. 1995.

IMPROVING HUMAN-ROBOT TEAMING

➢ **Question: How can iterative planning be leveraged to improve human-robot team function in high-risk environments?**

Scenario: Searching a large area for artifacts of interest, such as wildfires or hot spots, minimizing planning time, and maximizing predictability.

Insight: Use natural language and drawn annotations to include latent human knowledge and make the system more effective and more predictable.

Task: Online participants on Prolific will use our system to design aerial robot trajectories for wildfire search.

SYSTEM DESIGN

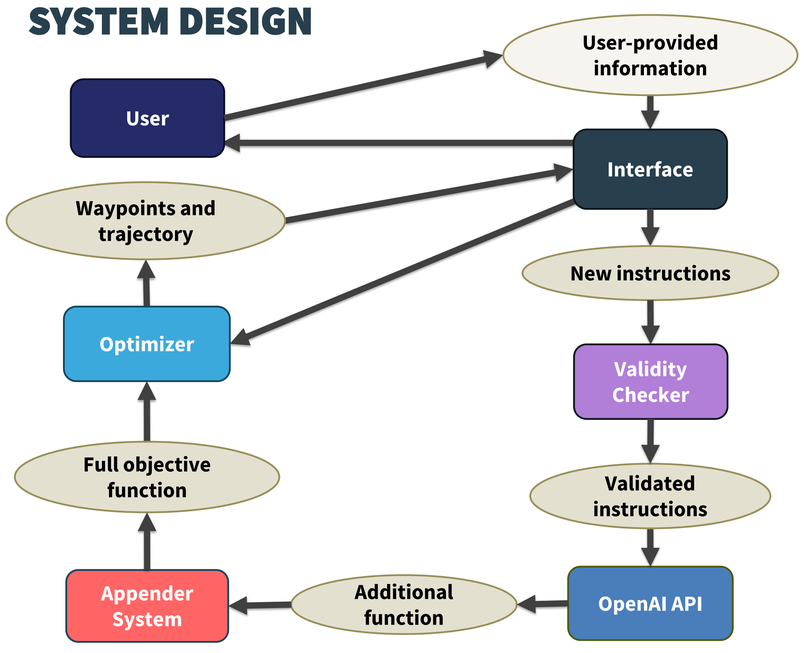

1. **User** first opens application and provides a rough **initial trajectory** sketch over the map in the **Interface**.
2. **Optimizer** **returns a trajectory** on the map that maximizes coverage.
3. **User** can give information to **(a) indicate regions of interest** on the map as well as **(b) provide instructions** that reference the regions.
4. **System** interprets these instructions and provides an **additional term** for the existing objective function.
5. New **augmented objective function is used to re-optimize** the trajectory displayed to the user on the **Interface**.
6. **Iterate** steps 3-5 as desired.

USER INTERFACE

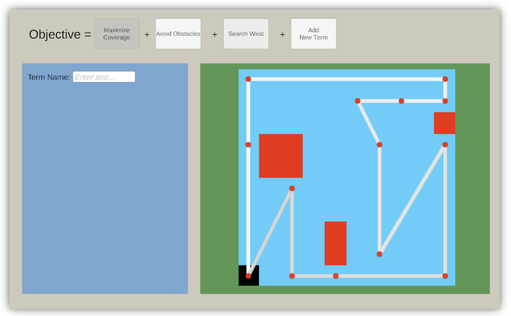

The interface allows a user to add new terms via drawn annotations and natural language, “turn off” objective terms if effects are undesired, and provide constrained inputs via fill-in-the-blank style word bank.

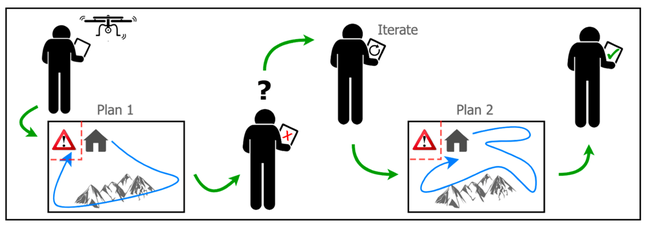

POINTS OF EVALUATION

- Understanding of how the trajectory was modified and how the final trajectory came to be
- Satisfaction with final trajectory
- Number of iterations provided
- Time spent on each iteration (sketch and instructions)
- Usability (System Usability Scale) [6]
- Instructions provided by user
- Trajectories
- Final coverage

EXPECTED OUTCOMES

We hypothesize that by **enabling iterative planning** between a human-robot team, users will:

- Achieve better **task outcomes**,
- Elicit more **predictable** robot behaviors, and
- Have a more **favorable user experience**

through use of **interactive, iterative refinements** versus traditional optimization interfaces.

A Large Deflection MEMS Spring to Enable Linear Out-of-Plane Movement

Tim J. Cheng[1,2], Robert D. White[1], and Kasia W. Oleske[3]

[1]Tufts University, [2]Draper Scholar, [3]Draper

ABSTRACT: In this work, designs for an existing silicon-based MEMS spring were modified and analyzed with analytical and numerical approaches to form a method for spring design mapping. A circular spring model performed similarly to its square counter-part found in literature[1], resulting in a 90% linear deflection at 1.5 mm and a shape that mitigates stress concentrations. An exploration into Ansys assumptions was made; however, changing them yielded little effect on deflection (<10%), so a recommendation to use the fastest method can be made to fully map out the design space for circular large deflection MEMS Springs to enable linear out-of-plane movement.

INTRODUCTION

- MEMS springs can be found in a variety of technologies including gyroscopes, accelerometers, biosensors, optical devices, speakers, atomic force microscopes (AFM), and vibration energy harvesters (VEH). MEMS speakers, self-sensing nanoindentation AFM probes, and VEH have the specific need for strictly out of plane springs with high deflections (~1mm).[1, 2]
- A literature search for high deflection MEMS springs resulted in a design[1] that could enable circular devices with minimal modifications. Only a change from square to circular would be needed, but the effects on deflection of this change are unknown. A circular device would enable incorporation into similarly shaped devices where the stress concentrations of a square design could be a problem.
- The springs in literature were also designed arbitrarily and do not map the effects of beam quantity/width on spring characteristics at a fixed spring constant.

METHODS

Using the Bernoulli–Euler equation for a beam's spring constant (k),

$$k = \frac{16Ewt^3}{l^3}$$

where *E* is the modulus of elasticity, *w* is the beam width, *t* is the beam thickness, and *l* is the beam length. A total linear model can be made by adding each individual beam in series or parallel. Non-linear effects were explored with Ansys. Many model inputs were varied to determine their effects on final deflection including 3D vs. 2D (shell), isotropic vs. anisotropic silicon properties, and mesh type. Since the main difference between the reference design was circularity, a comparison was made between circular and square designs with equal beam lengths. Results in Ansys were converged to within 2% based on deflection.

RESULTS

Comparison between the circular and square spring designs with equal beam lengths in Ansys.

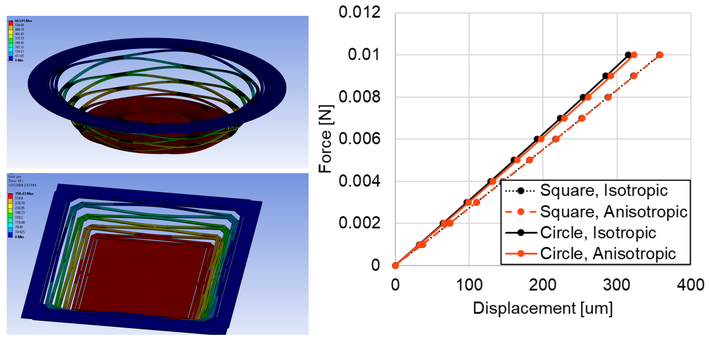

Aiming for a k = 23 N/m and maximizing the number of beams, MATLAB produced a spring with the following parameters,

w	*t*	*l*	# series beams	# parallel stacks
40 µm	*15 µm*	*~2 mm*	*9*	*4*

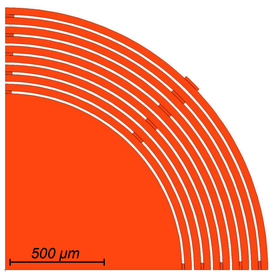

Quarter

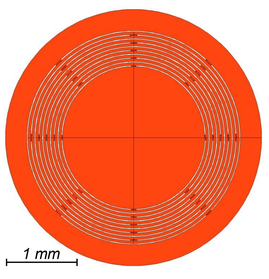

Full Spring

Modeling the spring generated from MATLAB in Ansys for linearity and a comparison to the Bernoulli–Euler equation.

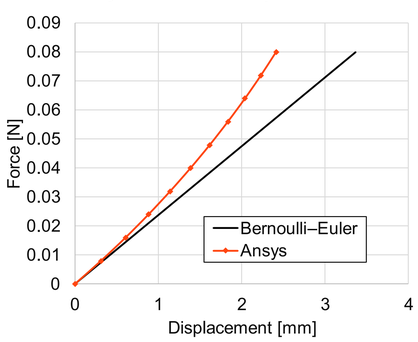

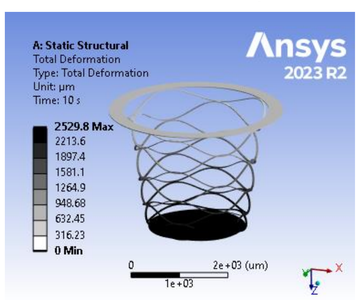

90% Linearity	*k @ 1.5 mm*
1.5 mm	*27 N/m*

DISCUSSION

- Utilizing the Bernoulli–Euler approximation for an initial design and Ansys for non-linear effects, as described by Grech[1], gave reasonable results for a circular spring yielding 90% linearity and a spring constant of 27 N/m (23 N/m Bernoulli–Euler approximation) at 1.5 mm. The non-linear effects shown in this Ansys modeling also fit well with findings by Grech where the resulting spring was stiffer by ~20% when compared to the linear Bernoulli-Euler equation.
- The Ansys model assumptions explored did not play a large roll in deflection results. This helps to determine how future tests are run on similar springs. It may be advisable to use the computationally fastest method to map the design space, because deflection error was <10% in in all cases.
- These simulations were not used for a stress or fracture analysis. This will be evaluated with further Ansys modeling and physical experimentation.
- Future work will also map spring characteristics (fracture and non-linearity) for given design constraints (i.e. spring constant and bounding dimensions) by varying number of beam and beam width.

CONCLUSIONS

A square MEMS spring found in literature was converted to a circular layout to reduce stress concentrations. MATLAB scripts were used to generate an example structure based on spring constant and the Bernoulli–Euler approximation. The spring performed as expected in Ansys simulations validating the design methodology. This method enables the rapid drawing of large deflection MEMS springs to map out the design space.

ACKNOWLEDGEMENTS / REFERENCES

Many thanks to Draper's IRaD group for knowlegable input including; Joseph J. Aghia, Brain J. Munroe, Jim Dombrowski, Ronald S. McNabb, and Ryann Hee.

1. Cheng, H.-H., et al., *On the design of piezoelectric MEMS microspeaker for the sound pressure level enhancement.* Sensors and Actuators A: Physical, 2020. **306**: p. 111960.
2. Grech, D., et al., *Highly linear and large spring deflection characteristics of a Quasi-Concertina MEMS device.* Microelectronic engineering, 2014. **119**: p. 75-78.

Provably Correct Machine Vision via Conformal Keypoint Mapping

Elijah Dabkowski, Evelyn A. Stump, Heng Yang

Draper Scholar, Draper, Harvard

ABSTRACT: Deep learning models perform extremely well in a variety of tasks, however even the most dominant algorithms that have been tested on public benchmarks can still be arbitrarily wrong. Because of this, there are some systems that eschew machine learning despite it possibly being a very practical and effective improvement to that system. We theorize that we can bind the uncertainty of machine learning practices to guarantee a minimum performance through the use of keypoint mapping. In this poster, we present the theoretical framework and propose steps to take moving forward to validate this hypothesis.

INTRODUCTION / MOTIVATION

- Machine learning has proved to be extremely useful and effective across many fields of science
- One drawback of certain machine learning practices is that the mathematical provability of these tools does not exist
- In turn, this leads to a lack of trust in these tools to be utilized in real world applications
- For a company like NASA, which spends a little over $40,000 to send one pound of material into space, trusting these machine learning tools simply because they work is not an option

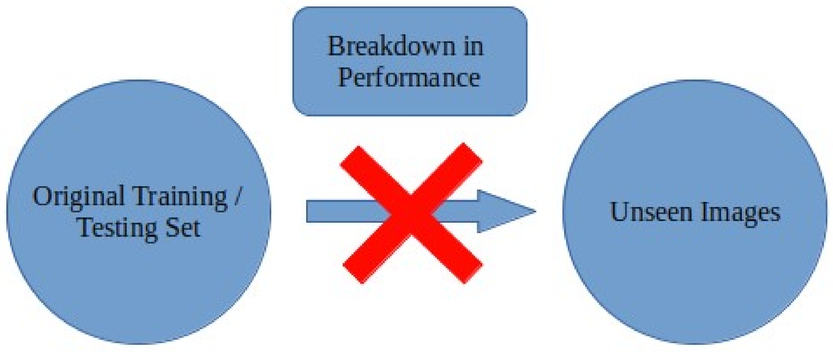

PREVIOUS UNCERTAINTY QUANTIFICATION WORK

- Attempting to apply uncertainty quantification techniques to deep learning models has been explored in the past, with methods such as Monte Carlo dropout and Markov chain Monte Carlo being explored [1]
- There has also been approaches to classify uncertainty bounds to problems involving object pose estimation [2]

CONFORMAL KEYPOINT DETECTION

The goal of conformal keypoint detection is to bind the uncertainty in the predictions of keypoint locations (y) to a user specified error bound

$$y = (y_1, .., y_k, .., y_K) \in (\mathbb{R}^2)^K$$

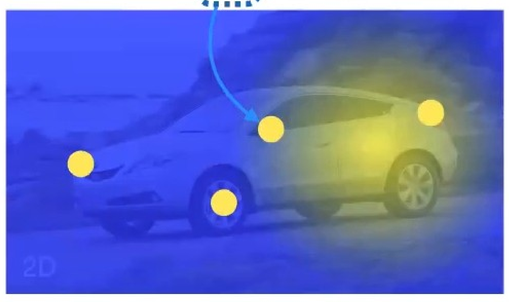

$f_k(x)$

- Three Necessities
  - (1) Unseen Calibration Set
  - (2) Nonconformity Function
  - (3) User Specified Error Margin

$$F^{\epsilon}(x_{l+1}) = \{y \in (\mathbb{R}^2)^K \mid ||y_k - q^*_{l+1,k}|| \leq r_k, \forall k\}$$

- The equation above specifies that for a new image, a set of predictions will be generated for each keypoint, where the ground-truth keypoint will lie within a circle that is centered around q^* with a radius of r_k

$$P[y_{l+1} \in F^{\epsilon}(x_{l+1})] \geq 1 - \epsilon$$

PROPOSED EXPERIMENTAL DESIGN

- We want to cast object detection as a keypoint estimation problem so that we an use conformal keypoint detection to bind the error on 2Dobject detection problem
- CenterNet is an architecture that predicts keypoints to predict a bounding box for a target [3]

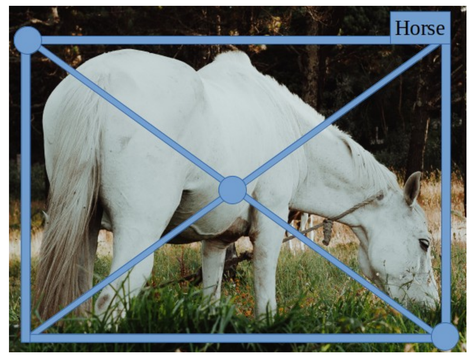

- The MS COCO dataset has official partitions necessary to obtain the unseen calibration set
- We want to start with an ablation study on MS COCO as proof of our method

SHORT TERM GOALS

- 1) Recreate the results from CenterNet
- 2) Run an ablation study on MS COCO
- 3) Prove that we can obtain a minimal performance level for object detection
- 4) Demonstrate the real world applicability on Draper proprietary object detection problems

REFERENCES

- [1] Abdar, Moloud, et al. "A review of uncertainty quantification in deep learning: Techniques, applications and challenges." Information fusion 76 (2021): 243-297.
- [2] Yang, Heng, and Marco Pavone. "Object pose estimation with statistical guarantees: Conformal keypoint detection and geometric uncertainty propagation." Proceedings of the IEEE/CVF Conference on Computer Vision and Pattern Recognition. 2023.
- [3] Duan, Kaiwen, et al. "Centernet: Keypoint triplets for object detection." Proceedings of the IEEE/CVF international conference on computer vision. 2019.

Assessing the Performance Impact Associated with Reusable Launch Vehicles Design Decisions

Ryan de Freitas Bart[1,2], Kevin Duda[3], and Jeffrey Hoffman[1]

[1]Massachusetts Institute of Technology, [2]Draper Scholar, [3]Draper

ABSTRACT: Hardware reusability is a promising solution to reduce the cost of operating in space, making it an attractive choice for commercial organizations. However, converting an expendable launch vehicle to a multi-use reusable system reduces its performance as measured by payload mass to its destination. Current methods to estimate this reduction for pre-PDR design trades of new launch vehicles use rule-of-thumb estimates or high-level factors. To bridge this gap, we developed a computational model which estimates the impact of converting a launch vehicle from expendable to reusable on system performance for pre-PDR designs. Using this model, we quantitatively assessed the impact on system mass and unit cost for a launch vehicle and determine adding reusability yields with an associated ~25% reduction in cost on average.

INTRODUCTION

- Hardware reusability is a promising solution to reduce cost of launching payloads into space
- Integrating reusability into space transportation systems entails a trade-off with performance [1]
- Quantifying this impact is crucial for the effective design optimization of reusable launch vehicles
- Important to understand impact of reuse on mass to orbit and cost when making design decisions
- This research develops a computational model to assess the performance impact of reusability on Earth-based launch vehicles

METHODS

- Multidisciplinary model to estimate impact of reuse on performance characteristics
  - Model composed of subsystem specific models which estimate impact of each subsystem on overall performance characteristics
- Enumeration of possible combinations of design variables shown in following table to generate a tradespace of designs
- Reuse Level defined by average per mission cost for additional flights as percent of Theoretical First Unit (TFU) cost

Design Variables	**Option 1**	**Option 2**	**Option 3**	**Option 4**
Reuse Level	Expendable	50% TFU Cost	10% TFU Cost	-
# Missions	1	5	10	25
Mass to LEO per mission[kg]	100	1,000	10,000	100,000
Propellant	LOX/H2	LOX/Meth.	LOX/RP1	-

METHODS (cont.)

- Design structure matrix for launch vehicle model with subsystem models on the main diagonal and input/output variables in other cells

Inputs	Propellant Mass to LEO	Reuse Level		Reuse Level # Missions	
	Propulsion	Thrust	Thrust, Engine mass		Thrust
		Control			Drag
		Mass	**Structure**	TFU Cost	Mass, Mass to orbit
	# Firings			**Reuse**	System Cost
					Outputs

RESULTS

- Impact on performance estimated by calculating cost and mass for different reuse levels

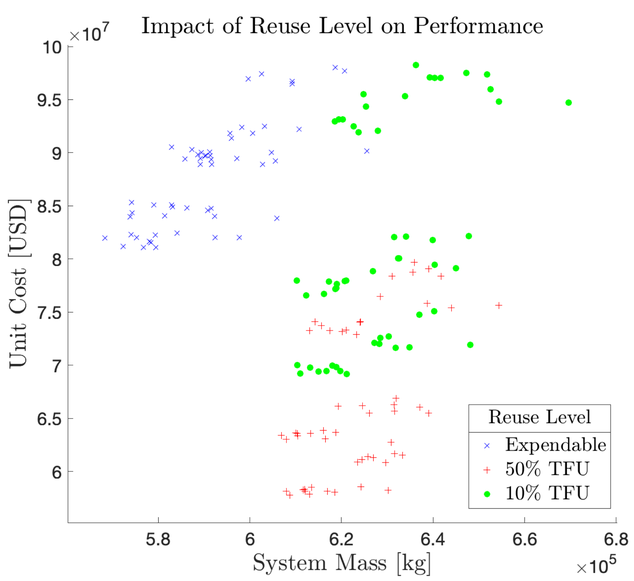

DISCUSSION

- Results show grouping of design performance by reuse level with expendable systems mostly having highest per unit costs and lowest masses compared to reusable designs
- Large loss of performance in terms of mass to orbit of ~25% for reusable designs
  - Due to additional system mass from adding capabilities for reuse
- Model facilitates early-stage trade studies and optimization of reusable space systems
- Model currently limited in fidelity using parametric estimates for system masses
- Difficult to follow original design specification limits usefulness of early design optimization

CONCLUSIONS

- Developed a model which predicts impact on system mass and unit cost when converting an expendable launch vehicle to reusable
- Enables early-stage evaluation and optimization of reusable space systems
- Future work
  - Increase model fidelity at subsystem level
  - Application of model to additional systems

ACKNOWLEDGEMENTS / REFERENCES

I would like to thank my advisors Prof. Jeffrey Hoffman and Dr. Kevin Duda for their insight and guidance. This work was supported by the Draper Scholar Program.

[1] "M. Ragab et al., 'Performance efficient launch vehicle recovery and reuse', in AIAA SPACE 2016

Improving geometric representations for optimization in robotics

Rebecca H. Jiang[1, 2, 3] Ravi Gondhalekar[2] Russ Tedrake[3]

[1]Draper Scholar [2]The Charles Stark Draper Laboratory [3]Massachusetts Institute of Technology

ABSTRACT: The objective of this research is to facilitate the use of rigorous computational methods in robotics applications to plan motions and design manipulators. We achieve this by using geometric representations of the problems of interest that are harmonious with optimization goals and constraints. Robotic manipulation requires reasoning about the geometries of the robot, obstacles, and objects of interest. Collision-free motion planning also requires us to utilize geometries in higher-dimensional spaces that represent the configuration or pose of the robot. In all of these contexts, the selected representation has great impact on downstream computation. Generally, the selection of this representation is ad hoc and does not receive careful attention. The proposed approaches achieve computational benefits through principled representation selection.

INTRODUCTION

We present three focus areas:

- Polytopic simplification: Reducing the complexity of representations of safe sets.
- End effector design: Co-optimization of contact surface shape and intended use for robotic tools.
  - Design of rigid manipulators **[1]**
  - Design of parallel-jaw grippers **[2]**
- Planning in pose space.

POLYTOPIC SIMPLIFICATION: METHODS

Polytopes (intersections of half-spaces) are often used to represent safe sets in motion planning. The number of faces (half-spaces) used to define a polytope drives runtimes. We compute inner approximations with fewer faces by iteratively translating faces inward and removing faces that become redundant. We guarantee a volume lower bound and respect constraints like retaining specific points and connectivity between specified polytopes.

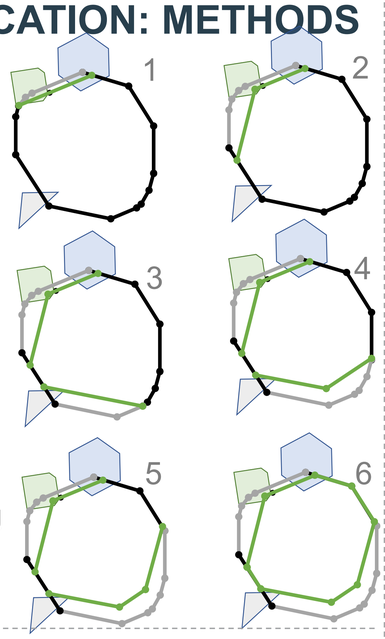

POLYTOPIC SIMPLIFICATION: RESULTS

Using sets of simplified polytopes speeds up planning by an order of magnitude (planning motions on a graph of 15 polytopes for a 10-dimensional robotic system).

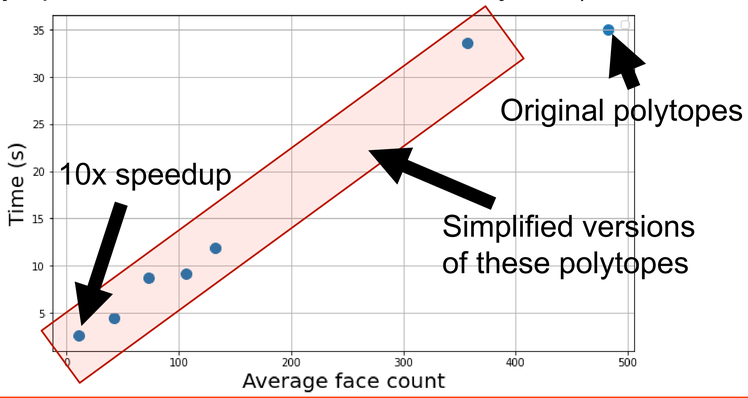

END EFFECTOR DESIGN: METHODS

- Key insight: representing objects in manipulator frames facilitates natural constraint expression.
- In the rigid manipulator problem **[1]**, this allows us to avoid explicitly parameterizing effector shape (notoriously tricky), instead imposing shape constraints on contact point trajectories.
- In the gripper problem **[2]**, we assess gripper shape and grasp stability via convex quadratic programs that can be solved rigorously and efficiently as a subproblem of the broader nonlinear program, using an augmented Lagrangian approach.

END EFFECTOR DESIGN: RESULTS

DISK PICKUP: Pivoting fingers lift disk via constant contact geometry. Finger inter-penetration can be constrained.

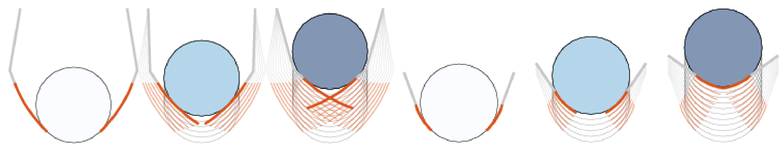

SCREWDRIVER PICKUP: Tool scoops screwdriver from a table without penetrating the table, two contact surfaces acting in coordination.

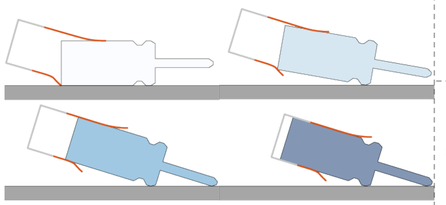

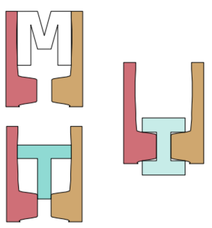

LETTERS: Simple gripper globally optimizes grasp stability, reusing gripper features across several grasps.

POLYGONS: Size-constrained gripper stably grasps polygons of varying shapes and sizes.

TOOLS: Hardware demo of optimized gripper with complex objects.

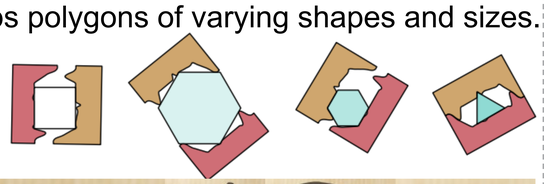

PLANNING IN POSE SPACE

- Robot motion planning is typically done in “configuration space” (C-space) – the space of joint coordinates.
- Recent methods require convex decompositions of collision-free space, but obstacles in C-space are oddly shaped, leading to conservative decompositions.
- We are at early stages of instead parameterizing plans in the space of pose coordinates in SO(2) or SO(3).
- We use a semidefinite program formulation to relax the SO(2) or SO(3) constraint to a convex constraint.
- We calculate free-space regions by converting separating hyperplanes between geometries to the pose coordinates.
- We expect motion plans to achieve more use of the full free space, including contact, relative to C-space plans.

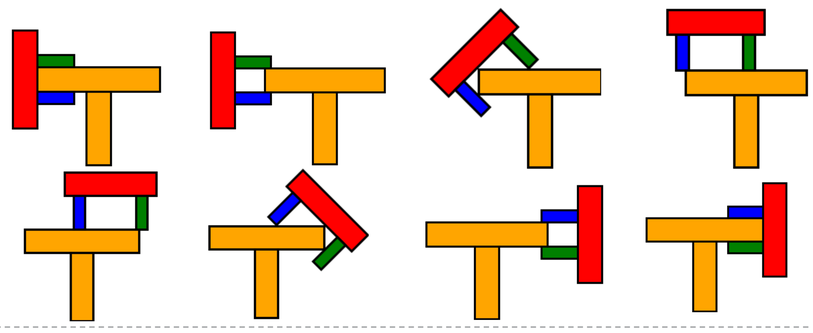

CONCLUSIONS

- Geometric representation can make or break an optimization problem’s tractability and quality of results.
- For design, posing constraints in the manipulator frame unlocks a tractable formulation **[1,2]**.
- For planning, current convex decompositions of free space are expensive and not conducive to allowing contact. We mitigate these issues by
  - Using simpler representations that speed up planning,
  - Using coordinates suited to the real constraints.

REFERENCES

[1] Jiang, Doshi, Gondhalekar, Rodriguez, *Shape and motion optimization of rigid planar effectors for contact trajectory satisfaction*, in IROS. IEEE/RSJ, 2022

[2] Jiang, Doshi, Gondhalekar, Rodriguez, *Parallel-Jaw Gripper and Grasp Co-Optimization for Sets of Planar Objects*, in IROS. IEEE/RSJ, 2023

Evaluation of Perfusion's Effect on Cancer Spheroids' Viability and Compound Delivery via Microfluidic Platforms

Alex W. Markoski (Draper Scholar)[1,2], Ian Y. Wong[2], Jeffrey T. Borenstein[1]

[1]Draper, Cambridge, MA, USA, [2]Brown University, Providence, RI, USA

ABSTRACT: In vitro microfluidic platforms are essential for collecting in vivo relevant data especially within the field of cancer research. Here, we show a scalable microfluidic platform capable of providing in vivo level flow conditions to cancer spheroids. This platform contains a unique capture geometry to hold the samples in place for exposure to active perfusion and consistent imaging over time. Cell death metrics were analyzed via an image analysis pipeline consisting of exported z stacks from Zen and the processing capabilities of ImageJ. This device along with additional high throughput platforms have be useful in developing a better understanding of flow's impact on compound delivery and viability while providing a foundation for future work focused on preclinical drug testing in cancer.

INTRODUCTION

- 2D Static culture methods are devoid of the complex in vivo stimuli and architecture required to produce impactful biological data within the cancer research.
- High throughput microfluidic devices are time intensive and difficult to create.
- Here we show both the power of microfluidics for data acquisition as well as a method for scalable and cheap microfluidic device creation via 3D Printing.

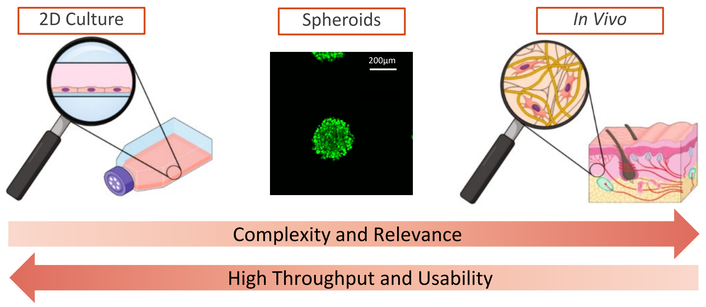

[1]

METHODS

- The Asiga MAX X27 Stereolithography 3D Printer was used in conjunction with the Pro3dure GR-10 resin.
- Flow's impact on viability and compound delivery (Staurosporine) was evaluated over the course of 3 days.
- CT26 spheroids were used in conjunction with flow to mimic in vivo conditions.
- CT26 cells were pre-treated with CellTracker Green and DRAQ7 for recording viability over time.

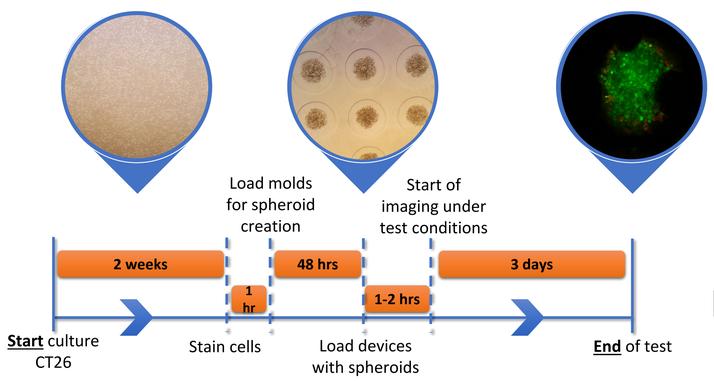

[2]

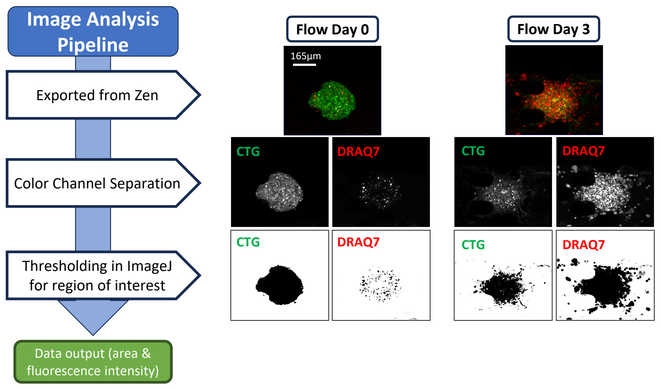

- Image analysis pipeline utilizing exported Zen images which are processed in ImageJ.

RESULTS

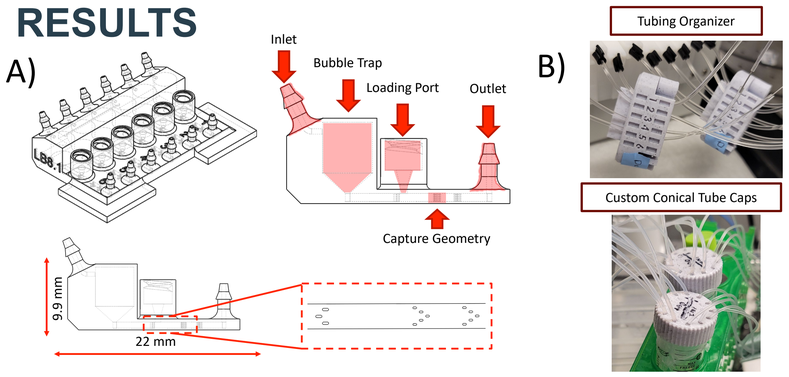

- Devices can be printed and ready for use within an hour and a half.
- Optimized to capture 200-500µm diameter spheroids.
- Additional custom parts were designed and 3D printed for setup optimization.

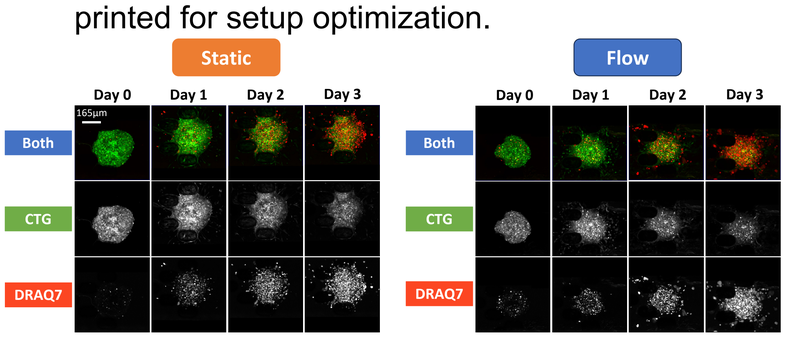

- Confocal Images of captured spheroids in flow and static conditions over 3 days. All z-stack images are channel separated for analysis

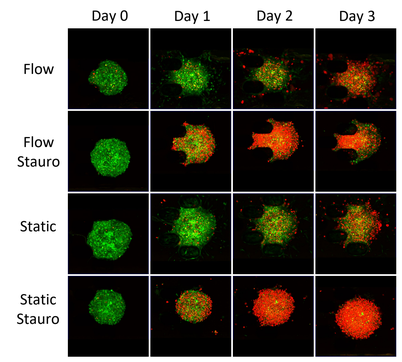

- Staurosporine exposed spheroids showed higher cell death immediately than controls.

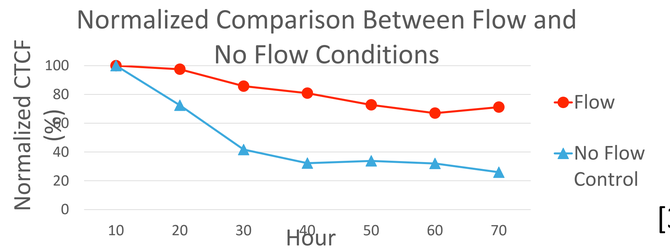

[3]

- Corrected total cell fluorescence (CTCF) for CTG decrease by 28% for flow and 74% for no flow control.

CONCLUSIONS

- The 3D printed device is versatile and its manufacturing process allows for rapid iteration. It is capable of spheroid capture, perfusion, and imaging.
- The platform proved to be capable of monitoring cell death over time as well as delivery of compounds via perfusion.

ACKNOWLEDGEMENTS / REFERENCES

Thanks to the Draper Scholars Program and Brown University for the support.

[1] Charwat et al, Cell Culture Technology, 2005
[2] Markoski A, Wong IY, Borenstein JT. Dynamic Tumor Perfusion and Real-Time Monitoring in a Multiplexed 3D Printed Microdevice. Methods Mol Biol. 2023;2679:287-304. doi: 10.1007/978-1-0716-3271-0_20. PMID: 37300624.
[3] Markoski A, Borenstein J, Wong I. 3D printed monolithic device for the microfluidic capture, perfusion, and analysis of multicellular spheroids. Frontiers in Medical Technology. 2021.

Model Predictive Planning

Matthew Wallace[1], Laurent Lessard[2], and Brett Streetmen[3]

[1]Northeastern Electrical Engineering & Draper Scholar, [2]Northeastern Mechanical Engineering, [3]Draper

ABSTRACT: This poster presents a motion planning scheme we call Model Predictive Planning (MPP), designed to optimize trajectories through obstacle-laden environments for underactuated systems, such as a fixed wing aircraft. The approach involves path planning to identify trajectory candidates, trajectory refinement through the solution of a quadratic program, and autonomous selection of optimal trajectories. MPP reliably produces feasible trajectories while matching the strong obstacle avoidance performance of RRT*, a state-of-the-art existing method.

Introduction

- In autonomous navigation for low-agility vehicles like fixed-wing aircraft, it is necessary to track a trajectory rather than a path.
- Paths, comprising spatial waypoints, lack timing, speed, or orientation considerations, suitable for highly actuated systems leveraging controllers like RRT* for obstacle avoidance.
- Trajectories become indispensable for low-agility vehicles due to maneuverability constraints. Tools like IPOPT and GPOPs enable offline trajectory planning, tackling various constraints iteratively.
- To address trajectory planner issues around obstacles, we developed MPP, a method integrating raytracing and convex optimization refines paths into trajectories, linked with a multi-path planner, and demonstrated the method on a longitudinal aircraft model.

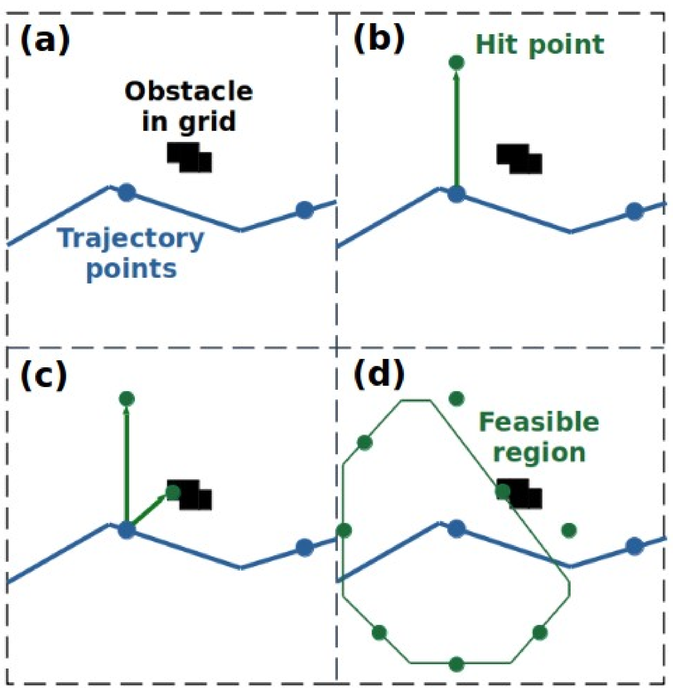

METHODS

- Our method begins by using RRT-AR to plan many paths through an obstacle field
- These paths are used to formulate a quadratic program with linear constraints that encode nearby obstacles as well as constraints requiring the dynamics of the system are obeyed
- By comparing the results of several optimization steps, we're able to consistently find a good trajectory through the obstacles

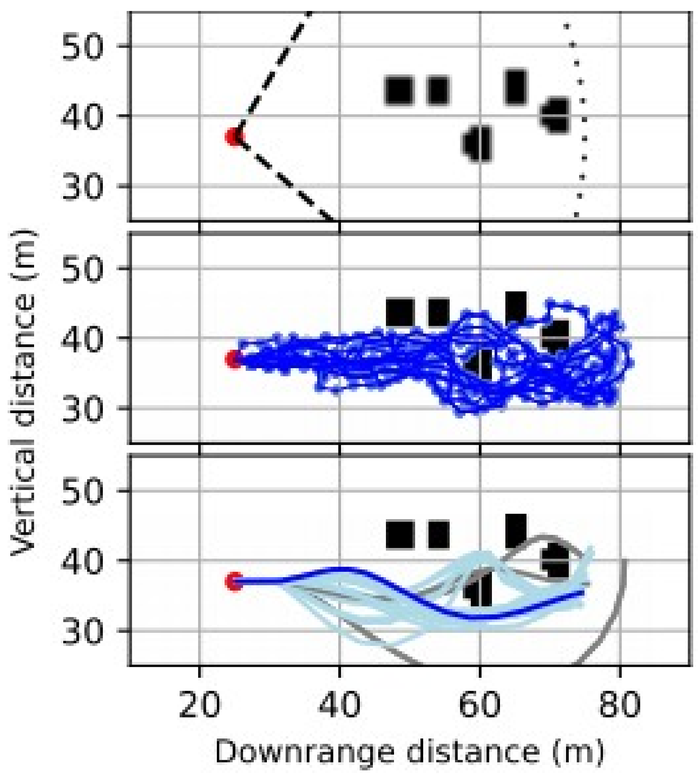

Results

- Refining trajectories from RRT* significantly improves performance at obstacle avoidance.
- MPP further improves this result with an increasing number of paths, demonstrating the necessity for multiple alternative routes to avoid local infeasibility issues.

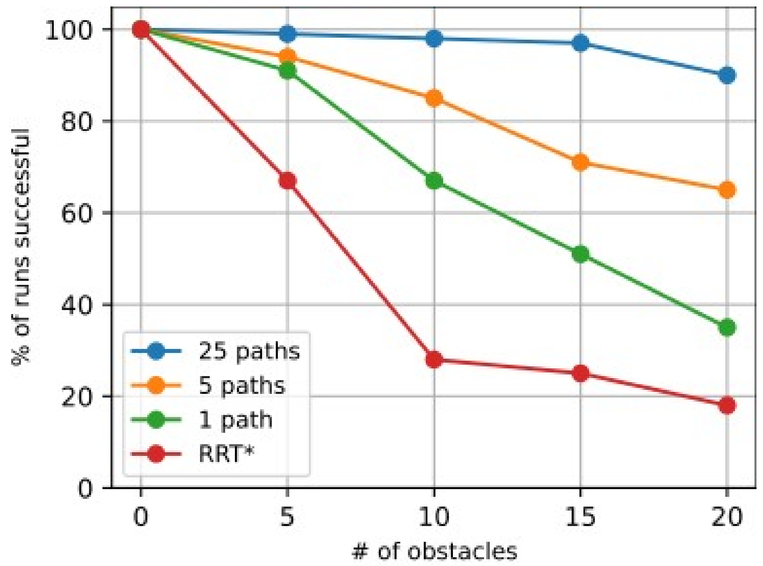

CONCLUSIONS

- MPP enhances traditional MPC by planning trajectories around obstacles through path planning, raytracing, and quadratic programming.
- Future advancements in MPP include refining the RRT*-AR path planner, exploring alternative collocation methods, and optimizing the raytracing procedure to enhance computational efficiency.

Selective Transfection via Electroporative Printing

Aric Lu[1,2,3,4], Carlos Marquez[1,2], Paul Stankey[1,2], Kayla Wolf[1,2], Jonathan Coppeta[4], and Jennifer Lewis[1,2]

[1]Harvard John Paulson School of Engineering and Applied Sciences, [2]Wyss Institute for Biologically Inspired Engineering, [3]Draper Scholar, [4]The Charles Stark Draper Laboratory

ABSTRACT: New tissue fabrication technologies are needed to produce engineered human tissues with functionally vital patterns of gene expression within a tissue. To address this technology gap, we developed Selective Transfection via Electroporative Printing (STEP), which combines electroporation, a physical method to change gene expression in cells via transfection of genetic instructions, with 3D bioprinting to create patterns of transfected cells during the tissue fabrication process. STEP can be used to print and transfect many different cell types to create patterns in a variety of tissues. Importantly, we can tune electroporation parameters used in STEP to produce effective gradients of gene expression through mixtures of transfected and non-transfected cells. STEP therefore provides a method to produce patterned tissues that may one day serve as therapies for organ repair or as enhanced models of human organs.

INTRODUCTION

- Extremely difficult to create patterns of gene expression in engineered tissues
- Existing methods require gene editing prior to tissue assembly and cannot be used to produce gradients of gene expression

Selective Transfection via Electroporative Printing:

- Functionalized nozzle applies high intensity electric fields to load genetic instructions into the cell during the printing process
- Nozzle electrodes can be switched on and off to control transfection within every voxel

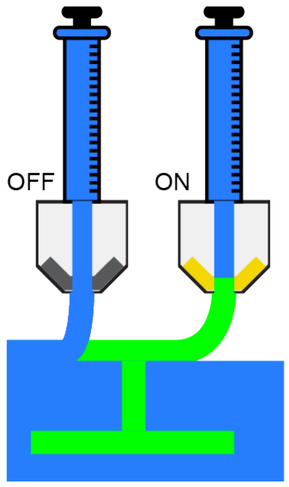

INK FORMULATION

- Developed a composite agarose + hyaluronic acid methacrylate (HAMA) microparticle ink formulation to support STEP
- Methacrylated polymers can be photo-crosslinked to solidify tissue in post-processing

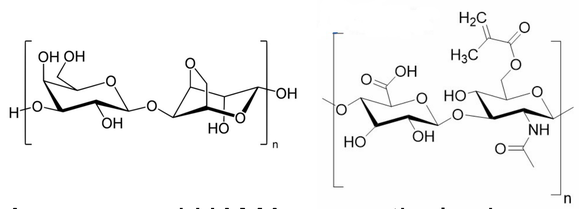

Agarose and HAMA – negatively charged polymers permit electroporation

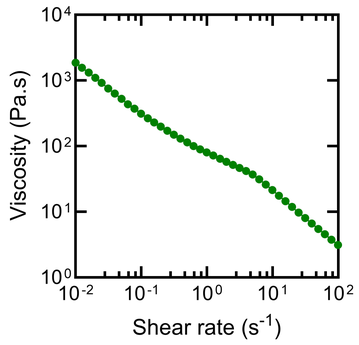

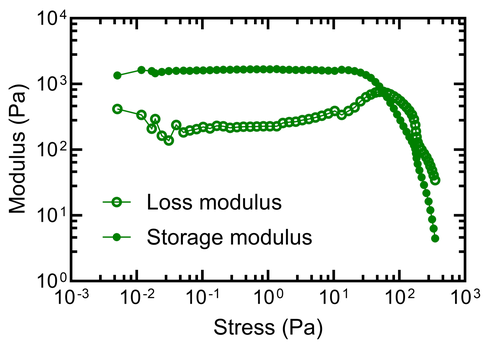

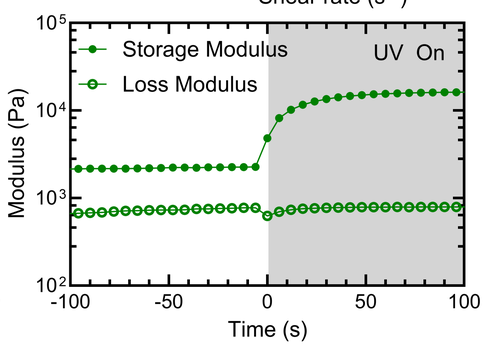

- Final ink formulation: 3 wt% agarose, 1 wt% HAMA microparticles, 100×106 cells/mL, 100 µg/mL eGFP-mRNA for transfection
- Inks exhibit shear thinning and yield stress rheology for 3D printing
- UV cross-linking produces a stiff, robust tissue

NOZZLE DESIGN

- 3D printed nozzle functionalized with platinum electrodes for electroporation
- Square channel outlet and parallel plate electrodes define voxel size

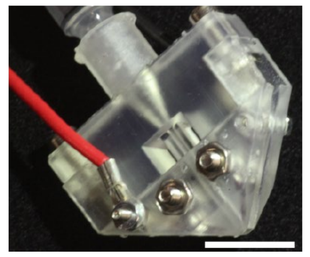

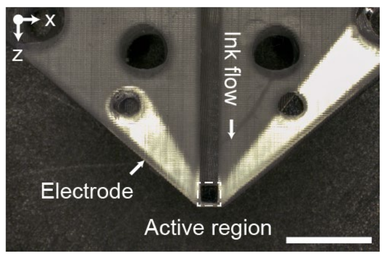

Electric field distribution within nozzle

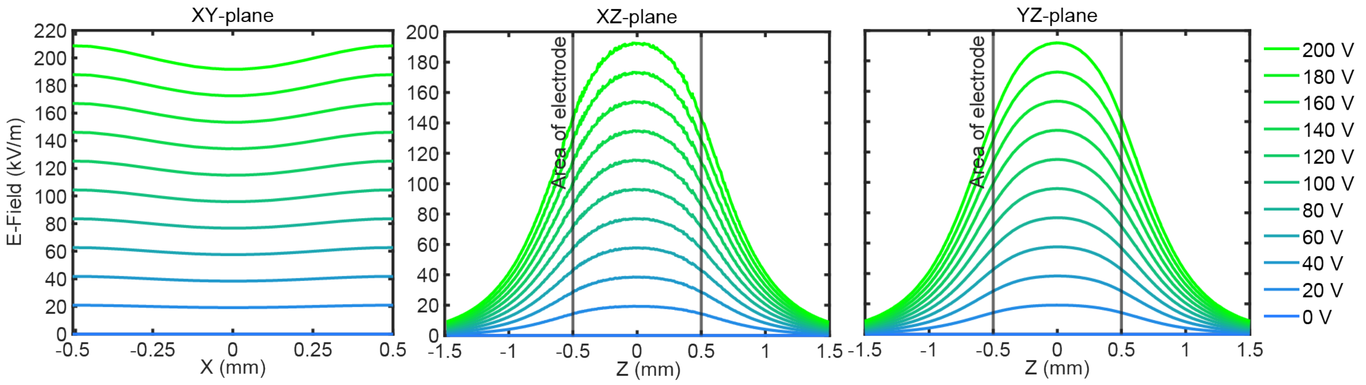

PRINTING TISSUES WITH STEP

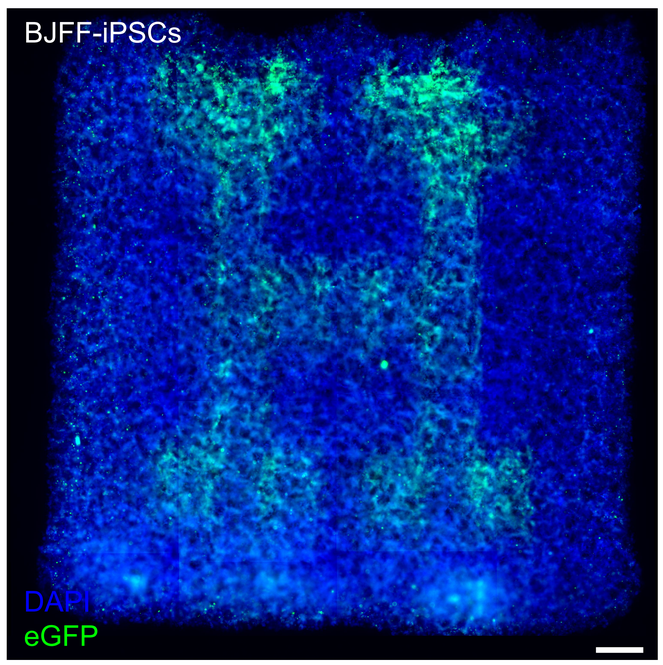

- Resolution of a single voxel: 1083 ± 38 µm
- Can reach transfected efficiency of >80%
- Viability of BJFF-iPSCs is around 40%

Programming gene expression gradients

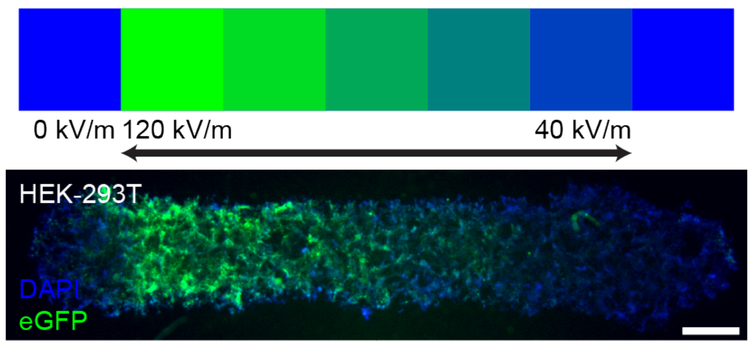

CONCLUSIONS AND NEXT STEPS

- Successfully produced patterns and gradients of eGFP expression using STEP
- Tissues can be printed with near-physiological cell densities with STEP

Next steps:

- Optimize formulation to improve iPSC cell viability
- Demonstrate transfection and patterning with additional mRNAs

Moon-Based Sensor Placement for Cislunar Orbit Determination: Object tracking considering non-Gaussian distributions

Erin Jarrett-Izzi (Draper Scholar)[1,2], Kenshiro Oguri[1], Michele Carpenter[2], and John Danis[2]

[1]Purdue University, [2]The Charles Stark Draper Laboratory

ABSTRACT: Orbit determination in cislunar space is an area of interest within several communities where cislunar space domain awareness is critical to operations. A multi-gravity dynamics model is employed to attempt to accurately describe the state. Both the state estimate and error in the state are propagated using a combination of the dynamics model and physical measurements. Previous work found challenges due to the non-linear dynamics of the system resulting in non-Gaussian distributions of the state. Through the implementation of a non-Gaussian based filter, a large portion of orbits under large uncertainties are able to be tracked.

INTRODUCTION

- As Cislunar space becomes increasingly active robust Space Domain Awareness (SDA) becomes crucial. While successful missions like NASA's CLPS program demonstrate the region's potential, existing tracking methods like DSN and GNSS struggle to keep up with the growing number of assets. Studies are ongoing to adapt these systems or develop new ones, but challenges remain due to the vastness of the region and the need for solutions that encompass diverse orbits. Addressing these challenges is essential for ensuring safe and sustainable exploration and development of Cislunar space.
- Previous work shows a baseline results to best inform a moon-based tracking, however this work strengthens the capabilities under larger uncertainty and more non-Gaussian regions.

METHODS

- Measurements are incorporated into the CR3BP dynamics model using a Gaussian Mixture Extended Kalman Filter with adaptive splitting and merge techniques. This filter propagates several Gaussian kernels with their associated means, covariances, and weights. They are combined in order to get the best estimate of the state.
- Measurements are simulated using angle measurements from a ‘true state’ with added noise. The sensor model includes brightness, field of regard, and conjunction exclusions.

RESULTS

- Below is a GM-EKF position error plot, with the 3 st dev bound in red, for an L2 northern halo orbit (left) and a L1 Lyapunov orbit (right). The bottom subplot shows what exclusion is occluding a measurement

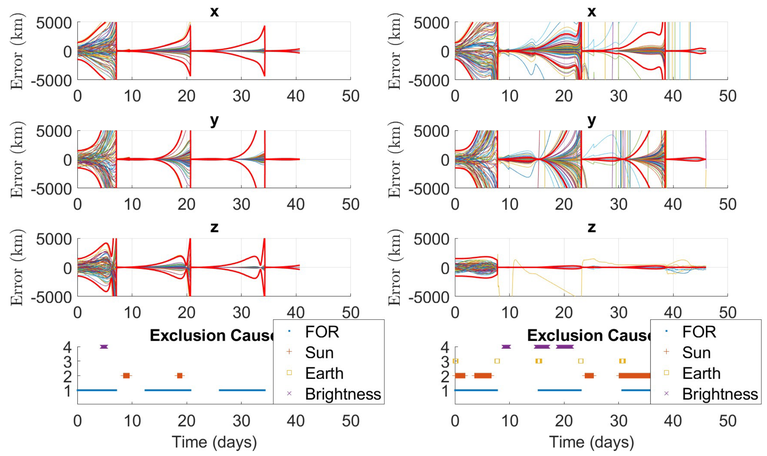

- The non-gaussian distribution of the state before a measurement is seen below for the L2 NH orbit

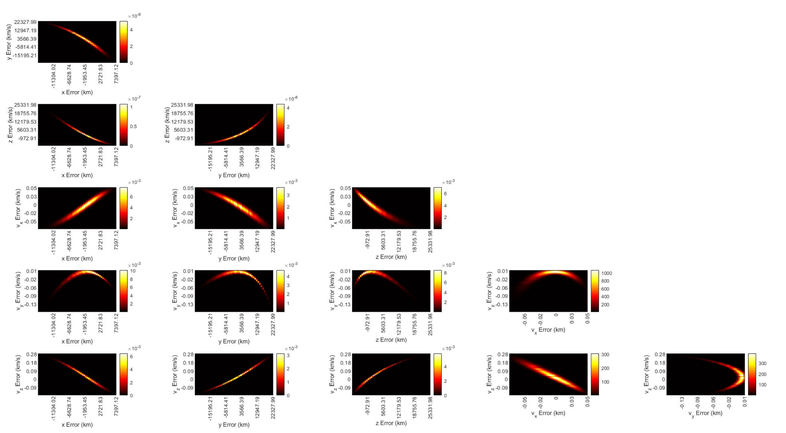

DISCUSSION

- The L2NH orbit previously failed under a large uncertainty without a model to incorporate non-gaussian distributions. Here we are able to see that the trails stay within the 3 st dev bounds, therefore improving the area that we are able to confidently track. The L1 Lyapunov orbit also previously failed, and while we do not see a perfect capability to track we are still successful 86/100 times.
- The distribution of the state after being propagated through the nonlinear dynamics is clearly shown to be non-gaussian from the bottom plot, therefore reinforcing the need for a non-gaussian tracking method.

CONCLUSIONS

- Overall, the GM-EKF allows for moon-based object tracking for an increased number of scenarios which have larger uncertainty and more prominent non-Gaussian distributions. Future work will incorporate the GM-EKF into multi-object tracking scenarios.

ACKNOWLEDGEMENTS / REFERENCES

N. Aeronautics and S. A. (NASA), Commercial Lunar Payload Services (CLPS). [Online].

A. Delépaut, E. Giordano, and A. Secci, “Use of GNSS for lunar missions and plans for lunar in-orbit development,” Open Astronomy, vol. 10, 2022

K. J. DeMars, R. H. Bishop, and M. K. Jah, “Entropy-based approach for uncertainty propagation of nonlinear dynamical systems,” Journal of Guidance, Control, and Dynamics, vol. 36, no. 4, pp. 1047–1057, 2013

The views expressed in this article are those of the author and do not reflect the official policy or position of the United States Air Force, Department of Defense, or the U.S. Government

The Impact of Helicopter Vibrations on the musculoskeletal heath of US Army Aviators

Julie Johnston[1,3], Jordan Dixon[2], and Brian Anthony[1]

[1]MIT, [2]Draper, [3]Draper Scholar

ABSTRACT: It is no secret that helicopter pilots are exposed to significant whole-body vibrations, but little has been done to mitigate the issue. Components have been added to the UH60M to reduce vibrations felt by the aviator, but injury is still prevalent. This project will aim to understand the extent of injury and pain endured by UH60 pilots, while testing the impact of UH60 M and L vibrations on a pilot. We intend to test spine models on a vibration table to understand the injuries sustained during long duration exposure and continued exposure to injured spine models. Additionally, a modified survey of past research will explore the efficacy of the AVCS in reducing vibration endured by pilots. We will also gain an understanding of alternative methods used by UH60 M and L pilots to mitigate or reduce the pain.

INTRODUCTION

US Army UH60:
1979: UH60A first entered service
1989: UH60L entered service
2006: UH60M entered service

The UH60M incorporates a new component, the **Active Vibration Control System** (AVCS).

Purpose of AVCS: reduce helicopter cockpit and cabin vibrations by mechanically generating additional airframe vibratory loads out-of-phase with the main rotor induced 4 per rev vibrations (vibration due to 4 blades per revolution of MR)
Additionally: adapt with varying rotor speeds between 90-105% rotor speed and changing flight conditions such as varying weight and CG due to fuel burn or mission equipment. (UH60M TM 1-1520-280-10)

AVCS Components:
Active Vibration Control Computer (AVCC)
AVCS Electronic Unit (EU)
Force Generators (x3)

Prevailing Issue: UH60 pilots experience chronic back pain and injury

Questions: Does the UH60M AVCS effectively reduce the helicopter vibrations endured by pilots? Do pilots who have flown only UH60L experience greater pain/injury than those who have flown only UH60M? Does mitigating care (massage, chiro, physical therapy, etc.) combat the issue and at what cost physically and monetarily?

Hypothesis: UH60M AVCS reduces the vibrations endured by pilots, but the incorporation of the AVCS does not mitigate the deterioration of pilot spinal health.

METHODS

Background:

- Past studies have shown strong correlation between the vibration of Army Helicopters and aviator injury
- USAARL Report 2017-12 shows the frequency of each aircraft:

Table 1: Rotary Wing Aircraft Frequencies. Obtained with data from MIL-STD-810G.

Aircraft	Frequencies (Hz)			
	Fundamental	Blade Pass	1st Harmonic	2nd Harmonic
AH-1	5.40	10.80	21.60	32.40
AH-6J	7.95	39.75	79.50	119.25
AH-6M	7.92	47.52	95.04	142.56
AH-64	4.86	19.44	38.88	58.32
CH-47D	3.75	11.25	22.50	33.75
MH-6H	7.80	39.00	78.00	117.00
OH-6A	8.10	32.40	64.80	97.20
OH-58AC	5.90	11.80	23.60	35.40
OH-58D	6.60	26.40	52.80	79.20
UH-1	5.40	10.80	21.60	32.40
UH-60	4.30	17.20	34.40	51.60

- Gap: UH60 is not broken down into M v L and therefore does not capture the efficacy of the AVCS in reducing vibrations
- USAARL Report 2013-07 highlights the effects of poor posture required to manipulate controls as a reason for musculoskeletal injury/pain:

TABLE II. MALADAPTIVE POSTURE REQUIRED OF HELICOPTER PILOTS.

Etiology	Pathophysical Posture	Resultant
Forward flexion of trunk and shoulders; cyclic control with RUE resting forearm on thigh	Kyphotic posture of thoracic and lumbar spine with middle to low thoracic spine fulcrum[1] and loss of normal lumbar lordosis	Isometric activity and resultant fatigue of spinal extensors (erector spinae, multifidus)
Neck extension; view instrument panel and environs through windshield	Compromised cervical spine segment posture	Degree of extension (with or without rotary component) and assoc. fatigue dependent upon pilot height, seat height, and other factors[2]
Unsupported sitting; feet required to operate antitorque pedals	No support base of feet; unable to place "flat on the floor" with LE support[3]	Hips and knees flexed (psoas and iliacus fatigue) with feet dorsiflexed. Posterior pelvic tilt rocking on ischial tuberosities[4]
Asymmetric collective control with LUE	Leftward rotational twist of trunk and lateral bend	RUE resting forearm on thigh contributes to leftward rotation; lateral bend to LUE use of collective lever[5]

RUE – right upper extremity; LUE – left upper extremity; LE – lower extremities.
[1] Compressive loads, particularly in the lower spine (L3-L5), higher in kyphotic than erect seated posture.
[2] Results exacerbated with addition of head-supported mass (e.g., night vision goggles).
[3] Some aircraft with stability augmentation or automatic flight control systems allow for "feet on the floor" flying rather than continuous antitorque pedal adjustment in cruise and other specified flight conditions.
[4] Trunk flexion exacerbated when seated with <70° knee flexion.
[5] Bend exacerbated in low-power settings with more horizontal collective lever position.

Survey:

- Approximately 250-500 participants (Goal)
- UH60L and UH60M pilots
- Retired, Active Duty, Reserve/Guard

METHODS CONT.

Vibration Experimentation:

- Utilize a vibration table and models of various spines using required positioning and different known injuries (bulging disk, herniated disk, fractured vertebrae)
- Apply known vibration signatures of both UH60M and UH60L to vibration table
- Observe impact of applied vibrations using high speed cameras of MIT Nano Lab (Dr. Anthony)

DISCUSSION

Understanding how the helicopter vibrations impact the musculoskeletal health of UH60 pilots has numerous nuances that are difficult to capture. How do the vibrations exacerbate the poor posture required of the pilots to manipulate the controls. This will expose many underlying issues of human factors integration in cockpit design and modernization.

EXPECTED OUTCOMES

At this time, no conclusions can be drawn given the infancy of the project.

Potential Conclusions:

- UH60M vibrations may not be reduced enough to truly mitigate the impact on aviators.
- We aim to quantify the efficacy of the AVCS to understand the additional measures required to mitigate the impact of helicopter vibrations on a US Army Aviator should be developed.

ACKNOWLEDGEMENTS / REFERENCES

We'd like to thank the aircrew members who will participate in the survey and USAARL for sharing information and techniques in this research.

Stochastic Guidance for Aerocapture at Uranus

Alex Meredith[1,2], Chris Jewison[3], Jonathan How[1]

[1]MIT Aerospace Controls Lab, [2]Draper Scholar, [3]Draper

ABSTRACT: Aerocapture is a key enabling technology for NASA's planned Uranus flagship mission. Previous studies have shown that aerocapture can reduce flight times to the ice giants by 5 years [1] and can increase payload mass by 40% [2] when compared to fully propulsive orbital insertion. However, atmospheric uncertainty significantly increases the difficulty of successful aerocapture at Uranus. This poster presents some preliminary results on modeling the atmosphere of Uranus as a Gaussian random field and proposes integrating this model into stochastic guidance algorithms for aerocapture at Uranus.

INTRODUCTION

Aerocapture is a maneuver where a spacecraft dives through the atmosphere of a body to slow down and prepare for orbital insertion, as an alternative to propulsive orbital insertion.

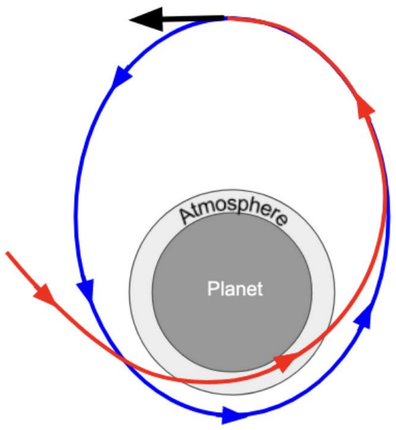

Conditions experienced during aerocapture are similar to those experienced during atmospheric entry and descent. A nominal aerocapture trajectory at Earth, using fully numerical predictor-corrector guidance (FNPAG) is shown below, with peak dynamic pressures on the order of 11 kPa. Atmospheric uncertainty poses a major challenge for aerocapture at Uranus.

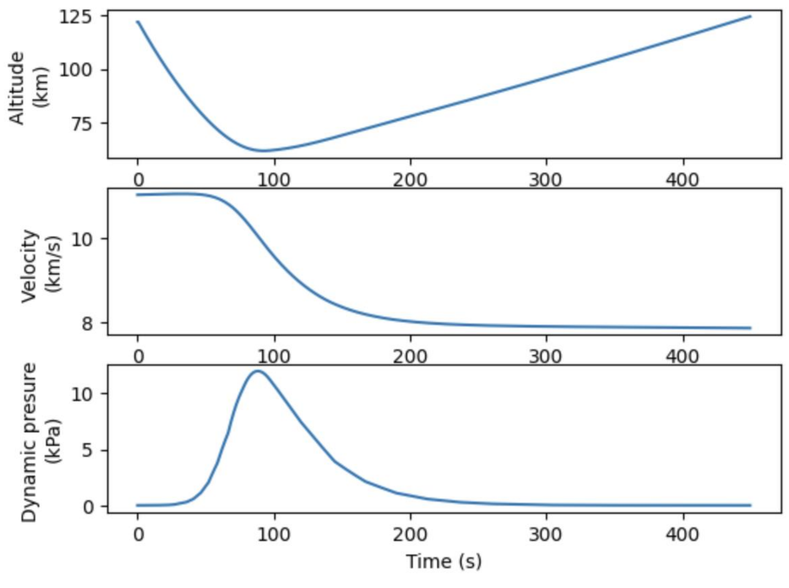

METHODS

We generated 1,000 possible Uranus atmospheres using UranusGRAM [3]. We then performed a Karhunen–Loève expansion (KLE) on empirical atmospheric perturbation data to get a discrete representation of a Gaussian random field representing the Uranus atmosphere. With λ and ϕ representing eigenvalues and eigenfunctions of the normalized density perturbation covariance matrix, respectively, the KLE density is given by [TODO cite]:

$$\rho(h) = \bar{\rho}(h) + \sum_{i=1}^{50} \mathcal{N}(0,1)\sqrt{\lambda_i}\phi_i(h)$$

RESULTS

The plot below shows density profiles sampled from UranusGRAM and from our KLE representation of density. Statistics are computed over 1,000 samples from each model.

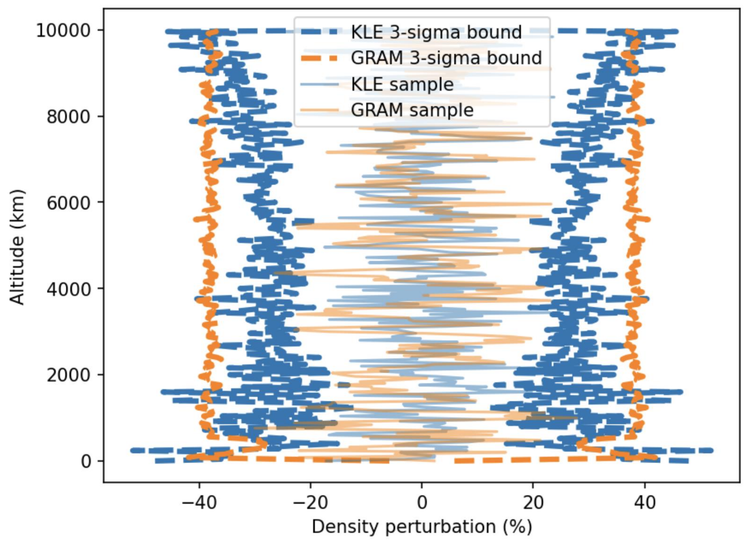

DISCUSSION

These results indicate that a KLE-generated Gaussian random field can represent density with similar statistics to UranusGRAM, as expected. Other researchers have previously found similar results for MarsGRAM [4]. Our results are consistent with the literature.

FUTURE WORK

These results are preliminary and are part of a broader research effort towards improving guidance, navigation, and control for aerocapture at Uranus.

We are currently developing stochastic optimization-based guidance algorithms so that we can optimize over a probabilistic distribution over atmospheric density during aerocapture. We expect that this will improve the fidelity of aerocapture guidance, and hope that it will reduce mean delta-V and reduce the probability that extreme atmospheric conditions lead to a crash or escape from the Uranus system.

REFERENCES

[1] J. L. Hall, T. R. Spilker, N. O'Kongo, and C. G. Justus, "Aerocapture Systems Analysis for a Neptune Mission," 2006.
[2] A. P. Girija, S. J. Saikia, J. M. Longuski, S. Bhaskaran, M. S. Smith, and J. A. Cutts, "Feasibility and Performance Analysis of Neptune Aerocapture Using Heritage Blunt-Body Aeroshells," Journal of Spacecraft and Rockets, vol. 57, no. 6, pp. 1186–1203, Nov. 2020, doi: 10.2514/1.A34719.
[3] H.L. Justh. "Uranus Global Reference Atmospheric Model (Uranus-GRAM)." In 2022 Global Reference Atmospheric Model (GRAM) Virtual Workshop. 2022.
[4] S. W. Albert, A. Doostan, and H. Schaub, "Onboard Density Modeling for Planetary Entry via Karhunen-Loève Expansion," in 2023 IEEE Aerospace Conference, Big Sky, MT, USA: IEEE, Mar. 2023, pp. 1–12..

Silicon Photomultipliers as Free-Space Optical Communication Sensors

Leonardo Gallo[1], Joseph Hollmann[2], Carl Hansen[2], and Kerri Cahoy[3]

[1]MIT Draper Scholar, [2]Draper, [3]MIT STAR Lab

ABSTRACT: Silicon Photomultipliers are solid state sensors with low voltage operation, single-photon quantification, and insensitivity to magnetic fields. They are commonly used for bio-imaging and lidar. The two output signals inherent to the SiPM architecture characterize the instantaneous photon flux and its derivative. These signals are denoted as the standard axis and fast axis signals, respectively. The simultaneous access to these signals enables pointing (slow axis) and free space optical communications (fast axis). The simulation of a 2x2 SiPM array scanned by a 2mm diameter beam resulted in an angle accuracy of $1\ \mu rads$. A model that simulates the response of a SiPM to high-speed pulses is introduced. Lastly, a power link budget for a crosslink of 1,000 km and Bit Error Rate (BER) requires a transmit power of at least 37.8 mW.

INTRODUCTION

- Silicon Photomultipliers (SiPMs) accurately quantify a signal of light at the single-photon level.
- Key advantages of this solid-state sensor include low voltage operation, insensitivity to magnetic fields, and uniformity in response.
- The sensor reports information on a slow axis (instantaneous photon flux) and fast axis (derivative of photon flux).
- The sensor performance is evaluated for a 3U CubeSat cross-link. The communication demonstration requires data rates of 20 Mbps and a link distance of 1000 km. The slow axis (100Hz) used for pointing, and the fast axis (200MHz) for communications.

Figure from STAR Lab's CLICK B/C Mission

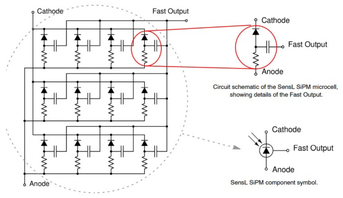

Figure from OnSemi's C Series SiPM

METHODS

- Pointing (2x2 SiPM Array)

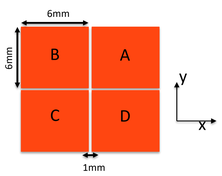

$$x = \frac{(N_a + N_d) - (N_b + N_c)}{N_a + N_b + N_c + N_d}$$

$$x = \frac{(N_a + N_d) - (N_b + N_c)}{N_a + N_b + N_c + N_d}$$

$$NEA(\theta_x, \theta_y) = \frac{1}{f_{PT\text{-}SNR}} \sqrt{\frac{1}{s_x^2} + \frac{1}{s_y^2}}$$

$$SNR_{ave} = \sqrt{sample_{ave}} SNR_i$$

$$sample_{ave} = \frac{f_{comms}}{f_{pntg}}$$

- High Speed Pulsing

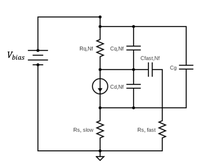

$$H(s) = \frac{Z_{th}}{s \cdot C_d + 1}$$

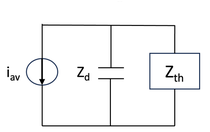

$$i_{avlch} = \delta \cdot Q_{avlch}$$

$$Q_{ave} = v_e \cdot C_d$$

$$H(s) = \frac{Z_{th}}{s \cdot C_d + 1} s \cdot C_d$$

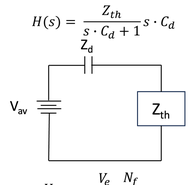

$$V_{avlch} = \frac{V_e}{s} \frac{N_f}{N_{total}}$$

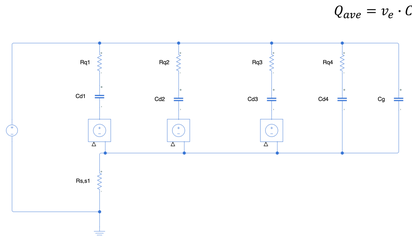

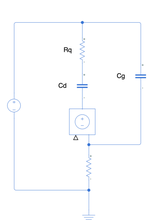

$$R_{Q,} = R_{Q,SIPM}/N_{cells}$$

$$C_{D,} = C_{Q,SiPM} \cdot N_{cells}$$

$$V_{step} = \frac{V_e}{s} \frac{N_f}{N_{total}}$$

RESULTS

- Optical Link Budget

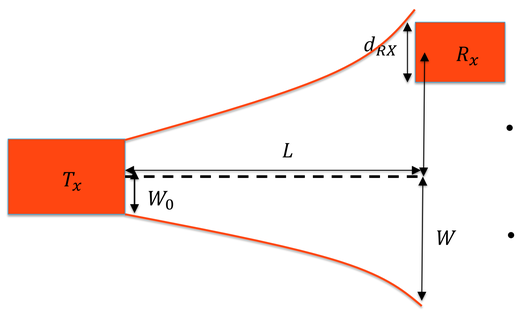

- Specifications
  $L = 1000\ km$
  $\lambda = 525\ nm$
- For a BER = 10^{-6} :
  $N \geq 125\ photons$
  $P_{tx} = 37.8mW$

- High Speed Pulsing

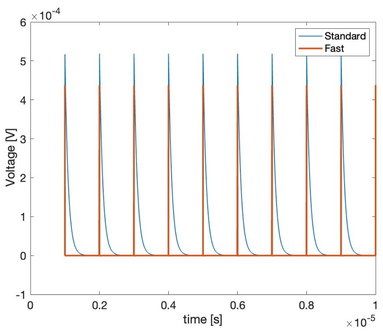

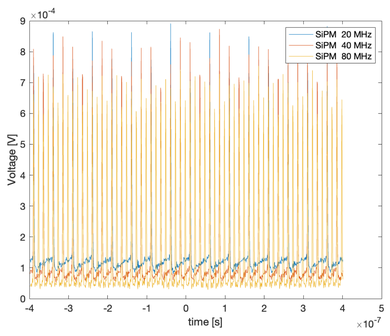

- Noise Equivalent Angle

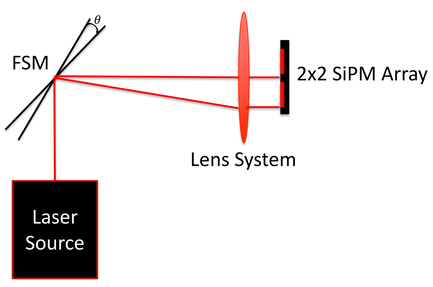

$$\theta_{min} = 1\ \mu rad$$
$$\theta_{max} = 122.2\ mrad$$

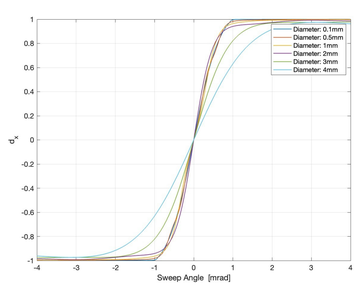

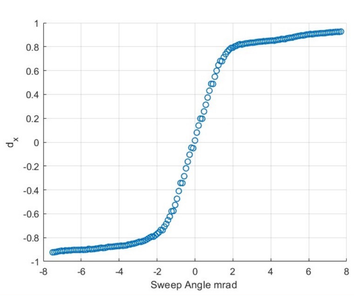

DISCUSSION

- The reported angle accuracy from the simulation is in the order of $1\ \mu rads$. In comparison, the TBIRD[2] mission accomplished $10\ \mu rads$.
- It is possible to further improve the angle accuracy by modifying the diameter of the collimated beam and decreasing the gap in between the sensor array.
- The experimental NEA is limited by the FSM (60 $\mu rads$)
- The required transmitted power to achieve a BER of 10^-6 for SiPMs is round 37.8 mW. This is an order of magnitude lower than the 200mW transmitted power for the CLICK BC Mission[3].
- For the high-speed pulsing simulation, the noise in the signal is modeled as shot noise.
- Experimentally, On-Semi's C-series SiPM is tested at 20, 40, and 80 MHz. The results match the simulated values.

CONCLUSIONS

- A COTS SiPM from OnSemi is shown to have angular resolution of $1\ \mu rads$ and a measurable response to 80 MHz pulses both in simulations and experiments.
- Additionally, the SiPM simulation correctly models the SiPM's avalanche current with no circuit complexity introduced when modifying the number of firing cells.
- Averaging the pointing signal directly decreases the NEA.
- For future experiments, an FSM with higher step resolution is needed to test the SiPMs NEA limit.
- Future work will include a case study of various geometries and material properties of the SiPM as well as a demonstration of simultaneous pointing and communication to the sensor with various modulation schemes.

ACKNOWLEDGEMENTS

- I'd like to thank Dr. JP Laine, Dr. Joseph Hollmann, Dr. Carl Hansen and Prof. Kerri Cahoy for their continued support and mentorship.

References

1. Long, M.J., "Pointing Acquisition and Tracking Design and Analysis for CubeSat Laser Communication Crosslinks," M.S. Thesis, Massachusetts Institute of Technology, February 2018.
2. Cahoy, Kerri, Grenfell, Peter, Crews, Angela, Long, Michael, Serra, Paul et al. 2019. "The CubeSat Laser Infrared CrosslinK Mission (CLICK)."
3. Serra, Paul. "Optical Front-End for a Quantum Key Distribution Cubesat." *International Conference on Space Optics Â€" ICSO 2020*. Vol. 11852. SPIE, 2021. 118523C–118523C–19. Web.

Undersea Wireless Power Transfer Systems: A Parametric Design Map

Derek Gess[1,3], Kasia Oleske[2,*], Robert Doyle[2], Peter Kerrebrock[2], Sara Barron[2], and Michael Short[3]

[1]Draper Scholar, [2]Draper Laboratory, [3]Massachusetts Institute of Technology

*Author to whom correspondence should be addressed

ABSTRACT: Inductive wireless power transfer (IWPT) has emerged as a promising alternative for charging high powered systems in air, surpassing traditional methods due to its advantages in efficiency, convenience, and robust design. Recently, IWPT has been employed in remote charging systems for autonomous underwater vehicles (AUVs) to increase mission length and travel distance and speed while decreasing required oversight to operate the system [1]. However, the technology used in air cannot be directly transferred to an underwater environment due to differing environmental conditions, such as, but not limited to, higher hydrostatic pressures, lower temperatures, ocean current disturbances, and a conductive medium [2]. This research aims to design an undersea IWPT system that is versatile, durable, and can transmit >1 kW of power by analyzing geometries and materials used in in-air WPT applications and comparing their performance with geometries that are applied to current AUV designs. The geometries were modeled using ANSYS Maxwell and the coupling coefficients of the primary and secondary coils were parametrically analyzed as a function of both gap distance and lateral misalignment. By maintaining a high coupling coefficient, a higher magnetic flux can be received by the secondary coil, therefore increasing charging efficiency. It was found that the R-type undersea coupling design performed similarly to the rectangular and circular in-air designs, while the CA-type and half CA-type coupling was comparatively suboptimal. The high coupling coefficient of the R-type design is advantageous for underwater IWPT systems as it can minimize magnetic field losses and maximize charging efficiency.

INTRODUCTION

- AUVs used for environmental, scientific and military applications [1].
- Undersea adds additional challenges to charging [2]:
  - Increased misalignment due to ocean currents.
  - Decreased coupling due to biofouling.
  - Decreased longevity due to enhanced corrosion.
  - Increased eddy current losses due to conductive saltwater medium.

Type	Pros	Cons
Direct Electrical Contact (DEC)	• Fast Charging • High efficiency	• Difficult alignment constraints • Lower life cycle • Weak concealment (corrosion/short circuit)
Solar	• Essentially unlimited range	• Slow charging • Location, season and weather dependent • Surface to charge • Weak concealment
Battery Swapping	• Fast charging	• Weak concealment • Manned • Requires resurfacing
Inductive WPT	• Strong concealment • kHz operating frequency	• Shorter transmission difference • Attenuation issues

Table 1: Various types of charging methods for AUV systems [1].

METHODS

- Goal: A robust, versatile and durable IWPT system capable of transmitting >1 kW of power.
- Present day state-of-the-art high-powered IWPT systems in-air and undersea were compared below.

Reference	Date	Output Power	End-to-end Efficiency	Operating Frequency	Geometry
[3]	2023	11 kW	93%	85 kHz	N/A
[3]	2019	120 kW	97%	22 kHz	DD
[4]	2012	60 kW	83%	20 kHz	I-Type
[5]	2015	38.7 kW	73%	10.8 kHz	DD

Table 2: Current high-powered WPT systems in an air environment.

Name	Date	Output Power	End-to-end Efficiency	Operating Frequency	Geometry
Tohoku University	2004	500 W	90%	N/A	Cone-type circular
Harbin IT	2020	630 W	89.7%	50 kHz	Dipole type
Nanjing IT	2023	575 W	92.51%	50 kHz	Circular Arc-type
Huazhong University	2017	1.0 kW	92.41%	465 kHz	Three Phase coil
Zhejiang University	2017	300 W	77%	52 kHz	R-Type

Table 3: Current high-powered WPT systems in an undersea environment [6].

RESULTS

In-Air		Undersea		
Rectangular	Circular	CA-Type	R-Type	Half CA-Type
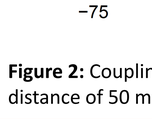		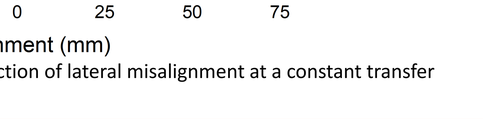		

Table 4: All designs were tested in air. The size of the coils was kept consistent, where the diameter is 400 mm, the copper coil thickness is 10 mm, and the ferrite thickness is 20 mm.

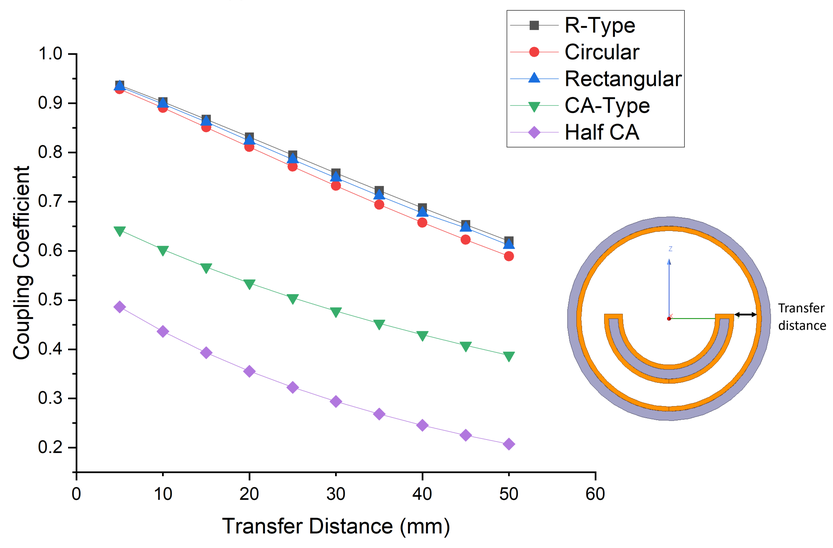

Figure 1: Coupling coefficient of coupled coils as a function of transfer distance. Transfer distance is the width of the gap between the primary and secondary coils.

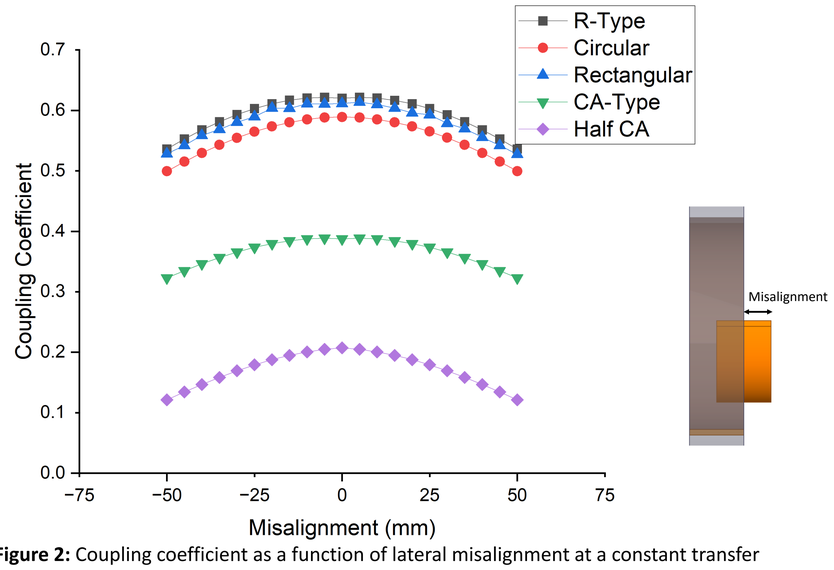

Figure 2: Coupling coefficient as a function of lateral misalignment at a constant transfer distance of 50 mm.

DISCUSSION

- The R-type coupling geometry kept comparable coupling coefficients to the in-air designs across the parametric analyses.
  - CA-type and half CA-type did not perform as well, most likely due to wasted surface area in the secondary coil that did not maximize magnetic flux.

Circular	Rectangular	R-type	CA-type	Half CA-type
0.9364	0.9286	0.9339	0.6423	0.4859

Table 5: Coupling coefficient in each design at a gap distance of 5 mm.

- However, the CA-type and half CA-type use significantly less materials than the R-type, as shown below.
  - This reduces both the weight and cost of the IWPT system.

Circular	Rectangular	R-type	CA-type	Half CA-type
0.00377	0.00480	0.00471	0.00368	0.00207

Table 6: Ferrite volume (m^3) in each design at a gap distance of 5 mm.

CONCLUSIONS

- Coupling coefficients for geometric coupling designs for undersea IWPT applications were analyzed.
  - R-type coupling geometry showed to be most comparable with state-of-the-art in-air geometry designs with a maximum coupling coefficient of 0.9339 at a gap distance of 5 mm.
- Further steps:
  - Test lateral misalignment in undersea applications while keeping a constant ferrite volume.
  - Continue to model various geometries to maximize coupling while minimizing material volume.
  - Change the operating region to seawater and compare results to air.
  - Simulate eddy current losses due to conductive saltwater medium.
  - Test the impact of hydrostatic pressure on different ferrite materials.

ACKNOWLEDGEMENTS / REFERENCES

I'd like to thank Isaac Ehrenberg and Akram Kalate for their help with ANSYS Maxwell and understanding magnetic material applications in IWPT.

References:

[1] C. R. Teeneti, T. T. Truscott, D. N. Beal and Z. Pantic, "Review of Wireless Charging Systems for Autonomous Underwater Vehicles," in *IEEE Journal of Oceanic Engineering*, vol. 46, no. 1, pp. 68-87, Jan. 2021. [2] Mohsan, S.A.H.; Khan, M.A.; Mazinani, A.; Alsharif, M.H.; Cho, H.S.; "Enabling Underwater Wireless Power Transfer towards Sixth Generation (6G) Wireless Networks: Opportunities, Recent Advances, and Technical Challenges," *J. Mar. Sci. Eng.* **2022**, 10, 1282.

[3] Bo Zhang, Richard B. Carlson, John G. Smart, Eric J. Dufek, Boryann Liaw, "Challenges of future high power wireless power transfer for light-duty electric vehicles----technology and risk management," *eTransportation*, Volume 2, **2019**, 100012, ISSN 2590-1168.

[4] S. Y. Choi, B. W. Gu, S. Y. Jeong and C. T. Rim, "Advances in Wireless Power Transfer Systems for Roadway-Powered Electric Vehicles," in *IEEE Journal of Emerging and Selected Topics in Power Electronics*, vol. 3, no. 1, pp. 18-36, March 2015.

[5] K. Ukita, T. Kashiwagi, Y. Sakamoto and T. Sasakawa, "Evaluation of a non-contact power supply system with a figure-of-eight coil for railway vehicles," *2015 IEEE PELS Workshop on Emerging Technologies: Wireless Power (2015 WoW)*, Daejeon, Korea (South), 2015, pp. 1-6.

[6] Xia, Tao, Hang Li, Haitao Yu, Yangfei Zhang, and Pengfei Hu. 2023. "A Circular-Arc-Type Magnetic Coupler with Strong Misalignment Tolerance for AUV Wireless Charging System" *Journal of Marine Science and Engineering* 11, no. 1: 162.

Multidisciplinary Design of Aeroassist Vehicles

Daniel Gochenaur[1,2], Marshall Galbraith[2], Dave Benson[3], and Olivier de Weck[2]

[1]Draper Scholar, [2]Massachusetts Institute of Technology, [3]Draper Laboratory

ABSTRACT: A multidisciplinary analysis framework is proposed to study challenges relevant to the design of space systems that use aerodynamic forces to modify trajectories, such as aerocapture and aero-gravity assist vehicles. The framework integrates toolsets to model vehicle geometries, analyze their aerodynamics, and propagate trajectories, among other disciplinary analyses. The investigation seeks to use the framework to identify optimal aeroassist vehicles. Particular focus is placed on the path-dependent coupling of vehicle shape, aerodynamics, and thermal response during flight accounting for the effects of vehicle shape change due to ablation.

WHAT ARE AEROASSIST VEHICLES?

- Aeroassist vehicles are space systems that use aerodynamic forces to modify their trajectories
- Examples include:
  - Aerocapture
  - Aero-gravity assist
  - Aerobraking
- The above examples offer a variety of advantages over purely propulsive maneuvering

Aerocapture Maneuver Diagram:

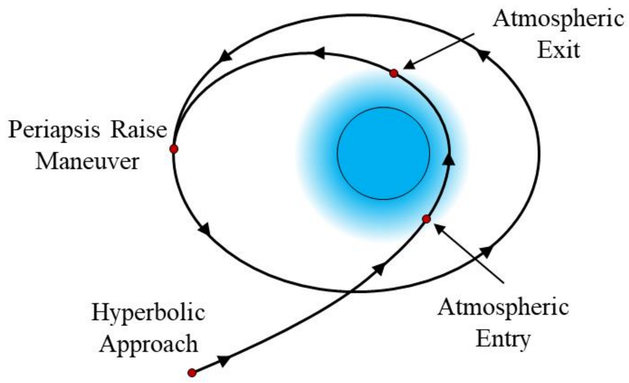

Aero-gravity Assist Maneuver Diagram:

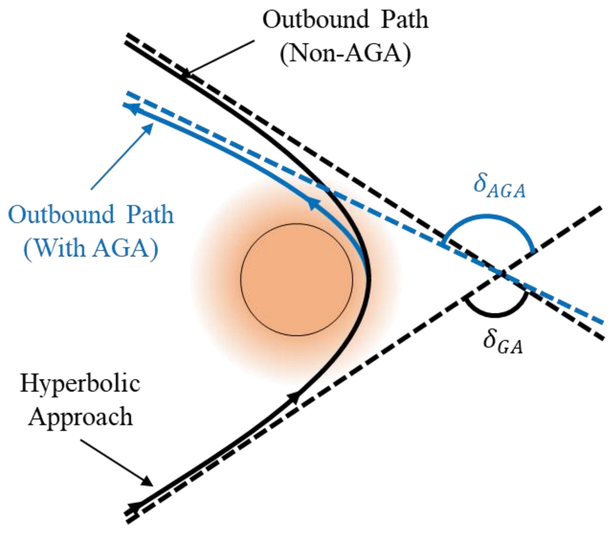

RESEARCH QUESTIONS

- Aeroassist vehicles experience considerable aerodynamic heating, causing mass ablation
- The effects of the resultant shape change are poorly understood, leading to the below research questions

1. What steps need to be taken to model and analyze systems undergoing shape change in flight?
2. What is the effect of recession on aerodynamics and the trajectory during aeroassist maneuvers?
3. What is the uncertainty in aerodynamic performance due to ablation at a variety of destinations?
4. What Pareto optimal vehicle designs can we identify for aerocapture and aero-gravity assist missions?

METHODS

- Develop a multidisciplinary analysis framework for the design and optimization of aeroassist vehicles
- Framework involves generation of geometries, aerodynamic analysis, ablation modeling, and trajectory propagation within design loop
- Ablation modeling handled using free-form deformation, where recession is represented as the alteration of splines that define the geometry

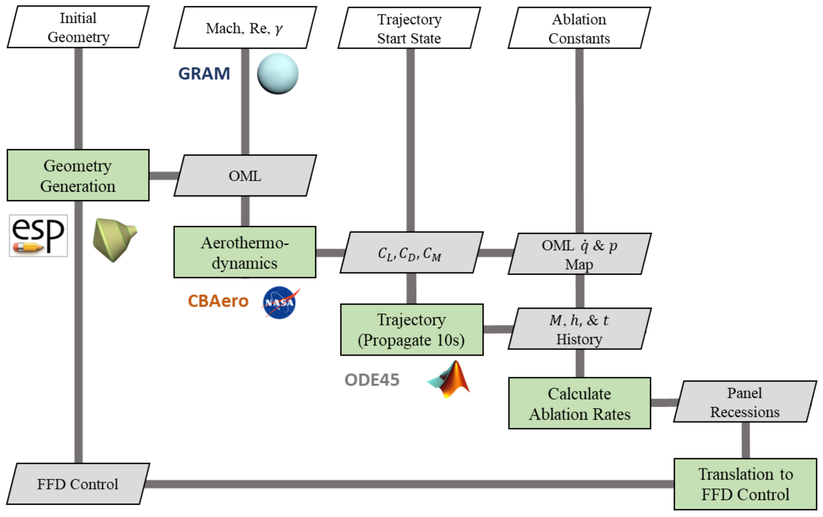

RESULTS

- Blunt and lifting-bodies modeled, analyzed, and propagated in aerocapture trajectory loop

Blunt-Body | Lifting-Body

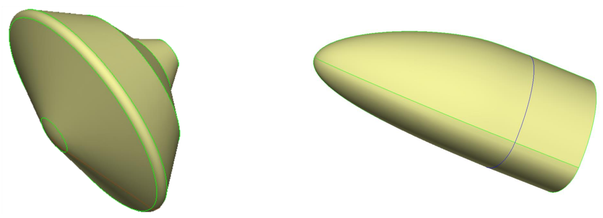

Blunt-Body Uranus Aerocapture Results

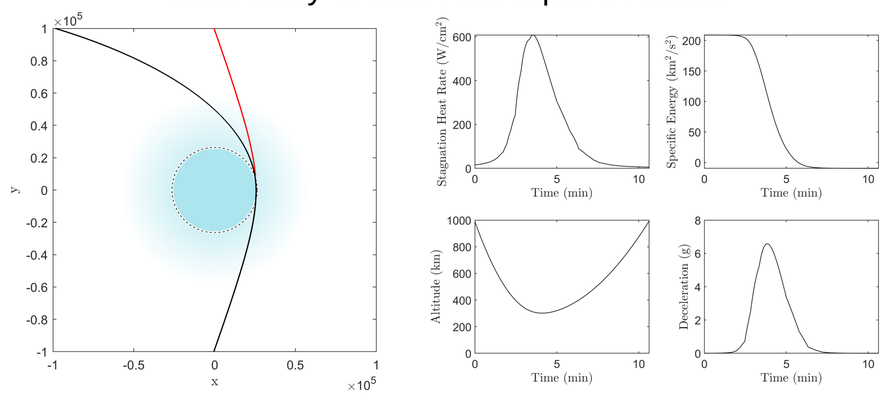

Lifting Wall Pressure

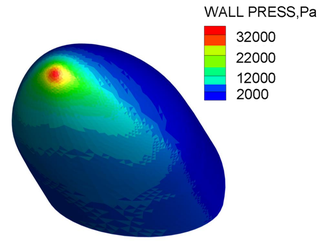

Blunt-Body Recession Mapping

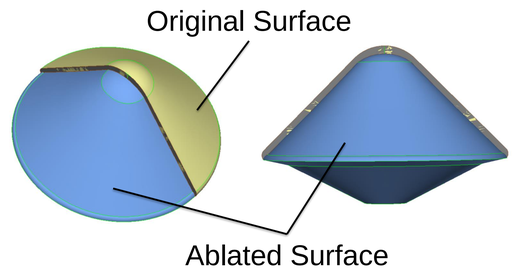

ACKNOWLEDGEMENTS

Financial support provided by the National Defense, Science, and Engineering Graduate Fellowship. Computing resources provided by the Army Engineering Research Development Center and MIT/Lincoln Labs SuperCloud.

Design Exploration of a MEMS Stirling Engine

Ryann Hee[1,2] , Kasia Oleske[3], Brian Munroe[3], Jim Bickford[3], Joseph Aghia[3], Jim Dombrowski[3], Ronald McNabb[3], Jeffrey Hoffman[1]

[1]Massachusetts Institute of Technology, [2]Draper Scholar, [3]The Charles Stark Draper Laboratory, Inc.

ABSTRACT: As technologies continue to advance there is a desire to make energy sources as small as possible and as powerful as possible. Space probes and other high reliability systems have a need for power in remote, harsh environments that require novel materials development to meet growing power and thermal management requirements while still maintaining small form factors. Today there are no micro power systems that have efficiencies greater than ~2% which meet all mechanical, thermal, and system requirements for space probes and other small form factor power needs [1]. However, Stirling engines are promising thermoelectric power conversion technology and are known to achieve high efficiency (30-40%) [2]. If this efficiency can be maintained in a small form factor, miniaturized Stirling engines would be a widely desired technology. This study seeks to explore the design space of a 2W miniaturized Stirling engine for applications in small-scale (mm), high efficiency power generation. Previous work has laid out a solid thermodynamic foundation for miniaturized Stirling engines and shown major gaps in the technology, one of those being the overwhelming parasitic losses that occur at such a small scale [3]. Our design aims to mitigate these losses and find an optimal efficiency through modeling done in Simulink. Early models have displayed a 7.1% mechanical efficiency at 2W. We predict that as continue to optimize each of the parameters in our model and focus on parasitic losses, we will be able to achieve a much greater efficiency compared to what is currently available.

INTRODUCTION

- Stirling engines operate by compressing and expanding a 'working fluid' to generate heat energy which can be converted into mechanical energy.
- Stirling engines have some of the highest efficiencies compared to competing technologies.
- Miniaturized Stirling engines were first studied in 1989 and a fundamental thermodynamic framework was built up from there.
- In 2018 a research group produced and tested a prototype at the mm scale. The prototype did not work as predicted and this was likely due to unaccounted parasitic losses[3]. Key components here are the heat source, working fluid (gas), free piston design, and regenerators

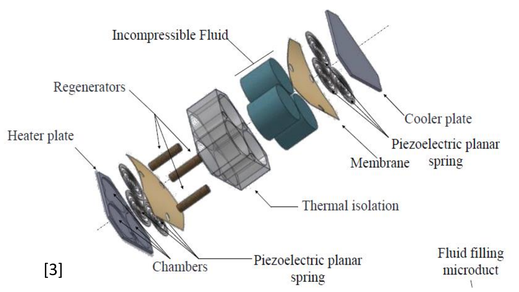

[3]

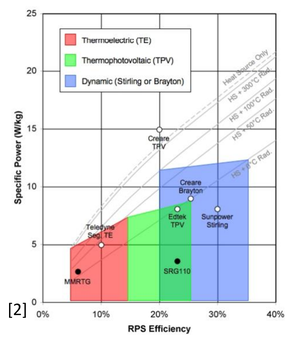

[2]

METHODS

Our design considered key findings in past work and prioritized mitigating parasitic losses.

- Firstly, Stirling engines gain efficiency based on the temperature differential, as you scale down it becomes exponentially harder to maintain a large temperature difference between hot and cold sides. This means that we want to create as much distance between the hot and cold side as possible → maximize piston length
- Second, we need to manage our parasitic losses one of the largest being conductive heat loss. A free piston design allows for a completely closed system (easier to contain heat), no mechanical linkage (reduces complexity and increases lifetime), and high thermal efficiency.
- Regenerators are also key component as they store excess heat that might normally be lost and maximize heat transfer between the pistons

RESULTS

Double acting Stirling with balanced pistons: At such a small-scale deviations in the piston motion could eventually lead to reduced efficiency or in some cases a non-operational system. The design need here is to make sure we have balanced piston motion.
We have also included regenerators in the system to help maximize heat transfer.

We were able to model this design using Simulink to start observing the engine performance and pull an estimated mechanical efficiency from the model. The idea is that each pair of pistons will create a sinusoidal motion to offset the other. However, our model first ran into stability issues resulting from the four pistons deviating. We corrected this issue by adding a hard stop to the ends of this pistons

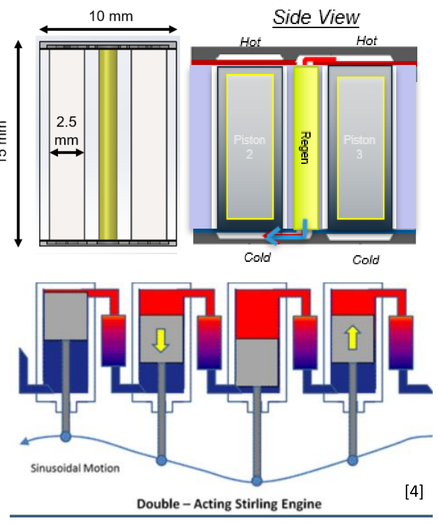

[4]

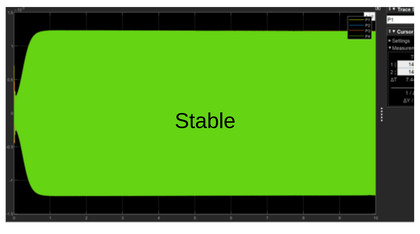

Key parameters:

- Damping
- Housing area
- Spring constant
- Piston mass
- Gas pressure
- Gas type
- Regenerator size

Model inputs:
- Material properties and dimensions (glass,si,cu, kapton – traditional MEMS materials)
- Temperature gradient

Model outputs:
- Piston motion
- Efficiency (mechanical efficiency)
- Total heat flow
- Heat flow through the housing

DISCUSSION

Glass was chosen as the housing around the pistons because of it's low thermoconductivity. Early runs of our model showed we were losing a significant portion of heat through the housing, which made this a priority parameter to optimize for. Since we can relate heat through the housing:

$$Q \propto \frac{(A \cdot Th)}{L}.$$

By reducing the overall housing area it increased our overall mechanical efficiency from 4% to 7%!

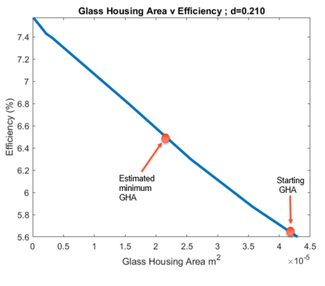

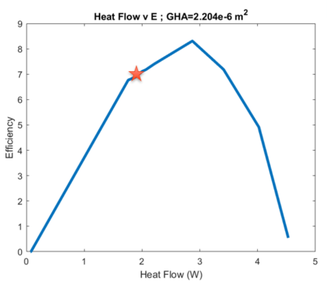

Parameter	Value	Units
Housing area	2.204	mm^2
Piston length	14	mm
Piston side	2.5	mm
Regen radius	0.65	mm
k	100	
d	0.0213	
Efficiency	~7.1%	
Power	2.00	W
Frequency	~ 100	Hz

CONCLUSIONS

We will continue to explore the model with the goal of establishing a viable design space for a MEMS Stirling engine given a 2W threshold. Our exploration will also explore the space for non-traditional materials in search of the highest attainable efficiency for this design.

ACKNOWLEDGEMENTS / REFERENCES

I would like to thank my advisors Kasia Oleske, Jeffrey Hoffman, and the rest of the Draper team for their support in this project.

[1] Wilson, et al. "Radioisotope Heater Unit-Based Stirling Power Converter Development at NASA Glenn Research Center," NASA/TM (2018).
[2] Lee S. Mason, "Realistic Specific Power Expectations for Advanced Radioisotope Power Systems," NASA, (2006).
[3] Begot, et al. "A novel model and design of a MEMS Stirling engine," International Journal of Heat and Technology, (2018).
[4] Velumani, Siriam. "Double - Acting Stirling Engine - Renewable Energy - Stirling Engine." *Renewable Energy - Stirling Engine*, 2016, https://sites.google.com/a/emich.edu/cae546816t5/history/types/double---acting-stirling-engine. (2016)

Seeking Computational Efficiency While Optimizing Formation Flying Trajectories in the Vicinity of Lagrange Points under the Influence of Solar Radiation Pressure

Hailee Hettrick[1,2], Begum Cannataro[3], and David Miller[1]

[1]Massachusetts Institute of Technology, [2]Draper Scholar, [3]Draper

ABSTRACT: To enable computational efficiency when optimizing for a mission's trajectory of two spacecraft flying in formation about a Lagrange point (where one is under the influence of solar radiation pressure), techniques from applied mathematics are employed to find approximate analytical solutions to the restricted three-body problem. Additionally, the approach for finding the mission's trajectory utilizes the naturally occurring dynamics of the regime, thereby minimizing fuel expenditures while maximizing science yield.

INTRODUCTION

- JPL's proposed mission, HabEx, was designed to take advantage of the formation flight of a space-based telescope and starshade about Sun-Earth L_2 for superior exoplanet characterization.
- The cost of superior characterization is the additional cost of second spacecraft and fuel expenditures.
- This work seeks to find a maximal yield path for imaging target stars that minimizes fuel expenditures via the naturally occurring dynamics of the regime during retargeting maneuvers.
- Additionally, this work desires to do so in a computationally efficient manner, since the dynamical model of this regime has no closed-form solutions.
- This work advances and builds on that of Sanchez [1] and Soto [2] and relies on mission design information from the HabEx Final Report [3].

METHODS

- To enable computational efficiency, and thereby enable the quick execution of simulations to achieve fuel and yield optimality, closed-form approximate analytical solutions for the dynamical models are required.
- The telescope may be modeled using the circular restricted three-body problem (CR3BP), but the starshade's large surface necessitates it being modeled as CR3BP with solar radiation pressure (SRP), which is generally a non-Hamiltonian system.
- The Lindstedt-Poincaré method with successive approximations is used to create approximate solutions for CR3BP and CR3BP with non-Hamiltonian SRP; therefore, numerical integration of the equations of motion is not required when designing the trajectory.
- Having determined closed-form solutions, a "star-first" approach is used that when a target star is observable with respect to the telescope's position, the necessary position of the starshade is calculated, and the closed-form solutions are used to identify if that position is coincident with a periodic orbit.

RESULTS

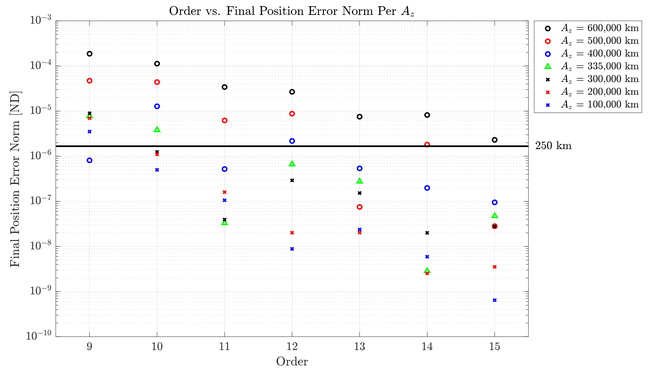

Figure 1. The final position error norm of several orders of analytical solutions compared to numerical solutions for various halo orbits in CR3BP

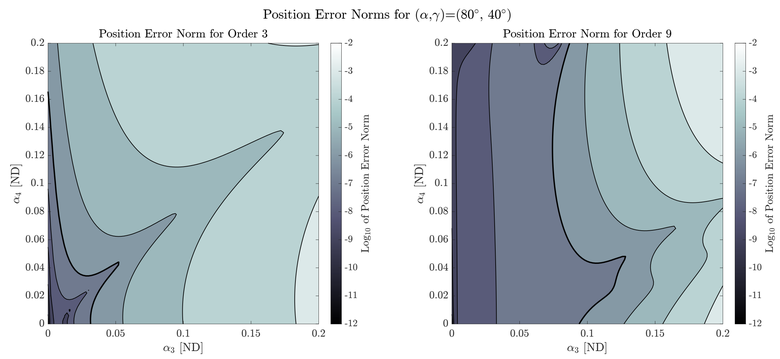

Figure 2. The final position error norm of third-order and ninth-order analytical solutions compared to numerical solutions for various orbits in CR3BP with non-Hamiltonian SRP

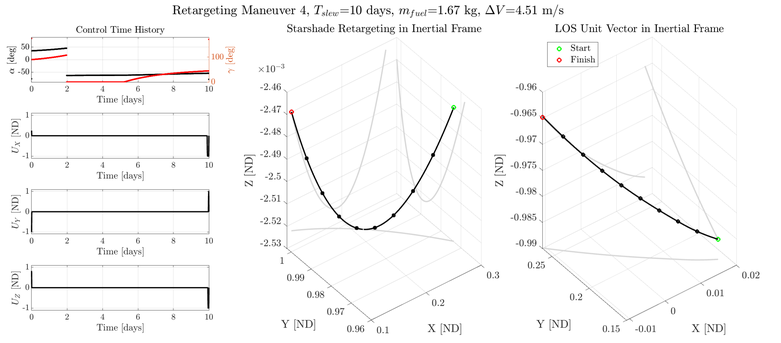

Figure 3. The first retargeting maneuver in a five-year mission. The left-hand plots indicate the control time history, the middle plot illustrates the starshade's path, and the right-hand plot shows how the line-of-sight vector moves in the inertial frame.

DISCUSSION

- Both position error norm plots show that the accuracy of the approximate solutions increase as the order of the solution increases. Moreover, the accuracy of the solution decreases as the amplitudes increase. Therefore, a sufficiently ordered solution should be used for the desired amplitude to achieve sufficient accuracy (Figures 1 and 2).
- This work improves on Soto [2] by utilizing the naturally occurring dynamics of the starshade during retargeting.
- This work improves on Sanchez [1] by considering SRP when modeling the starshade and the required imaging time for exoplanet characterization.
- Using the approximate solutions in the optimization for finding the full mission path results in the naturally occurring dynamics being used (Figure 3).

CONCLUSIONS

- Key contributions from this work include the development of closed-form, approximate solutions for CR3BP with non-Hamiltonian SRP and the identification of a periodic orbit given a position in space. Both enable the computationally efficient optimization of the trajectories of two spacecraft flying in formation for exoplanet characterization.
- One next step is to include removing the assumption of the telescope remaining on a single halo orbit – permit it to move across an energy-optimal neighborhood, thereby opening up the solution space of the optimal path finder

REFERENCES

[1] W. D. Sanchez, "Towards fuel-efficient formation lying of an observatory and external occulter at sun-earth l2," Ph.D. dissertation, Massachusetts Institute of Technology, 2020.

[2] G. J.Soto, "Orbital design tools and scheduling techniques for optimizing space science and exoplanet-finding missions," Ph.D. dissertation, Cornell University, 2020.

[3] B.S.Gaudi, S.Seager, B. Mennesson, A. Kiessling, K.Warield, K. Cahoy, J.T. Clarke, S. Domagal-Goldman, L. Feinberg, O. Guyon, et al. , "The habitable exoplanet observatory (habex) mission concept study final report," arXiv preprint arXiv:2001.06683 , 2020

Learning-Enhanced Model Predictive Guidance for FW-sUAS

C. Alexander Hirst[1,3], Chris Reale[2], and Eric Frew[1]

[1]University of Colorado Boulder, [2]Charles Stark Draper Laboratories Inc., [3]Draper Scholar

ABSTRACT: Fixed-wing small uncrewed aircraft systems (FW-sUAS) are a versatile and cost-effective platform for information gathering tasks in challenging environments, however fast, accurate path-following guidance remains a challenge. In pursuit of high-performance guidance, this work develops a novel algorithm for enhancing generic nonlinear model predictive controllers with a learned meta-level policy. Our key insight is to reason over the combined MPC-plant dynamics. This allows for the formulation of a meta-level optimal control problem wherein a meta-level policy takes actions which adaptively parameterize the MPC controller for improved closed-loop performance. Utilizing approximate dynamic programming, an expert meta-level policy is created and used to to train a neural network approximation via imitation learning. Extensive simulation experiments showcase the performance and computational efficiency of our method when applied to the 3D path-following guidance problem, with real-world flight test results coming soon.

INTRODUCTION

- Fast and accurate 3D path-following guidance for autonomous FW-sUAS is a fundamental yet challenging problem due to nonlinear dynamics, limited control authority, strong disturbances, and constrained onboard computation.
- Model predictive control (MPC) is SOTA for high-performance applications; explicitly optimizing controls over dynamics and constraints.
- Path-following MPC often jointly optimizes control and path reference, increasing OCP complexity

Fig. 1: CU Boulder RAAVEN conducting a low pass maneuver.

METHODS

Given an optimal control problem (OCP) at time i:

$$U_i^* = \underset{U^{N-1}}{\operatorname{argmin}} \sum_{k=0}^{N-1} J_k(\boldsymbol{x}_k, \boldsymbol{u}_k | \boldsymbol{z}_i) + J_N(\boldsymbol{x}_N | \boldsymbol{z}_i)$$
$$s.t.\ \ \boldsymbol{x}_{k+1} = F(\boldsymbol{x}_k, \boldsymbol{u}_k, \boldsymbol{w}_k)$$
$$\boldsymbol{x}_{k=0} = \boldsymbol{x}_i, \qquad \boldsymbol{w}_k = \boldsymbol{w}_i$$
$$h_k(\boldsymbol{x}_k, \boldsymbol{u}_k) \leq 0 \quad \forall\, k \in [0, \dots, N-1]$$

The resulting MPC policy is: $\pi_{MPC}(\boldsymbol{x}_i, \boldsymbol{w}_i\ \boldsymbol{z}_i, \boldsymbol{c}_i) = \boldsymbol{u}_0^*$, where $\boldsymbol{z}$ are cost parameters and $\boldsymbol{c}$ is the MPC solver state. A meta-level OCP is defined by combining MPC and aircraft systems into a *meta-level system*: $\boldsymbol{s}_{i+1} = [\boldsymbol{x}_{i+1}, \boldsymbol{c}_{i+1}, \boldsymbol{a}_i] = F_s(\boldsymbol{s}_i, \boldsymbol{a}_i, \boldsymbol{w}_i)$ with meta-level action $\boldsymbol{a}_i = \boldsymbol{z}_i$. Reasoning over meta-level dynamics improves performance with real-time iteration SQP methods commonly used in robotics. One-step lookahead w/ rollout (OLR) finds a meta-level policy by solving:

$$\pi_{ML}(\mathbf{s}_i, \mathbf{w}_i) = \underset{\mathbf{a}_i \in \bar{\mathcal{A}}}{\arg\min} \left(g(\mathbf{s}_i, \mathbf{a}_i, \mathbf{w}_i) + \mathcal{J}^{\tilde{\pi}_{ML}}(\mathbf{s}_{i+1}) \right)$$

However, OLR is too complex to run online, and is therefore used to train a meta-level policy via offline imitation learning.

RESULTS

After training Learning-Enhanced MPC (LE-MPC), Monte Carlo Experiments compared against two baseline MPC methods and a lookahead method.

Table 1: Mean Performance Statistics on Training Path

	Path Error [m]	Airspeed [m/s]	Lap Time [s]	Solve Time [ms]
MPCC	2.9 (---)	19.6 (---)	115.3 (---)	2.15 (---)
Lookahead	14.5 (+394.9%)	18.0 (-7.7%)	153.9 (33.4%)	---
CR-MPC	3.4 (+ 14.7%)	19.7 (+0.6%)	110.5 (-4.1%)	1.62 (-24.5%)
LE-MPC	**2.3 (-20.1%)**	**20.3 (+3.9%)**	**109.3 (-5.2%)**	**1.62 (-24.6%)**

Table 2: Mean Performance Statistics Over Unseen Test Path

	Path Error [m]	Airspeed [m/s]	Lap Time [s]	Solve Time [ms]
MPCC	0.788 (---)	21.5 (---)	150.5 (---)	2.15 (---)
LE-MPC	**0.693 (-12.0%)**	**21.5 (+0.01%)**	**149.8 (-0.43%)**	**1.62 (-24.6%)**

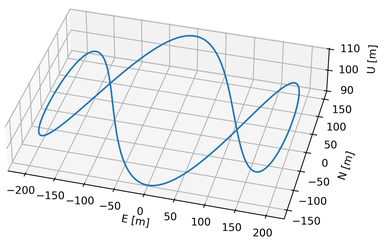

Fig. 2: Training Path

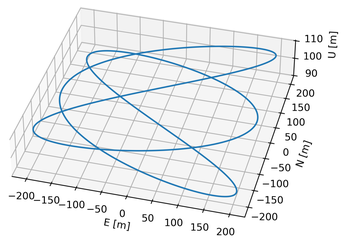

Fig. 3: Unseen Test Path

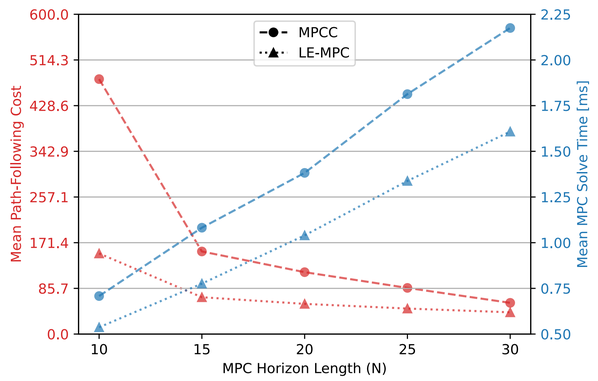

Fig. 4: Effects of Horizon Length on Cost and Solve Time

Path-Following Cost:

$$g(\mathbf{s}, \mathbf{a}, \mathbf{w}) = \mu ||V_{a,max} - V_a||_2^2 + ||\mathbf{r} - \mathbf{r}_P(\psi^*)||_2^2$$

DISCUSSION

Simulation experiments demonstrate how LE-MPC:

- outperforms state-of-the-art controllers across **all metrics** in Monte Carlo simulations.
- **reduces solve times by 25%** from MPCC.
- shows **good generalization** to unseen paths, via local path segment inputs during training.
- **reduces MPC sensitivity** to short horizons.

Limitations of the current work are:

- assumed an accurate model, full 3D wind knowledge, and no feedback delay.
- the OLR-MPC meta-level policy is computationally expensive, scaling with number of rollouts, rollout length, and MPC solve time. This makes data gathering slow (~1 hour).

CONCLUSIONS

- Learned meta-level policies provide a flexible and effective framework to dynamically parameterize MPC algorithms while maintaining constraint satisfaction and interpretability of traditional MPC.
- LE-MPC successfully applies meta-level policies to path-following guidance for FW-sUAS.
- Ongoing work is deploying LE-MPC and baseline guidance algorithms in flight tests onboard the RAAVEN FW-sUAS (Figure 1). Flight tests will validate the controllers' performance under real-world plant-model mismatch, sensor noise, computational delays, and disturbances.

ACKNOWLEDGEMENTS / REFERENCES

1. Hirst, C. A., Bird, J. J., Reale, C., & Frew, E. (2022, March). Nonlinear Model Predictive Control for Agile Guidance of Fixed-Wing sUAS. In 2022 IEEE Aerospace Conference (AERO) (pp. 1-11). IEEE
2. Hirst, C. A., Reale, C., & Frew, E. Learning-Enhanced Model Predictive Control for Path-Following Guidance of Fixed-Wing sUAS. *In Review*.
3. Hirst, C. A., Reale, C., & Frew, E. 3D Path-Following Guidance via Nonlinear Model Predictive Control for FW-sUAS. *In Preparation*.

Privacy Preserving Machine Learning Sensors

Jacob Huckelberry[1,3], Matthew Stewart[1], Vijay Janapa Reddi[1] , and Felipe Vilas-Boas[2]

[1]Harvard University, [2]Charles Stark Draper Laboratory, [3]Draper Scholar

ABSTRACT: Machine learning and artificial intelligence methods have made significant progress in recent years, enabling their deployment on compact edge computing devices. In academia, this field of research is commonly referred to as TinyML and explores the coupling of low-power embedded systems and machine learning models. As with any computing field in its infancy, proper hardware and software security mechanisms are often initially overlooked, allowing data leaks, privacy breaches, and other malicious activity. To address these issues, this project aims to provide a series of implementation standards for the hardware through software levels of TinyML devices to enable safe development, deployment, and usage of these pieces of technology.

INTRODUCTION

Motivation:

- TinyML explores the coupling of low-power edge devices and machine learning models resulting in intrinsic compute, memory, and power constraints
- TinyML devices have a variety of use cases similar to those of traditional IoT devices and as a result are often physically accessible
- These devices contain proprietary software, model parameters, and observed phenomena which if exposed or tampered with can lead to loss of intellectual property, privacy breaches, or erratic behavior
- These threats are exacerbated by their physical accessibility
- Implementation specific security mechanisms must be put in place to prevent the TinyML devices from being compromised

Research Question:

What controls can be implemented to maximize the security of TinyML devices given constrained compute, memory, and power resources?

RESEARCH FOCUS POINTS

Hardware:

1. What hardware controls and components are required to enable robust system security while maintaining sufficient resources for machine learning models?

Side Channels:

2. What controls can be implemented to prevent side channel attacks such as power analysis or timing attacks?

Software/Firmware:

3. What cryptographic schemes can run on the resource constrained TinyML architecture?

ML Model:

4. What mechanisms can be put in place to ensure secure execution of the ML model and prevent data leakage or privacy breaches?

POTENTIAL CONTROLS

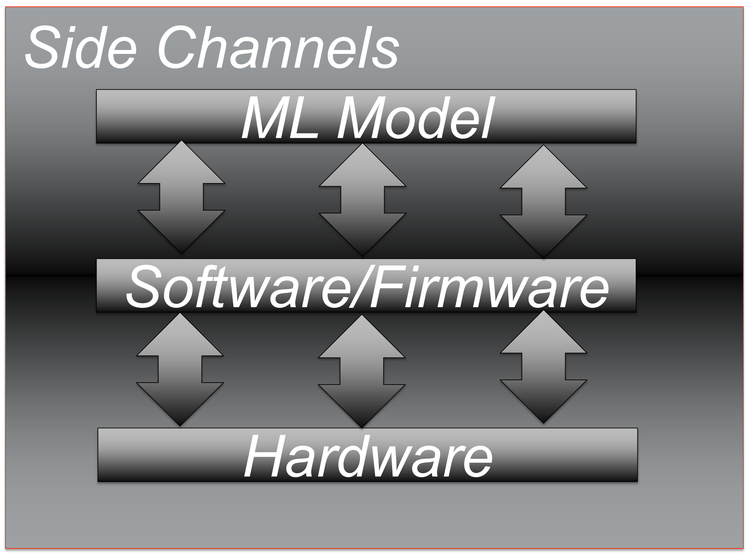

Figure 1: Typical TinyML Module Configuration

Hardware Controls:

- Build system with crypto-sensitive chip and/or integrated Trusted Platform Module used for key management, certificate management, and cryptographic operations
- Implement cryptographic authentication for connections to JTAG/USB/Programmable ports

Side Channel Controls:

- Data masking / elimination techniques
- Cryptographic process randomization
- Physical shielding

Software/Firmware Controls:

- Lightweight AES, Ascon
- Secure boot to authenticate and protect device firmware

ML Model Controls:

- Encrypt model when inactive, decrypt when making inference
- Federated Learning and Differential Privacy

PROPOSED APPROACH

The crux of this research is managing the intrinsic compute, memory, and power constraints introduced by TinyML implementations. Traditional IoT devices and embedded systems do not have to sustain the large overhead of a machine learning model. As such, many of the standard approaches for securing these devices must be altered if they are to be applied to TinyML devices. Moving forward the following steps must be taken.

1. Survey the current landscape of embedded platforms that can support the overhead of cryptographic schemes and TinyML implementations
2. Explore existing IoT/embedded system vulnerability controls, side channel attack safeguards, and cryptographic schemes
3. Build a framework to test and optimize candidate controls for TinyML architecture
4. Select feasible controls and build a series of secure TinyML implementation standards
5. Integrate selected controls and hardware to produce a proof-of-concept based on the PA1 Person Detection Module developed at Harvard University [1,2]

ACKNOWLEDGEMENTS / REFERENCES

[1] P. Warden, et al., “Machine Learning Sensors,” Arxiv, 2023.

[2] M.Stewart, et al., “Datasheets for Machine Learning Sensors,” Arxiv, 2023.

Single Event Activated Radiation Effects in Microelectronics

Paul Johnson[1,2], Sukesh Aghara[1], Daniel Valencia[3]

[1]University of Massachusetts Lowell – Nuclear Engineering, [2]Draper Scholar - The Charles Stark Draper Laboratory, Inc.,
[3]The Charles Stark Draper Laboratory, Inc.

ABSTRACT: Magnetic tunnel junctions (MTJ) in magnetoresistive RAM (MRAM) are an emerging non-volatile memory (NVM) bit cell expected to be inherently space radiation hardened, [1] but the physics of heavy ion single event upsets (SEU) are not fully studied. [2] Ions from solar flares or galactic cosmic rays are a concern for polar orbits, through the South Atlantic anomaly, or beyond the protective van Allen belts and recent studies predict a SEU probability per strike of 8/100 for worst case particles[3] , further it is not well known how to predict their radiation response. This study predicts MTJ magnetocaloric properties from heavy ion test data, estimating a MTJ switchable free layer $T_{Curie} \in 550 - 850\ K$ and effective anisotropy energy density $K_{eff0} \in 0.3 - 0.8\ MJ/m^3$ which depends on two-temperature model parameters.

INTRODUCTION

- **Applications:** Advanced AI chips in space & rad-hard memory rely on MTJ.
- **Literature:** No modeling of transient thermal effects causing MRAM SEU have been demonstrated.[2,3]
- **Previous work:** Single event activation (SEA) was proposed to model MRAM SEU but failed taking electron = phonon temp.

Aim: Apply a two-temperature model to predict device bit error response assuming Arrhenius activation rate equation.

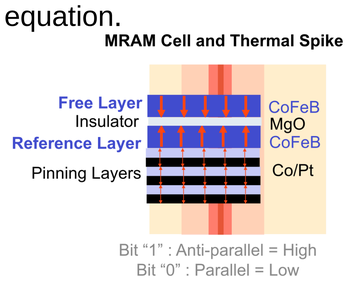

- **Presented:** Bit error probability is fit to test data [3] given, Curie T_C., energy density K_{eff}, intrinsic switch time τ_0.
- **Results:** Statistically significant results to predict T_{Curie} and τ_0 are reached, but the fitted model does not reproduce reported thermal stability factor $\Delta \propto K_{eff}(T)$ of similar device[7]

METHODS

Define dosimetry – constant linear energy transfer (LET) → Simulate thermal transient in Fe bulk properties at 300 K → Obtain magetocaloric property by fit to radiation test data

- **A Gaussian pulse in time, space $A(r,t)$** – is normalized to heavy ion LET,
- **The two-temperature model of the free-layer** is linear with electron and phonon temperatures $T_e(r,t), T_p(r,t)$[4,5]

$$C_e \partial_t T_e = K_e \nabla^2 T_e - g_{ep}(T_e - T_p) + A(r,t)$$
$$C_p \partial_t T_p = K_p \nabla^2 T_p + g_{ep}(T_e - T_p)$$
$$\sigma_{SEU} = A_{FL} \int \tau_0^{-1} e^{-K_{eff} V_{FL}/k_B T_p}\, dt$$
$$K_{eff} = K_{eff}(T \sim 0K)\left(1 - \frac{T_p}{T_{Curie}}\right)^2$$

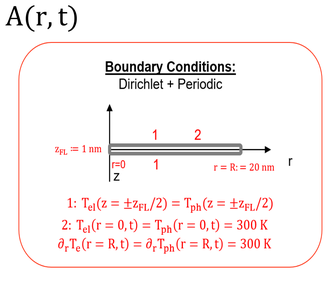

- **Cross section $\sigma_{SEU}(cm^2/bit)$** fits magnetocaloric properties for a direct ion hit to the MTJ w/ stability $\Delta = K_{eff}(T, T_{Curie}) V_{FL}/k_B T_p$.
- **$T_p(r,t)$ is found w/ integral method[12] & COMSOL Finite Element Method (FEM)**

THERMAL CARRIERS DURING SINGLE EVENT

Electron System Timeline
$T_{el,max}(r = 20\ nm) = 10^3 - 10^4\ K$
(1) 0.1-5 fs: Gaussian distributed electrons in $r < 0.66$ nm [11]
(2) 5-25 fs: Electron-electron scattering causes peak electron temperature

Phonon System Timeline
$T_{p,max}(r = 20\ nm) = 380 - 900\ K$
(3) 0.01-5 ps: electron-phonon scatter increases phonon temperature, equilibrate
(4) 10-30 ps: Mean time to bit error for Arrhenius activation model
(5) 1-5 ns: System relaxation T_p to 300 K

SINGLE EVENT RESPONSE IN MRAM

- L: FEM solution $T_e(t)$-Solid & $T_p(t)$-Dash vs. LET
- R: $\sigma_{SEU}(LET), LET \in$ (15-125) $MeVcm^2/mg$ integral method

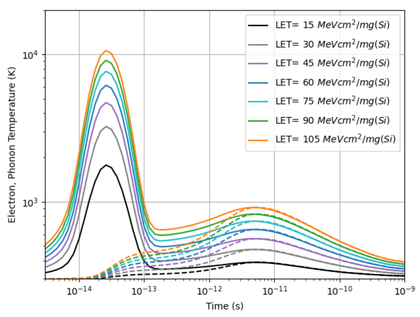

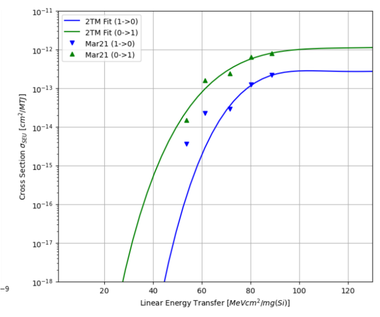

Results and Literature	Δ	T_{Curie}(K)	K_{eff0} (MJ/m^3)	τ_0(ns)
MTJ Data in Literature				
Radiation test (CoFeB)*[6]	50-75	$730 - 1300$	$0.13 - 0.19$*	1
D = 40 nm MTJ: $0 \rightarrow 1$ [3,7]	~108	-	-	
D = 40 nm MTJ: $1 \rightarrow 0$ [3,7]	~80	-	-	
Two-Temperature Model Numerical Solution				
FEM-Insulated $1 \rightarrow 0$	**92**	$\mathbf{810 \pm 50}$	$\mathbf{0.73 \pm 0.66}$	$\mathbf{0.8 \pm 0.2}$
FEM-Insulated $0 \rightarrow 1$	**40**	$\mathbf{790 \pm 90}$	$\mathbf{0.33 \pm 0.34}$	$\mathbf{0.34 \pm 0.09}$
Integral solution-open $1 \rightarrow 0$	**59**	$\mathbf{560 \pm 27}$	$\mathbf{0.66 \pm 0.59}$	$\mathbf{0.35 \pm 0.07}$
Integral solution-open $0 \rightarrow 1$	**30**	$\mathbf{552 \pm 35}$	$\mathbf{0.30 \pm 0.28}$	$\mathbf{0.13 \pm 0.02}$

DISCUSSION

- **Fitted result of $\Delta(T_p, K_{eff0}, T_{Curie})$ matches expectation for observed SEU probability** (↓ SEU probability = ↑ K_{eff0}, T_{Curie}) but under-predicts magnetocaloric properties and are not coupled as expected to write-efficiency Δ/I_{c0} reported [9]
- **Possible explanations**: (A) invalidity of our energy density model (B) an impact of spin dynamics [9] .
- **Coefficient of variation of result fit are equal** for COMSOL and integral solution method near ~0.4
- **No major distinction between states $1 \rightarrow 0, 0 \rightarrow 1$** in K_{eff0} (MJ/m^3) and T_{Curie} contributing to Δ
- **Limitations:**
  (1) Ignores spin dynamics. [9]
  (2) Ignores non-linear property effects in the two-temperature model[4,11]

CONCLUSIONS

- **Characterization of MTJ** may be executed with radiation test and with dosimetry-thermal-device response models.
- **This work demonstrates the importance of the two-temperature solution** to model non-equilibrium radiation induced device response.
- **Next steps - higher precision model with analysis of:**
  (1) Dosimetry
  (2) Non-linear thermal effects
  (3) Spin dynamics
  (4) Experimental uncertainty propagation, overfitting of data.

ACKNOWLEDGEMENTS / REFERENCES

The author wishes to graciously thank the co-authors for their mentorship, the Draper Scholar's program, Jim Bickford and Douglas Martin for their support and initial data in this research.

1. J. Heideker et al. 2013, NASA DocID: 20140000668.
2. M.J. Marinella 2021, IEEE TNS vol. 68, no.5. 3074139
3. D. Martin et al. 2021, IEEE 32nd TMRC 9605128.
4. Z.G. Wang et al. 1994, J. Phys. Condens. Matter 6 6733
5. Lin et al. 2008, Phys. Rev. B. 77, 075133.
6. D. Kobayashi et al. 2017 Jpn. J. Appl. Phys. 56 0802B4
7. Wolf et al. 2020, IEEE LMAG.2020.3001487
8. B. Koopmans et al. 2009, Nat. Mat. 10.1038
9. Evans et al. 2014, J. Phys. Condens. Matter 26 103202
10. Cahill et al. 2002, J. Appl. Phys, 793-818
11. Daraszewicz and Duffy, 2011, Phys. Rev. B. 269
12. Lifshitz et al. 1960, J. Nucl Energy 12 69-78

Combatting Stress in Aircrews

Jeffrey Johnston[1,2], Srinivasan Radhakrishnan[1], Jared Shamwell[3], and Kathryn Feltman[4]

[1]Northeastern University, [2]Draper Scholar, [3]Draper Laboratory, [4]U.S. Army Aeromedical Research Laboratory

ABSTRACT: Aviation is considered one of the most dangerous professions. Army Aviators are constantly exposed to high stress environments and must practice resilience and stress management to effectively operate in high operational tempos. The purpose of this study is to analyze and evaluate aviator physiological data such as heart rate and level of strain throughout a flight and match the personal data to aircraft flight data. The goal of the analysis is to uncover trends and identify relationships throughout modes of flight and levels of high stress in order to find methods of combatting stress response in aircrews.




INTRODUCTION

Aviators must effectively manipulate controls, communicate on multiple radios, navigate, remain alert to the surrounding environment and coordinate both internally as a crew and externally as a flight of multiple aircraft to execute missions safely and successfully.

Stress and Fatigue affect many areas of performance critical to aviation

- Attention
- Memory
- Communication

METHODS

Utilizing data collected through USAARL from aviation Human Factors Evaluation (HFE) events and Upset Prevention and Recovery Training (UPRT)

- Participant Data
- Flight Data
- Physiological Response Data
  - Eye Tracking
  - fNIRS
  - Electrocardiography*
  - Respiration*
  - Skin conductance*
  - Electroencephalography*
  - Electromyography

Previous studies validated the use of EEG to determine physiologic relationships during flight.[1]

ANTICIPATED RESULTS

It is anticipated that during data analysis relationships will be detected between modes of flight, such as reacting or recovering from an emergency and the pilot's physiological response. Data collection is on-going through USAARL aviation studies.



B-Alert x10 or x24
EEG

Tiger Tech
Warfighter Monitor
ECG and PPG

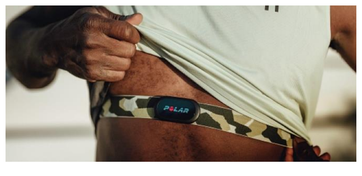

Polar H10
ECG and PPG

*These three devices currently have an airworthiness release (AWR) for military aircraft.

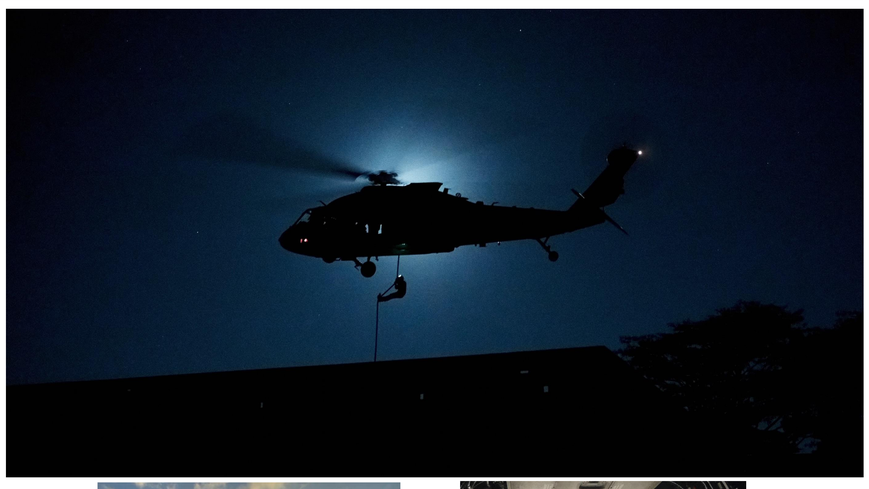

CONCLUSIONS

Analyzing relationships between how pilots react to certain situations can help improve resilience and stress response, enabling aviators to maintain composure throughout stressful missions.
The Future Vertical Lift program intends to incorporate operator monitoring through physiological means. Future work to incorporate stress monitoring and management can help keep aviators operating safely.

ACKNOWLEDGEMENTS / REFERENCES

Thank you to Tanya Smith at Olive Tree Photography and Abraham Williams for some of the photos. A special thanks goes to aircrew members around the world.

1. Feltman, K.A. et al. "Electrophysiological Data and Aviator Performance: Identifying Measures for Operator State Monitoring," USAARL, 2022

Neural Operators as Surrogate Models for Hypersonic Flow Fields

Kyle Jung[1,3], Khemraj Shukla[1], Sean George[2], Arthur Huang[2] , George Karniadakis[1]

[1]Brown University, [2]Draper, [3]Draper Scholar

ABSTRACT: The high computational cost of resolving hypersonic flows necessitates the development of reduced order modeling (ROM) methods for practical engineering design problems such as aero-optical mitigation. Traditional ROM methods rely on linear mappings with poor generalization capabilities. The development of neural operators introduces a method to encode operator mappings using neural networks. The application of neural operators to hypersonic flows provides a more expressive alternative to traditional ROM with potentially better generalization capabilities. In this project, we apply a particular neural operator framework, the Deep Operator Network (DeepONet), to the hypersonic benchmark double-cone problem and present model results. Additionally, aero-optical quantities are presented from the DeepONet outputs.

INTRODUCTION

- The high cost of resolving flow fields can be reduced by reduced order modeling (ROM) methods with some accuracy tradeoffs. In this study, we implement Deep Operator Networks (DeepONets) as a more expressive alternative to traditional ROM.
- We look at the benchmark double-cone geometry, which contain various hypersonic flow features such as multiple shock formations and flow separation [1].

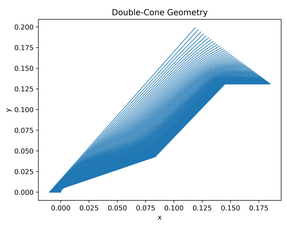

Double-Cone geometry

METHODS

- DeepONets are neural operators based on the universal approximation theorem for neural operators [2].
- We train our model on a set of 45 simulations of Mach numbers ranging from 8.1 to 12.9 for the double-cone geometry.

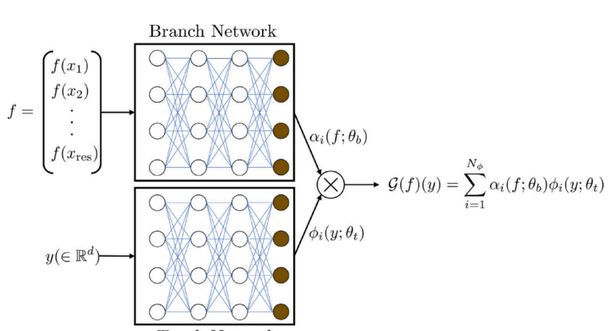

DeepONet Framework from [2]

RESULTS

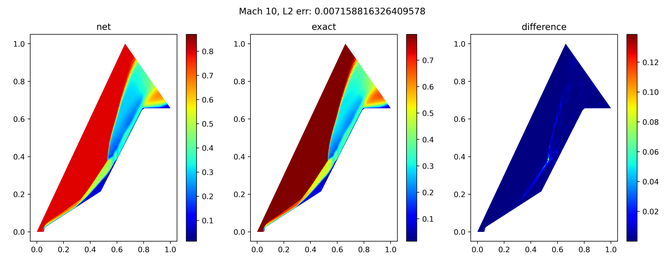

Horizontal Velocity DeepONet prediction for Mach 10 (left), exact solution (middle), and point wise error (right). Scales are normalized from 0 to 1.

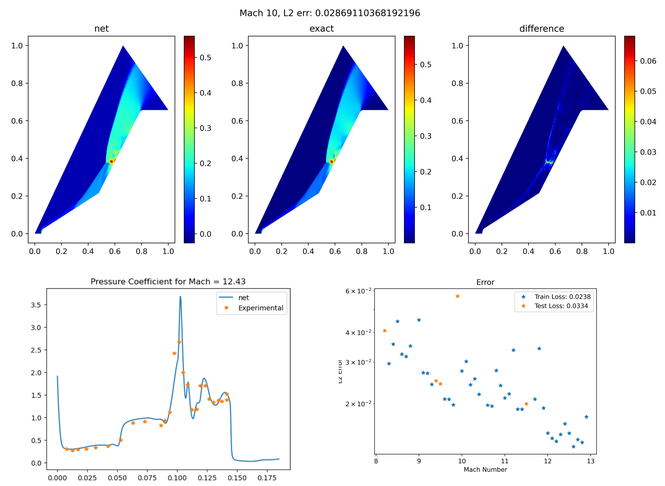

Pressure predictions: bottom left figure gives the pressure coefficient predictions on the boundary compared to experimental data at Mach 12.43, and bottom right presents the error for each data sample. Scales are normalized from 0 to 1.

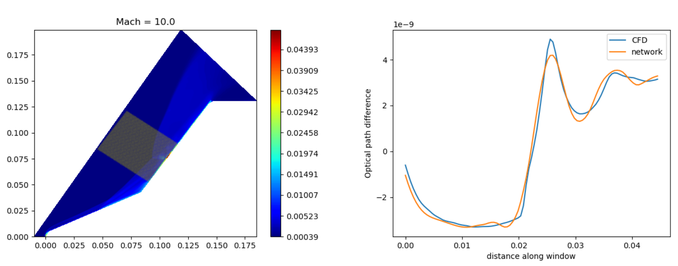

Density predictions and optical path difference calculations for a ray along the yellow path on the right contour for Mach 10. Scales are physical units [m³] and [kg/m³].

	Density	Pressure	u velocity	v velocity	Temperature
Train Error	0.0389826	0.0252185	0.0068947	0.0125646	0.0157085
Test Error	0.0476106	0.0362204	0.0153533	0.0250283	0.0221599

Relative L2 errors for each field variable for a trained model

DISCUSSION

- Neural operators are accurate surrogate models for the double cone problem. The pressure coefficient predictions at the boundary along with test error calculations demonstrate good generalization capabilities. More prominent errors occur around shocks and complex interaction regions.
- DeepONet predictions can be applied to engineering design problems that require many CFD simulations such as aero-optical mitigation. The optical difference calculations from the density field demonstrates a practical use case.
- The training of the DeepONet requires upfront CFD data generation to learn the solution space. Then, flow solutions can be generated within seconds using the trained model.

CONCLUSIONS

- DeepONets serve as accurate surrogate models for hypersonic flows, capturing relevant flow features.
- After initial training, neural operators provide significant speed-up in predicting hypersonic flows.
- Initial training neural operators can be computationally expensive. Further algorithmic development and research will improve the training of these models.

ACKNOWLEDGEMENTS / REFERENCES

[1] Ray, J., Blonigan, P., Phipps, E., & Maupin, K. (2022). An Assessment of the Laminar Hypersonic Double-Cone Experiments in the LENS-XX Tunnel. Presented at the AIAA SciTech 2023, National Harbor, MD. Sandia National Laboratories. https://doi.org/10.2514/6.2023-0856

[2]Shukla, K., Oommen, V., Peyvan, A., Penwarden, M., Plewacki, N., Bravo, L., Ghoshal, A., Kirby, R. M., & Karniadakis, G. E. (2024). Deep neural operators as accurate surrogates for shape optimization. *Engineering Applications of Artificial Intelligence*, 129, 107615. https://doi.org/10.1016/j.engappai.2023.107615

Data set came from the Farhat Research Group at Stanford

Accelerating Vision System Prototyping with Reinforcement Learning

Tzofi Klinghoffer*, Kushagra Tiwary, Nikhil Behari, Bhavya Agrawalla, Ramesh Raskar

Massachusetts Institute of Technology * Draper Scholar (Mentor: Margaret Duff)

Abstract: Rapid prototyping of vision systems is critical in many areas, such as scientific discovery, robotic design, responding to evolving threats on the battlefield, and more. We propose the use of reinforcement learning to *co-design* imaging hardware with vision algorithms, enabling highly automated design of task-specific vision systems. Vision systems consist of cameras to encode visual information about the world and perception models to interpret this encoding. Cameras contain (1) illumination sources, (2) optical elements, and (3) sensors, while perception models use (4) algorithms. Directly searching over all combinations of these four building blocks to design a vision system is challenging due to the size of the search space. Moreover, cameras and perception models are often designed independently, leading to sub-optimal task performance. We formulate these four building blocks of vision systems as a context-free grammar (CFG), which can be automatically searched over with a learned camera designer to jointly optimize the imaging system with task-specific perception models. By transforming the CFG to a state-action space, we then show how the camera designer can be implemented with reinforcement learning to intelligently search over the combinatorial space of possible imaging system configurations. We demonstrate our approach on two tasks, depth estimation and camera rig design for autonomous vehicles, showing that our method yields rigs that outperform industry-wide standards in simulation.

OVERVIEW

Rapid prototyping of vision systems is critical

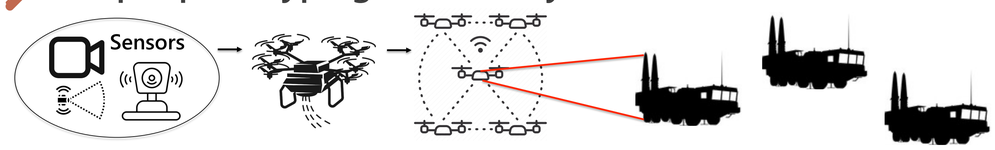

Vision system design is challenging

1. Combinatorial search space
2. Non-differentiable Simulation

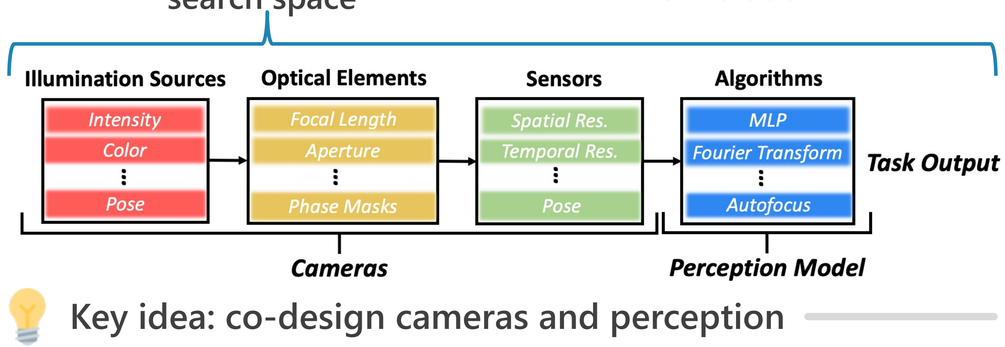

Key idea: co-design cameras and perception

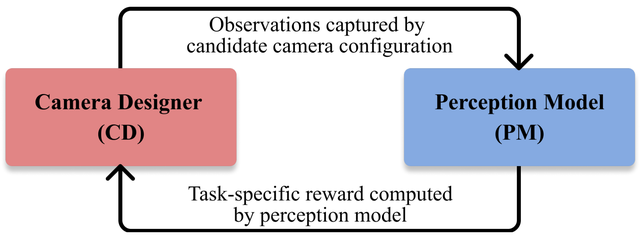

SEARCH SPACE

A Language for Vision Systems

Vision Context-Free Grammar

$$
\begin{aligned}
\mathrm{R} &\rightarrow \mathrm{XSXA} && (1)\\
\mathrm{X} &\rightarrow \mathcal{I}\mathrm{X}|\mathrm{OSX}|\mathrm{A}_2\mathrm{X}|\epsilon && (2)\\
\mathrm{O} &\rightarrow \mathcal{O}\mathrm{O}|\epsilon && (3)\\
\mathrm{A}_1 &\rightarrow \mathcal{A}_1\mathrm{A}_1|\mathcal{A}_1 && (4)\\
\mathrm{A}_2 &\rightarrow \mathcal{A}_2\mathrm{O}\mathcal{S}|\mathcal{A}_2\mathcal{I}|\mathcal{A}_2\mathcal{S}|\epsilon && (5)\\
\mathcal{S} &:= \{s_p s_{hw} s_t s_\lambda s_q\}_{p\in\mathbb{R}^6,h,w,t,q\in\mathbb{Z}} && (6)\\
\mathcal{O} &:= \{o_f o_d\}_{f\in\mathbb{R},D\in\mathbb{Z}} && (7)\\
\mathcal{I} &:= \{i_p i_i\}_{p\in\mathbb{R}^6,i\in\mathbb{Z}} && (8)\\
\mathcal{A}_1 &:= \{a_{nn}, a_{fourier}, \ldots\} && (9)\\
\mathcal{A}_2 &:= \{\text{autofocus}, \ldots\} && (10)
\end{aligned}
$$

Examples of instantiations

Stereo

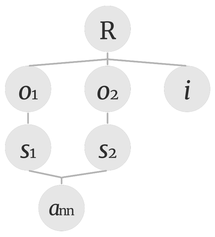

Structured Light

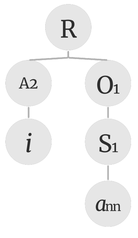

We use context-free grammar to define our search space

METHODOLOGY

Searching vision systems with reinforcement learning

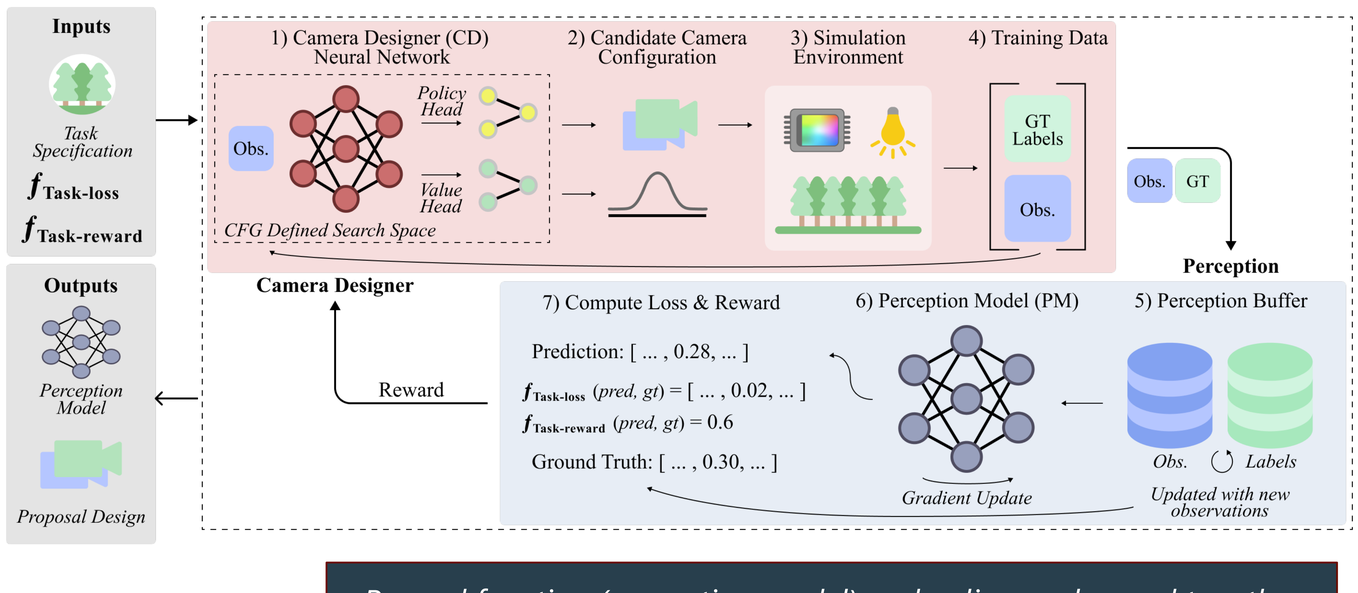

Reward function (perception model) and policy are learned together

RESULTS

Autonomous Vehicle Rig Design

Single-Camera Rig

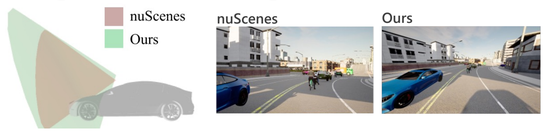

Multi-Camera Rig

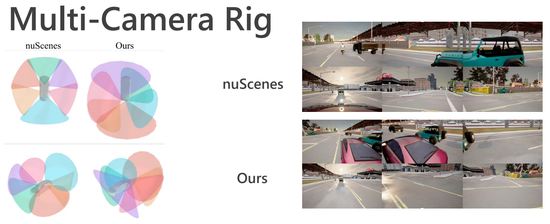

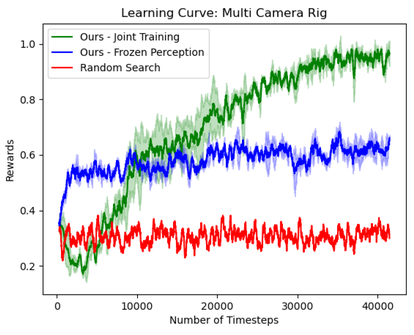

Comparison

	Single-Cam	Multi-Cam
nuScenes rig	0.267	0.355
Our rig	0.341	0.427

Strategies

- Distribute views and FoVs
- Maximize height
- Maximize pixels on road

This work was published at ICCV 2023.

Depth Estimation

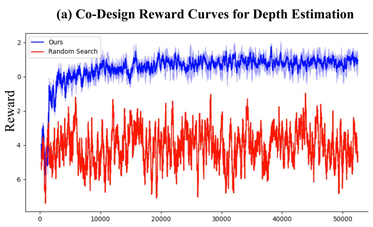

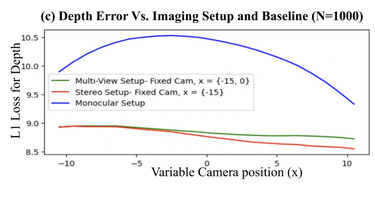

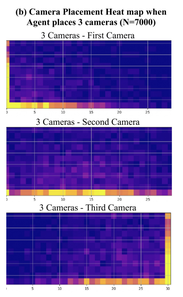

FUTURE WORK

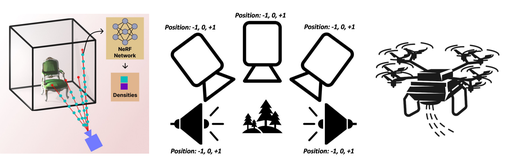

Learned simulation *Adaptive Sensing* *Robotic Navigation*

mit media lab camera culture

April 8, 2024

DRAPER® SCHOLARS RESEARCH SYMPOSIUM

Increasing Enterprise Performance

A Case Study in System Dynamics Modeling

Julia Koron[1,3] ; Chad Gibson[2] ; Hung Phan[3], Ph.D

[1]Draper Scholar; [2]The Charles Stark Draper Laboratory, Inc., 555 Technology Square, Cambridge, MA, 02139; [3]Department of Mathematics and Statistics, University of Massachusetts Lowell, Lowell, MA, 01852

ABSTRACT: Project-driven companies face a unique complex system when it comes to hiring and staffing project-based employees. Companies must manage their supply, project-based employees, and their demand, project-based work. A common assumption is determining employee headcount from a revenue projection. However, this assumes both supply and demand are static. Demand can come and go over various time scales and employees are not interchangeable. Companies want to be ready to meet demand needs, while minimizing employee idle time and turnover. A company needs to decide whether they want to hire based on incoming demand or ensure they have the staff available to readily take on new projects as they arrive. In short, enterprises of this nature are very complex, where multiple environmental factors impact the business and, as a result, supply and demand forecasting. By utilizing System Dynamics Modeling, we created a model that represents the complexity project-driven companies face. **With this tool, companies will be able to conduct scenario planning and better understand their decision implications on the enterprise, increasing overall enterprise performance.**

INTRODUCTION

System Dynamics Modeling is an engineering discipline. Specifically, it is a technique to frame, understand, and discuss complex systems. There are many complex systems in engineering, and that complexity is represented by dynamic modeling. Modeling creates the ability to understand the relationships that exist between the variables in the complex system. For this project we are leveraging S.D Modeling to represent a complex human enterprise.

There are dynamics in the enterprise that impact its performance. Situations on the ground can make people and processes change and interact differently, depending on their state within the operating parameters. **Modeling feedback loops allow leadership to understand how the system changes over time.**

Instead of focusing on making a model for a given prediction, we utilized company leadership in the model construction process to simulate their view on the current system. A model diagram was created and presented in various focus group meetings with company leadership across multiple departments. The goal was to ensure we created a model that leadership will use.

METHODS

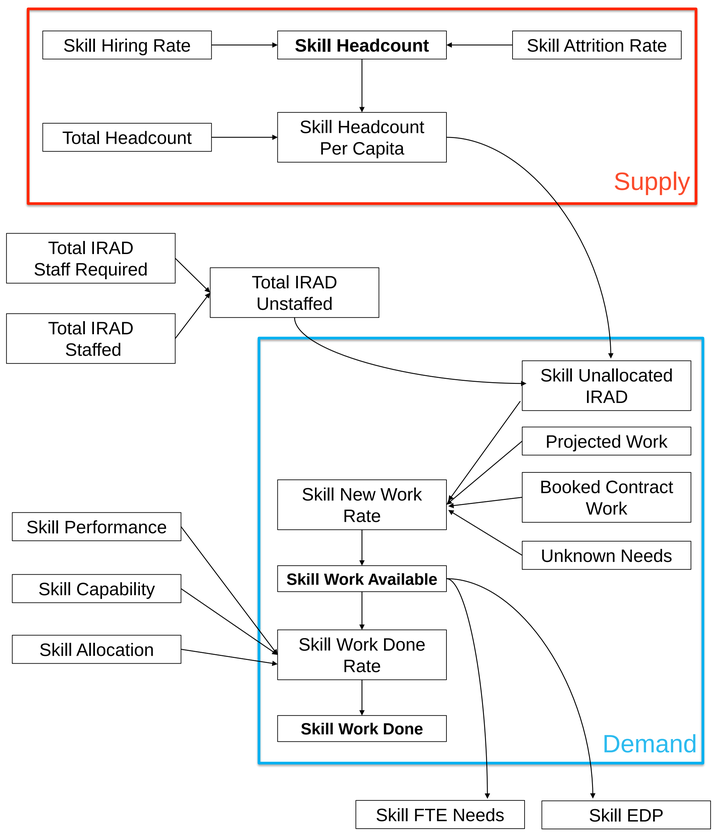

Figure 1. Supply and Demand model breakdown

METHODS: Impact of Feedback Loops

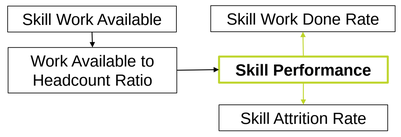

	Hoarding	Burnout
Range	Work Available to Headcount Ratio < -10%	Work Available to Headcount Ratio > 10%
Impact to Work Done Rate	Decrease by 10-15%	Decrease by 5%
Impact to Attrition Rate	Increase by 50-100%	Increase by 25%

Figure 2. Hoarding/Burnout Loop

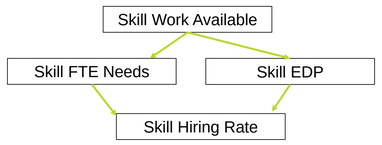

	FTE Needs	Skill EDP
Range	FTE Needs > 10%	Skill EDP > 10%
Impact to Hiring Rate	Increase by 50%	Decrease by 75%

Figure 3. "On the Ground" Hiring Loop

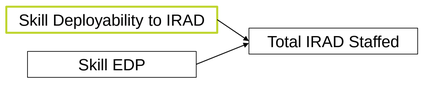

Ability to move employees to Internal Research & Development. Assumption: 90%

Figure 4. Skill Deployability to IRAD Loop

METHODS: Variable Definitions

Skill Capability

Skill Capability Calculation		
Rating	**Impact to Work Done Rate**	**Range Value**
Very Low	0.90	x =< 0.65
Low	0.95	0.65 < x =< 0.8
AVG	1.00	0.8 < x =< 1.1
High	1.05	1.1< x =< 1.25
Very High	1.10	x > 1.25

- Ratings are determined by Average Years of Service (time at the company) and Average Years of Experience (time since Bachelors Degree)
- Some skill sets have a higher capability based on years of experience and years of service i.e., a skill set with three new employees will not be as effective or complete as much work as a skill set with three experienced employees
- Skills with very high capability get more work done

Projected Work

- Projected Work = Demand Profile – Booked Work
- Allows for scenario planning and sensitivity analysis: create future demand profiles based on pending proposals, revenue goals, etc.
- Creates scenarios for evaluating robustness of the modeled enterprise

Skill Allocation

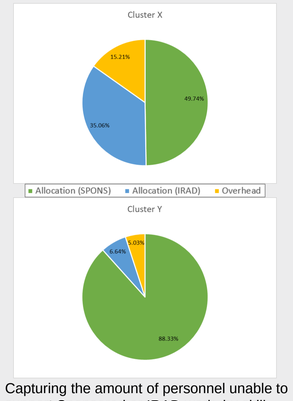

- Capturing the amount of personnel unable to support Sponsored or IRAD work, by skill

METHODS: Inputs and Model

Total ENG Headcount (FTE)
Initial Skill Headcount (FTE)
Input Hiring Rate (FTE/Month)
Input Attrition Rate (FTE/Month)
Initial Work Available (FTE)
Skill Unknown Needs (FTE)
Skill Deployability to IRAD
Skill Capability
Skill Allocation
Projected Work
Total IRAD Staff Required (FTE)
Total IRAD Staffed (FTE)

Figure 5. Model Input Table

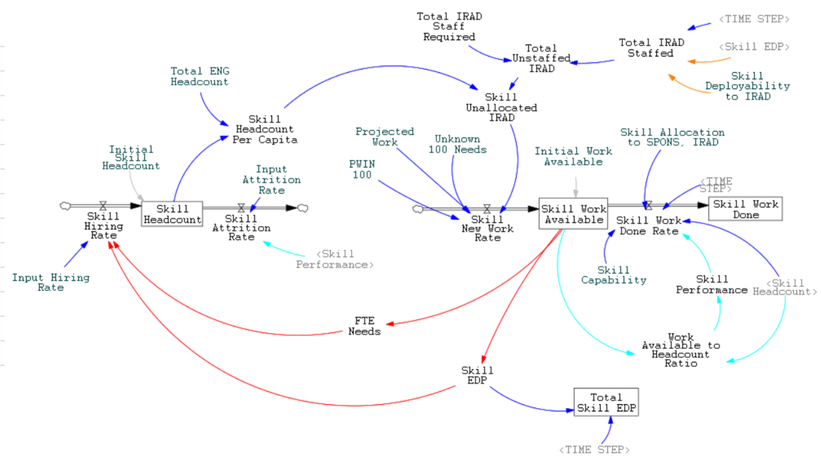

Figure 6. Model View in Vensim®

RESULTS:

Scenario 1

Input Table

	C9-SteadyBase	C9-Steady2Hire	C9-SteadyUnk	C9-SteadyAtt	C9-SteadyHireUnk	C9-SteadyCap	C9-SteadyIRAD
Total ENG Headcount (FTE)	1310	1310	1310	1310	1310	1310	1310
Initial Skill Headcount (FTE)	121	121	121	121	121	121	121
Input Hiring Rate (FTE/Month)	0.25	0.50	0.25	0.25	0.50	0.25	0.25
Input Attrition Rate (FTE/Month)	0.333	0.333	0.333	0.1665	0.333	0.333	0.333
Initial Work Available (FTE)	0	0	0	0	0	0	0
Skill Unknown Needs (FTE)	2.42	2.42	1.21	2.42	1.21	2.42	2.42
Skill Deployability to IRAD	0.90	0.90	0.90	0.90	0.90	0.90	0.90
Skill Capability	1.10	1.10	1.10	1.10	1.10	1.133	1.10
Skill Allocation	0.903	0.903	0.903	0.903	0.903	0.903	0.903
Projected Work	Steady	Steady	Steady	Steady	Steady	Steady	Steady
Total IRAD Staff Required (FTE)	100	100	100	100	100	100	95
Total IRAD Staffed (FTE)	50	50	50	50	50	50	47.5

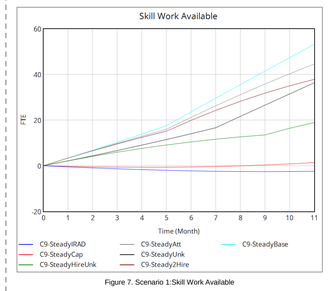

Figure 7. Scenario 1:Skill Work Available

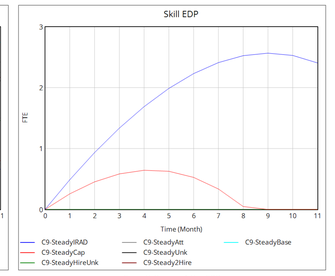

Figure 8. Scenario 1:Skill EDP

Scenario 2

Input Table

	C9-5%	C9-5%2Hire	C9-5%Unk	C9-5%Att	C9-5%HireUnk	C9-5%Cap	C9-5%IRAD
Total ENG Headcount (FTE)	1310	1310	1310	1310	1310	1310	1310
Initial Skill Headcount (FTE)	121	121	121	121	121	121	121
Input Hiring Rate (FTE/Month)	0.25	0.50	0.25	0.25	0.50	0.25	0.25
Input Attrition Rate (FTE/Month)	0.333	0.333	0.333	0.1665	0.333	0.333	0.333
Initial Work Available (FTE)	0	0	0	0	0	0	0
Skill Unknown Needs (FTE)	2.42	2.42	1.21	2.42	1.21	2.42	2.42
Skill Deployability to IRAD	0.90	0.90	0.90	0.90	0.90	0.90	0.90
Skill Capability	1.10	1.10	1.10	1.10	1.155	1.10	1.10
Skill Allocation	0.903	0.903	0.903	0.903	0.903	0.903	0.903
Projected Work	5% Revenue Growth	5% Revenue Growth	5% Revenue Growth	5% Revenue Growth	5% Revenue Growth	5% Revenue Growth	5% Revenue Growth
Total IRAD Staff Required (FTE)	100	100	100	100	100	100	90
Total IRAD Staffed (FTE)	50	50	50	50	50	50	45

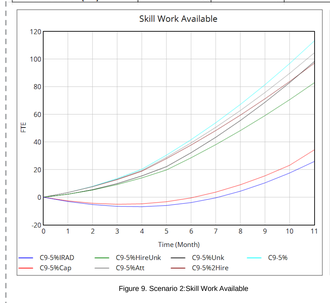

Figure 9. Scenario 2:Skill Work Available

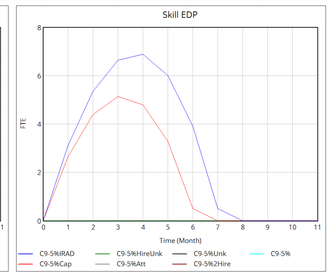

Figure 10. Scenario 2:Skill EDP

DISCUSSION:

- Each column in the Input Table represents a model run. The highlighted value indicates a change occurred from the base run.
- Every time a scenario is created, there is a base run. Alternating model inputs allows the user to see how their changes impact the overall system.
- **Depending on the end goal, minimize EDP, minimize the Work Available, maximize Work Done, maximize Revenue etc., the model can be tweaked (under the current base settings) to increase enterprise performance.**
- High Work Available indicates there is work and money being left on the table. Optimal: Work Available is close to zero, meaning there is a balance between supply and demand.
- For Scenario 1, Projected Work is assumed to be "Steady" (initial booked contract work = final booked contract work). Increasing Skill Capability by 3%, minimized the Work Available while also minimizing Skill EDP. (Figure 7).
- For Scenario 2, Projected Work is based on a 5% Revenue Growth goal. Increasing Skill Capability and decreasing the IRAD Budget had a similar effect as Scenario 1 on the Work Available (Figure 9).

CONCLUSIONS:

- A model was created that represents the complexity of supply and demand management Project-Driven companies face.
- **With this tool, leadership can conduct scenario planning and determine where the enterprise can increase performance to achieve future goals.**

REFERENCES:

- Morecroft, John, and John Sterman. *Modeling for Learning Organizations*. Productivity Press, 1994.
- Sterman, John. *Business Dynamics : Systems Thinking and Modeling for a Complex World*. Boston, Irwin/Mcgraw-Hill, 2000

UMASS LOWELL

April 8, 2024

DRAPER® SCHOLARS RESEARCH SYMPOSIUM

LLM-Directed Agent Models in Cyberspace

Sam Laney[1,2], Stephen Moskal[2], Una-May O'Reilly[2], and Felipe Vilas-Boas[3]

[1]Draper Scholar, [2]MIT CSAIL, [3]Draper

ABSTRACT: This work explores the use of Large Language Models (LLMs) as autonomous cyber agents. Overcoming the inherent challenges faced by LLMs in strategic planning and adaptability within complex security landscapes, we implement a hierarchical architecture that simplifies the penetration testing process into sequential steps, enabling strategic decision-making. This work tests evaluates various approaches to creating such agents and highlights the potential use of LLMs in enhancing cybersecurity operations.

INTRODUCTION

- LLMs, with their impressive natural language understanding and generation capabilities, have demonstrated potential in various domains, ranging from text completion to complex problem-solving tasks.
- Penetration tests often involve a series of interconnected steps, requiring a deep understanding of the subject matter and unique network environment, strategic planning, and the ability to adapt to dynamic situations.
- LLMs, in their current state, struggle with tasks that necessitate exploration, strategic lookahead, and the retention of information over extended interactions.
- Hypothesis: A hierarchical architecture enables complex, multi-stage cyber task completion.

METHODS

LLM Cyber Benchmarking:

- Utilizing a collection of cyber CTF challenges, we investigate the impact on completion capability varying the following:
  - Language model used
  - Agent structure
  - Response format
  - History representation
- This enables understanding of of model performance areas, provides the ability to benchmark and track model performance, and inspires agent design

Pentesting Agent Development

- We utilize these lessons learned to create a hierarchical automated agent framework to complete penetration testing challenges

RESULTS

Agent Strategies

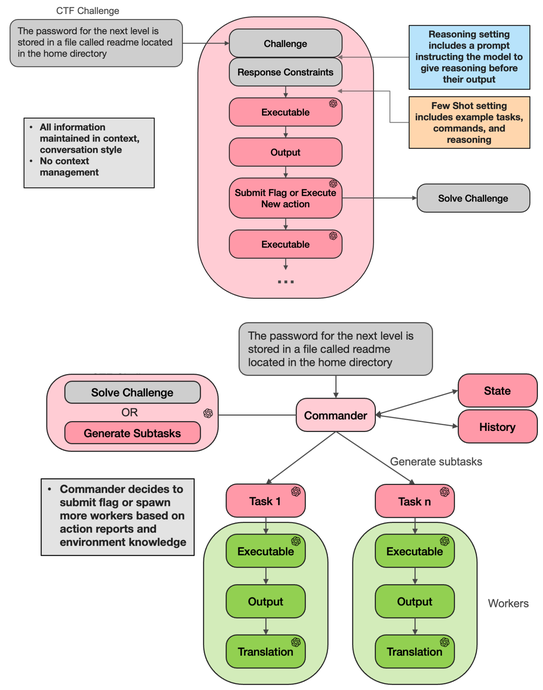

Results

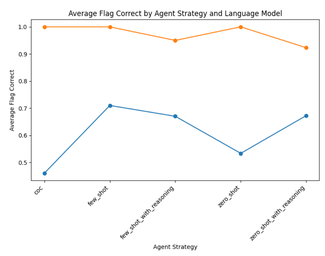

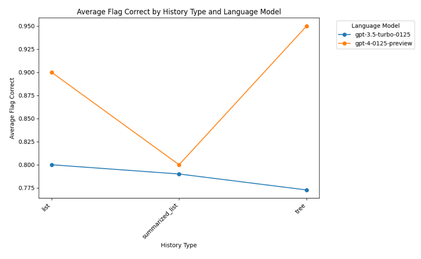

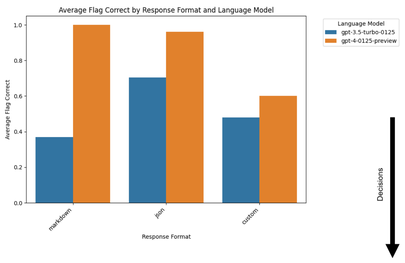

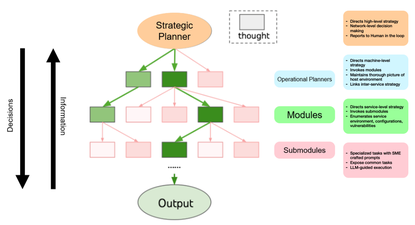

DISCUSSION

- Capability of LLM-enabled agents depends most heavily on the model used rather than the architecture of the system itself
- LLMs are biased towards focusing on more recent information.
- Implementing a structure for task decomposition and context management hinders simple task performance, but enables long-spanning tasks and flexibility to blind spots
- JSON response format offers the best performance for parsing and interfacing LLM outputs into code
- Future work includes testing on a wider array of challenge types and further development of automated and assisted-copilot frameworks

CONCLUSIONS

- As the LLM space continues to evolve rapidly, developing model-independent architectures and understanding core capabilities is critical
- Our LLM-enabled cyber agent framework accomplishes multi-stage reasoning to automate cyber-attack planning and execution.
- Enhancing the interpretability and accountability of LLM-enabled cyber agents is imperative to ensure ethical use and trustworthiness in automated cyber operations

ACKNOWLEDGEMENTS / REFERENCES

Work done in conjunction with MIT CSAIL's ALFA Group, led by Una-May O'Reilly
Thank you to my advisor, Felipe Vilas-Boas, and collaborator, Stephen Moskal (MIT Postdoc)

Resilient Architecture for Automated Vehicles

Emmett Lepp[1,2,3], Jason Rife[1], Tiffany DiNota[2]

[1]Tufts University, [2]Charles Stark Draper Laboratory, [3]Draper Scholar

ABSTRACT: Automated vehicles represent a disruptive technology to the traditional human-driver vehicle model; yet research must evolve to ensure the safety of these systems are optimized. Utilizing systems design tools, this research focuses on examining design errors and failures in the current architecture for automated vehicles, while identifying architectural improvements that advance System Safety standards. This research has the potential to mitigate safety concerns and allow automated vehicles to operate more reliably in austere environments

INTRODUCTION

- In 2021 the National Highway Traffic Safety Administration reported 39,508 fatalities [1].
- STPA has been applied to a variety of topics ranging from guidance cyber security systems to the airline industry.
- This work builds upon the current body of knowledge by providing a new insight into design limitations of automated vehicles through the lens of STPA, as opposed to event-based models of accident causality.

Non-Automated Vehicles
4.1 crashes/ million miles driven

Automated Vehicles
9.1 crashes/ million miles driven

Our goal is to guide design changes that provide assured and resilient architectures for safe automated vehicles operations.

METHODS

This research involves two distinct steps:

❑ Designing the automated vehicle architecture, through the use of STPA to highlight existing errors and faults that may be present within automated vehicles.

- ❑ STPA is a design tool that utilizes the control structure of a system to analyze likely points of errors & failures to inform design improvements.

❑ Vehicle driving simulation to confirm qualitative analysis of STPA process –modeling representative & dynamic driving-based scenarios, in an effort to the determine the prevalence and severity of particular faults

RESULTS

Preliminary analysis of subcomponent interactions among automated vehicles is crucial to determine where they may fail.

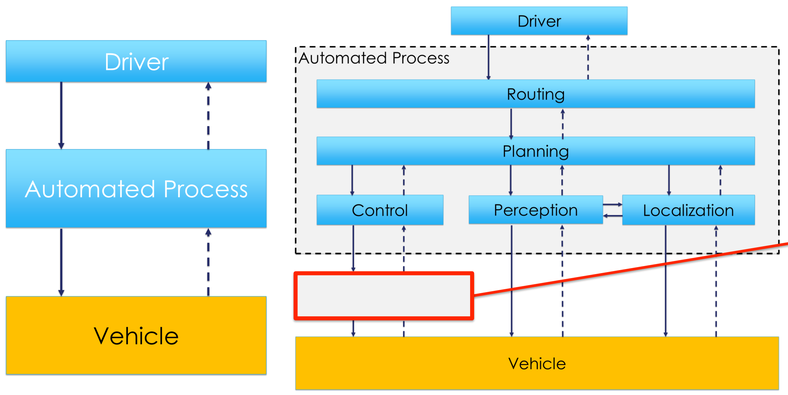

Figure 1: High-level & Detailed Control Structure for an Automated Vehicle

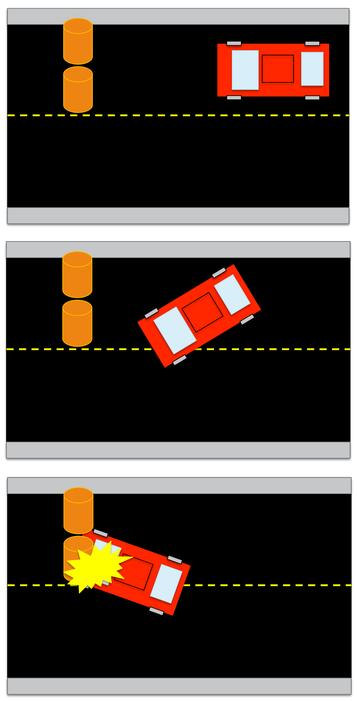

1: Driver notices object in the road, that automated process fails to detect.

2: Driver swerves to avoid the object in the road, changing the heading of the vehicle.

3: Automated process corrects the driver's actions causing the vehicle to crash into the object.

Figure 2: STPA Fault Example.

DISCUSSION

❖ This work is still in the beginning stages of the STPA analysis. We have created a control structure, mapped the hazards, and are in the process of creating an expansive list of hazardous contexts and loss scenario which may be present within automated vehicles.

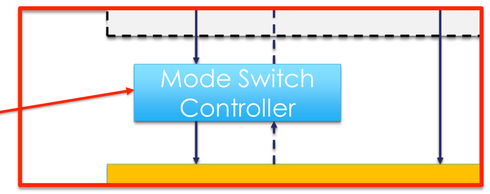

Figure 3: Example of Proposed Architectural Improvement

CONCLUSIONS

- ❖ By better conceiving how automated vehicles are designed, this framework can be utilized to improve architectural decisions and increase system resiliency safety.
- ❖ Future work will include
  - ❖ Development of a robust list of fault modes and loss-scenarios
  - ❖ Creation and testing of a simulation capable of detecting when faults arise
  - ❖ Architectural decisions to improve design and reduce a vehicle's risk of error failure

ACKNOWLEDGEMENTS / REFERENCES

[1] U.S. Department of Transportation, "Transportation Statistics Annual Report (TSAR) 2017," Washington, DC, 2017.
[2] Levenson, N. G., & Thomas, J. P. (2018). Retrieved from https://psas.scripts.mit.edu/home/get_file.php?name=STPA_handbook.pdf.

Pathogen-agnostic metagenomic sequencing of wastewater for early detection

Lennart Justen[1,2], Simon Grimm[2,3], Jeff Kaufman[2,3], Daniel Rice[2,3], Charles Whittaker[4], William Bradshaw[2,3], Michael McLaren[2,3], Daniel Cunningham-Bryant[5], and Kevin Esvelt[2,3]

[1]Draper Scholar, [2]Massachusetts Institute of Technology, [3]SecureBio, [4]Imperial College London, [5]Draper

ABSTRACT: Wastewater metagenomic sequencing (WW-MGS) offers a promising approach for early pathogen detection and infectious disease surveillance by profiling all pathogens in wastewater samples without needing prior knowledge of specific threats. However, realizing this potential requires an improved understanding of microbial dynamics in wastewater samples and advances in computational threat detection methods. We analyzed existing WW-MGS datasets to start quantifying human infecting viruses and explored computational detection methods for novel threats. While our results suggest that WW-MGS is a feasible strategy for pathogen-agnostic early detection, more work is needed to elucidate optimal wastewater sampling and processing strategies and to develop computational workflows that can accurately identify novel pathogens amid complex WW-MGS data.

INTRODUCTION

- Reliable defense against future pandemics and disease outbreaks requires the development of novel pathogen agnostic detection tools.
- Traditional detection methods for pathogen, such as PCR, require detailed prior biochemical knowledge of the pathogen.
- Wastewater metagenomic sequencing (WW-MGS) provides the potential for truly pathogen-agnostic biosurveillance that would enable early detection of all current and future pathogens[1].
- Realizing this potential requires further advancements in understanding wastewater's microbial dynamics and improving computational methods for threat detection in WW-MGS data.

METHODS

- We analyzed data from existing WW-MGS studies to determine the relative abundance (RA) of different human infecting pathogens and linked RA to local disease prevalence and incidence estimates[2].
- We have begun preliminary analysis of different detection approaches for novel pathogen identification, including homology-based detection, growth-based detection, genetic engineering detection, and novelty detection.
- We collected aggregate wastewater samples from a wastewater treatment plant and an airport but have not yet performed untargeted sequencing on these samples.

RESULTS

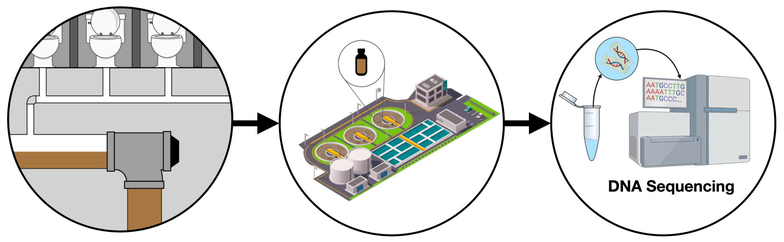

Figure 1. Overview of WW-MGS sampling strategy for treatment plants. A) Pathogens are excreted into sewage, B) the influent arriving at the treatment plant is sampled, C) the influent sample is processed and sequenced.

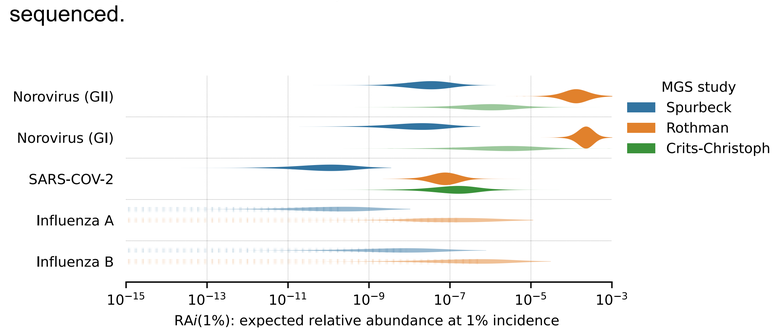

Figure 2. Predicted relative abundance (RA) of acute viruses at 1% weekly incidence (RAi(1%)) across three studies.

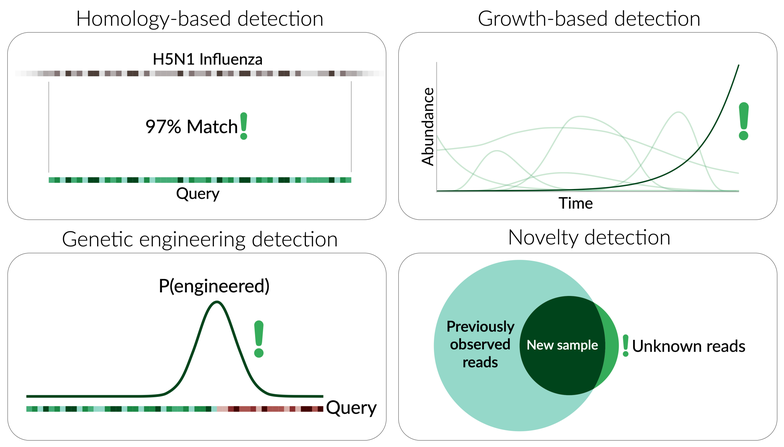

Figure 3: Approaches to threat detection in WW-MGS data. *Homology-based detection* tags viruses based on their similarity to known threats. *Genetic engineering detection* identifies signatures of artificial sequence tampering. *Growth-based detection* uses sequence count time-series data to track and flag suspicious growth patterns. *Novelty detection* uses previously seen sequencing data as a reference against which to identify and flag novel sequences.

DISCUSSION

- Wastewater samples from treatment plants and airports hold potential for the MGS-based detection of emerging pathogens.
- The low relative abundance of human-infecting pathogens in wastewater indicate that a WW-MGS detection system would incur substantial sequencing costs and benefit from improved protocols for pathogen enrichment.
- To enhance the detection capabilities, a combination of computational methods could be deployed.
- Regular sampling would facilitate growth-based detection and aid in developing a wastewater metagenome reference database for novelty detection.

CONCLUSIONS

- WW-MGS could enable pathogen-agnostic biosurveillance and provide critical early warning of infectious disease outbreaks.
- Our future work aims to:
  1) Determine the optimal wastewater sampling strategy (e.g., airport vs. treatment plant) and processing for early pathogen detection.
  2) Develop computational threat detection methods for WW-MGS data.

REFERENCES

1. The Nucleic Acid Observatory Consortium. “A Global Nucleic Acid Observatory for Biodefense and Planetary Health.” arXiv, 2021.
2. Grimm, Simon, et al. “Inferring the Sensitivity of Wastewater Metagenomic Sequencing for Pathogen Early Detection.” medRxiv, 2024.
3. Spurbeck, Rachel, et al. “Analysis of Metatranscriptomic Methods to Enable Wastewater-Based Biosurveillance of All Infectious Diseases.” Frontiers in Public Health, 2023.
4. Rothman, Jason A., et al. “RNA Viromics of Southern California Wastewater and Detection of SARS-CoV-2 Single-Nucleotide Variants.” Applied and Environmental Microbiology, 2021..
5.Crits-Christoph, Alexander, et al. “Genome Sequencing of Sewage Detects Regionally Prevalent SARS-CoV-2 Variants.” mBio, 2021.

Improving Methods for Detection, Characterization, and Attribution of Novel Biosecurity Threats

William Mo[1,2,3], Chris J. Myers[1], Chris A. Vaiana[2]

[1]University of Colorado Boulder, [2]Charles Stark Draper Laboratory, [3]Draper Scholar

ABSTRACT: Recent advances in biotechnology make the prospect of developing biological agents capable of inflicting enormous damage more feasible than ever before. We reviewed a significant amount of current work in biosecurity and found a heavy focus on DNA screening. As screening is not infallible, we recommend developing additional ways to stop dangerous biological agents from conception all the way through deployment. This can be aided via research focused on three distinct problem areas of DNA engineering detection, characterization, and attribution. To help solve the characterization problem, we further propose adapting novel tools for genetic design into novel tools for genetic reverse-engineering.

CHRONOLOGY OF IDEAL BIOSECURITY MEASURES TO MINIMIZE THREATS

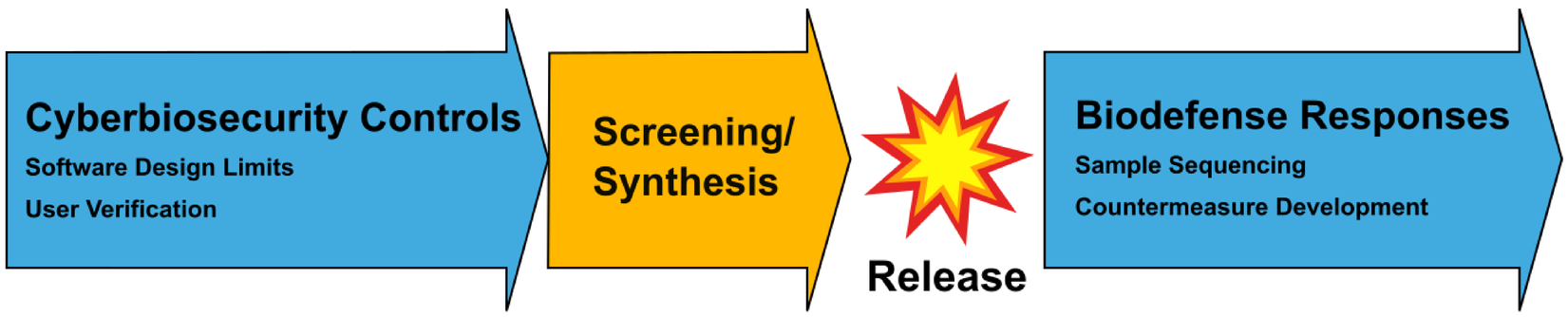

INTRODUCTION

- There is now clear evidence that a biological agent with the right properties like COVID-19 can have a crippling impact by killing millions and damaging global economy and infrastructure.
- In 2001, a primitive bioterrorist act, the anthrax mail attacks, was difficult to react to and some still doubt the following investigation's conclusions.

Cost of Creating New DNA[1]

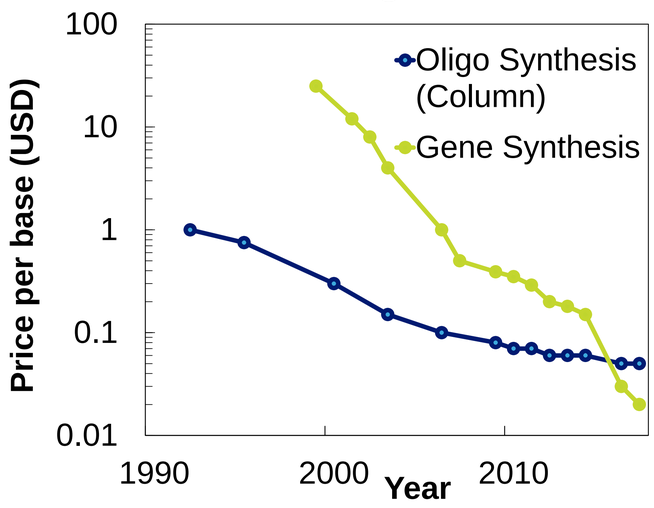

- Creation of synthetic DNA is set to have a Moore's Law-like fall in cost and difficulty. The potential for misuse of biotechnology is more realistic than ever.
- **How can we stop a manmade biological threat that is as dangerous as COVID and as elusive as anthrax?**

METHODS

- We reviewed current biosecurity practices to find out which of several opportunities to catch and stop engineered biological threats is in most need of further development. By doing so, we can make biosecurity practice more robust.

RESULTS

- Only one checkpoint, colored orange above, is a key focus in current work. We highlight other applications, above in blue, that can be improved by incorporating novel advances in related fields.

1. **During the design process of a potential biosecurity threat,** applying cybersecurity and cryptography-based controls forms a novel subfield of cyberbiosecurity. This secures genetic designs by ensuring only authorized researchers can work with possibly harmful genetic designs.
2. **Prior to commercial synthesis of an engineered sequence,** screening the submitted sequence can reveal possible danger. This is the current focus of the biosecurity field and the only step with recent HHS involvement[2] as it is positioned to intercept threats just before release.
3. **Following the release of a dangerous agent**, identifying the agent and being able to capture it in the environment for sequencing is essential for developing the appropriate response. This is often termed biodefense but tackles the same kinds of questions as biosecurity work does.

DISCUSSION

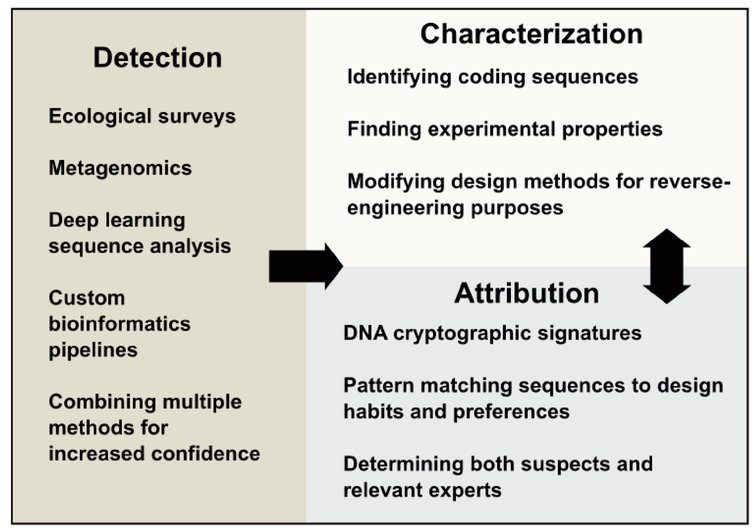

- After analyzing the current needs of each group of biosecurity application, we define three main types of problems involving DNA sequences where new breakthroughs can be used to improve biosecurity.
  - **Detection:** determining if engineering has occurred in suspicious DNA sequences.
  - **Characterization:** finding the properties of engineered DNA to evaluate the threat.
  - **Attribution:** guessing who designed the DNA to establish context and develop next steps.
- Characterization and Attribution are tackled in parallel, and each outcome can help solve the other.
- Many wet and dry lab tools exist to help researchers create genetic designs. Some are genetic analogs to electronics tools like function generators. Our review sees untapped biosecurity potential in these tools.
- **Going forward, we propose learning from and adapting genetic design tools to analyze unknown DNA sequences and help solve the characterization problem.**

ACKNOWLEDGMENTS

[1] Data credit: Rob Carlson, 2018
[2] Department of Health and Human Services Screening Framework Guidance, updated 2023

Review of Free Space Optical Neural Networks

Alexander Montes McNeil[1,2], Lin Deng[1], Michael Moebius[3], and Yongmin Liu[1,4]

[1] Department of Electrical and Computer Engineering, Northeastern University, Boston, MA, USA, montesmcneil.a@northeastern.edu
[2] Draper Scholar, Draper, Cambridge, MA, USA, amontes-mcneil@draper.com
[3] Draper, Cambridge, MA, USA, mmoebius@draper.com
[4] Department of Mechanical and Industrial Engineering, Northeastern University, Boston, MA, USA, y.liu@northeastern.edu

ABSTRACT: Recently, machine learning has impacted nearly every field of science, providing a new wave of innovative techniques for data analysis. Despite these achievements, these algorithms are limited by the speed and power required to design and run them on conventional computers. This has propelled a boon in the research of optical neural networks, which have already shown the ability to improve the speed and power of Analytical Neural Networks (ANNs) algorithms by orders of magnitude. This poster compares the working principles of Free Space Optical Neural Networks to more traditional ANNs and highlights their differences.

Introduction

- Each Analytical Neural Network (ANN) in Figure 1 is designed to classify images from the MNIST handwritten digit dataset, which is a standard benchmark for ANN architectures.
- Part A portrays a Fully Connected Neural Network (FCNN), traditionally one of the simplest forms of an ANN. The input stage converts the 2D image of a handwritten digit to a 1D vector in preparation for the hidden layers. The FCNN processes each element of the flattened input in parallel. The output is a 10-element vector, which contains the likelihood that the digit is a member of each class.
- Part B shows an Integrated Photonic Neural Network (IPNN). This architecture is very similar to the FCNN, except the input vector must be converted to light before and after the computation in the hidden layers. The Mach-Zehnder Interferometer (MZI) mesh shown in the hidden layers has emerged as the most prominent architecture for IPNNs due to their high tunability.[1]
- Part C shows a Free Space Optical Neural Network (FSONN). Here, the input stage encodes the handwritten digit directly onto the incident light, maintaining its 2D properties. Then, in the hidden layers, the input propagates through metasurfaces where each pixel can apply amplitude and phase manipulation at subwavelength scales. Researchers report implementing over 200k neurons per layer. At the output, the hidden layers focus the light onto a series of detectors.[2] The ratio of the intensity across the detector array determines the likelihood of each digit.

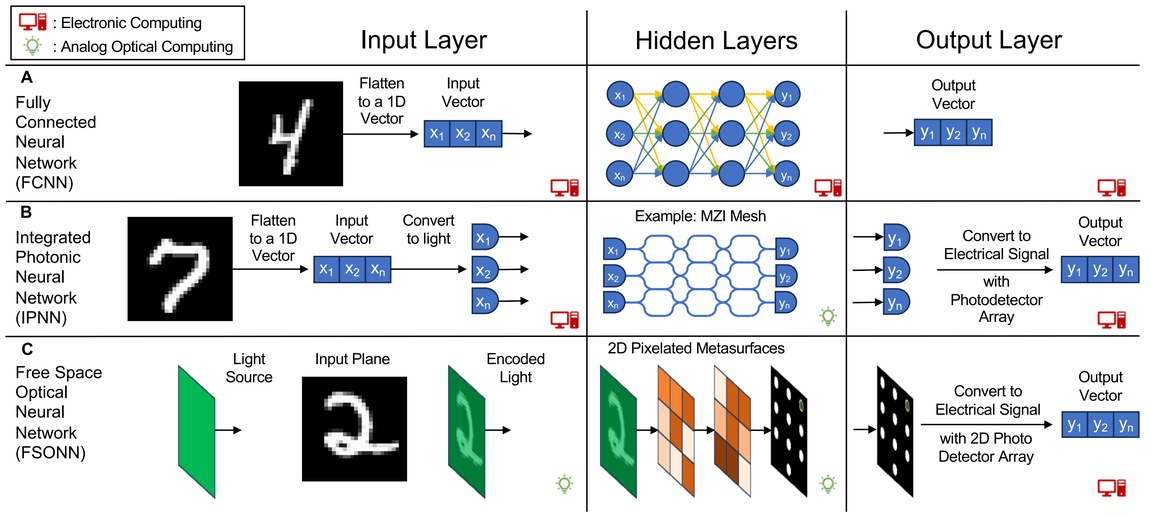

Figure 1. Comparison of ANN Architectures. Every ANN consists of 3 critical data handling stages: the input, hidden, and output layers. The key (top left) indicates if the step uses electronic or analog optical computing.

Methods

- Part A shows a layer transition through an FCNN. Each element in layer $l-1$ is connected to each element in layer l by a weight, and Eq. 1 shows the calculation of v_0^l in layer l. These weights and the bias term b_0 represent the trainable parameters in the FCNN. f_a represents a non-linear activation function that determines if the value for v_0^l should be passed on to the next layer.
- Part B shows a layer transition through an FSONN. Eq. 2 shows the calculation of $\boldsymbol{v}_0^l$ in layer l. a and φ represent trainable parameters, $\boldsymbol{d}_{ik}^l$ is the distance between the layers, and f_p is the propagation function used in the model. Critically, ONNs lack activation functions, which prevent them from approximating non-linear functions. Despite that, researchers have achieved greater than 97% accuracy on the MNIST dataset.[3]

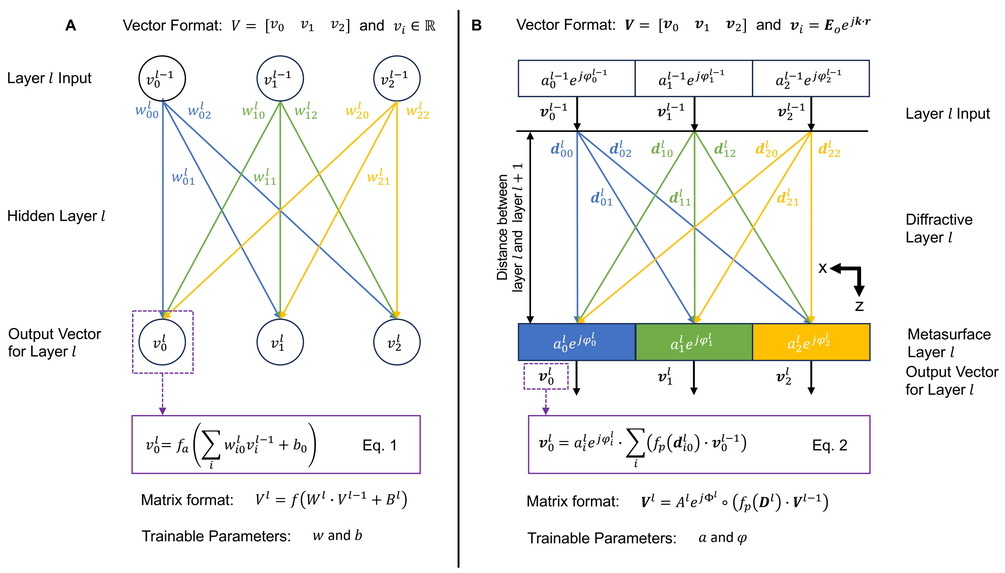

Figure 2. Hidden Layer Calculation. A 1D 3-element vector transitions between hidden layer $l-1$ and hidden layer l for parts A and B. We limit electromagnetic wave propagation in part B to the xz plane for simplification.

CONCLUSIONS

- ONNs demonstrate orders of magnitude improvement to the speed and power of ANNs that use electronic computing architectures.
- Optical approaches provide a single high-intensity output, reducing the complexity of signals processed electronically. This can dramatically increase the throughput of image classification systems like Figure 1.
- In the future, we will broaden the scope of FSONNs and implement them in realistic applications.

REFERENCES

1. Shen, Y., et al., Deep learning with coherent nanophotonic circuits. Nature photonics, 2017. 11(7): p. 441-446.
2. Lin, X., et al., All-optical machine learning using diffractive deep neural networks. Science, 2018. 361(6406): p. 1004-1008.
3. Mengu, D., et al., Analysis of Diffractive Optical Neural Networks and Their Integration With Electronic Neural Networks. IEEE Journal of Selected Topics in Quantum Electronics, 2020. 26(1): p. 1-14.

PIPE-Cleaner: Developer-centric Configurable Fuzzing for Software Vulnerability Discovery

Draper Scholar Allison Naaktgeboren[1], Andrew Tolmach[1], Greg Sullivan[2], and Silviu Chiricescu[2]

[1]Portland State University (PSU), [2]Draper

ABSTRACT: "Fuzzing" is an automated way of finding inputs that cause software crashes. However, finding and fixing the root cause (the underlying vulnerability) that leads to a crash is still very difficult. The Draper PIPE (Processor Interlocks for Policy Enforcement) project lets developers specify security policies that should be checked at runtime in deployed systems, potentially using the Draper hardware extension. However, it would better to catch (and fix) these violations prior to deployment. The envisioned *PIPE-Cleaner* tool will apply fuzzing to automatically find vulnerabilities in software based on Draper PIPE policies. The PIPE-Cleaner project will leverage the Draper VMF (Vader Modular Fuzzer) tool to implement fuzzing, and will build on the Tagged-C project at Portland State University to specify security policies.

INTRODUCTION

- Software vulnerabilities are dangerous and expensive (~ $2.4 trillion in 2022).
- *Fuzzing* is a common technique to find vulnerabilities using synthetic program inputs
- **Problem**: Fuzzing produces program crashes, but crashes are not sufficient to identify and fix root cause flaws (aka vulnerabilities):
  - Same vulnerability may cause many crashes
  - Program may run for long time between vulnerability and crash
- **Solution**: Use Draper PIPE (Processor Interlocks for Policy Enforcement) which provides a way to define and detect large classes of vulnerabilities, instead of relying on OS crash signals
  - Use PIPE-inspired policies and enforcement, with inputs automatically generated by fuzzing, to find precise vulnerability locations
  - Stop & report at point of vulnerability, rather than crash much later

METHODS

- **Tagged-C**: The Tagged-C project at PSU makes security properties easier to specify, compared to Draper PIPE policy language
- **VMF:** The VMF (Vader Modular Fuzzer) project at Draper enables combining fuzzing and analysis tools in novel ways
- **Initial Proof of Concept**
  - Tagged-C interpreter + VMF = PIPE-Cleaner
  - Will be slow, but will validate approach on small applications
- **Scaling up in speed and size**
  - Implement Tagged-C as C-to-C inline reference monitors
  - Able to run policies on Draper PIPE hardware rather than in simulation

RESULTS

Vulnerable C program

```
#include <stdlib.h>
#include <stdio.h>
#define MAX_SIZE 80 /*1024*/
int foo (int n) { return (n*n)+1;}
int foo2 (int n) {return 2*n;}

int main() {
   int* x = (int*) malloc(sizeof(int));
   *x = 3;
   char* input = (char*) malloc(MAX_SIZE * sizeof(char));
   printf("enter some input:");
   fgets(input, MAX_SIZE, stdin);
   printf("You entered %s. Hope it doesn't have a problem!", input);
   int flag = (char) input[1];
   if (!(flag % 2)) { free (input);}
   else { free (input); }
   input[0] = foo2(foo(input[0]));
   if (!(flag % 3)) { free (input); }
```

Root cause: `input` is freed twice

PIPE-Cleaner Prototype Sample Output

```
---------------------------------
Output Summary
Unique Sec Policy Failures: 3
Total (nonunique) Failures: 2633
Unique Standard Crashes   : 0
Total (nonunique) Crashes : 0
Unique Hangs              : 0
Total (nonunique) Hangs   : 0
Total Saved Testcases     : 1259
Total Testcases Executed  : 5765
Results saved in base dir : output-cc-multi/0118_175124
---------------------------------
PIPE Security Policy Violations Details
        For each violation, only the first detected test case is saved.
        Total records tagged in storage: 3
Problem Root-cause:
        Policy Violated: DoubleFree.
        Failed Rule: FreeT detects two frees.
        Memory first freed at location
…/tests/double_free_confused_cleanup_multi_handlabelled.c:81 was freed again at
location …/tests/double_free_confused_cleanup_multi_handlabelled.c:83
TC Filename/ID : 3
TC buffer size : 4
Testcase/Input : 22p
```

Finds violation

Anticipated Results

- # of reported vulnerabilities / # of true vulnerabilities
  - Ideal ratio is 1
- # of reported crashless vulnerabilities
  - More is better.
- Coverage / Program Size / Time
  - More coverage, larger programs, in < time
  - Goal: comparable to SOTA fuzzers (e.g. AFL++)

DISCUSSION

- PIPE-Cleaner finds violations of specific security properties, rather than simple program crashes
- Furthermore, PIPE-Cleaner can find vulnerabilities that do not cause crashes and cannot be found by traditional fuzzing
- Specific, actionable bug reports reduce signal-to-noise problems of fuzzing and dramatically reduce the time from problem identification to time of triage and fix
- Integration into CI/CD finds vulnerabilities earlier (pre-deployment) than PIPE hardware alone

CONCLUSIONS

- Draper GNC and other software is security and safety critical
- Tools to find bugs quicker, and to support rapid triage and fixing, are desperately needed
- PIPE-Cleaner applies SOTA fuzzing combined with Draper PIPE policies specified in Tagged-C to rapidly identify specific violations of security properties

ACKNOWLEDGEMENTS / REFERENCES

Thanks to Sean Noble Anderson at PSU; also Mike Shields from US TMRC for Summer funding.

- Sean Anderson, Allison Naaktgeboren, and Andrew Tolmach, 2023. *Flexible Runtime Security Enforcement with Tagged C*.
- A. A. d. Amorim *et al.*, 2015. *Micro-Policies: Formally Verified, Tag-Based Security Monitors.*
- B. P. Miller, M. Zhang and E. R. Heymann, 2022. *The Relevance of Classic Fuzz Testing: Have We Solved This One?*.
- Synopsys, Consortium for Information & Software Quality, 2022. *The Cost of Poor Software Quality in the US: A 2022 Report.*

Scimitar: Functional Programs as Optimization Problems

Nate F.F. Bragg[1,3], Jeffrey S. Foster[1], and Philip Zucker[2]

[1]Tufts University, [2]Draper , [3]Draper Scholar

ABSTRACT: We introduce Scimitar, which compiles functional programs to optimization problems, encoding abstractions at a high level. This allows solve-time conditionals, recursive functions, and other language constructs. We demonstrate Scimitar using a number of examples and benchmarks including classic optimization domains and more complex problems. Our goal is to explore the benefits of a dedicated optimization solver over the general purpose solvers explored in prior work. Potential applications include tuning online parameters, algorithm heuristics, and program synthesis of minimal programs given some high level constraints.

INTRODUCTION

- Scimitar is an **optimization-aided language** that seamlessly integrates mixed integer linear programming (MILP) problems in functional code
- MILP is a powerful and widely used approach to solving optimization and logistics problems.
- Researchers have previously explored integrating SMT constraint solvers into programming languages, e.g., Rosette [Torlak and Bodik]
- Others have explored compile-time optimizers [Diamond and Boyd]
- Scimitar lets programmers minimize values in programs using encodings for *solve time* operations like conditionals, vector indexing, recursion and loops, e.g.:

```
1  #lang scimitar
2  (optimum-ref x
3    (maximize x
4     (if x
5      (assert (=  x 0))
6      (assert (<= x 1)))))
```

DESIGN

- Interleaves functional and optimization code, switching between host and solver semantics
- Programmers invoke the solver and interpret results via **maximize** and **optimum-ref** syntax
- Uses a set of constraint encodings to compile code directly into mixed integer linear constraints
- E.g., multiplication uses McCormick envelopes:

$$[\![x \cdot y]\!] \geq x^l \cdot y + x \cdot y^l - x^l \cdot y^l$$
$$[\![x \cdot y]\!] \geq x^u \cdot y + x \cdot y^u - x^u \cdot y^u$$

- Also uses approximate encodings for e.g. recursion, via a conditionally infeasible sentinel
- Uses the popular off-the-shelf Gurobi MILP solver [Gurobi Optimization]

DISCUSSION

- We implemented several programs showcasing the features of Scimitar
- Both *pipes* and *logistics* demonstrate classic domains targeting optimization solvers
- The *malloc* benchmark shows a real-world use: distributing allocated memory over time. It exercises host-solver boundary marshalling
- The power of Scimitar is demonstrated by the *imp* benchmark, which implements an imperative language with unbounded loops and mutation
- We compare Scimitar to Rosette, which uses Z3, and to a plain constraint language *O*
- To a certain extent the benchmarks measure the efficiency of Gurobi's vs Z3's internal algorithms
- A goal of ours is to give evidence of the benefits of a dedicated optimization solver over SMT
- In both Scimitar and Rosette, the overall time is split between compile and solve time
- Scimitar constructs its encodings at compile time, whereas Rosette's output language is rather simple, leaving encoding entirely to Z3
- Times shown are the average over multiple runs
- Scimitar variables and rows correspond to the overall compile and solve times

Table 1. Measurements in seconds for SCIMITAR, optimization language, and Rosette programs

			SCIMITAR		*O*		Rosette	
	vars	**rows**	**compile**	**solve**	**compile**	**solve**	**compile**	**solve**
pipes	172	190	36.7ms	0.47ms	0.60ms	18.8ms	0.44ms	22.2ms
logistics-s	273	298	53.1ms	1.7ms	1.4ms	21.3ms	14.4ms	18.6ms
logistics-h	10909	14051	485.1ms	971.3ms	674.3ms	112.6ms	63.5ms	>20m[2]
trivial	265	361	33.5ms	1.3ms	0.52ms	2.3ms	0.08ms	19.7ms
malloc	239	251	153.2ms	6.3ms	—[1]	—[1]	8.0ms	101.3ms
imp-s	10312	8325	172.7ms	18.4ms	—[1]	—[1]	—[1]	—[1]
imp-h	13128	11122	669.2ms	35.5ms	—[1]	—[1]	—[1]	—[1]

[1] These benchmarks do not have a corresponding non-SCIMITAR version.
[2] This benchmark exceeds a 20 minute time out.

EVALUATION

- Scimitar spends most of its time in our compiler whereas Rosette spends most of its time in Z3
- Scimitar's compiler is a performance bottleneck which compares unfavorably with Rosette
- Conversely, the solve time of our encoding is dramatically better than in Rosette
- Performance of simple operations slows down when you have hundreds or thousands of them
- Users must have solver awareness due to compile-time issues with e.g. inlining bounds, numerical precision
- Our compiler implementation was in Racket, a slow language. An implementation in C would probably outperform Rosette overall

CONCLUSIONS

- Scimitar allows users to automatically take advantage of encoding techniques that must normally be written by hand, enabling solve-time conditionals, bounded inlining and more
- We have also given a number of examples of Scimitar in action, including benchmarks that demonstrate Scimitar's features
- We promote its use in building and modeling optimization problems in a more maintainable way

REFERENCES

- Emina Torlak and Rastislav Bodik, 2013. Growing solver-aided languages w/rosette. *Onward! '13*
- Gurobi Optimization, LLC, 2023. Gurobi Optimizer Reference Manual
- Steven Diamond and Stephen Boyd. 2016. CVXPY: A Python-embedded modeling language for convex optimization. *Journal of Machine Learning Research*

Using a Microphysiological System PREDICT96 to Study the Role of Shear Stress in Severe COVID-19

Michelle Nguyen[1,2,5], Corin Williams[3], Ashley Gard[3], and John Connor[1,4,5]

[1]Department of Pharmacology, Physiology, & Biophysics, Boston University School of Medicine, Boston, MA, [2]Draper Scholar Program, Cambridge, MA, [3]The Charles Stark Draper Laboratory Inc., Cambridge, MA, [4]Department of Virology, Immunology, & Microbiology, Boston University School of Medicine, Boston, MA
[5]National Emerging Infectious Diseases Laboratories, Boston University, Boston, MA

ABSTRACT: Blood clots or thrombi are characteristics symptoms of severe COVID-19, especially among patients with cardiovascular comorbidities. Thrombi tend to arise when the inner lining of blood vessels, the endothelium, becomes dysfunctional. While clotting symptoms are frequent in patients with severe COVID-19, the mechanism driving this vascular phenomenon is unknown. Here, we employ a high-throughput, microphysiological system (PREDICT96) in a high containment lab (BSL3) to investigate how SARS-CoV-2, the causative agent of COVID-19, interacts with the endothelium. We show that SARS-CoV-2 alone does not drive vascular impairment.

INTRODUCTION

Severe COVID-19 can lead to Blood Clots

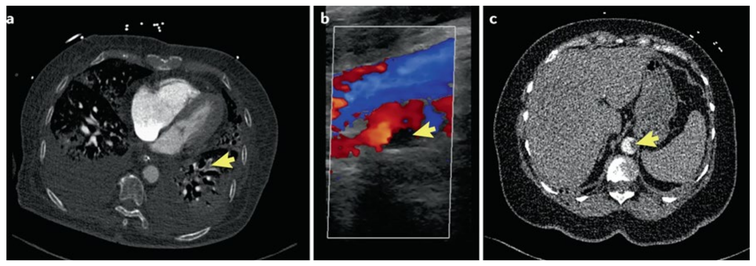

Figure 1. Clinical imaging of fatal thrombotic complications in COVID-19 patients and with multiple cardiovascular risk factors. (A) Pulmonary emboli (arrow) involving the anterobasilar arteries in the left lower lobe of the lung. (B) Deep vein thrombus in vein (arrow). (C) Thrombus in Abdominal Aorta (arrow). Ref: DOI: 10.1038/s41569-020-00469-1

A Context for Blood Clots: Endothelial Cells Lose their Function

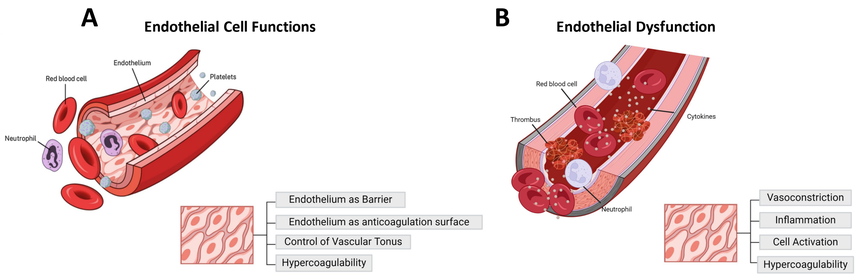

Figure 2. Endothelial Functions in Health and Disease: (A) represents features of the inner lining of blood vessels in a healthy state and (B) unhealthy state of the endothelium and support blood clotting. Adapted from: DOI:10.1016/j.transci.2022.103368.

How SARS-CoV-2 Leads to Endothelial Dysfunction: Three Possible Mechanisms

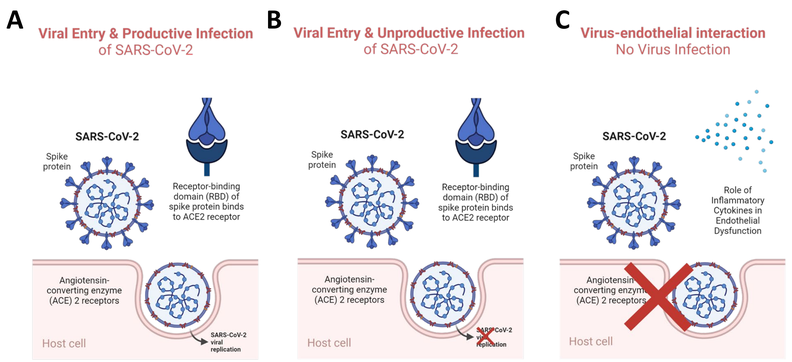

Figure 3. Proposed mechanism on how SARS-CoV-2 leads to Endothelial Dysfunction: (A) direct infection, (B) direct infection without virus replication, (C) interactions between virus and cell with cell exposure to circulating inflammatory signals in the body.

GOAL: To understand how SARS-CoV-2 damages blood vessels in physiologically relevant conditions.

HYPOTHESIS: SARS-CoV-2 infects human umbilical cord vein endothelial cells under fluid shear stress (FSS).

METHODS

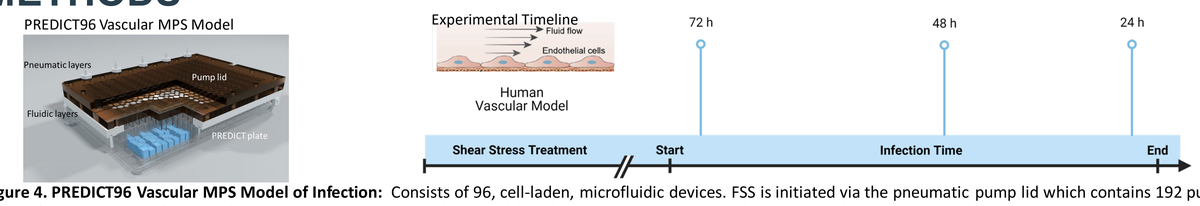

Figure 4. PREDICT96 Vascular MPS Model of Infection: Consists of 96, cell-laden, microfluidic devices. FSS is initiated via the pneumatic pump lid which contains 192 pumps. Devices experience FSS (0.5 dyn/cm^2 or 7 dyn/cm^2) before and during infections to recapitulate physiological conditions in blood vessels. After the infection, devices are fixed, stained for biomarkers, and used for downstream immunofluorescence analyses.

RESULTS

SARS-CoV-2 does not Infect Endothelial Cells in PREDICT96 (48 h)

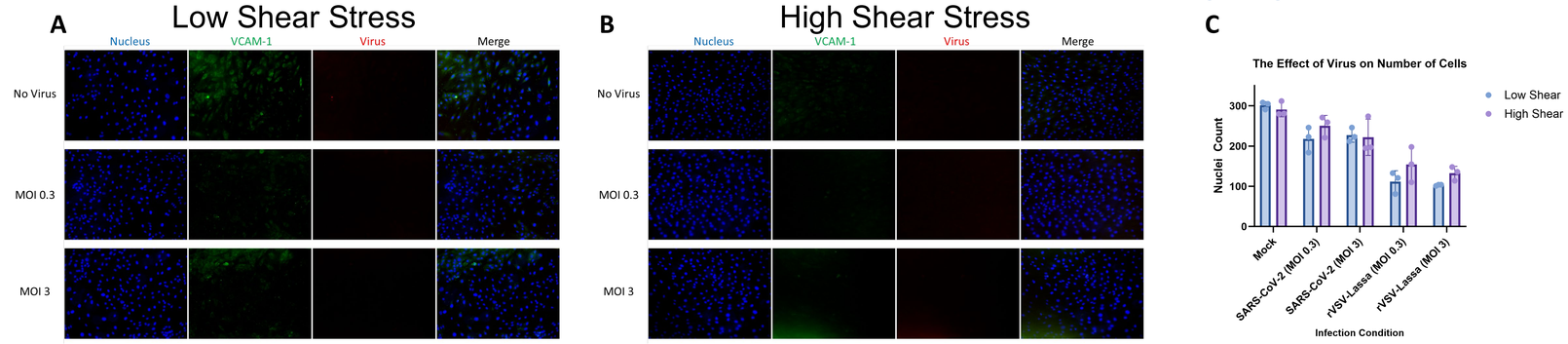

Figure 5. Comparison of Endothelial Responses to SARS-CoV-2: under (A) low FSS (0.5 dyn/cm^2) and (B) high FSS (7 dyn/cm^2). (C) Quantification of cell loss in response to infection in all tested conditions. Endothelial cells remain uninfected, irrespective of FSS profile and MOI. MOI = multiplicity of infection and represents the ratio of viruses to number of cells in the device.

Infection is Possible in PREDICT96: Lassa Glycoprotein (GP)-Driven Endothelial Damage (48 h)

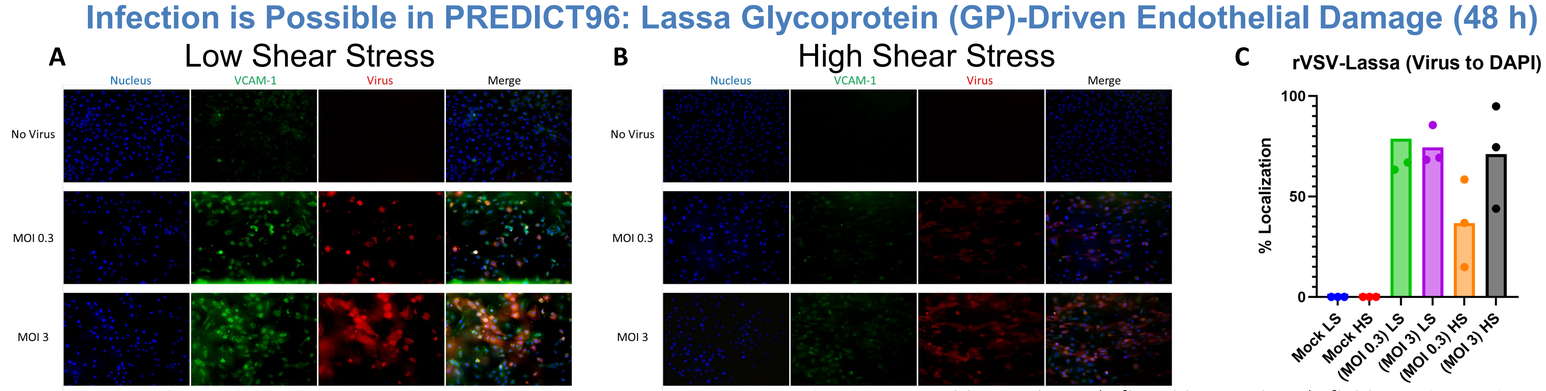

Figure 6. Comparison of Endothelial Responses to a pseudotyped Lassa virus which served as a positive control for infection under (A) low FSS (0.5 dyn/cm^2) and (B) high FSS (7 dyn/cm^2). (C) Quantification of ratio of infected to non-infected cells in devices positive for infection. MOI = multiplicity of infection and represents the ratio of viruses to number of cells in the device.

DISCUSSION

- Endothelial cells are resistant to SARS-CoV-2 infection (MOI 0.3 and MOI 3) *in vitro* under low FSS (0.5 dyn/cm^2) and high FSS (7 dyn/cm^2).
- High FSS (7 dyn/cm^2) is protective to the endothelium (no VCAM-1 induction).
- Lassa-GP overcomes this protective effect, shows productive infection and extensive vascular damage.
- **Limitations**: This study used healthy cells, while pathology is seen in patients with cardiovascular comorbidities (e.g., diabetes, atherosclerosis). Infection may be specific to the pseudotyping system.

CONCLUSIONS

- Characterize flow-driven infection using SARS-CoV-2 and recombinant virus to represent Lassa-GP entry.
- SARS-CoV-2 likely does not drive endothelial dysfunction on its own.
- Lassa GP-directed infections leads to VCAM-1 induction irrespective of FSS profile and MOI.
- **Future Directions:** Infection with SARS-CoV-2 from an unhealthy state (via COVID-19 patient serum treatment) may be avenue forward to observe endothelial damage. Identification of other relevant endothelial cell types may also be necessary for these observations.

Improved Extracorporeal Oxygenation through Continuous Hemocompatible Microfluidic Microbubble Generation

André Pincot[1,2,3], Anthony Quinnert[1], Brett Isenberg[1], Ryan Dubay[1], Gareth McKinley[3], David Sutherland[1]

[1]Draper Labs, [2]Draper Scholar, [3]Hatsopoulos Microfluids Lab, MIT Department of Mechanical Engineering

ABSTRACT: Severe trauma, whether systemic or to the lungs specifically, can compromise the body's ability to effectively exchange oxygen and distribute it as necessary throughout the circulatory system. Current extracorporeal membrane oxygenators (ECMO) require high blood flowrates to operate effectively, leading to high shear within the device and significant blood trauma. When operated for long durations in a paired circuit with a ventilator, this leads to high device complication and mortality rates. As such, we have developed a spatially efficient device to supersaturate blood with oxygen via microbubble generation. This allows the device to boost the oxygen content of processed blood beyond physiological ranges, reducing the necessary blood to be circulated from the body to meet oxygen requirements thus potentially increasing system reliability and blood health over the medium and long terms. Further development of this concept promises new pathways for engineers and physicians to develop and deploy more effective and portable microfluidic oxygenators with superior operative longevity.

INTRODUCTION

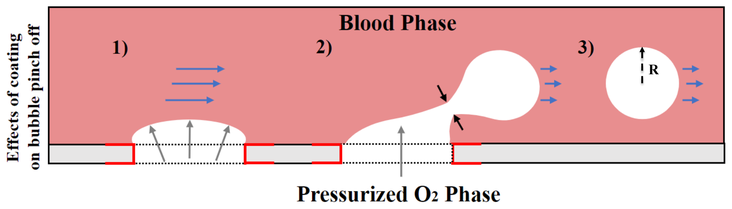

Figure 1: Bubble pinch-off in a cross-flow microfluidic channel.

- Current treatments for Acute Respiratory Distress Syndrome (ARDS) are insufficient to ensure patient recovery due to thrombosis, trauma, and organ failure.
- We aim to leverage oxygen supersaturation of blood to improve device efficiency and reduce long term thrombus formation. We can accomplish this via the introduction of microbubbles that are sufficiently small to be fixed by yield stress.

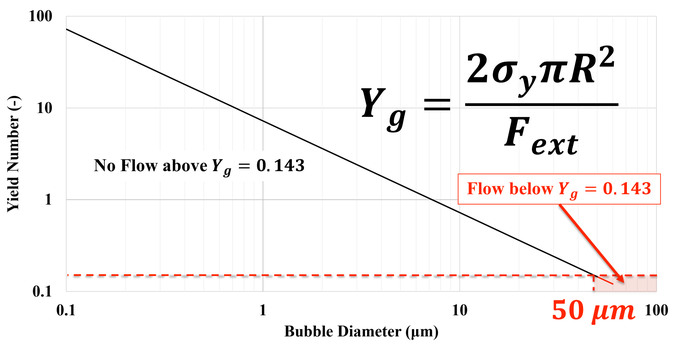

Figure 2: Depiction of yield number evolution over oxygen bubble diameters in human blood[1].

METHODS

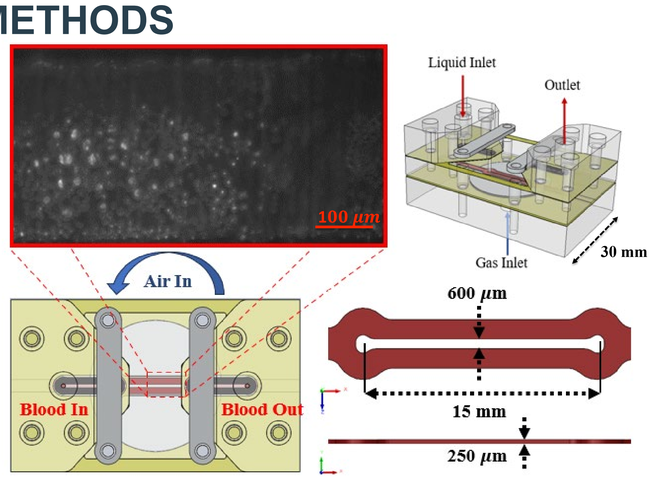

Figure 3: Device setup and dimensions.

- Oxygenation is accomplished via the use of a commercial 0.2 μm alumina membrane, coated with a hydrophobic fluorosilane to promote airflow.
- Gas flow is moderated via a Dolomite pump and fluid flow via syringe pump.

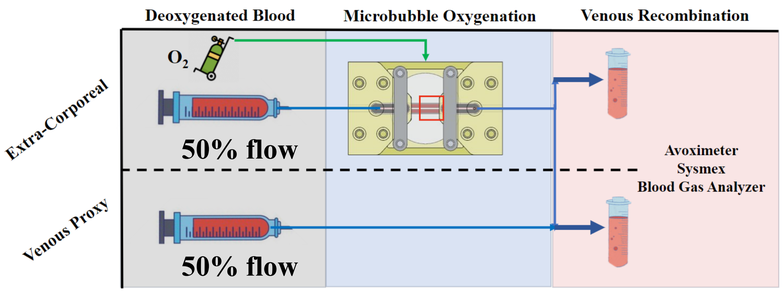

Figure 4: Experimental circuit setup for venous recombination simulation. To assess recombination with deoxygenated venous blood, the supersaturated blood is combined with the venous flow at a 50% ratio.

RESULTS

- Generated bubbles ranged from 15-60um, measured using the ImageJ particle analysis package (Figure 5).
- Measurements of both direct supersaturation and combined circuit outputs suggest that the devices have successfully achieved oxygen supersaturation in blood, consistently exceeding physiological oxygen volume percents of 5% as shown in Figure 6.

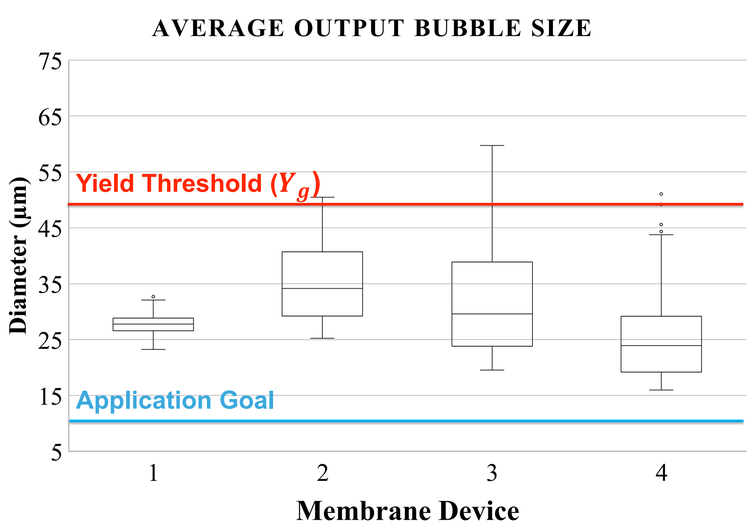

Figure 5: Output bubble diameters for aluminum oxide membrane (AOM) devices.

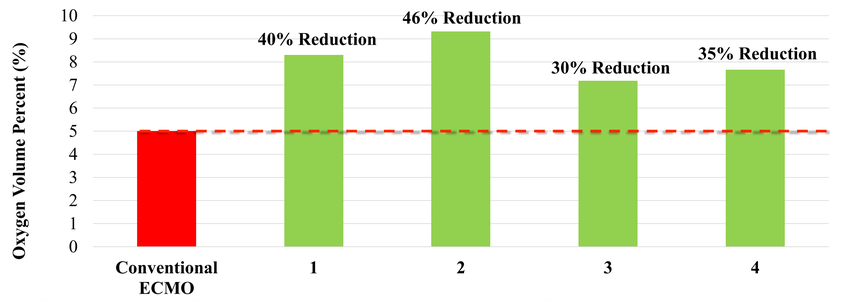

Figure 6: Oxygen volume percent of combined circuit output for each tested membrane, annotated with corresponding reductions in flow rate from conventional ECMO oxygenation.

DISCUSSION

- As demonstrated in Figure 5, the diameters of the produced bubbles generally remained under the yield threshold. This indicates that the bubbles will tend to stay "fixed" by the blood yield stress, preventing them from rising out of the fluid and maximizing their ability to diffuse oxygen into the blood over time.
- Dramatic increases in relative volume percent beyond a baseline of 5% suggests the potential of microfluidic membrane oxygenators in blood oxygen supersaturation. Additionally, exerted shear stress in the membrane device does not exceed 5 Pa, potentially reducing thrombus formation[2].

CONCLUSIONS

- Future efforts in developing this technology would seek to shrink the output bubble size closer to size range of red blood cells, around 8 – 10 μm. This size range would ensure the patient safety while permitting effective supersaturation
- Implementation in the medical context will be aided by further development of more affordable, robust, and adaptable custom membranes with increased operation time and bubble production consistency.

ACKNOWLEDGEMENTS / REFERENCES

1. Beris AN et al. Creeping motion of a sphere through a Bingham plastic. Journal of Fluid Mechanics. 1985;158:219-244. doi:10.1017/S0022112085002622
2. B. C. Isenberg, E. et al , A Clinical-Scale Microfluidic Respiratory Assist Device with 3D Branching Vascular Networks. Adv. Sci. 2023, 10, 2207455. https://doi.org/10.1002/advs.202207455

My deepest thanks to the scholars and engineers of MIT and Draper who enable my research and professional development

Universal AUV Docking Station

Erik Pryal[1], Michael Ricard[2], Katie Levinson[2], and CDR Christopher MacLean[3]

[1]MIT Draper Scholar, [2]Draper, [3]MIT

ABSTRACT: This project aims to develop a versatile docking solution tailored for both present-day and upcoming generations of Autonomous Underwater Vehicles (AUVs) to facilitate efficient electric charging. With the increasing adoption of AUVs for various underwater tasks, a standardized docking mechanism is essential to streamline charging operations across diverse vehicle models. The proposed solution integrates an external latching mechanism (component that attaches to the existing AUV) to ensure compatibility with existing vehicle infrastructures. This universal docking system promises to enhance the sustainability and operability of underwater exploration and monitoring missions, contributing to the advancement of marine research and industry applications.

INTRODUCTION

AUVs provide an efficient and cost-effective means of exploring and monitoring the underwater environment such as underwater mapping and offshore infrastructure inspections. However, their operational endurance is limited by their energy capacity. To address this, AUV charging docking stations have emerged as a solution. These stations serve has hubs for the vehicles to autonomously recharge batteries and offload data to extend their operational capabilities and reduce need for resurfacing.

Current charging docking stations are designed for a singular AUVs leaving no room for other or future systems capable to use the dock. This creates a need for a universal docking solution. A universal docking mechanism allows for flexibility in AUV designs to operate different sized and shaped vessels off the same dock.

BACKGROUND

Existing Designs

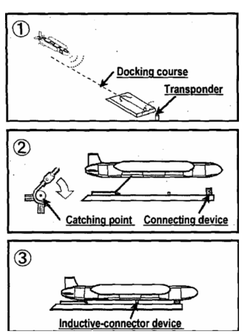

Odyssey Docking Station[1] (right)
- vertical pole with a circular movable carriage that forces vehicle into position

Pro: Simple 'whisker' attachment creates a sturdy connection

Con: Limits vehicle to have a rounded bottom to guide itself into correct docking orientation

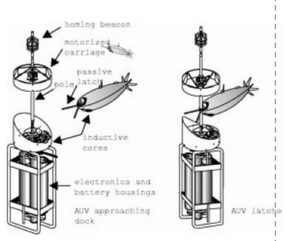

'Marine Bird' Dock[2] (left)
- vehicle catches V-shaped guide on the base by its catching arms
- Similar to aircraft carrier landings

Pro: Easy connection to create a precision charging connection

Con: Requires external ballast tanks to control docking

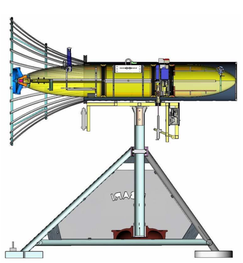

REMUS Docking Stations
- REMUS Woods Hole Oceanographic Institute[3] (right)
- Monterey Bay Aquarium Research Institute[4] (left)

–Both are an open funnel style that latches the vehicle to the dock

Pro: Funnel shape reduces precision needed in near field navigation

Con: Restricts vehicles size and shape to be cylindrical

METHODS

- Creation of SolidWorks models

Model Structural Analyses
- Finite Element Analysis – Loading conditions, stress, strain and deformation
- Fatigue Analysis – Fatigue failure points from cyclic loads and lifetime prediction
- Safety Factor Assessments – Critical components meet safety standards

Model Hydrodynamic Analysis
- Computational Fluid Dynamics – Evaluate drag, lift, and added mass
- Current and Wave impact – variations in water conditions impact on stability
- Vortex Shedding Analysis – potential for vortex shedding and vortex induced vibrations

RESULTS

INITIAL DESIGNS

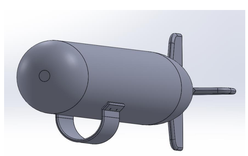

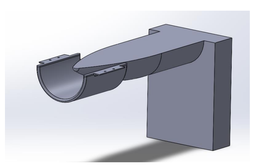

C-clamp
- Attaches to a halved tapered cylinder for docking

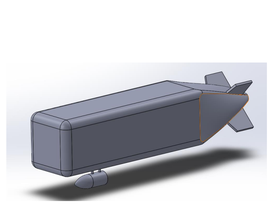

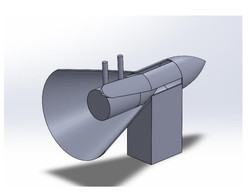

Funnel shape
- inspired by Remus designs
- Utilizes external cylinder so variety of shaped and sized vehicles can be docked

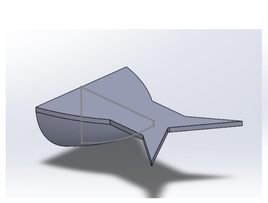

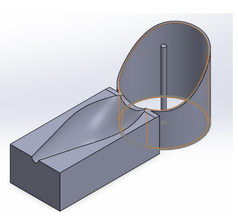

V-latch
- Odyssey inspiration.
- Uses rounded hull on external features to guide AUV to holding seat.

SolidWorks Models for Docking Mechanisms

DISCUSSION

- Universal docking station designs use styles of existing systems but allows for the attachment of any shaped or sized vehicle.
- An external component removes the restrictions on vessel shape and size by keeping charging dependence within the latching components.
- Currently SolidWorks Models have been created to be tested in its Flow Simulation software.
- The proposed designs will be optimized to reduce hydrodynamic forces such as lift and drag and be strengthen to support load forces of the AUV.
- Simulations to validate the latches stability during docking and undocking will be created to demonstrate the smooth transition and precision.
- Method to securely latch external mechanism into docking station is being investigated.

CONCLUSIONS

- The integration of an external latching component simplifies the docking process by providing a robust connection that is easily accessible to different AUV designs, minimizing the adaption of the vehicle.
- Standardizing the docking interface on AUVs will catalyze new discoveries and advancements in marine research.
- Further research could implement a communication interface to allow the docking station and AUV to exchange information such as battery status and charging requirements
- Power management and data transfers could be investigated as well to create the most efficient transfer rates from smaller to larger vehicles.

ACKNOWLEDGEMENTS / REFERENCES

Special thanks to Dr. Ricard and Katie Levinson for their guidance on this project. Additional thanks to my MIT advisor CDR MacLean.

[1] https://apps.dtic.mil/sti/tr/pdf/ADA356301.pdf
[2] https://ieeexplore.ieee.org/abstract/document/1282819
[3] https://ieeexplore.ieee.org/document/4099107
[4] https://ieeexplore-ieee-org.libproxy.mit.edu/document/4769696

Ensemble Methods for Detecting Anomalies within Continuous Data Flows

Gregg Puttkammer[1,2], Mark Ward[1], Jeff Cipolloni[3]

[1]Purdue University, [2]Draper Scholar, [3]The Charles Stark Draper Laboratory, Inc.

ABSTRACT: Intrusion detection systems are currently designed to operate on static data and, as a result, are not well suited to detect anomalies within variable data flows. In the past, discrete machine learning and streaming data methods have been applied in attempts to overcome these deficiencies with some success. Based on the literature, we believe a more promising approach for detecting anomalies can be achieved by merging supervised and unsupervised learning methods with streaming data analysis techniques. Furthermore, we posit that our approach will produce a set of ensemble methods that will decrease the time it currently takes to detect anomalies and increase the certainty of those detections within variable data flows. The ensemble detection methods will then be applied to network traffic data to determine their efficacy.

INTRODUCTION

Modern digital environments receive a constant flow of data that changes as time progresses. Due to the temporal nature of the data within these systems, robust, real-time anomaly detection methods are required to ensure data integrity. The need to trust the quality of real-time data is especially critical in modern data exchange infrastructures where new anomalies arrive in the data at aperiodic intervals and with unknown characteristics. A review of the literature has demonstrated the efficacy of applying supervised and unsupervised machine learning models to batch datasets. Furthermore, limited attempts to use supervised and unsupervised machine learning on continuous datasets has shown promise for real-time anomaly detection. However, additional research is required to prove the efficacy of the use of these models as a robust detection technique. Our research combines traditional machine learning methods with streaming data analysis techniques to improve detection rates of known and unknown anomalies in continuous data flows.

METHODS

- We shall leverage the Center for Applied Internet Data Analysis (CAIDA) at University of California, San Diego (UCSD) Network Telescope[1] datasets to validate our methods. These datasets are built on passive, real-world network traffic that include instances of anomalous and malicious activity.
- We will use the technique of unsupervised learning for feature selection to create additional inputs in the supervised model.
- We will also use unsupervised learning for anomaly detection to group certain network traffic as anomalous. Certainty of prediction will be achieved by using both the groupings from the unsupervised model and the patterns identified in the supervised model.
- The ensemble set of detection models will be applied to continuous data environment sets where the data distribution and thresholds for detection are constantly changing .
- Finally, we will apply the developed ensemble methods to broader datasets in order to detect defects and anomalies within real-world manufacturing, imagery and financial systems.

RESULTS

- Previous research developed frameworks for ensemble methods as explored in our research. **Figures 1** and **2** show sample architectures that will help guide our own work.
- **Figure 1** illustrates a sample architecture for the processing of continuous data. Included in this framework are steps for data transformations through Minhashed Virtual Vector (MV2), group identification within specified memory limits with Jaccard-Index Grouping (JIG), signature-group generation (SG2) and Automatic Whitelisting (AWL).

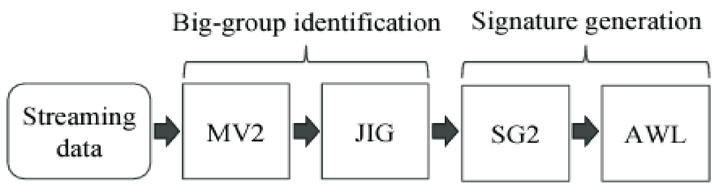

Figure 1. Architecture for Processing Continuous Data[2]

- The Adaptive Deep Log Anomaly Detector Framework (ADAF), illustrated in **Figure 2,** outlines the individual steps of a proposed architecture that applies online deep learning to optimize computations and an adaptive threshold for identifying anomalies. The ADAF increases robustness and reduces false alarms by continuously adapting to the changing data. The ADAF can capture both short and long-term trends in continuous data with minimal storage requirements.

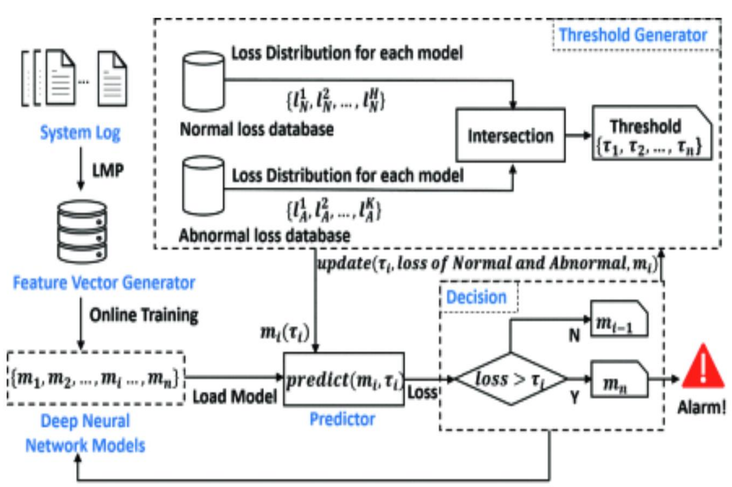

Figure 2. ADAF for Continuous Data Flows[3]

DISCUSSION

- We posit that there are promising detection methods developed in previous works that can be adapted to improve the performance of anomaly detection in dynamic data environments.
- Initial reviews of the literature leads us to believe that robust anomaly detection techniques will require advanced data management and preprocessing before real-time anomaly detection models can be developed.
- We plan to utilize grouping methods, such as subspace and Expectation-Maximization (EM) clustering, to supplement supervised learning models and provide additional information to improve performance for real-time anomaly detection.
- Domain knowledge is an essential component of working with anomaly detection models. Detection methods will be dependent on the characteristics of the distinctive datasets.

CONCLUSIONS

Current research supports the hypotheses that increased accuracy of anomaly detection in dynamic systems can be achieved through the application of the ensemble of adaptive frameworks. The application of the proposed ensemble methods should provide increasing confidence in the quality of dynamic data in the domains of cyber, autonomy and digital engineering, as examples. The ability to update detection models, while monitoring continuous data streams, should reduce the latency between the time when anomalies occur and when they are detected. As a result, rapid anomaly detection should increase the decision-maker's ability to respond quickly and appropriately to abnormalities detected in the data.

ACKNOWLEDGEMENTS / REFERENCES

[1] The CAIDA UCSD Network Telescope Educational Dataset, https://www.caida.org/catalog/datasets/telescope-educational_dataset

[2] H. Seo and M. Yoon, "**Generative Intrusion Detection and Prevention on Data Stream**", presented at the 32nd USENIX Security Symposium (USENIX Security 23), 2023, pp. 4319–4335. Accessed: Feb. 20, 2024. [Online].

[3] Y. Yuan, S. Srikant Adhatarao, M. Lin, Y. Yuan, Z. Liu and X. Fu, "**ADA: Adaptive Deep Log Anomaly Detector**", IEEE INFOCOM 2020 - IEEE Conference on Computer Communications, Toronto, ON, Canada, 2020, pp. 2449-2458, doi: 10.1109/INFOCOM41043.2020.9155487.

Automated Testing for Discovering Pre-Silicon Microarchitectural Security Vulnerabilities in Modern Processors

Draper Scholar

Draper Scholar Joseph Ravichandran[1], Mengjia Yan[1], and Silviu Chiricescu[2]

[1]MIT, [2]Draper

ABSTRACT: Pre-silicon verification is a requirement for today's complicated processor designs. However, it can be costly and inefficient to discover every vulnerability manually, and history has shown that many microarchitectural security problems have been missed by verification engineers. We propose a new fuzzing architecture designed specifically to aid with pre-silicon verification work to automatically discover microarchitectural security problems prior to chip tapeout.

INTRODUCTION

- Time and time again, researchers have shown that verifying processors is a challenging problem by demonstrating various microarchitectural attacks against consumer products.
- Speculative execution attacks have been shown to be difficult to find with traditional verification techniques and have devastating consequences on system security.
- Randomized testing is a technique commonly used in verification workflows, but prior work has focused on random testing for verifying ISA compliance.
- We aim to develop a modular, extensible, and scaleable verification framework specifically designed for pre-silicon randomized testing to discover microarchitectural vulnerabilities, rather than ISA compliance.

METHODS

- The fuzzer begins by generating a long sequence of random ISA instructions and executes them on multiple simulators in parallel.
- The fuzzer supports multiple simulator backends (such as Verilator, ModelSim, or FPGA targets).
- Each fuzzer invocation runs multiple simulation jobs with different secret values.
- The RTL coverage analyzer analyzes the RTL state over time to determine A) whether or not the test case uncovered new stimulation of the chip and B) whether or not the secret's value induced a difference in execution traces between simulator jobs.
- The bug detector utilizes the RTL coverage analyzer's findings to determine whether or not any differences have security implications.
- Finally, the mutator generates a new test case, utilizing feedback from the coverage analysis.

RESULTS

- Figure 1 provides an overview of the proposed fuzzing architecture.
- The interconnections between each phase will be modular, allowing for substituting components easily for different fuzzing strategies.
- Our proposed instruction generation strategy limits test cases to speculative constant-time programs.
- If the fuzzer finds a speculative constant-time instruction sequence that generates a timing or data difference dependent on the secret value, we conclude the fuzzer has identified a security-relevant information disclosure vulnerability.
- While ISA compliance is not a first-class design goal, the fuzzing strategy could be optimized to also test for ISA compliance eg. by comparing against a gold model such as RVFI for RISC-V designs.
- Our test case strategy avoids structural contention issues, which we assume are trivial. We want to report deeper issues than simple contention.

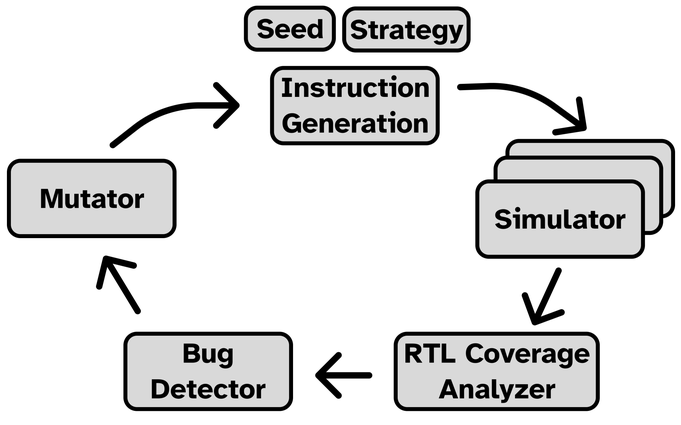

Figure 1
Proposed Architecture

DISCUSSION

- Microarchitectural security vulnerabilities have plagued modern systems for years.
- Pre-silicon verification is a challenging problem with much existing literature around it.
- Our fuzzer will contribute a new modular infrastructure for testing processors before tapeout to automatically discover microarchitectural security vulnerabilities that may not have been foreseen by the chip designers.
- By focusing on microarchitectural security vulnerabilities instead of ISA compliance, our fuzzer contributes a new practical scaleable framework for improving verification workflows in real-world chip designs.

CONCLUSIONS

- Fuzzing as a verification strategy is a promising approach as it requires little human intervention to discover vulnerabilities.
- Pre-silicon verification is a compelling use case for this technology, preventing chip designers from taping out chips with problems by discovering vulnerabilities before tapeout.
- Our fuzzer will utilize a novel approach for targeting microarchitectural security issues while avoiding simple structural contention problems.
- The next step is to engineer and profile the proposed architecture against open-source cores.

ACKNOWLEDGEMENTS / REFERENCES

Flavien Solt, Katharina Ceesay-Seitz, Kaveh Razavi. *Cascade: CPU Fuzzing via Intricate Program Generation.*

P. Kocher, J. Horn, A. Fogh, et al., *"Spectre Attacks: Exploiting Speculative Execution," in S&P, 2019.*

Accelerating Open Source Homomorphic Encryption with GPUs

Frank Rossi[1], David Kaeli[2], and Andrea Webb[3]

[1]Northeastern University & Draper Scholar, [2]Northeastern University, [3]Draper

ABSTRACT: Fully Homomorphic Encryption (FHE) is an emerging technology that allows for secure computations on encrypted data. The largest and most complete open source library of FHE is OpenFHE, which provides a highly abstracted API for use of all FHE functionality, but is limited in that it only supports computations on CPUs. This work extends OpenFHE's implementation of the Cheon-Kim-Kim-Song FHE scheme to accelerate homomorphic arithmetic with a GPU while retaining all other functionality of OpenFHE. This is done through the creation of a raw ciphertext format that can be moved between the GPU and CPU as necessary.

INTRODUCTION

- FHE is a technology that has applications anywhere it is desired that sensitive data be securely processed remotely, at a potentially vulnerable location. Through FHE, data is protected via encryption the whole time it is processed on the remote server.
- The largest and most complete open source library of FHE by far is OpenFHE, which provides a highly functional and abstracted environment for FHE applications to support key generation, encryption/decryption, bootstrapping, and more.
- GPU libraries exist for FHE, but their functionality beyond anything but basic arithmetic is quite limited.
- This work aims to accelerate homomorphic arithmetic via GPUs while retaining the functionality of OpenFHE.

METHODS

- A new format for storing ciphertexts was created containing only the most basic values necessary (raw format) that can be stored on the GPU.
- Functionality was created to transition ciphertexts between OpenFHE and raw formats.
- Homomorphic Addition and Multiplication were implemented in this raw format on the GPU.

Raw Ciphertext Illustration

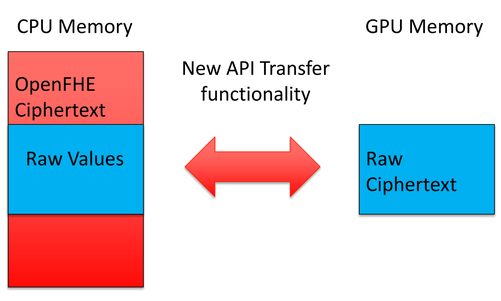

RESULTS

- Functionality was tested on ciphertexts comparing the original OpenFHE CPU implementation and the accelerated GPU implementation.
- Parameters for testing were standard 128-bit security parameters from OpenFHE, with:
  - Ring Dimension N = 2^16
  - Precision/prime moduli q = 50 bits
  - Limbs/Level L = 40
- Hardware comparison was AMD A100 vs EPYC 64-Core CPU
- Current results show ~5-10x faster execution time for homomorphic addition on the GPU implementation across multiple numbers of ciphertexts processed in parallel.

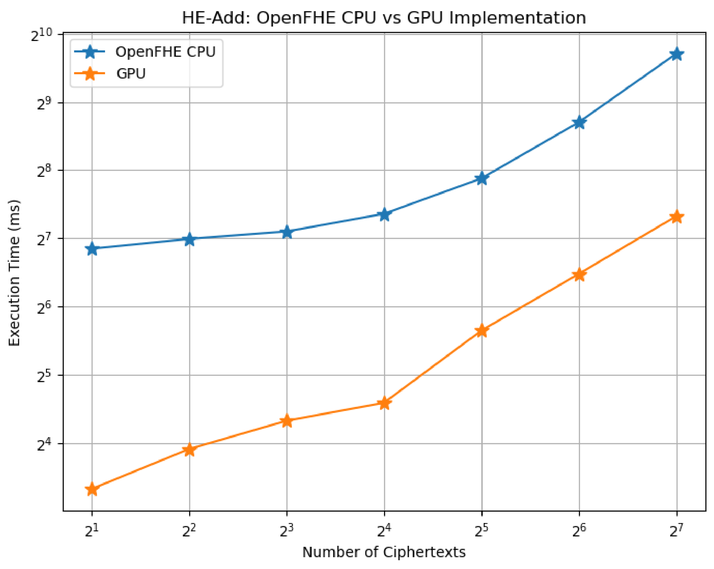

DISCUSSION

- Acceleration of homomorphic arithmetic was achieved on a GPU compared to the original CPU implementation in OpenFHE. This work is valuable in retaining the functionality of OpenFHE alongside this acceleration. However, this result still lags behind other GPU libraries such as LiberateFHE and PhantomFHE, although PhantomFHE does not support bootstrapping and both libraries are much more limited in the parameters they can support along with a much lower production quality found in OpenFHE.

CONCLUSIONS

- Homomorphic Operations can be accelerated on GPUs while retaining the functionality of existing libraries. More work needs to be done to bring this implementation on the level of other GPU libraries along with implementing matrix multiplication and more.

ACKNOWLEDGEMENTS / REFERENCES

Thank you to Andrea Webb, Dr. Kaeli, Kaustubh Shivdikar, and the rest of the NUCAR team for teaching me so much and supporting me in my work.

[1] Badawi et al. "OpenFHE: Open Source Fully Homomorphic Encryption Library," https://eprint.iacr.org/2022/915.
[2] Desilo. "Liberate.FHE" https://github.com/Desilo/liberate-fhe.
[3] Yang et al. "Phantom: a CUDA-Accelerated Word-Wise Homomorphic Encryption Library," https://eprint.iacr.org/2023/049.

A Cislunar Cold-Start Solution for Navigation under CR3BP Dynamics

Jillian Ross[1], Dr. Carolin Frueh[1], Peter Neirinckx[2]

[1]Purdue Aeronautics and Astronautics [2]Draper Laboratory

ABSTRACT: This analysis probabilistically assesses an object's state in cislunar space by generating admissible regions in a range and range-rate space according to dynamics in the Circular-restricted Three Body Problem of the Earth-Moon system. Optical angle measurements from a space-based observer in a geosynchronous orbit provide line-of-sight to a cislunar object and constrain a region of motion according to the object's Jacobi Constant for statistical orbit determination. The approach can then be adapted to generate admissible regions for optical and x-ray measurements of a pulsar star, ultimately enabling an onboard cold-start navigation solution in cislunar space.

INTRODUCTION

- Reliable methods of object-tracking and state estimation are significant in developing navigation infrastructure towards increased traffic around the moon
- Milani et al. formulated a method of probabilistic orbit determination by constraining an object's range and range-rate as a set denoted as an *admissible region* according to the Keplerian energy of the object [1]; such a set is representative of a uniform PDF that can be used for initial orbit determination (IOD) initialization
- In a similar manner, this work offers a method of constraining an admissible region according to the Jacobi Constant (JC), or pseudo-energy, from a measurement providing angles and angle-rates of an object in an orbit governed by dynamics of the Circular-restricted Three Body Problem (CR3BP) in the Earth-Moon system.
- Eventually, the admissible regions can be generated for a satellite taking optical and x-ray range measurements of a pulsar star, enabling a statistical initial orbit determination method via x-ray navigation

METHODS

- The relative velocity is defined with respect to the Jacobi Constant of the Lagrange points to define range-rate as a function of range
- This is currently performed to estimate the state of an observed object but will be implemented for onboard state estimation from a pulsar measurement

$$JC_{Li} = \epsilon_{Li}^2 + \eta_{Li}^2 + \frac{2(1-\mu)}{d} + \frac{2\mu}{r}$$

$$r = \sqrt{(\epsilon - 1 + \mu)^2 + \eta^2 + \zeta^2}$$

$$d = \sqrt{(\epsilon + \mu)^2 + \eta^2 + \zeta^2}$$

$$v_{rel}^2 = \epsilon_P^2 + \eta_P^2 + \frac{2(1-\mu)}{d} + \frac{2\mu}{r} - JC_{Li}$$

$$\dot{\rho} > \sqrt{v_{rel}^2 - n^2\rho}$$

Re-dimensionalize

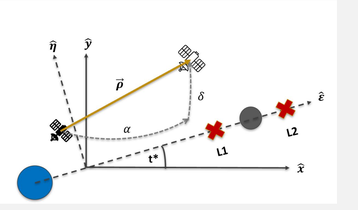

Attributable:

- Two angles and angle-rates measured from observer to pulsar: $A = (\alpha, \delta, \dot{\alpha}, \dot{\delta})$
- Reference direction for α: $\hat{\varepsilon}$ axis
- Reference direction for δ: $\hat{\eta}$ axis
- X-ray range measurement

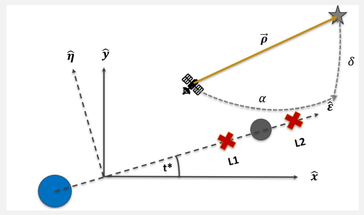

Frame:

- Earth and Moon rotate about common barycenter
- Origin at barycenter of Earth and Moon
- μ represents mass parameter
- ε, η, ζ represent rotating coordinates in CR3BP rotating frame
- n represents proper motion of measured object

RESULTS

- An object in an L2 Halo orbit with Jacobi Constant 3.1518 and an object in an L1 Lyapunov orbit with Jacobi Constant 3.1559 are propagated with simulated optical and range measurements from a geostationary observer to the object
- Optical measurements generate upper and lower bounds for the range and range-rate
- If range is measured as well (i.e. via an x-ray sensor for a pulsar measurement), this provides a constraint to the region
- A continuum of ranges and their associated range-rates is defined according to the Jacobi Constant relative to the second and third Lagrange points
- The true state is plotted in range and range-rate to confirm accuracy of the boundaries

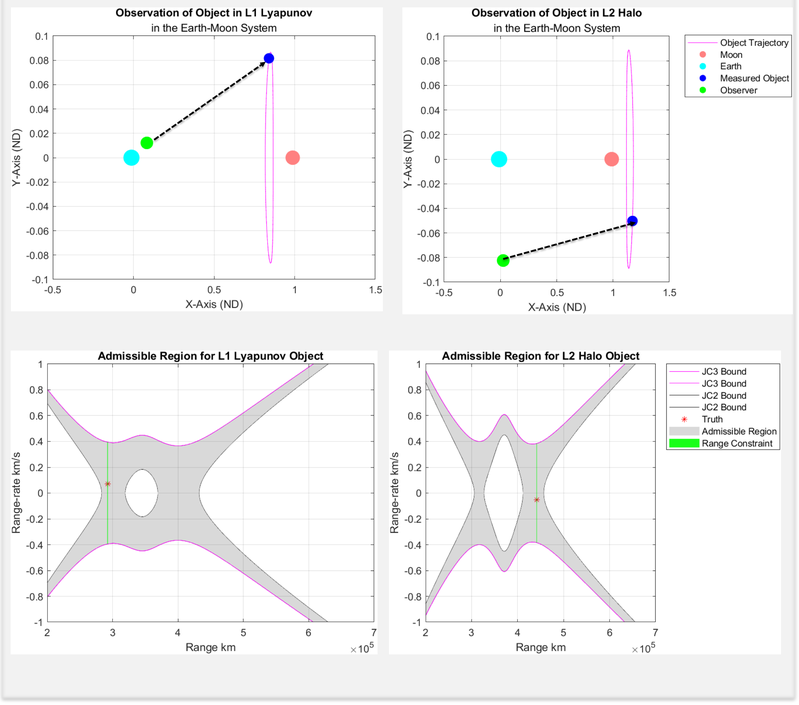

DISCUSSION

- Milani et al. [1] is provided for CR3BP dynamics
- Constraining an admissible region via optical measurements, range, and the Jacobi Constant of an object is confirmed to encompass the true range and range-rate of an object
- A Monte Carlo analysis can be performed in which samples are drawn in this region and uncertainty is quantified.
- Analysis also yields accurate results for L1 Halo orbits, L2 Lyapunov orbits, and lunar DRO's
- An update to the admissible region can be applied via an Extended Kalman Filter to enable a framework for navigation simulation.

CONCLUSIONS

- Admissible regions that constrain an object's state via its Jacobi Constant provide the opportunity for probabilistic orbit determination within CR3BP.
- Future work will involve adapting the admissible regions approach to that of a satellite probabilistically estimating its state from a pulsar measurement
- A pulsar-based admissible region will provide a uniform PDF to initialize orbit determination for a cold-start navigation approach in cislunar space

ACKNOWLEDGEMENTS / REFERENCES

[1] Milani, A., Gronchi, G. F., Vitturi, M. D., & Knežević, Z. (2004). Orbit determination with very short arcs. I admissible regions. *Celestial Mechanics and Dynamical Astronomy*, *90*(1–2), 57–85. https://doi.org/10.1007/s10569-004-6593-5

[2] Wang Sang Koon et al. Dynamical Systems, The Three-Body Problem, and Space Mission Design. 2006

Implementing Machine Learning Techniques to Improve Aerocapture for Orbit Entry

Dominic Rudakevych*, ***, Aaron Buysse**, Dr. Stephen Becker***

Draper Scholar*, Draper**, CU Boulder***

ABSTRACT: Aerocapture is a theoretical orbital transfer maneuver which promises to provide mass savings over current propulsion based orbit insertion techniques. To make aerocapture more reliable, this research looks to leverage Machine Learning methods to improve current environmental models for Uranus. A sensitivity analysis of parameters in the current Spherical Harmonics gravity model suggests guidance for aerocapture is robust to perturbations of these parameters. This result indicates Machine Learning methods may have more impact on aerocapture performance by improving other environmental models of Uranus, such as atmospheric models.

INTRODUCTION

- NASA has highlighted the Uranus Orbiter and Probe (UOP) flagship mission the highest priority for 2023-2032. One theoretical method for orbit insertion at Uranus is aerocapture. Through aerocapture, a satellite dips into a planet's atmosphere, creating drag and decreasing velocity. Aerocapture would more efficiently let satellites reach orbital velocity by using drag to dissipate energy instead of carrying propellent and firing thrusters. Aerocapture is currently not being used due to thin margins of error and necessary in-situ corrections. Advances in Machine Learning and Deep Learning (ML/DL) techniques offer improvements to gravity and atmosphere modeling necessary for aerocapture effectiveness.

METHODS

- Multiple gravity and atmosphere ML/DL models will be examined, such as Long Short Term Memory (LSTM) and Physics Informed Neural Networks (PINN)
- Monte Carlo Simulations are done on Draper's Uranus Simulation to observe affects on aerocapture performance

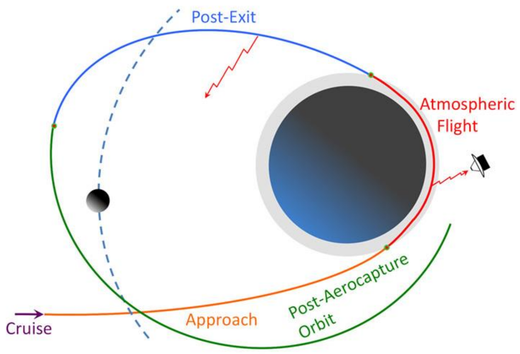

Figure 1: Aerocapture Schematic[3]

PRELIMINARY RESULTS

- NASA has provided physical parameters for celestial bodies with confident intervals. Using these values, current results focus on motivating whether improving gravity modeling is productive for aerocapture success. A sensitivity analysis on parameters used in the current Spherical Harmonics gravity model showed minimal variation in aerocapture metrics when perturbing parameters of interest. Perturbations were applied to the gravitational parameter *Mu*, and these perturbed values were compared to multiple aerocapture performance metrics (n = 50), as shown in figure 2.

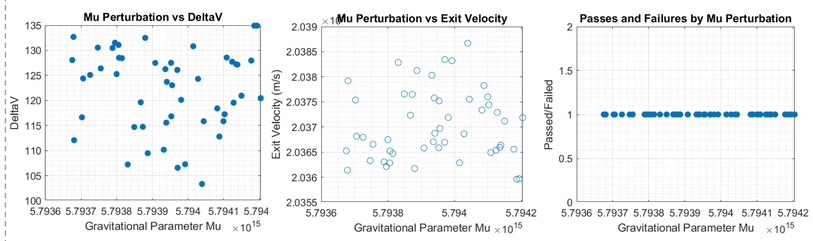

Figure 2: Aerocapture Metrics vs. *Mu* Perturbations

- Another parameter, *J2,* was perturbed and has similar effects on aerocapture metrics as *Mu*. When updating guidance with the perturbed values of *J2,* only minor improvement in aerocapture performance was observed.

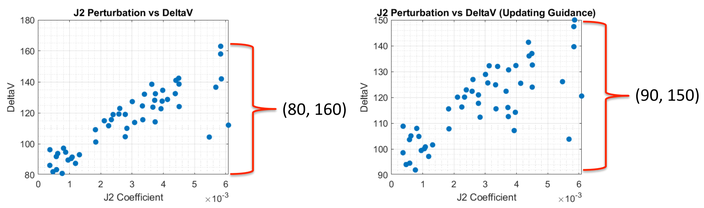

Figure 3: *J2* guidance change

DISCUSSION

- Sensitivity analysis results suggest guidance is robust to parameters in the Spherical Harmonics gravity model currently being implemented.

CONCLUSIONS

- Guidance is robust to uncertainties in the parameters used for Spherical Harmonic gravity modeling
- ML/DL techniques may have more impact on aerocapture performance by improving modeling other environment systems of Uranus (atmosphere)

ACKNOWLEDGEMENTS / REFERENCES

1. California Institute of Technology, "Planetary Physical Parameters." NASA Jet Propulsion Laboratory, Solar System Dynamics.
2. Martin, J., Schaub, H. "Physics-informed neural networks for gravity field modeling of the Earth and Moon." Celest Mech Dyn Astr 134, 13 (2022).
3. Spilker, T., et al., "Qualitative Assessment of Aerocapture and Applications to Future Missions." American Institute of Aeronautics and Astronautics, 2018.

User Location Verification in Non-Terrestrial Cellular Networks

Nathan Schatz[1], Moe Win[2], Michael Ricard[3], and Tyler Klein[3]

[1]Draper Scholars Program [2]Wireless Information and Network Sciences Laboratory, MIT [3]Draper Laboratory

ABSTRACT: Next-generation cellular networks will soon include direct links between smartphones and low earth orbit (LEO) satellites in order to provide seamless global coverage. This requires accurate knowledge of the user's location for satellite beam assignment, Doppler shift correction, core network assignment, lawful intercept procedures, public safety, and other applications. Current implementations of non-terrestrial networks (NTN) rely on users computing and reporting their own locations via GNSS, presenting a security flaw that can be exploited by malicious users in order to tamper with the network. This research investigates a method for LEO satellite networks to independently verify reported locations and detect users who are attempting to illegally spoof their locations.

INTRODUCTION

- Terrestrial location verification is typically accomplished through cell-id (CID) verification, which leverages the small coverage area of each connected cell tower or base station
- In a global NTN scenario, each LEO satellite would serve many users across a large area, including across national borders
- The network must independently verify the user's location using radio-dependent methods such as multiple round trip timing measurements (multi-RTT), or angle of arrival estimation (AoA)
- September 2023: AST SpaceMobile successfully performed a 5G call using direct satellite-to-smartphone links between Hawaii and Spain (in collaboration with AT&T, Vodaphone, and Nokia)

METHODS

- Precisely describe the geometric model (satellite orbits, user position, Earth's surface) and measurement model (multi-RTT, AoA azimuth and elevation) mathematically
- Derive an accurate probabilistic model for real errors (altitude, RTT error, AoA estimation granularity, satellite location/orientation)
- Formulate a hypothesis testing problem that reliably detects malicious users
- Implement this decision rule in simulation software in order to verify its accuracy
- Compare the performance of this method with requirements for precision, error probability, and computing resources
- Extend the scenario to find the performance limits of accurate detection of malicious users (high altitude, high speed, etc.)

RESULTS

- Geometric model

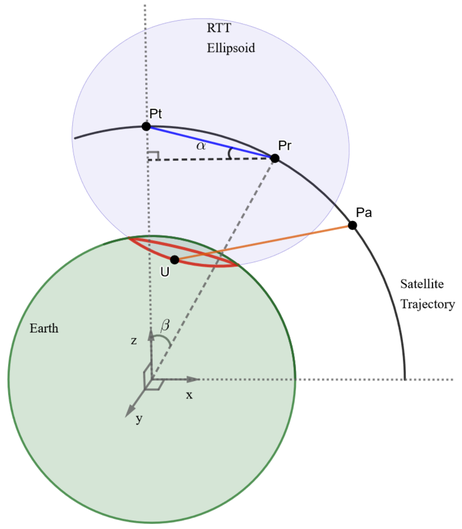

- Location estimation model (deterministic)

$$\arg\min_{\mathbf{p}} \quad d_1(\mathbf{p})^2 + d_2(\mathbf{p})^2 + d_3(\mathbf{p})^2$$

$$d_1(\mathbf{p}) = ||\mathbf{p}|| - R_e$$

$$d_2(\mathbf{p}) = ||(\mathbf{p} - \mathbf{p_a}) \times \hat{\mathbf{d}}||$$

$$d_3(\mathbf{p}) = \frac{||\mathbf{p} - \mathbf{p_r}|| + ||\mathbf{p} - \mathbf{p_t}|| - ct_{RTT}}{2}$$

- Location estimation simulation in a deterministic (error-free) scenario

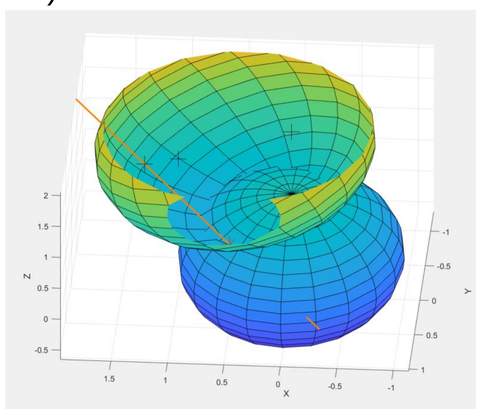

- This semester/summer: adding probabilistic elements and implementing the hypothesis testing scheme

DISCUSSION

- No statistical results have been evaluated yet (first year of research)
- The expected contribution of this work is the development, simulation, and performance evaluation of a LEO-based NTN location verification system that enables a satellite network to detect malicious users who report false locations
- This work will not attempt to derive the fundamental limits of spoofing capabilities or malicious user detection, however it will provide a realistic performance evaluation of a reliable algorithm that protects LEO satellite networks from malicious users

CONCLUSIONS

- Non-terrestrial networks provide opportunities for significant improvements in 5G/6G cellular
- The NTN scenario unveils new challenges that must be solved for secure and reliable operation
- Relying on a user's reported position presents inherent security flaws
- A reliable procedure is required to effectively detect malicious users attempting to tamper with the network by independently verifying reported location data

ACKNOWLEDGEMENTS

Special acknowledgement for the support and advice of Girim Kwon, Seungnyun Kim, Bernardo Tedeschini, and James Morrison

Hypersonic Cavity Flow to Improve Optical Quality

Matthew Schofield[1], Arthur Huang[2], and Wesley Harris[3]

[1]Massachusetts Institute of Technology and Draper Scholar, [2]The Charles Stark Draper Laboratory Inc, [3]Massachusetts Institute of Technology

ABSTRACT: Extreme surface temperatures on hypersonic vehicles induce significant heating rates into glass windows located on the surface which cause deformation and optical degradation. Recessing the window into the surface produces a cavity geometry that reduces this heating. Contrasting this reduction with the aero-optical distortions induced by the complex flow these geometries create, I find a length-to-depth ratio that optimizes select measures of optical quality.

INTRODUCTION

- Window deformation caused by thermal gradients degrade optical quality. These gradients, in addition to general high temperatures, produce a poor optical environment.

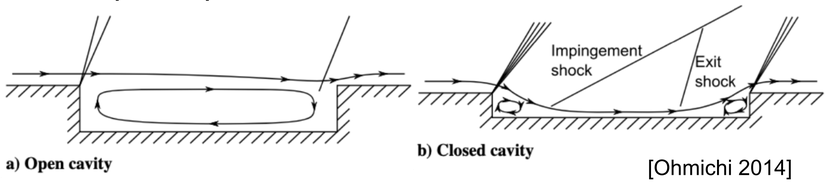

[Ohmichi 2014]

- Cavity recession of the window can reduce window temperatures and, consequently, may decrease window distortion and increase optical quality; however, this complicates the flow and may cause significant aero-optical distortion.
- Two different cavity geometries are simulated and their optical effects are analyzed.

METHODS

- US3D, an unstructured, implicit, finite-volume solver, simulates each flow geometry for 60 seconds, the three flow geometries being L/D = 2, L/D = 16, and the flat plate case.
- Conjugate heat transfer allows for wall and window temperatures to update with time.
- The vehicle solid is made out of Aluminum 6061, with the window made of sapphire (Al_2O_3) glass.
- ANSYS Mechanical simulates window deformation.

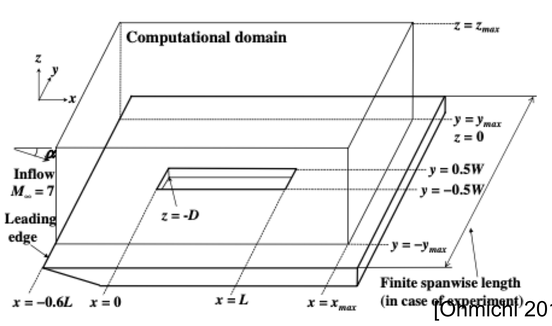

[Ohmichi 2014]

RESULTS

- Deformation for L/D = 2:

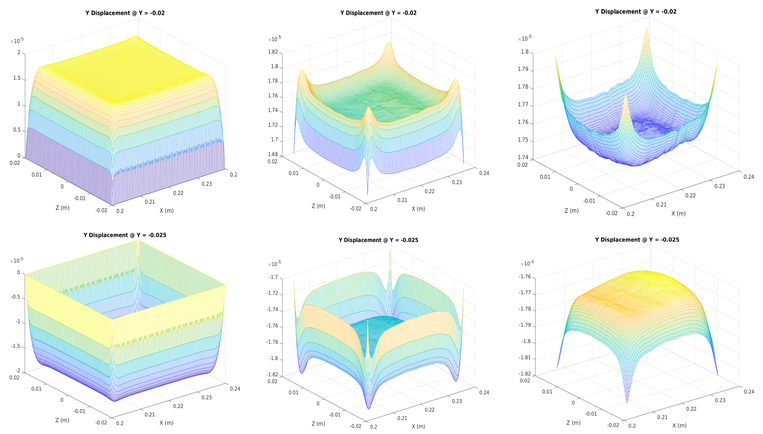

- Optical Quality Analysis:

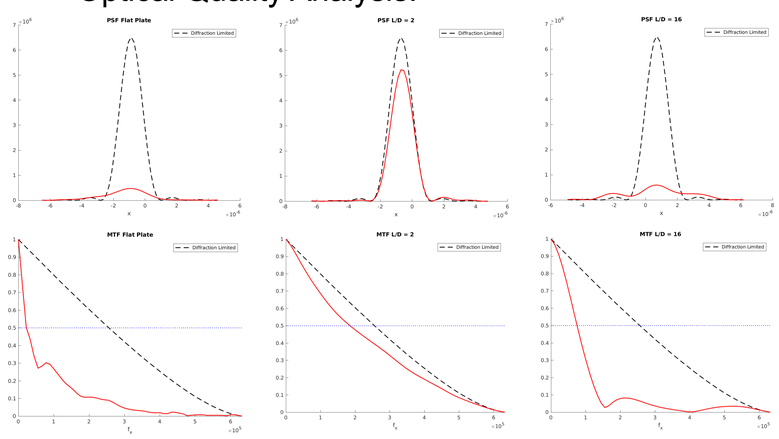

- The Strehl ratio is a measure of intensity, boresight error is a measure of alignment error, and MTF50-based detail recovery is a measure of contrast.

Al-6061	Flat Plate	L/D = 2	L/D = 16
Strehl Ratio	0.0731	0.8023	0.0912
Boresight Error	(-73.85, -8.79)	(-1.76, -7.03)	(10.55, 7.03)
Detail Recovery	30.01 μm	5.30 μm	12.86 μm

DISCUSSION

- The flat plate case shows significant optical degradation for all measurements. While the L/D = 16 case offers a decrease in boresight error, it fails to improve Strehl ratio and detail recovery.
- Following my initial hypothesis, the L/D = 2 case produces the best optical quality. Importantly, the Strehl ratio is greater than 0.8, which meets the Maréchal criterion.
- While the cavity geometry greatly reduces the window deformation, the full effect of the aero-optics, which is thought to be less significant, has yet to be fully investigated.

CONCLUSIONS

- Cavity recession does improve optical quality in high-temperature environments, but only for cavities that fall into the open cavity regime.
- The time scale that governs thermal development in the window is many orders of magnitude larger than that of the flow within the cavity. This causes an equivalent disparity in time scales present in the optical environment. Both must be simulated to produce an accurate description of the optical quality.

ACKNOWLEDGEMENTS / REFERENCES

Acknowledgements:

- Jeff DeFelice for answering all of my optics questions and providing me with plenty of resources to base my results off of.
- John Reinert for helping me install and configure his US3D Conjugate Heat Transfer plugin.

References:

- Ohmichi, Y., & Suzuki, K. (2014). Flow structures and heating augmentation around finite-width cavity in hypersonic flow. AIAA Journal, 52(8), 1624–1631. https://doi.org/10.2514/1.j052647

Towards Ephemeris Free Skymark through Dynamic Simultaneous Localization and Mapping

Kian Shakerin[1*], Andrew Spielvogel[2#], and Jay McMahon[1+]

[1]University of Colorado, Boulder, [2]The Charles Stark Draper Laboratory, Inc.,
*Draper Scholar, #Senior Navigation Algorithms Engineer, +Associate Professor

ABSTRACT: The ability to autonomously navigate in communication restricted or GPS-denied environments is critical to the success of a wide variety of modern missions, ranging from terrestrial to deep space. This research seeks to develop methods of navigation for Earth-based observers using optical-only measurements of artificial satellites without the use of known satellite ephemeris. This work aims to leverage and build on Simultaneous Localization and Mapping (SLAM) techniques, which have shown significant success in both robotics and space-based applications, by integrating estimation of dynamic landmarks. Initial analysis with an EKF-based SLAM algorithm show observer and landmark position errors of <1km.

INTRODUCTION and MOTIVATION

- The Skymark system relies on highly accurate and up-to-date ephemeris for robust performance.
- There is a need for optical-only navigation tools that can be used when satellite ephemeris are stale or unavailable.
- Simultaneous Localization and Mapping (SLAM) provides a framework for navigation in unseen environments with little a priori information.
- Traditionally, SLAM involves mapping of fixed landmarks, but satellites are moving targets
- This research seeks to build on recent work in SLAM with dynamic landmarks to develop new algorithms and insights.[1]

GENERAL PROBLEM SETUP

This graphic describes an observer estimating the states of two satellites whilst also estimating its own state from optical measurements using a SLAM framework.

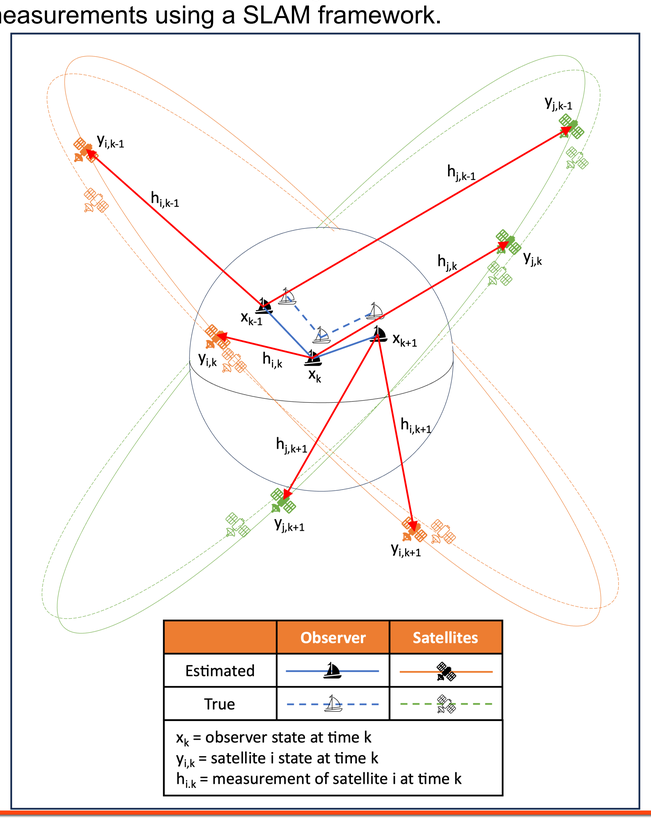

METHODS

For the results shown below the following were used:

- Extended Kalman Filter (EKF) SLAM
- Stationary, Earth-fixed observer
- 8 stationary, inertially-fixed landmarks in Low Earth Orbit (LEO)
- Optical and range measurements
  - Camera IFOV: 2.79×10^{-4} rad/pixel
- Complete landmark initialization
- Perfect data association

RESULTS

Observer state errors with 3-sigma bounds shows decent filter performance over three days of measurements.

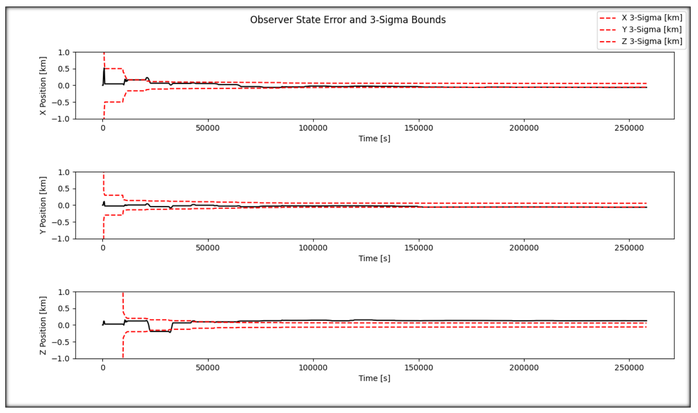

The magnitude of the landmark state errors decrease as more measurements are processed.

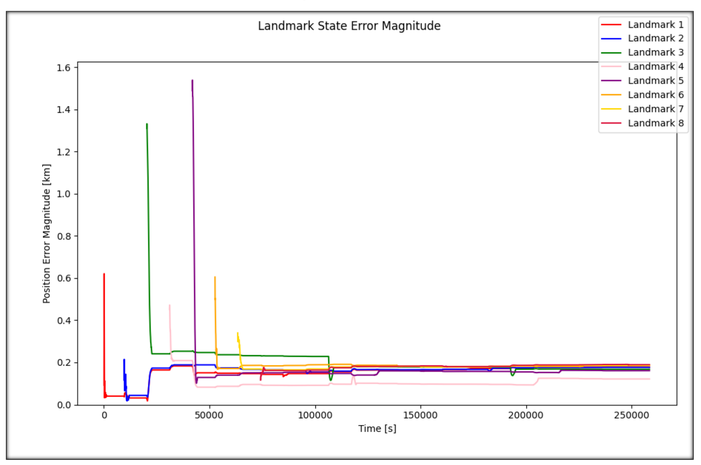

ONGOING WORK

- Development of a robust code base
- Development of an example demo with EKF-SLAM to better understand the problem space and gain experience with SLAM algorithms
- Implementation of optical-only measurements and inverse depth parameterization
- Exploration of state-of-the-art SLAM theory through literature review
- Ingestion and propagation of publicly available Two-Line Elements (TLEs)

FUTURE RESEARCH

- Integration of data association into the simulation pipeline to better mimic real-world scenarios.
- Implementation of graph-based SLAM algorithms.
  - Represents state of-the-art.
- Research into estimating dynamic landmarks.
  - Non-traditional and area of active work.
- Research into alternative dynamics representations of satellite orbits.
  - Goal of reducing the largest sources of uncertainty from in-track motion along the orbit.
  - Orbital element space may allow for fixed landmarks and map.
- Research into application of Lie theory in SLAM
- Characterization of system performance.
  - Are the solutions accurate enough for navigation purposes?

REFERENCES

1. Macario Barros, A., Michel, M., Moline, Y., Corre, G., & Carrel, F. (2022). A Comprehensive Survey of Visual SLAM Algorithms. Robotics 2022, Vol. 11, Page 24, 11(1), 24. https://doi.org/10.3390/ROBOTICS11010024
2. Givens, M. W., & McMahon, J. W. (2023). Square-Root Extended Information Filter for Visual-Inertial Odometry for Planetary Landing. Journal of Guidance, Control, and Dynamics, 46(2), 231–245. https://doi.org/10.2514/1.G006849/ASSET/IMAGES/LARGE/FIGURE18.JPEG

Multimodal Physiological Estimates of Situation Awareness

Kieran Smith[1,2], Torin Clark[1], Tristan Endsley[3]

[1]University of Colorado – Boulder, Aerospace Engineering Sciences, [2]Draper Scholar, The Charles Stark Draper Laboratory, Inc., [3]The Charles Stark Draper Laboratory, Inc.

ABSTRACT: Physiological estimates of situation awareness (SA) could improve safety in human spaceflight operations by enabling real-time, SA-based adaptation from autonomous systems. Here, we show that preliminary multimodal physiological models capture substantial (up to 76%) variance in objective measures of human operator SA; however, model performance decreases for higher-order cognitive processes. Future work aims to employ more rigorous cross-validation performance to evaluate model generalizability, to collect additional datapoints, and to incorporate more advanced physiological features.

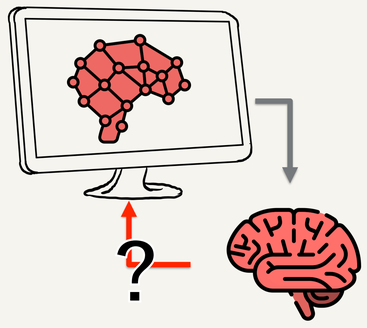

INTRODUCTION

Situation Awareness (SA) is an astronaut's ability to:

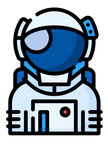

1. **perceive** mission-critical information[1]
2. **comprehend** its meaning
3. **project** its current state into the future

SA is critical for safety[2] but is degraded by stressors of spaceflight and modern operational complexity:

Brain Fog

Information density[3-4]

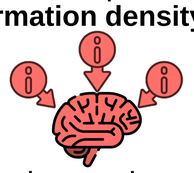

Automation[5-6]

Physiological signals have shown sensitivity to SA[7], but a multi-modal sensor suite has not been employed to estimate objective, 3-level measurements of SA across different users. Such estimates could **enable systems that understand and adapt to an astronaut's SA with nuance and overcome these stressor-induced SA degradations[8-10].**

METHODS

8 Participants (3F), aged 21-27, operated a flight simulator while wearing a suite of physiological sensors.

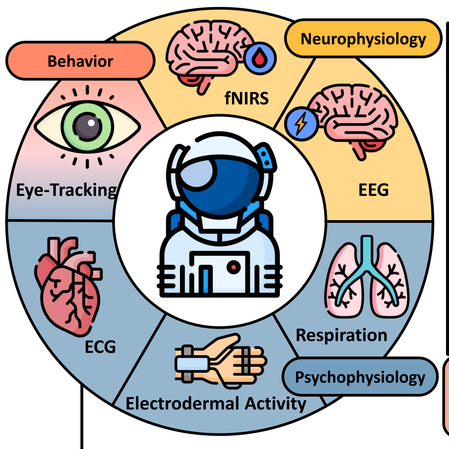

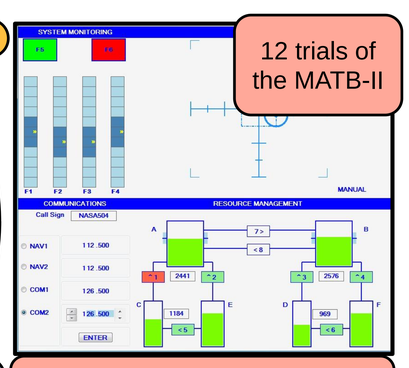

12 trials of the MATB-II

18-Question objective goal-directed SA Assessments[1]

All Physiological Features → SA Scores → Stabilized Least Absolute Squares Shrinkage Operator[12] → Stable Feature Sets → SA Scores → Ordinary Least Squares Regression → **Final Model Fit**

Test Split

RESULTS

To avoid overfitting†, models must have: 1) 5x more observations than features **(N_F)** and 2) similar‡ performance on training data **(R^2)** & held-out participants **(Q^2_P)** and trials **(Q^2_T)**

Level 1 SA: Perception

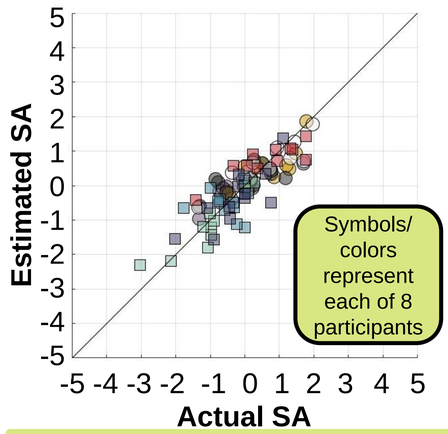

Symbols/ colors represent each of 8 participants

Model uses features from:
- Eye Tracking
- Electrodermal Activity
- fNIRS, and
- EEG

R^2	0.70
N_F	16
Q^2_P	0.52
Q^2_T	0.56

3 psycophys.

13 neurophys. features

Level 2 SA: Comprehension

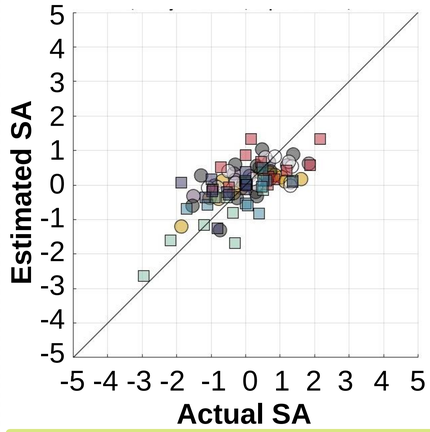

Model uses features from fNIRS only

R^2	0.42
N_F	7
Q^2_P	0.31
Q^2_T	0.32

7 neurophys. features

‡All Q^2 values are within 0.2 of R^2 values.

Total SA: Perception, Comprehension, & Projection

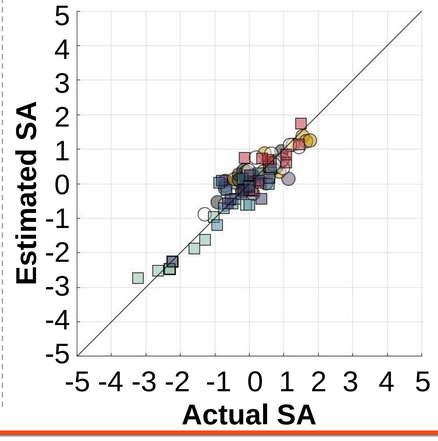

Model uses features from:
- Electrodermal Activity
- fNIRS, and
- EEG

R^2	0.85
N_F	16
Q^2_P	0.76
Q^2_T	0.78

3 psycophys.

13 neurophys. features

†Omitted Level 3 models did not meet above criteria.

DISCUSSION

Physiological models capture up to 76% of variance in SA scores (85% in training data). However, model performance varies across levels of SA, and Level 3 (comprehension) models did not meet generalizability criteria. Promising results support additional data collection to investigate potential improvements in model generalizability. Some work suggests that high cross-validation performance in low signal-to-noise ratio domains (e.g., cognitive state estimation) is indicative of overfitting[11], and caution should be taken in interpretation.

Selected features differ between models, and psychophysiological signals only appear in models predicting Level 1 SA. Higher cognitive processes (e.g., Level 3 SA) may require more complex features to capture changes.

CONCLUSIONS

Differences between the three models aligns with the notion that levels of SA capture unique cognitive processes and losses in each level may require unique responses. By presenting comprehensive estimates of SA, this work moves towards enabling such nuanced responses.

Future work will cross-validate feature selection steps to confirm model performance on entirely unseen data. Additionally, future models will incorporate more complex features such as gaze recurrence, functional connectivity, and multimodal responses like fixation-related potentials that could capture higher-order cognitive processes.

REFERENCES

[1] Endsley, M. R. (1988) *Proc. IEEE Natl Aero Elect Conf*, 3, 789-795. [2] Jones, D. G. and Endsley, M. R., (1996) *Aviat. Space Env. Med.*, 67, 507-512. [3] Dahm, W. (2010), *Air University Press*. [4] Endsley, M. R. (2012), *CRC Press*. [5] Carmody, M. A. and Gluckman, J. P. (1993), *AFAIC*, 13–18. [6] Wickens, C. D. (2008), *Hum Factors*, 50(3), 397-403 [7] Zhang, T. *et al.* (2020), *Hum Factors*, 65(5),737-758 [8] Feigh, K. M., *et al.* (2012), *Hum Factors*, 54(6), 1008–1024 [9] Galster, S. M. and Johnson, E. M. (2013), *DTIC*. [10] Committee on Human-System Integration Research Topics for the 711th Human Performance Wing of the Air Force Research Laboratory, *et al.* (2021) *National Academies Press*, 26355 [11] D'Mello, S. K. and Booth, B. M. (2023), *IEEE Int Sys*, 38(1), 76–84. [12] Buchner, S. (2022), University of Colorado Boulder.

Density Estimation for 6-DOF Uranus Aerocapture Simulation

Kyle Sonandres[1], Thomas Palazzo[2], and Jonathan How[3]

[1]Draper Scholar, MIT, [2]Draper, [3]Professor of Aeronautics and Astronautics, MIT

ABSTRACT:

NASA's 2023-2032 Planetary Science Decadal Survey has recommended the Uranus Orbiter and Probe (UOP) as the highest priority flagship mission. Aerocapture, a maneuver that uses atmospheric drag to insert a spacecraft into orbit via a single pass through the atmosphere, has the potential to significantly reduce flight time, increase delivered mass, and reduce costs in comparison to traditional chemical capture and aerobraking. Atmospheric uncertainty is the primary contributor to aerocapture error, and therefore aerocapture guidance and control systems can benefit greatly from real time estimation and prediction of atmospheric properties.

INTRODUCTION

- Goal: during each guidance cycle, process incoming navigation information to adaptively improve guidance's knowledge of the atmosphere in real time
- Accurate downstream density profile prediction greatly improves the trajectory prediction phase of predictor-corrector guidance algorithms, like FNPAG [1]
- We compare the performance of three onboard density estimation techniques applied to 6-DOF UOP aerocapture simulation (best fit polynomial, density scale factor, density interpolator) and identify future areas of improvement aimed at advancing the state-of-the-art

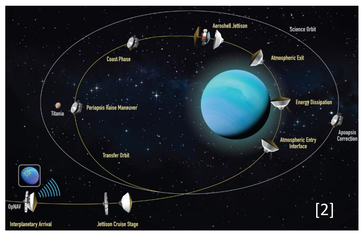

[2]

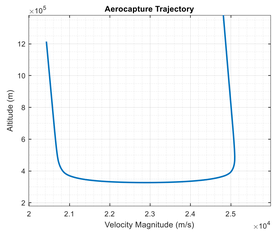

EXPERIMENTAL SETUP

- Aerocapture trajectories are simulated using a 6 degree of freedom simulation written in MATLAB/ Simulink
- A Monte Carlo (MC) set of 500 simulations was ran for each density estimation technique. Nominal entry conditions and dispersions are given below

Parameter	Nominal Value	Dispersion (3 sigma)
Atmosphere	UranusGRAM	N/A
Altitude	1000 km	N/A
Velocity	24.9 km/s	N/A
Entry Flight Path Angle	-11.1 deg	0.15 deg
Mass	m_0	10%
C_L	$C_{L,0}$	20%
C_D	$C_{D,0}$	20%
Target Apoapsis	550000 km	N/A
Target Periapsis	4000 km	N/A

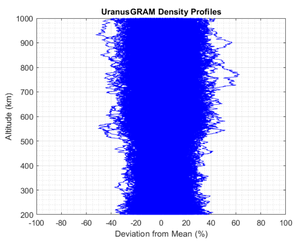

- Estimation performance is quantified and compared in three ways
  - ΔV stats (mean, 3-sig)
  - Apoapsis Targeting Error
  - Forward Looking Prediction Error (FL-RMSE)

$$e_i = \begin{bmatrix} \rho_{i+1}^{est} - \rho_{i+1}^{truth} \\ \rho_{i+2}^{est} - \rho_{i+2}^{truth} \\ \dots \end{bmatrix} \qquad RMSE_i = \frac{1}{N}\sqrt{e_i^T e_i}$$

METHODS

Estimation Techniques

- Best Fit Polynomial

1) Interpolate from stored profile

$$\ln \rho = \frac{c_1 + c_3 h + c_5 h^2 + c_7 h^3 + c_9 h^4}{1 + c_2 h + c_4 h^2 + c_6 h^3 + c_8 h^4}$$

- Density Scale Factor (DSF)

1) Compute sensed density $\rho_{est} = \frac{2m\|a_{sens}\|}{\|v^2\| C_D A_{ref}}$

2) Ratio of sensed to expected $K_{est} = \frac{\rho_{est}}{\rho_{nom}}$, $\rho_{nom} =$ stored profile

3) Apply first order memory fading filter $K_p^i = (1 - K_{gain}) K_{est} + K_{gain} K_p^{i-1}$

4) Constant Bias for predictor cycle $\rho^k = \rho_{nom} K_p^i$

- Density Interpolator (DI)

1) Do steps 1-3 of density scale factor, store density history $\rho_{est} = \frac{2m\|a_{sens}\|}{\|v^2\| C_D A_{ref}}$

2) Determine prediction method

$if\ h^k(predictor\ alt) \leq h^i(current\ alt) \rightarrow DSF\ (4),$
$if\ h^k > h^i \rightarrow interpolate\ from\ history$

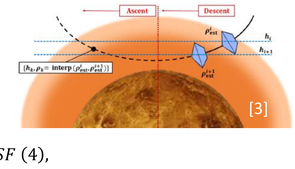

[3]

- LSTM-based Deep Learning Network (In Development)

$$[\boldsymbol{x_0}, \boldsymbol{x_1}, \dots, \boldsymbol{x_i}], \boldsymbol{x_i} = (r_i, \theta_i, \varphi_i, V_i, \gamma_i, \psi_i, a_{x,i}, a_{y,i}, a_{z,i})$$

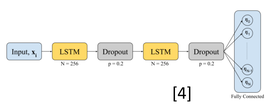

[4]

$$[\rho_{300km}, \rho_{305km}, \dots, \rho_{600km}]$$

RESULTS

Figure 1: ΔV Histogram and Table

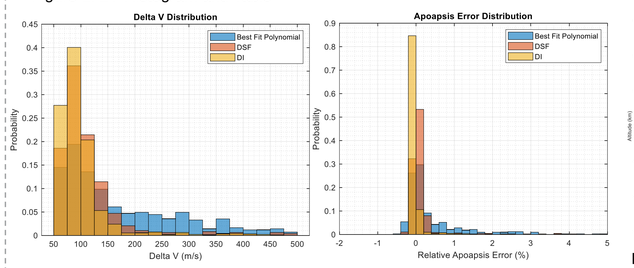

Technique	ΔV Mean	ΔV 3-sig
Best Fit Polynomial	171.42	317.97
DSF	113.65	190.41
DI	99.79	148.68

Technique	Error Mean (%)	Error 3-sig (%)
Best Fit Polynomial	1.08	15.59
DSF	0.40	9.02
DI	0.06	2.64

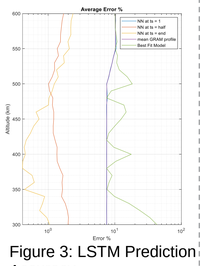

Figure 3: LSTM Prediction Accuracy

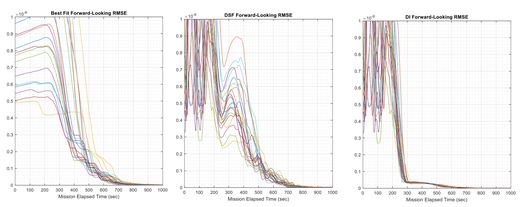

Figure 2: FL-RMSE

Technique	FL-RMSE at Periapsis +- 50 sec
Best Fit Polynomial	8.45e-07
DSF	5.11e-07
DI	1.59e-07

DISCUSSION

- The best fit baseline is unable to adapt to day-of-flight variation
- Compared to the best fit model, the DSF yields 33.7/ 40.1% mean/ 3-sig ΔV improvement, a 63/ 42.1% mean/ 3-sig targeting accuracy improvement (fig 1), and a 39% FL-RMSE improvement near periapsis (fig 2)
- DSF predicts downstream density by scaling the stored density profile by a constant factor along the entire prediction cycle, leading to oscillatory prediction accuracy when time-of-flight variations are not constant
- Compared to DSF, the DI [3] yields 12.2/ 21.9% mean/ 3-sig ΔV improvement, an 85/ 70.7% mean/ 3-sig targeting accuracy improvement (fig 1), and a 68.8% FL-RMSE improvement near periapsis (fig 2)
- The DI is not constant bias during the interpolation phase and reduces reliance on a stored profile, but assumes density is a function of altitude only. An atmosphere model with dependence on latitude and longitude would likely lead to performance degradation
- The LSTM approach has not yet been tested in MC simulation but has been shown to predict and reconstruct the true density to within 0.4-2% relative error by periapsis (fig 3). Previous work shows similar performance and demonstrates targeting accuracy benefits for Mars EDL [4].

CONCLUSIONS

- Onboard density estimation greatly improves UOP aerocapture performance
- Future work is aimed at implementing and testing the first application of deep learning for density estimation during aerocapture
- Long term goals are aimed at advancing the state of the art in aerocapture density estimation by implementing cutting edge deep learning architectures, such as transformer-based networks

ACKNOWLEDGEMENTS / REFERENCES

[1] Lu, P., Cerimele, C. J., Tigges, M. A., and Matz, D. A., "Optimal Aerocapture Guidance," Journal of Guidance, Control, and Dynamics, Vol. 38, No. 4, 2015, p. 553–565. https://doi.org/10.2514/1.g000713, URL http://dx.doi.org/10.2514/1.G000713.
[2] Matz, D., Johnson, B., Geiser, J., Sandoval, S., Deshmukh, R., Lugo, R., Dutta, S., Chadalavada, P., "Analysis of a Bank Angle Control Guidance for Aerocapture at Uranus," AIAA Paper 2024-0717, 2024. https://doi.org/10.2514/1.A35197.
[3] Roelke, E., McMahon, J., Braun, R., and Hattis, P., "Atmospheric Density Estimation Techniques for Aerocapture, " Journal of Spacecraft and Rockets, Vol. 60, No. 3, 2023, pp.942-946. https://doi.org/10.2514/1.A35197.
[4] Rataczak, J., Amato, D., and McMahon, J., "Density Estimation for Entry Guidance Problems using Deep Learning," AIAA Paper 2024-0946, 2024. https://doi.org/10.2514/6.2024-0946.

Miniaturization of Microwave Imaging Systems for Breast Cancer Detection

Melania St.Cyr

Draper Scholar - Massachusetts Institute of Technology

ABSTRACT: Microwave imaging is a promising technology for early detection of breast cancer. It has many advantages over current imaging standards, and multiple research groups around the world have been focusing on bringing such systems to a clinical level. However, there is still a need for more portable microwave imaging systems to increase accessibility for patients. “Miniaturization of Microwave Imaging Systems for Breast Cancer Detection” presented by Melania St.Cyr, Ph.D. student at MIT and Draper Scholar, assesses current literature on microwave imaging, addresses portability and its challenges, and discusses early steps towards a new prototype system.

INTRODUCTION

Benefits	Ultrasound	Mammography	Magnetic Resonance Imaging	Microwave Imaging
No radiation risk	X		X	X
Painless	X		X	X
High resolution		X		X
Relatively low cost	X		X	X
Early detection	X		X	X

Microwave imaging has many potential benefits over traditional breast cancer imaging systems and has the potential to be **portable.**

METHODS

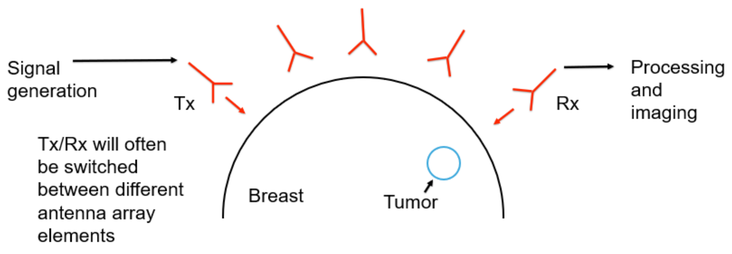

- Tumors can have higher permittivity than other parts of the breast
- Permittivity differences can be detected by transmitting and receiving microwave signals at multiple locations at the surface of the breast
- Collected data is sent to image processing

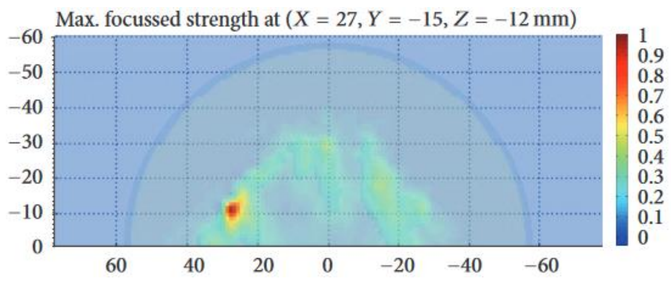

Imaging output example from Bristol University [3]

SYSTEM REVIEW

Comparisons of developed MWI systems are detailed below:

	DC [15]–[19]	MARIA® [20]–[26]	TSAR [27]–[30]	HU [33]	SUST [34]	MU [35], [36]	SU [37], [38]
							
Largest trial:	150	223	8 patients	5 patients	11 patients	13 volunteers	2 patients
Scan time:	5 min	10 s	30 min	14 min	4 min	5 min	3 min
Position:	prone	prone	prone	supine	prone	seated	prone
Coupling:	medium	shell	medium	shell	medium	shell	shell
Table:	✓	✓	✓	✗	✓	✗	✓
Array type:	synthetic	hardware	synthetic	synthetic	synthetic	stationary	hardware
Acquisition:	frequency	frequency	frequency	time	frequency	time	frequency
Antenna:	monopole	slot	vivaldi	planar slot	horn	microstrip	stacked patch
Multistatic:	✓	✓	✗	✓	✓	✓	✓
Artefact:	—	rotation	neighbour-based	averaging	adaptive filtering	differential	rotation
Imaging:	tomography	IDAS	DAS	DAS	DAS	DAS	DAS

Table from [1]

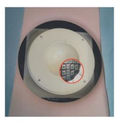

University of Bristol’s MARIA system has been producing clinical results since 2010 featuring a 60 element array with 10 second scan time.

[1]

Hiroshima University’s system utilizes integrated circuits to replace large electronics.

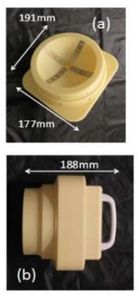

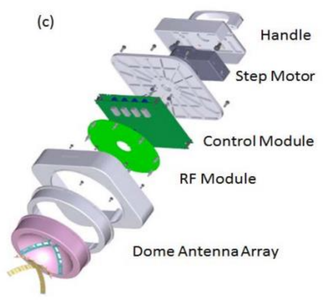

[4]

[1]

Dartmouth College’s microwave tomography based system was the first clinically tested MWI system.

McGill University has been working towards a wearable bra system and has replaced some electronics with integrated circuits.

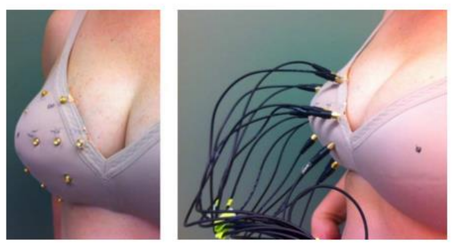

[5]

DISCUSSION

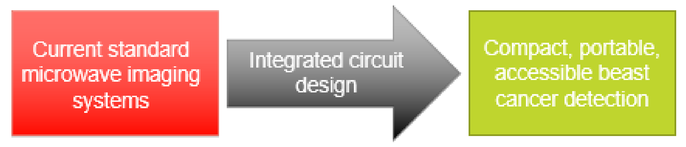

Understanding current systems while implementing new circuit designs can lead to portable breast cancer monitoring.

CONCLUSIONS

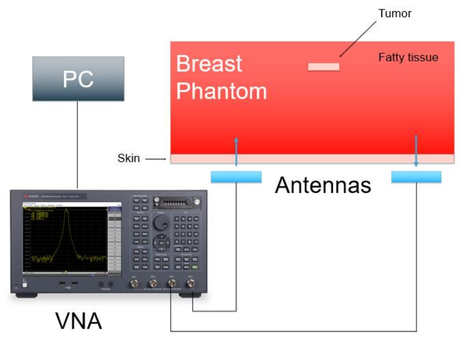

First steps towards a test system:

- Simplified breast model for testing
- Minimal number of antennas
- Standard electronics

A simplified breast phantom consists of a homogeneous fatty breast, skin layer, and tumor replica.

ACKNOWLEDGEMENTS / REFERENCES

Acknowledgements to my Draper advisor, Azin Zarrasvand, and my MIT research advisor, Professor Negar Reiskarimian, for their guidance throughout defining my research project.

[1] https://doi.org/10.1109/TBME.2018.2809541
[2] https://doi.org/10.3390/jimaging8050123
[3] https://doi.org/10.1155/2016/5054912
[4] https://doi.org/10.1038/s41598-017-16617-6
[5] https://doi.org/10.1109/TMI.2016.2518489

Predictive Transcriptional Analysis of Engineered Microbes in Austere Environments

Jessica Sun[1,2], Jai Padmakumar[1], Christopher Voigt[1], Else Vedula[3]

[1]Massachusetts Institute of Technology, [2]Draper Scholar, [3]Draper

ABSTRACT: Bacteria can be programmed to execute desired functions and respond to specific stimuli via genetic circuits, but it is difficult to deploy engineered cells in relevant environments. While genetic circuit design has been rapidly improving by expanding the signals that bacteria can detect, such as explosives or human DNA and by improving engineering strategies to construct more complex logic gates in bacteria, it is a challenge to deploy synthetic microbes in relevant environments, like the soil or human microbiome[1-4]. Engineered strains often break down outside of nutrient rich, controlled laboratory environments due to the resource burden placed on the cell by the synthetic circuit[5]. Here, we aim to measure the transcriptional activity of engineered microbes in various environments to inform a model to predict cellular behavior in new contexts and develop robust engineering strategies for prolonged persistence in relevant environments.

INTRODUCTION

- Synthetic genetic circuits allow bacteria to dynamically respond to external stimuli, but they place a resource burden on a bacterial cell.
- Circuit performance is dependent on the environment (liquid media, agar plate, soil, human gut tissue, etc.), which makes it difficult to apply synthetic biology in biotechnology applications.

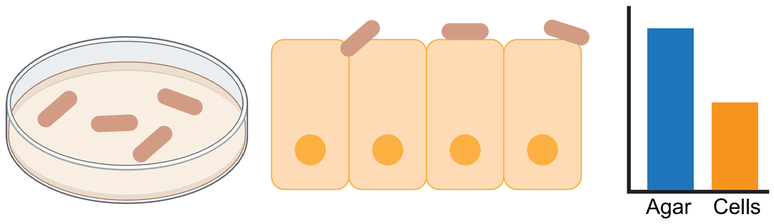

Hypothesis: By characterizing the transcriptional activity of cells across environments, we can develop a data-driven model to predict the performance of an engineered cell in a new environment.

TECHNICAL APPROACH

- Characterize the response of engineered cells in different perturbed environments
- Combine data into a model to predict how a cell will respond in a different environment
- Evaluate cells in new environmental context

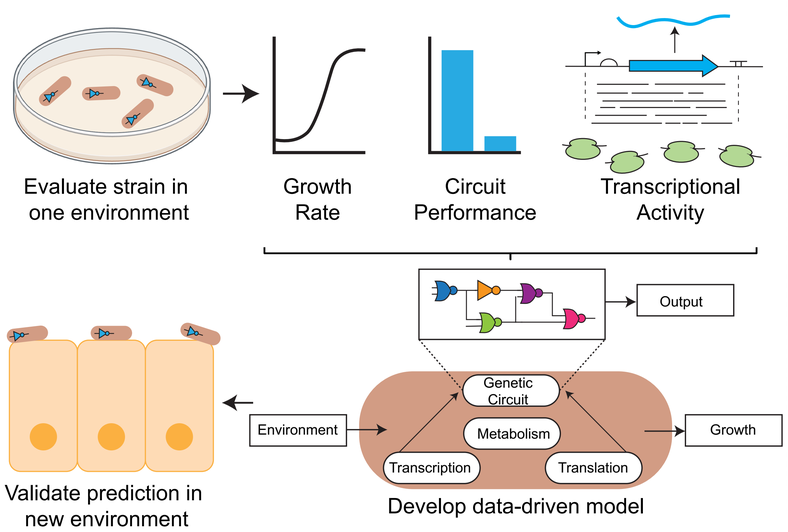

RESULTS

- Developed a library of 12 orthogonal phage repressor in *E. coli* MG1655, which can be used as NOT gates to build Boolean logic[6].

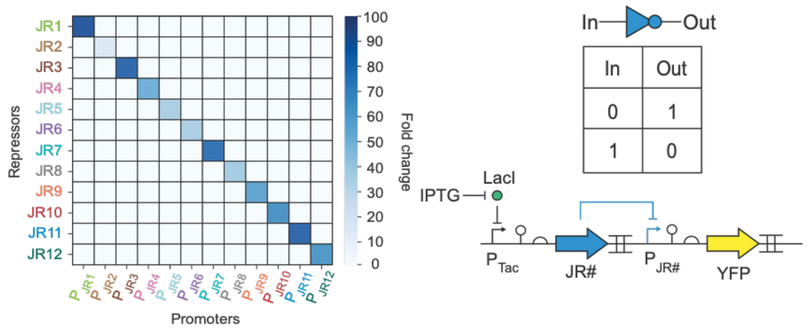

- Built genetic circuits of varying complexity which function as designed[6].

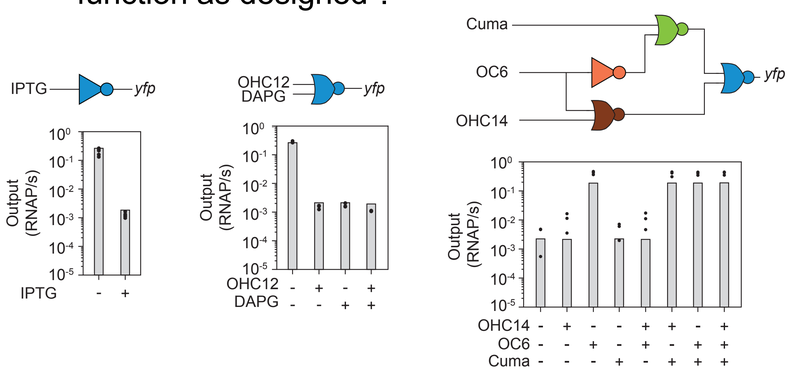

- Preliminary ribosome profiling and RNA-seq protocol development produces fragments of correct length.

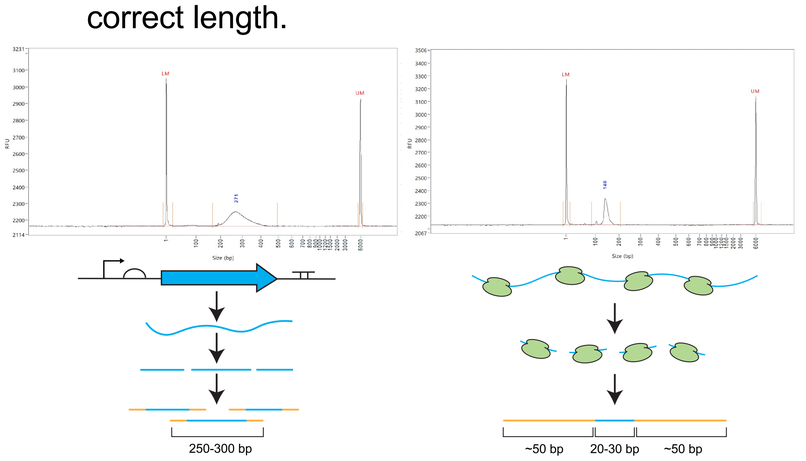

DISCUSSION

- With a set of orthogonal NOT logic gates, we can construct NOR gates. NOT/NOR gates are universal Boolean logic gates which allows for the construction of any desired genetic circuit.
- Previously constructed genetic circuits will be used to evaluate how genetic circuit size affects cellular response in different conditions.
- Optimization of RNA-seq and ribosome profiling protocols will be critical for quantifying and predicting transcription and translation across various environments.

NEXT STEPS

- Evaluate synthetic genetic circuits in different context and sample over time at different states to collect data to inform model of cellular behavior.

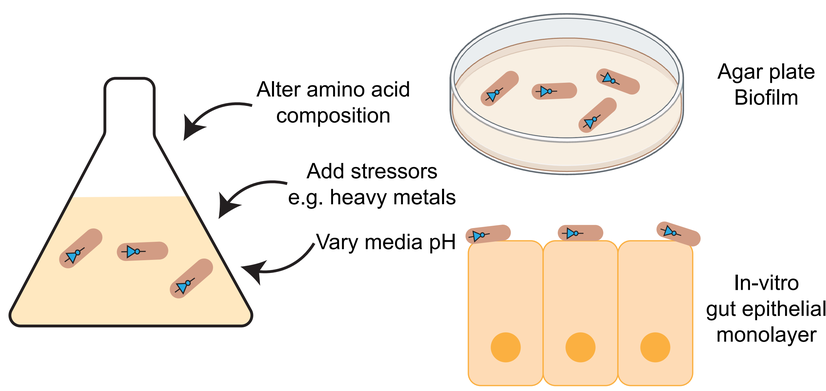

REFERENCES

1. Brophy, J.A., Voigt, C.A. *Nat Methods* **11**, 508-520 (2014).
2. Henshke, Y., Shemer, B. & Belkin, S. *Current Research in Biotechnology* **2**, 21-28 (2021).
3. Nou, X.A., Voigt, C.A. *Nat Chem Biol* **20**, 211–220 (2024)
4. Park, Y., *et al. Mol. Syst. Biol.* **16**, e9584 (2020).
5. Sleight, S.C., Bartley, B.A., Lieviant, J.A. *et al. J Biol Eng* **4**, 12 (2010).
6. Padmakumar, J. *et al. Submitted* (2024).

Machine learning analysis of high content image tissue structure and pathogenesis in airway culture system high priority pathogen infection studies

Edward Tang[1,2], Kevin Kit Parker[1], Jeffrey Borenstein[3]

[1]Havard University School of Engineering and Applied Sciences, [2]Draper Scholar, The Charles Stark Draper Laboratory, Inc., [3]The Charles Stark Draper Laboratory, Inc.

ABSTRACT: Respiratory viruses including influenza and COVID-19 pose a significant global health risk. A method of developing effective therapeutics is through modeling these diseases using human primary airway epithelial cells grown in the PREDICT96-ALI microchannel-based culture chambers with an air-liquid interface. The tissue structure and differentiation within these systems are dependent on media composition, which is difficult to optimize through time and resource-expensive experimentation. We plan to use machine learning to determine the effects of media factors on tissue quality and differentiation metrics within the PREDICT96-ALI system and increase tissue quality for study of physiological responses to respiratory virus infection.

INTRODUCTION

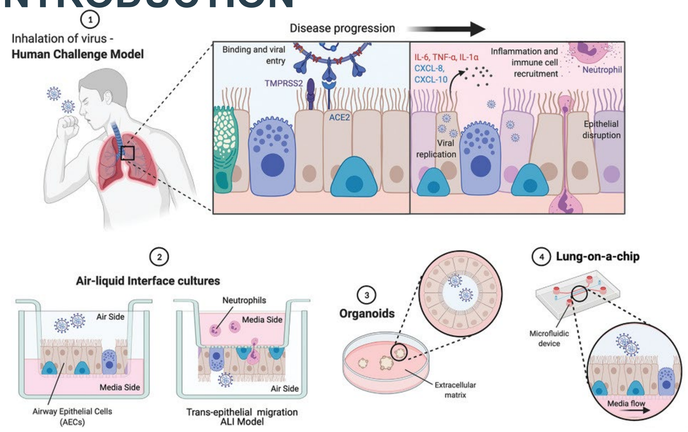

Woodall et al., *J. Physiol.*, 2021

- Respiratory viruses can be modeled through a variety of methods, including air-liquid interface (ALI) cultures
- These models inform therapeutic development

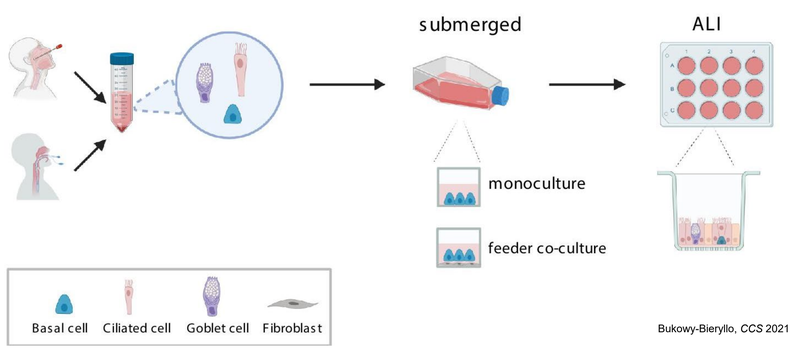

Bukowy-Bieryllo, *CCS* 2021

- Tissue differentiation and quality impacting model results depend on a variety of culture factors, including media composition

CONCEPTS

Predict96 ALI System

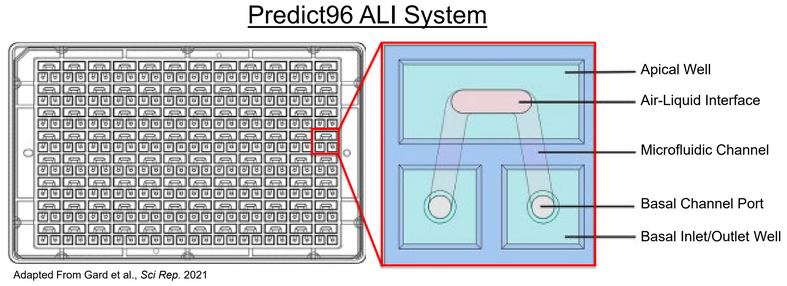

Adapted From Gard et al., *Sci Rep.* 2021

- The Predict96 ALI system models the effects of respiratory viruses on epithelial airway tissue
- Tissues in the Predict96 ALI imaged through high-content imaging, which maximizes data capture of cellular and chemical factors

PROJECT AIMS

- **Aim 1:** Identify cellular metrics that determine tissue and differentiation quality within Predict96 ALI high content images

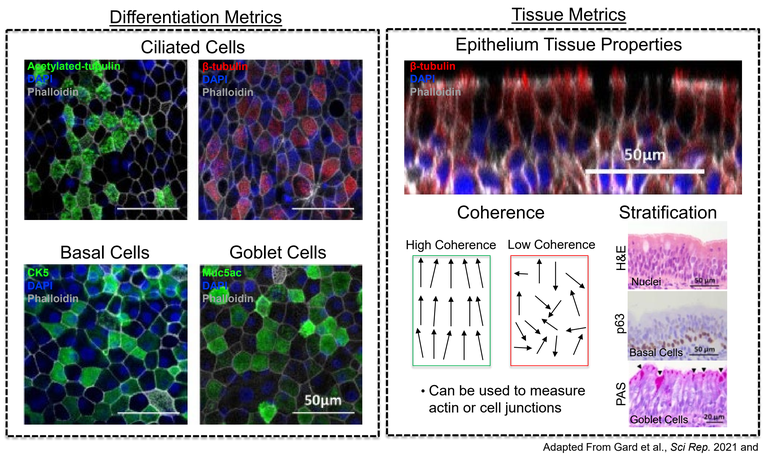

Adapted From Gard et al., *Sci Rep.* 2021 and

- **Aim 2:** Use computer vision to quantify cellular metrics between media conditions to develop machine learning dataset

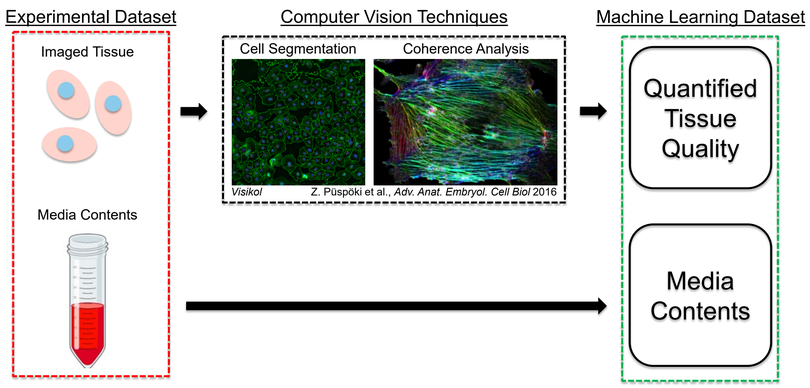

- **Aim 3:** Train a machine learning model to optimize media variables for tissue and differentiation quality

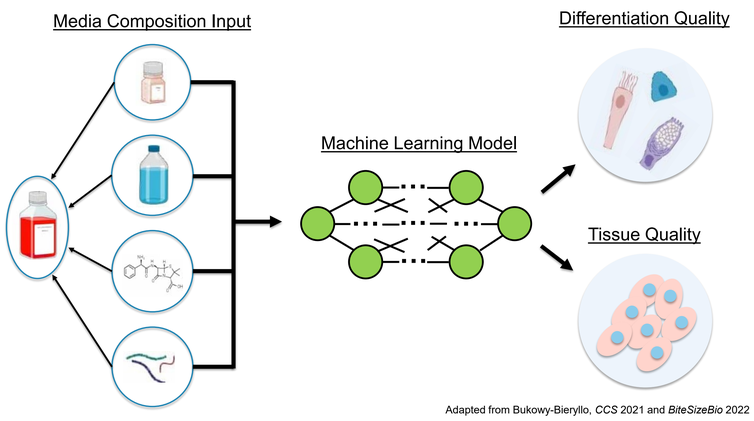

Adapted from Bukowy-Bieryllo, *CCS* 2021 and *BiteSizeBio* 2022

OUTCOME

ML-Informed Media Optimization Loop

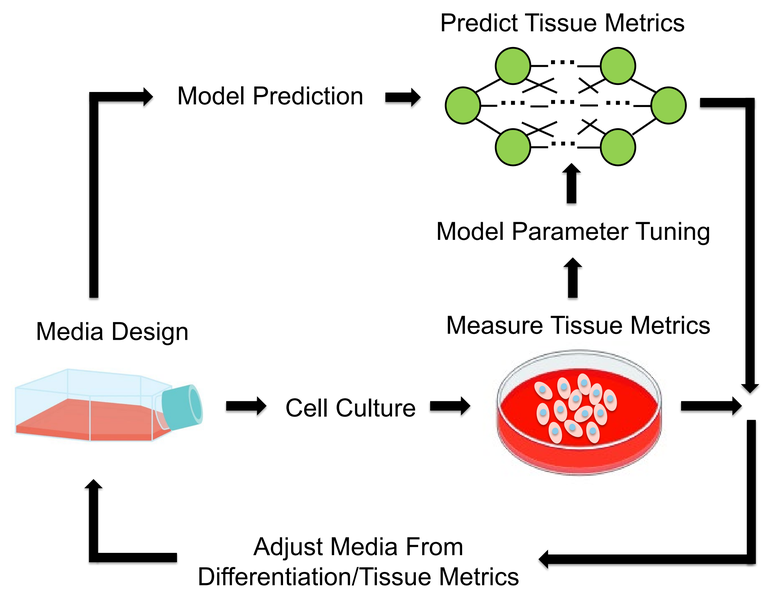

- Machine learning can be used as a design aid in media optimization for tissue and differentiation quality
- Model predictions can be experimentally validated to inform an iterative training process

IMPACT

- Model predictions can reduce the search space for optimal media composition and avoid costly experimentation
- Higher quality tissues allow for more accurate modeling of respiratory viruses and can help expedite treatment development

ACKNOWLEDGEMENTS / REFERENCES

- Bukowy-Bieryłło Z, Daca-Roszak P, Jurczak J, Przystałowska-Macioła H, Jaksik R, Witt M, Ziętkiewicz E. In vitro differentiation of ciliated cells in ALI-cultured human airway epithelium - The framework for functional studies on airway differentiation in ciliopathies. Eur J Cell Biol. 2022 Jan;101(1):151189. doi: 10.1016/j.ejcb.2021.151189. Epub 2021 Dec 2. PMID: 34896770.
- Cozens D, Grahame E, Sutherland E, Taylor G, Berry CC, Davies RL. Development and optimization of a differentiated airway epithelial cell model of the bovine respiratory tract. Sci Rep. 2018 Jan 16;8(1):853. doi: 10.1038/s41598-017-19079-y. PMID: 29339818; PMCID: PMC5770467.
- Gard AL, Luu RJ, Miller CR, Maloney R, Cain BP, Marr EE, Burns DM, Gaibler R, Mulhern TJ, Wong CA, Alladina J, Coppeta JR, Liu P, Wang JP, Azizgolshani H, Fezzie RF, Balestrini JL, Isenberg BC, Medoff BD, Finberg RW, Borenstein JT. High-throughput human primary cell-based airway model for evaluating influenza, coronavirus, or other respiratory viruses in vitro. Sci Rep. 2021 Jul 22;11(1):14961. doi: 10.1038/s41598-021-94095-7. PMID: 34294757; PMCID: PMC8298517.
- Woodall MNJ, Masonou T, Case KM, Smith CM. Human models for COVID-19 research. J Physiol. 2021 Sep;599(18):4255-4267. doi: 10.1113/JP281499. Epub 2021 Aug 17. PMID: 34287894; PMCID: PMC8447334.

Assessing Nontraditional Sensor Utility in Evolving Space Situational Awareness Architectures

Maj Christopher Tommila[1], Dr. Ian Claypool[2], Dr. Olivier de Weck[3]

[1] Draper Scholar, MIT Department of Aeronautics & Astronautics; [2] The Charles Stark Draper Laboratory, Inc.; [3]MIT Department of Aeronautics & Astronautics

The number of satellites in Earth orbit has increased rapidly over the past 5 years, with US Space Command's public catalog now containing over 28,000 tracked satellites and pieces of orbital debris greater than 10 cm in diameter [1]. According to the NASA Orbital Debris Program Office, there are over 100 million manmade objects in Earth orbit greater than 1 mm in diameter, the majority of which remain untracked [2]. Even small pieces of orbital debris, often traveling at relative velocities over 10 km/s, can cause damage to or destroy operational spacecraft. Figure 2 is an image of a damaged Space Shuttle window which was struck by a particle approximately 0.1 mm in diameter; the size of a grain of sand [3]. Research is being conducted to assess the utility of non-traditional sensors as legacy space situational awareness (SSA) sensor networks evolve to keep pace with the growing need for detection and tracking of the manmade objects in Earth orbit. Initial research evaluated the performance and resilience impacts of augmenting a legacy ground-based electro-optical (EO) sensor network with constellations of opportunistic space-based EO sensors. Continuing research seeks to develop a systems design methodology which incorporates operational utility measures, system performance attributes more directly related to high-level mission objectives, to guide the analysis of candidate SSA sensor architectures.

INTRODUCTION

The US Space Command's Space Surveillance Network (SSN), combining ground-based radar and EO sensors with a small complement of space-based EO sensors, provides the preponderance of SSA data to government and commercial spacecraft operators [4]. However, commercial SSA capabilities continue to grow, presenting opportunities to evolve SSA networks like the SSN to incorporate these non-traditional data sources [5]. In addition to dedicated SSA sensors, emerging programs, like DARPA's Space-WATCH, seek to take advantage of the proliferation of commercial spacecraft in near-Earth orbit by using in-situ sensor data, like star tracker imagery, as sources of SSA information [6].

With this rise in sensor diversity has come an increase in literature related to the optimal design and evolution of space surveillance architectures to incorporate multi-domain and multi-modal sensors [7]–[11]. These studies have measured performance using technical figures of merit (FOMs) like resident space object (RSO) state uncertainty [8], minimum observable cross-section [7], coverage area [11], and observational revisit rate [7], [8], [10]. This research assesses whether these technical FOMs adequately capture the emergent performance of a fused sensor network and are sufficient to predict the impact of sensor data on operational decision processes. The goal of this research is to identify and employ operational utility measures in the evolution of legacy SSA sensor networks.

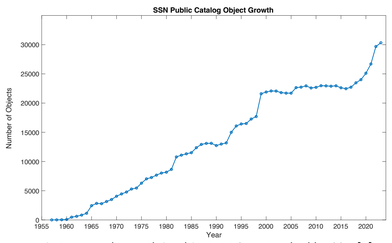

Fig 1: Annual growth in objects >10 cm tracked by SSN [1]

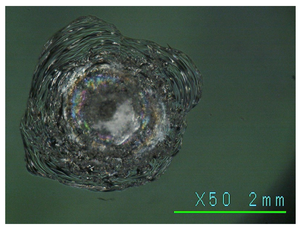

Fig 2: Damage to Space Shuttle Window [3]

METHODS

Initial research evaluated the performance and resilience impacts of augmenting an existing SSA network of Earth-based EO sensors with space-based opportunistic EO sensors [10]. The space-based sensors modeled in this research are described in Table 2 and are opportunistic in that they do not steer to track target RSOs. Instead, the cameras are mounted in body-fixed anti-nadir configurations.

Location	Latitude	Longitude	Altitude (m)
Haleakala, Hawai'i	20.07^o	-156.3^o	3,055
Nairobi, Kenya	-1.17^o	36.49^o	1,795
Albuquerque, New Mexico	35.06^o	-106.36^o	1,514
Exmouth, Western Australia	-21.53^o	114.05^o	650

Table 1: Nominal Ground-Based Sensor Sites [10]

Variable	Type	Range	Units
Inclination	Integer	0 to 100	deg
Number of Planes	Integer	1 to 10	#
Satellites per Plane	Integer	1 to 10	#
Altitude	Fixed	500	km
Field of View	Integer	1,3,5	deg
Solar Exclusion	Fixed	10	deg

Table 2: Space-Based Sensor Design Variables [10]

This research focused primarily on the relative geometry of the observation problem. The primary performance figure of merit (FOM) investigated is maximum observational latency: the amount of time that an RSO is not observable by any sensor in the network. The relationship between sensors and target RSO's can be represented as a bi-partite graph in which edges represent viewing opportunity between a sensor-RSO pair. An object is considered observable, and thus an edge exists, if it meets the criteria below [10].

$$E = \{(u_i, v_j) | C_{FOV}(u_i, v_j) \wedge C_{Illuminated}(v_j) \wedge C_{Sun}(u_i) = 1\}$$

Constraint	Criteria
C_{FOV}	$C_{FOV}(u_i, v_j) = \begin{cases} 1, & v_j \text{ in FOV of } u_i \\ 0, & \text{otherwise} \end{cases}$
$C_{Illuminated}$	$C_{illuminated}(v_j) = \begin{cases} 1, & v_j \text{ is illuminated} \\ 0, & \text{otherwise} \end{cases}$
C_{Solar}	$C_{Solar}(u_i) = \begin{cases} 1, & \text{Sun Excluded} \\ 0, & \text{otherwise} \end{cases}$

Table 3: Edge (Observation) Criteria [10]

RESULTS

Initial test cases simulated observations of 78 RSOs in Medium Earth Orbit (MEO) and Geosynchronous Orbit (GEO) over a 24-hour period with over 3000 sensor architectures. The worst case maximum observational latency is shown in Figure 3 [10]. The total number of satellites required for the space-based sensors is considered a surrogate for cost and a Pareto frontier represents the non-dominated architectures when considering cost and performance [10].

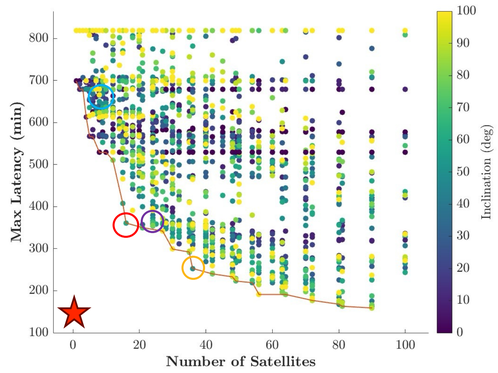

Figure 3: Maximum Latency vs Number of Opportunistic Sensors [7]

Ground site sensor outages were simulated to assess the resilience, or percentage of performance retained in the presence of a disturbance, of the architectures in the figure above. By removing only the ground sensors, this research isolates the impact of the opportunistic space-based sensors on the total system resilience. The figures below show the resilience as a function of the maximum latency FOM.

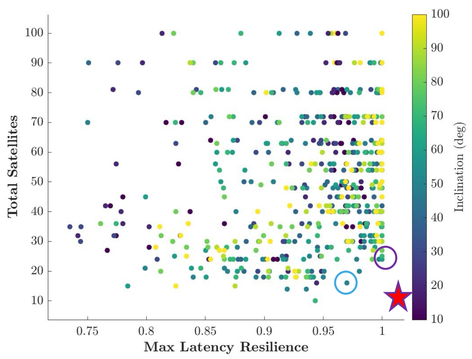

Figure 4: Maximum Latency Resilience vs Number of Opportunistic Sensors [10]

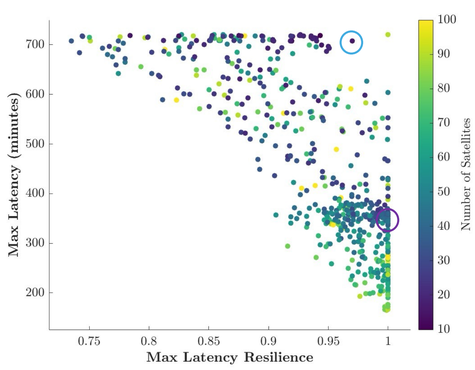

Figure 5: Maximum Latency Resilience vs (Perturbed) Maximum Latency

DISCUSSION

General trends shown in Figures 3-5 suggests that choosing inclinations close to those of the MEO satellites (~55 deg) allows for improved baseline performance and resilience with respect to the maximum latency between observations, especially when balancing cost of the opportunistic sensor network. Table 4 provides a comparison of four architectures which are highlighted on the Pareto frontier in either Figure 3 or 4.

					Units
Max Latency	253	361	730	362	min
Max Latency Resilience	N/A	N/A	0.97	1	
Inclination	50	60	50	60	deg
Number of Planes	6	4	8	4	#
Satellites per Plane	6	4	2	6	#
Total Satellites	36	16	16	24	#

Table 4: Performance and Resilience of Selected Architectures

Table 4 shows that the highest performing architectures are not necessarily resilient to system disturbances. For instance, the architectures circled in yellow and red on Figure 3 are on the Pareto frontier of performance and cost. Yet, their resilience is listed as N/A in Table 4 because, when one or more ground sites are removed, an RSO in the scenario will be unobserved for >24 hours. Table 4 also shows that consideration of an architecture's resilience alone may lead to selection of architectures with low baseline performance. For instance, while the architecture circled in blue on Figures 3-5 maintains 97% of its baseline performance when all four ground sites are removed, its baseline maximum latency was relatively poor at over 12 hours. The architecture circled in purple on Figures 3-5 strikes a balance of proximity to the Pareto frontier of cost and performance while maintaining 100% of its baseline performance in a perturbed environment.

CONCLUSIONS

Initial work introduced in [10] and continued here provides a methodology for considering the potential performance and resilience impacts of incorporating non-traditional sensors in the evolution of SSA sensor networks. Results demonstrate the sensitivity of architecture selection to the FOMs evaluated and thus, the criticality of determining which FOMs best capture the operational utility of SSA architectures. Future research will be focused on identifying these operational utility metrics and incorporating them, along with consideration of sensor fusion processes, in the multi-objective optimized evolution of legacy SSA architectures. Figure 6 is an initial extended design structure matrix (XDSM) [12] showing the relationships between models and simulations in this future analysis.

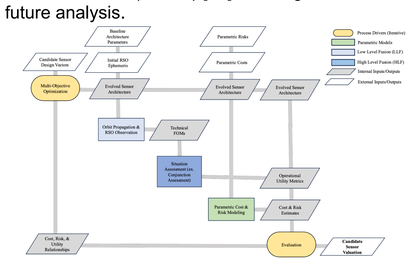

Figure 6: Master Diagram of Continuing Research

ACKNOWLEDGEMENTS & REFERENCES

The authors would like to thank The Charles Stark Draper Laboratory, Inc., and the Draper Scholars program for continued support of this research. The authors would also like to thank DARPA and MIT Lincoln Laboratory for their support of research related to in-situ sensor utilization. The views expressed in this paper are those of the authors and do not reflect the official policy or position of the United States Air Force, Department of Defense, or the U.S. Government.

[1] 18th Space Defense Squadron, "Space-Track.Org," Satellite Catalog. Accessed: Mar. 28, 2023. [Online]. Available: https://www.space-track.org/
[2] "ARES | Orbital Debris Program Office | Frequently Asked Questions." Accessed: Feb. 14, 2024. [Online]. Available: https://orbitaldebris.jsc.nasa.gov/faq/#
[3] "ARES | HyperVelocity Impact Technology | Impact Images | Space Shuttle." Accessed: Feb. 14, 2024. [Online]. Available: https://hvit.jsc.nasa.gov/impact-images/space-shuttle.cfm
[4] STARCOM, "SDP 3-100 Space Domain Awareness Doctrine for Space Forces." USSF, 2023.
[5] US GAO, "Space Situational Awareness: DoD Should Evaluate How It Can Use Commercial Data." Apr. 2023.
[6] DARPA, "Program Solicitation Space-domain Wide Area Tracking and Characterization (Space-WATCH)," Defense Advanced Research Projects Agency, DARPA-PS-23-06, Jan. 2023. [Online]. Available: https://sam.gov/opp/8a0e5857e43c422aa9b86b0cadaa311f/view
[7] J. M. Colombi, J. L. Stern, S. T. Wachtel, D. W. Meyer, and R. G. Cobb, "Multi-Objective Parallel Optimization of Geosynchronous Space Situational Awareness Architectures," Journal of Spacecraft and Rockets, vol. 55, no. 6, pp. 1453–1465, Nov. 2018, doi: 10.2514/1.A34043.
[8] C. Harris, D. Thomas, J. Kadan, D. K. Schroeder, and J. Black, "Expanding the Space Surveillance Network with Space-Based Sensors Using Metaheuristic Optimization Techniques," presented at the AMOS, Maui, HI, 2021.
[9] A. P. Koenig, "A Systems Framework for Multi-Messenger Astronomy," MIT, Cambridge, MA, 2022.
[10] C. D. Tommila, M. P. Jones, and O. de Weck, "Mission Resilience Impacts of Space-Based Opportunistic Sensors in Distributed Space Situational Awareness Architectures," presented at the AIAA SciTech, Orlando, FL, 2024.
[11] A. R. Vasso, R. G. Cobb, J. M. Colombi, B. D. Little, and D. W. Meyer, "Multi-day evaluation of space domain awareness architectures via decision analysis and multi-objective optimization," Journal of Defense Modeling & Simulation, p. 154851292110677, Jan. 2022, doi: 10.1177/15485129211067767.
[12] A. B. Lambe and J. R. R. A. Martins, "Extensions to the design structure matrix for the description of multidisciplinary design, analysis, and optimization processes," Struct Multidisc Optim, vol. 46, no. 2, pp. 273–284, Aug. 2012, doi: 10.1007/s00158-012-0763-y.

Using LLMs for Hierarchical Task Planning: A Human Factors Perspective

Courtney Tse[1,2,3], Nayani Modugula[1], Ifrah Idrees[1], Shreyas Sundara Raman[1], Kelly Sprehn[2], and Stefanie Tellex[1]

[1]Brown University, [2]Draper, [3]Draper Scholar

ABSTRACT: Previous work in robot task planning assumes that handcrafted hierarchical task specifications exist for robotic tasks. However, hand-coding task specification for complex tasks is difficult, as it requires significant domain knowledge and engineering effort. LLMs offer a source of knowledge and common sense that have the potential to reduce this workload and effort, and build calibrated trust. We use natural language task descriptions with LLMs for complex task planning. The distribution of tasks that we target are hierarchical in nature, which means they can be further divided into subgoals and primitive actions that the robot can execute. We compare our results against baselines to demonstrate the efficacy of LLMs in hierarchical task planning and execution, and we evaluate trust and usability from the human perspective.

INTRODUCTION

- The primary objective of this project is to revolutionize human-robot interaction by advancing the capabilities of robots through the integration of natural language commands. Our work focuses on modeling complex, multistep robot tasks such as arranging laundry and washing dishes to enable more natural communication between human and robot.

METHODS

- We propose an approach to generate hierarchical task plans that uses a Large Language Model (LLM) to provide instructions for high-level, multi-step tasks and execute them in the environment. We also test our approach's feasibility in generating hierarchical task plans by identifying essential characteristics such as natural language proficiency, hierarchical task organization, and handling of order-agnostic instructions to generate hierarchical task plans.
- Our approach builds upon GPT 3.5, an OpenAI-developed model. We use in-context learning to generate task plans for hierarchical tasks, which are then parsed and mapped to the action space of the agent for execution in the environment. We aim to generate task plans that lead to successful task completion. We conduct an ablation study to identify task patterns that cause failures in existing task planners, such as rigidly coded plans, a lack of generalized solutions, and failure to handle constraints within prompts. Through an iterative process of evaluating baselines and identifying limitations, we enhanced our prompt-engineering approach for the task planner to support hierarchical tasks and address these shortcomings. We tested our task planners in the VirtualHome environment, a simulator replicating household activities, and compared them with the SayCan baseline[1].

RESULTS

- We compared and evaluated the performance of two robotic task planning approaches-- the baseline, SayCan [1], and our hierarchical prompting approach-- for 100 household tasks in a VirtualHome simulator environment [2]. Our evaluation was based on three metrics: percentage executability, percentage parsability, and longest common subsequence (LCS). A lower percentage executability means that the agent or robot in the simulated environment was unable to execute all the generated steps. Parsability refers to the percentage of steps that can be analyzed from VirtualHome. Our prompting approach improved on all three metrics for the 100 tasks that are hierarchical in nature.

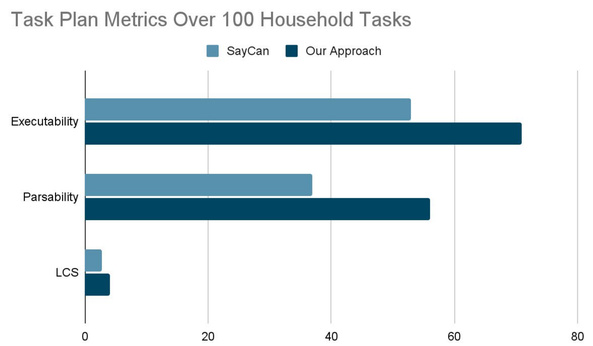

- In our preliminary qualitative results, we achieved significant improvements in the LLM output. For example, the LLM for the task “wash teeth” identified hierarchical goals such as “walk to the toilet” and further split the task into smaller sub-goals like “find toothbrush holder” and “squeeze toothpaste.” This is unlike the plan generated by the baseline SayCan, which lacked the hierarchical component of goals and subgoals. Our preliminary findings suggest that our hierarchical prompting approach can improve the task planning performance for household tasks in the VirtualHome environment.

DISCUSSION

- We expect to be able to engineer prompts that properly translate hierarchical tasks for robot task plans. Hierarchical tasks involve a certain structure that is different from linear tasks, where each subtask is completed in order. For example, if the task is “clean the kitchen,” this task would contain a hierarchy of subtasks, such as “wash the dishes,” “wipe the counter,” “sweep the floor,” and each subtask can be broken down further into more subtasks. Wash the dishes may include “handwash the pots” and “load the dishwasher.” These tasks form a hierarchy where order of tasks might or might not be specified.
- Currently these tasks are difficult to be translated into task plans for robots because of their unique structure, but we plan to make progress toward translating these types of tasks into executable task plans.

CONCLUSIONS

- Using LLMs for human machine/robot interaction effectively allows users to communicate with robots using everyday language.
- Prompt engineering can be crucial for obtaining accurate, relevant, and contextually appropriate outputs from the model. In the case of task-oriented prompts, the wording and structure of the prompt become crucial to ensure the model understands and generates an executable plan for the intended household task.

REFERENCES

- [1] Ahn, Michael, et al. "Do as i can, not as i say: Grounding language in robotic affordances." arXiv preprint arXiv:2204.01691 (2022).
- [2] X. Puig, K. Ra, M. Boben, J. Li, T. Wang, S. Fidler, and A. Torralba, “VirtualHome: Simulating Household Activities via Programs,” in Proceedings of the IEEE Conference on Computer Vision and Pattern Recognition, 2018, pp. 8494–8502.

Multi-Agent Reinforcement Learning for Autonomous Robotics

Caroline Vincent (Draper Scholar)[1,2], Michael Ricard[1], Begum Cannataro[1], and Sertac Karaman[2]

[1]Draper, [2]Massachusetts Institute of Technology

ABSTRACT: Multi-agent robotic technology requires complex motion planning for agents to successfully collaborate at increasingly high speeds without collisions. This work applies reinforcement learning to an autonomous multi-agent system to teach agents within a swarm to complete tasks without colliding into obstacles or other agents. The developed architecture incorporates flexible mechanisms enabling the system's potential for future applications across various scenarios with real-world uncertainties.

INTRODUCTION

- Autonomous robotics provide novel solutions to ordinary problems
- Multi-agent systems greatly scale the impact of integrating robotics into real-world applications
- Major barrier to implementation is the complex motion planning required to avoid collisions among agents and obstacles

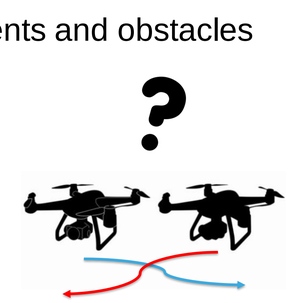

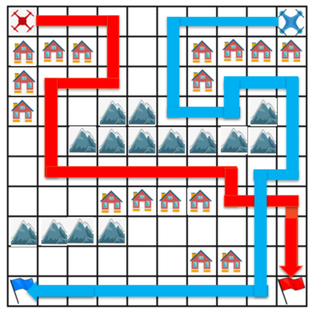

METHODS

- Centralized reinforcement learning (RL)
- Conducting simulations in a custom environment built in OpenAI Gym to generate the states, agents, actions, obstacles, goals, reward system
- Training the model with RL algorithm "Proximal Policy Optimization (PPO)" to generate policies
- Deploying RL techniques such as a "warm start" to enhance training efficiency
- Testing many simulation environments encompassing a range of real-world applications such as a narrow passageway and densely populated terrain

RESULTS

- Two agents in a 10x10 grid with randomized start locations and fixed goal locations
- "Warm" start - first trained them without any obstacles so they learn to navigate without colliding into each other

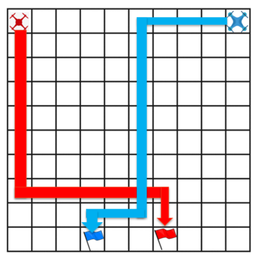

- One trained without obstacles, feed the model a new environment with obstacles
- "Warm" start vs "cold" start with obstacles:

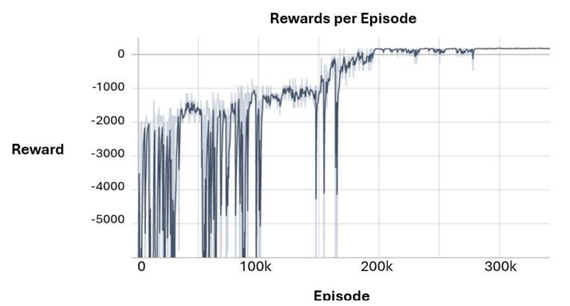

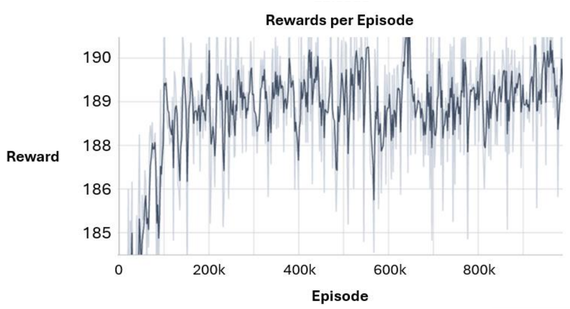

- Example mastered scenario: narrow passage
- Learned behavior: wait for each other to go one at a time

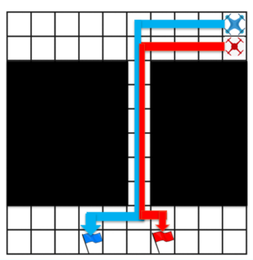

DISCUSSION

- The number of agents, arrangement of obstacles, and grid size are adjustable to form new scenarios for agents to train on and solve
- The flexible architecture allows this model to fit a variety of solution spaces / applications; all that is needed is to retrain rather than redesign
- Using a warm start without obstacles enhances the learning efficiency by breaking the problem into several pieces to solve one at a time

CONCLUSIONS

- The flexible mechanisms incorporated in this architecture allow this work to apply to a range of use cases that contain differing number or agents, environment sizes, and obstacles
- Using RL to solve multi-agent motion planning is far more robust than fixed algorithms for real-world applications that incorporate uncertainty because of its adaptability and generalization

ACKNOWLEDGEMENTS

- Draper Advisors: Michael Ricard, Begum Cannataro
- MIT Advisors: Sertac Karaman, Andrea Henshall

Design Optimization for Impact Absorption with Machine Learning

Charles Wade[1], Devon Beck[2], Robert MacCurdy[3]

[1]Draper Scholar, University of Colorado Boulder, [2]The Charles Stark Draper Laboratory
[3]University of Colorado Boulder

ABSTRACT: We investigate the optimization of plate lattice structures for enhanced impact absorption through specific simulation and machine learning techniques. Our aim is to surpass the limitations of conventional impact mitigation materials, such as foams or packing peanuts, by leveraging automated, optimization-driven design. A Finite Element Analysis (FEA) model enables the rapid evaluation of thousands of plate lattice designs under varied impact conditions. We use this performance data to train a neural network, facilitating fast and accurate predictions of design and impact parameter performance. This approach sidesteps the computational demands of direct FEA simulation, scaling our evaluation space to millions of design candidates. Employing a genetic optimizer, with the neural network surrogate model as the fitness evaluator, allows us to discover geometries that yield the best performance. Our method not only aids in identifying geometries engineered for optimal performance across a range of impact energies but also enables the rapid assessment of millions of design candidates, marking a notable advance in the field of impact-absorbing structures.

Motivation

Standard Foams

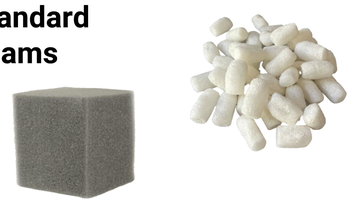

Architected Materials

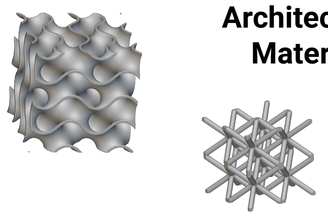

- Cannot be tuned beyond density and quantity
- Stochastic geometry

- Many tunable parameters
- Architected geometry

Need more protection from larger impacts?

➖ *Use more material* | ➕ *Optimize the geometry*

Architected Materials: The Plate Lattice

Our research focuses on the plate lattice, which provides **key advantages over other structures**:

- **Superior tunability** of structure's response to specific impact energies (wall thickness and pre-buckling).
- **Spatial Grading** of both wall thickness and pre-buckling allows for greater control over the impact absorption profile, enabling the customization of the structure for a wide spectrum of impact energies.
- **Easily 3D printed**

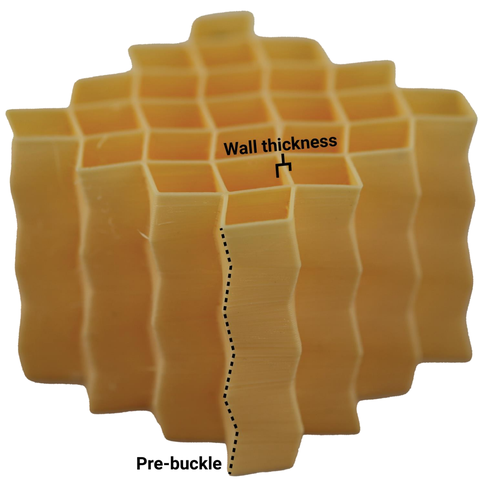

Finite Element Simulation

A high-fidelity finite element simulation can accurately predict the performance of set of design parameters*.

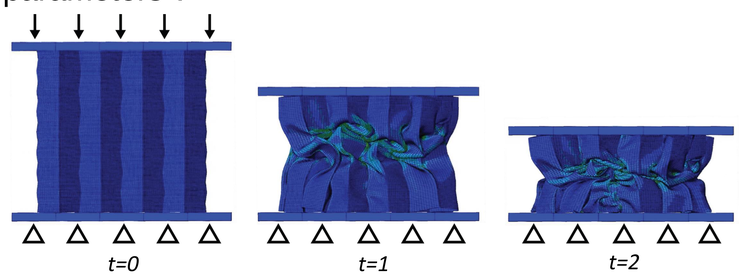

Automated Design Synthesis

Use *simulation* and *optimization* to discover the best designs

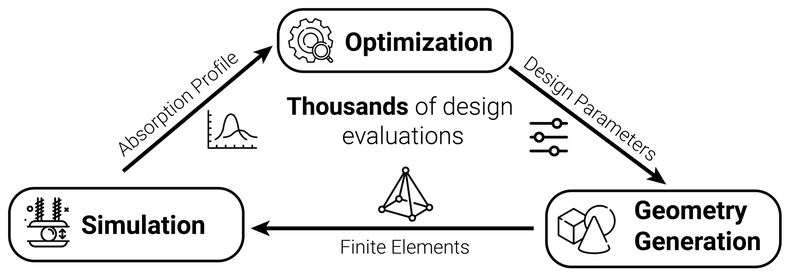

Bottleneck: Evaluating the designs with simulation is computationally expensive. *This limits how much of the design space we can explore.*

Surrogate Modeling

Can we use *machine learning* to *replace simulations* in the optimization loop?

- Given a design and impact scenario, predict the physical performance

~ 5,000 real simulations ➡ Train a network ➡ 93% accuracy at predicting performance of designs (compared with simulation)

* Finite element simulation model has an average of 7% error compared with real world testing

A single evaluation of the surrogate model takes milliseconds compared with several minuets in simulation.

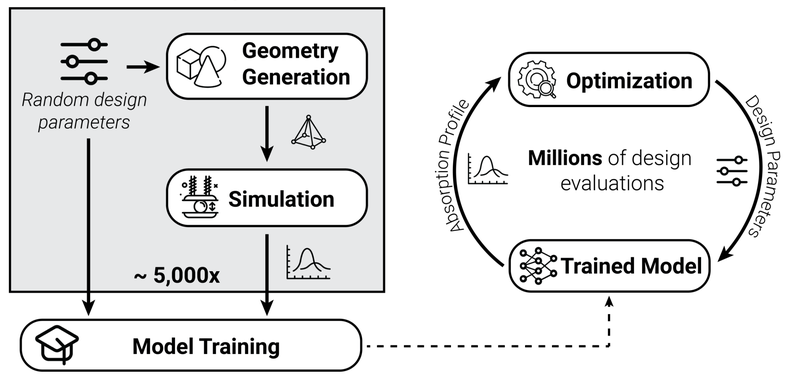

Upshot: Surrogate modeling expands design space exploration from thousands of candidates to millions of candidates

Results & Conclusion

- A two-objective (high and low impact energies) optimization study was conducted
- Pareto frontier plot below represents the tradeoffs between the best designs candidates

Goal: *Minimize both axes*

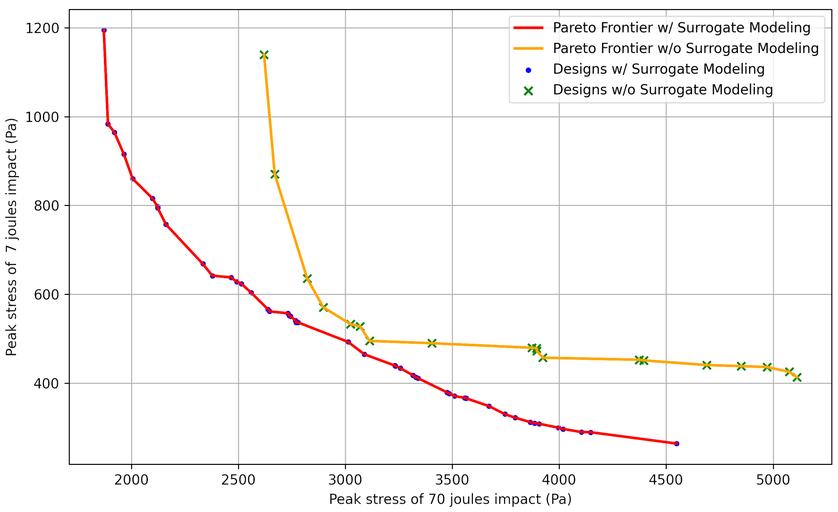

Key takeaway: using our *surrogate model* the automated design process *discovered superior designs* when compared with *using simulation alone*

A Decision-Theoretic Framework for Vision-based Sensing and Control

Eric Wendel[1,3], John Baillieul[1], Joseph Hollmann[2]

[1]Boston University Systems Engineering Division, [2]The Charles Stark Draper Laboratory, Inc., [3]Draper Scholar

ABSTRACT: Where should a robot look when it steers [5]? How do autonomous systems measure risk and make decisions? Our research applies statistical decision theory in order to understand how a particular class of real-time SLAM algorithms processes visual information in service of a particular visual navigation task. Focusing on the simplest case of a monocular camera moving straight down a hallway, we identify the central role of the Fisher Information Matrix in determining the performance of a robot as it attempts to detect interesting visual features and obstacles in its path.

INTRODUCTION

Our work is focused on the performance of **photometric bundle adjustment (PBA)** algorithms for visual navigation tasks requiring joint estimation and control. We are specifically interested in DSO [1] and SVO [2] as prototypical (semi-)**direct methods** utilizing large-scale, real-time **Gauss-Newton solvers** in SLAM architectures with **strongly coupled frontend and backend.**

METHODS

Visual navigation requires estimating functions of the **scene and motion parameters**

$$\theta_t = (\rho_t, u_t), \xi_t \in \boldsymbol{R^3}\times\boldsymbol{R^6}$$

(ρ_t, u_t) = point feature inverse scene depth & pixel location at time t

$\xi_t = (\omega_t, v_t)$ = camera angular & linear velocity

Monocular Visual Odometry (VO) performance relies on accurate estimates of the **loom frequency**

$$\rho_t v_t \in \boldsymbol{R^3}\ \ [Hz]$$

from observations of **optical flow**, modeled as increments of the Itô SDE

$$du_t = h(\theta_t)dt + \Sigma^{1/2}dw_t$$

$\dot{u}_t = h(\theta_t)$ = optical flow ODE

dw_t = standard Brownian motion

The **Cramér-Rao Lower Bound (CRLB)** on unbiased loom frequency estimates is obtained from the **Fisher Information Matrix (FIM)**

$$J(\theta_t) = -E\left[\nabla_\theta^2 \log p_{\theta_t}\right]^{-1}$$

where $p_{\theta_t} = N(h(\theta_t), \Sigma)$ is the likelihood of a discrete-time optical flow observation.

The figures at right show the loom frequency CRLB as a function of the number of images, for point features sampled from a typical hallway scene.

RESULTS

For the simplest case of straight-line motion aligned with the optical axis, the **loom frequency CRLB** decreases with each image, and varies inversely with:

1. point feature distance from the optical axis normalized by the Brownian motion intensity, and
2. the loom-to-frame-rate ratio $\rho_t v_t / f$, where $f = 1/\Delta t$ is the camera's sampling rate.

For $N \geq 6$ images the CRLB decreases as $N^{-1/2}$. The **real-time performance** of PBA is bounded by the CRLB in the non-asymptotic regime $N < 6$.

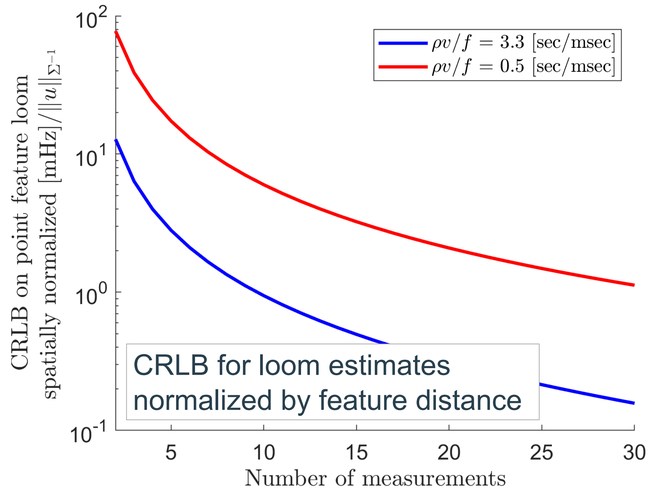

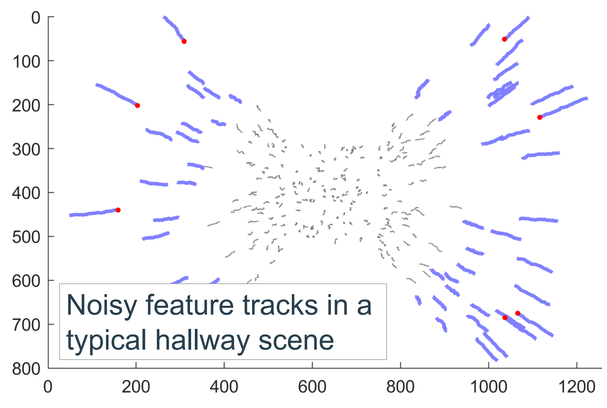

DISCUSSION

How can a robot visually detect looming obstacles? Gauss-Newton algorithms estimate loom by solving a sequence of **Binary Hypothesis Tests (BHTs)** of the (notional) form

$$P_i: \quad \hat{\theta}_t = \theta^{(i)}$$

$$Q_i: \quad \hat{\theta}_t = \theta^{(i)} + \delta\theta$$

where $\theta^{(i)}$ is the estimate of θ_t at the i^{th} iteration, and the alternative hypothesis Q_i is constructed from the **locally quadratic property** of the **Kullback-Leibler divergence** [3]

$$-E\left[\ln \frac{dP_i}{dQ_i}\right] \approx \ln p_{\theta^{(i)}} + \delta\theta^T \nabla_\theta \ln p_{\theta^{(i)}} + \delta\theta^T J\left(\theta^{(i)}\right)\delta\theta$$

We conclude that in a PBA algorithm the **probability of obstacle detection error** depends on a **sequence of local tests** [4] each defined by a FIM $J\left(\theta^{(i)}\right)$.

CONCLUSIONS

- The loom frequency **CRLB decreases faster than $N^{-1/2}$** for $N < 6$ images.
- The FIM is central to **sequential analysis** of photometric bundle adjustment (PBA) algorithms.

REFERENCES

[1] Engel, J., Koltun, V. and Cremers, D., 2017. Direct sparse odometry. IEEE transactions on pattern analysis and machine intelligence, 40(3), pp.611-625.

[2] Forster, C., Pizzoli, M. and Scaramuzza, D., 2014, May. SVO: Fast semi-direct monocular visual odometry. In 2014 IEEE international conference on robotics and automation (ICRA) (pp. 15-22). IEEE.

[3] Polyanskiy, Y. and Wu, Y., 2024. Information theory: From coding to learning.

[4] Basseville, M. and Benveniste, A. eds., 1986. Detection of abrupt changes in signals and dynamical systems. Berlin, Heidelberg: Springer Berlin Heidelberg.

[5] Land, M.F. and Lee, D.N., 1994. Where we look when we steer. Nature, 369(6483), pp.742-744.

Enabling Language Model Execution of Untrained Tools with Retrieval Augmented Generation

Finn Westenfelder[12], Stephen Moskal[2], Una May O'Reilly[2], and Silviu Chiricescu[3]

[1]Draper Scholar, [2]Massachusetts Institute of Technology, [3]Draper Laboratory

ABSTRACT: Language Models (LMs) contain large cybersecurity knowledge bases, enabling the automation of penetrating testing tasks. LM-based penetrating testing frameworks can execute well-documented public tools but fail to execute private tools absent from the LM's training data. This research shows that Retrieval Augmented Generation (RAG) enables autonomous frameworks to utilize private toolkits and recommends methods for improving retrieval and generation accuracy.

INTRODUCTION

Background:

- Language models (LMs) contain large cybersecurity knowledge bases [1] enabling automated penetration testing [2,3]
- Automated frameworks fail to execute private tools (scripts, binaries, exploits, etc.) absent from the LM's training data
- Retrieval Augmented Generation (RAG) [4] enables LMs to access private external data and improves generation accuracy
  - Retrieval: What is the correct tool for this task?
  - Generation: What is the command for this tool to execute the task?
- This research examines how data tags and varying context levels impact RAG for tool retrieval and command generation

Hypotheses:

- (1) If embedded context is tagged, then retrieval accuracy will increase because tagging increases semantic similarity
- (2) Maximum retrieval and generation accuracy will occur at an intermediate context level because too much or too little context will decrease accuracy due to a lack of information or the lost-in-the-middle (LITM) phenomenon [5], respectively

METHODS

Synthetic Dataset:

- We created a small synthetic dataset of 15 penetration testing tools to simulate an organization's private toolkit
- Each datapoint includes:
- Tool name, version, operating system, description, help message, specification, and example commands
  - Combinations of this information form different context levels
- MITRE ATT&CK framework tactic and technique tags
- Tool retrieval prompts including MITRE ATT&CK tags
- Command generation prompts with validation regexes

Tool Retrieval Testing:

- Embedding models create embeddings for retrieval prompts and context levels with and without tags
- Embeddings are compared with cosine similarity

Command Generation Testing:

- Language models generate commands based on generation prompts including varying context levels
- Generated commands are compared with verified regexes

RESULTS

Tool Retrieval Results:

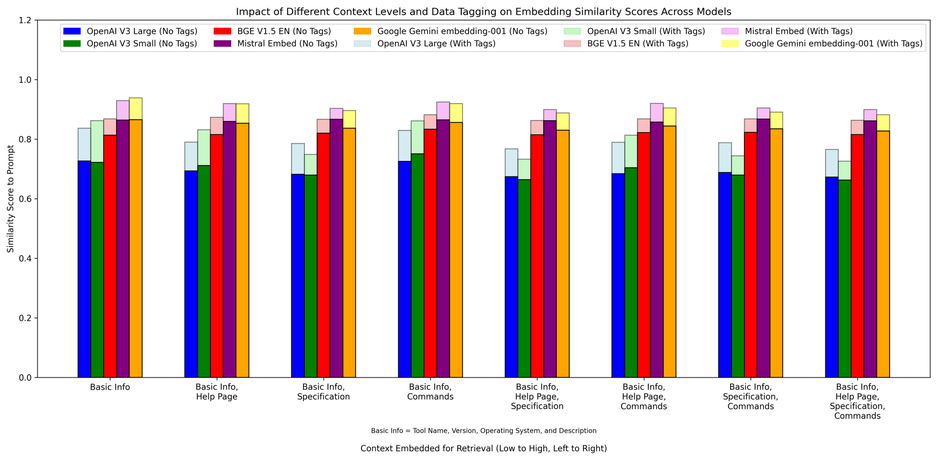

Command Generation Results:

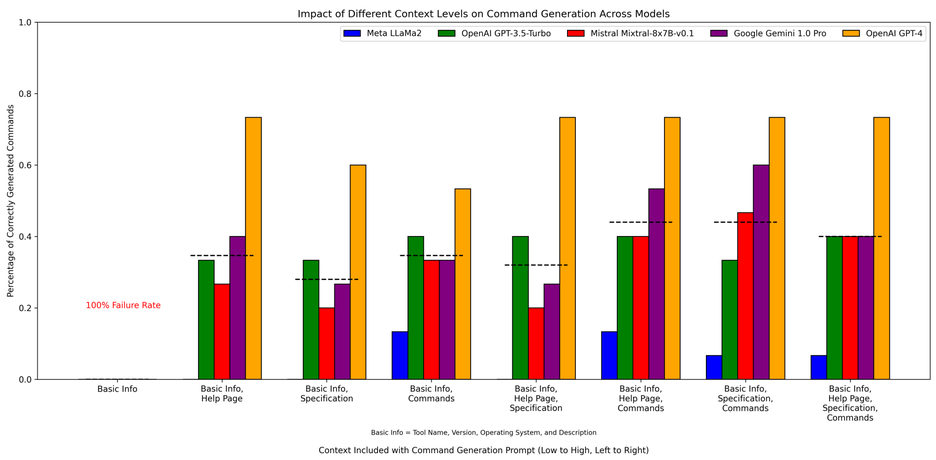

Failed Command Generation Example:

Base Prompt: Output a command to accomplish the following task. Use the additional information to format the tool parameters. Only include the parameters provided in the prompt. Do not override default parameters unless specified in the prompt. Only output the command. Do not include any additional information. Do not include markdown or other formatting.

Command Generation Prompt (Penetration Testing Task): Run a verbose scan on http://www.domain.com and save the report to C:\users\me\desktop\domain-report.txt

Context Level: Tool name, version, operating system, description, and specification

Meta LLaMa2 Response: Sure! Here's an example command that you can use to accomplish the task you described: `FastDirCrack.exe -u http://www.domain.com -wl <wordlist> -t 5 -sp / -v –rl C:\users\me\desktop\domain-report.txt`

= Invalid Parameters **= Assumed Parameters** **= Additional Text**

DISCUSSION

- Analysis of results is limited due to the small size of the synthetic testing dataset

Retrieval Results:

- Tagging tools with MITRE ATT&CK tactics and techniques increases semantic similarity, improving retrieval accuracy across models [Supports (1)]
- Similarity scores do not change significantly between context levels, indicating there is no optimal level or the experiment fails to isolate important context [Refutes (2)]

Generation Results:

- All models fail to generate commands at the lowest context level due to a lack of information [Supports (2)]
- Despite higher average accuracy at higher context levels, accuracy varies greatly between models, indicating internal model capabilities are more significant than using an optimal context level for command generation [Refutes (2)]

CONCLUSIONS

- RAG enables automated frameworks to retrieve and execute private tools that were absent from training data
- While varying context levels do not significantly impact retrieval accuracy, tagging improves semantic similarity
- A minimum context including a help page, specification, or example commands is necessary for command generation
- Beyond the minimum context, generation accuracy depends more on the capabilities of the model than the context level

Future Work:

- Create more data and study the impact of dataset size
- Test generation accuracy with source code as context
- Compare RAG results with a small finetuned LM

ACKNOWLEDGEMENTS / REFERENCES

[1] Ethan Garza, Stephen Moskal, Erik Hemberg, and Una-May O'Reilly. Assessing large language model's knowledge of threat behavior in mitre att&ck, 2023.

[2] Stephen Moskal, Sam Laney, Erik Hemberg, and Una-May O'Reilly. Llms killed the script kiddie: How agents supported by large language models change the landscape of network threat testing, 2023.

[3] Gelei Deng, Yi Liu, V´ictor Mayoral-Vilches, Peng Liu, Yuekang Li, Yuan Xu, Tianwei Zhang, Yang Liu, Martin Pinzger, and Stefan Rass. Pentestgpt: An llm-empowered automatic penetration testing tool, 2023.

[4] Peitian Zhang, Shitao Xiao, Zheng Liu, Zhicheng Dou, and Jian-Yun Nie. Retrieve anything to augment large language models, 2023.

[5] Nelson F. Liu, Kevin Lin, John Hewitt, Ashwin Paranjape, Michele Bevilacqua, Fabio Petroni, Percy Liang. Lost in the Middle: How Language Models Use Long Contexts, 2023.